AES/RE/13-11 **Comparative study of the S-shaped and Hoek-Brown failure criterion by finite-difference modelling, Northparkes, NSW, Australia**

28/06/2013 **M.H.A. Korenromp**

TUDelft Delft University of Technology

Challenge the future

Title	:	Comparative study of the S-shaped and Hoek-Brown failure criterion by finite-difference modelling, Northparkes, NSW, Australia
Author	:	M.H.A. Korenromp
Date	:	28 June 2013
Professors	:	Dr. M.W.N. Buxton
		Dr. ir. D.J.M. Ngan-Tillard
External supervisors	:	Dr. A.S.E. Moss
		Ir. G.J. van Hout
TA Report number	:	AES/RE/13-11
Postal Address	:	Section for Resource Engineering
		Department of Geoscience & Engineering
		Delft University of Technology
		P.O. Box 5028
		The Netherlands
Telephone	:	(31) 15 2781328 (secretary)
Telefax	:	(31) 15 2781189

Abstract

Cave mining operations produce bulked ore from self-sustainable propagating caves in high stress regimes. Undercut development creates even higher abutment stresses and a stress-shadow which have significant impact on extraction level stability. Geotechnical assessment of the infrastructure is vital for the safety performance and continuity of production. Northparkes Mines (NPM) is a block caving operation located in New South Wales, Australia. They deployed a post-undercutting strategy to develop the E48 deposit, exposing all tunnels and draw bells at the extraction level to high abutment stresses. Convergence of the extraction drifts and relative displacements in the brittle rock mass have been monitored during this process.

The current industry standard for geotechnical analyses of hard rock in stressed environments is the non-linear Hoek-Brown failure criterion. It estimates the resistance to shear failure of jointed to heavily jointed rock masses by rock mass strength degradation. However, brittle rock masses fail in a tensile mode in low confinement zones around excavations. The most recently developed hypothesis in this field of work is the S-shaped failure criterion. It assumes spalling at low confinement and an inhibition of tensile failure processes at relatively high confinements, where shear bands are the dominant structures causing failure. In other words, it suggests that the Hoek-Brown failure criterion underestimates the rock mass strength in highly confined zones of brittle rock masses. Validated principles to establish the rate of degradation in high confinement zones are currently not available and the S-shaped approach is therefore not yet ready for engineering purposes.

The aim of this project is to indicate differences in results derived from numerical modelling when either the Hoek-Brown or the S-shaped failure criterion is applied and relate those differences to geotechnical data obtained at NPM. A three-dimensional, parameterized environment has been created by applying the mesh generator *KUBRIX* Geo on a Computer-Aided Design of the extraction level. Undercut development was simulated by an adequate stress-path using the Finite Difference Method in FLAC^{3D}.

An evaluation of the response of extensometer stations to an advancing undercut front at NPM has revealed immediate and abrupt dilative behaviour of the rock mass once the cave line has passed. Scenarios using the S-shaped failure criterion were able to simulate this behaviour if rock mass degradation was sufficiently contained at high confinement, while the scenario using the Hoek-Brown failure criterion was unable to do so. The extent of yield, stresses in pillar cores and stress-strain responses of the rock mass indicate stronger pillars in scenarios using the S-shaped failure criterion. The S-shaped failure criterion is a state-of-the-art approach and although the basic concept is finding more support, the definition of its parameters will require more research in the coming years. This project improves the understanding of the application of the S-shaped failure criterion in continuum modelling and highlights its strengths and shortcomings.

Contents

Appendices

List of figures

List of tables

Acknowledgements

Nomenclature

It has been necessary to alter the notation of some parameters with respect to their original notation in papers in order to be consistent throughout the report.

σ_{ij}	Pa	Component of the stress tensor
σ_1	Pa	Major principal stress
σ_2	Pa	Intermediate principal stress
σ_3	Pa	Minor principal stress
σ_v	Pa	Vertical stress
σ_h	Pa	Horizontal stress
σ_{UCS}	Pa	Unconfined compressive strength: intact sample
σ_c	Pa	Unconfined compressive strength: rock mass
σ_{cm}	Pa	Global rock mass strength
σ_{ci}	Pa	Crack initiation stress
σ_{cd}	Pa	Crack coalescence stress
σ_{tot}	Pa	Total stress
σ_{ind}	Pa	Induced stress
σ_{tec}	Pa	Tectonic stress component
σ_{grav}	Pa	Gravitational stress component
σ_n'	Pa	Effective normal stress
σ_t	Pa	Tensile strength
σ_{cn}	Pa	Contact normal stress
ε_{ij}^p		Component of the plastic strain tensor
ε_1^p		Plastic major principal strain
ε_3^p		plastic minor principal strain
ε_v^p		Plastic volumetric strain
$\dot{\varepsilon}_1^p$		Axial plastic strain increment
$\dot{\varepsilon}_3^p$		Lateral plastic strain increment
$\dot{\varepsilon}_v^p$		Volumetric plastic strain increment
e_3^{p*}		Critical minimum principal strain
e_s^{p*}		Critical shear plastic strain
ε_c^f		Critical strain for frictional strength
ε_c^p		Critical strain for cohesional strength
A_0	m^2	True contact area
A_1	m^2	Assumed contact area
C_m		Degradation factor in H-B failure criterion
C_s		Degradation factor in H-B failure criterion
D_e	m	Equivalent dimension
E_h	Pa	Horizontal elastic modulus
E_{av}	Pa	Average Young's Modulus
E_i	Pa	Elastic Modulus of intact rock
E_{rm}	Pa	Elastic Modulus of the rock mass
E_s	Pa	Secant Young's Modulus
E_t	Pa	Tangent Young's Modulus
J_C		Joint condition
J_a		Discontinuity alteration
J_n		Number of discontinuity sets
J_r		Discontinuity roughness
J_w		Discontinuity water reduction factor
V_b	m^3	Block volume

a_g		H-B plastic potential "curvature" parameter
c_l	m	Half crack length
m_b		Hoek-Brown "friction" parameter of the rock mass
m_g		H-B plastic potential "dilation" parameter
m_i		Hoek-Brown "friction" parameter of intact rock
s_g		H-B plastic potential parameter
γ_f		Flow parameter
γ_p		Plastic shear strain
γ_s	N/m	Specific surface energy
υ_{rm}		Poisson's ratio of the rock mass
ϕ'	$^\circ$	Peak drained friction angle
ϕ_b	$^\circ$	Basic friction angle
ϕ_r	$^\circ$	Residual friction angle
B		Bulking factor
D		Disturbance factor
E	Pa	Elastic Modulus
F		Plastic yield stress function
G	Pa	Shear Modulus
K	Pa	Bulk Modulus
M		Degradation factor above the spalling limit
R		Equivalent roughness factor
S	Pa	Particle strength factor
V	m^3	Volume
a		Hoek-Brown "curvature" parameter
c	Pa	Cohesion
d	m	Diameter
g		Plastic potential function
i		Structural component of strength
k		Horizontal-to-vertical *in situ* stress ratio
n		Porosity
s		Hoek-Brown parameter
z	m	Depth
γ	N/m^3	Unit weight
ρ	kg/m^3	Density
τ	Pa	Shear stress
υ		Poisson's Ratio
ψ	$^\circ$	Dilation angle

Abbreviations

ASCII	American Standard Code for Information Interchange
BRIC	Brazil, Russia, India, China
CAD	Computer-Aided Design
CWFS	Cohesion Weakening and Frictional Strengthening
DDL	Dynamic Link Library
DEM	Discrete Element Method
DFN	Discrete Fracture Network
DIP	Digital Image Processing
ESR	Excavation Support Ratio
FEM	Finite Element Model
FLAC^{3D}	Fast Langrangian Analysis of Continua in 3 Dimensions
FQS	Faulted, quartz-sericite shear zones
GDP	Gross Domestic Product
GRC	Ground Reaction Curve
GSI	Geological Strength Index
HoD	Height of Draw
HR	Hydraulic Radius
IRMR	Intact Rock Mass Rating
JCR	Joint Condition Rating
JSR	Joint Spacing Rating
LDP	Longitudinal Deformation Profile
LHD	Load Haul Dump machine
LTE	Latitic lavas and sills
LTI	Lost Time Incident
MPBX	Multi-Point Borehole eXtensometer
MRMR	Mining Rock Mass Rating
NPM	Northparkes Mines
NPV	Net Present Value
NURBS	Non-Uniform Rational Basis Spline
POR	Quartz Monzonite Porphory
Q Index	Rock Tunnelling Quality Index
RBS	Rock Block Strength
RCM	Resolution Copper Mine
RCM	Resolution Copper Mine
RMR	Rock Mass Rating
ROM	Run-Of-Mine
RQD	Rock Quality Designation
SMART	Stretch Measurement to Assess Reinforcement Tension
SRC	Support Reaction Curve
SRF	Stress Reduction Factor
SRM	Synthetic Rock Mass
STL	STereoLithography
TBS	Tunnel Boring System
TDR	Time Domain Reflectometry
UCS	Uniaxial Compressive Strength
	Unconfined Compressive Strength
UDM	User-Defined Model
VSS	Volcanic sandstones

1 Introduction

The strong demand for copper, in particular from China and India, will remain high in the coming years, although significant economic uncertainties are present worldwide. As shown in Figure 1, the market price for copper has been high for a number of years, stimulating companies to invest and develop new ore bodies. Some of these projects reach their production stage in 2013, creating a small copper surplus on the market for this year and the three years after. Mid and long term growth drivers remain as well as concerns of limited supply in the future. Thus, copper deficits are predicted for the 2020's. (White, 2013)
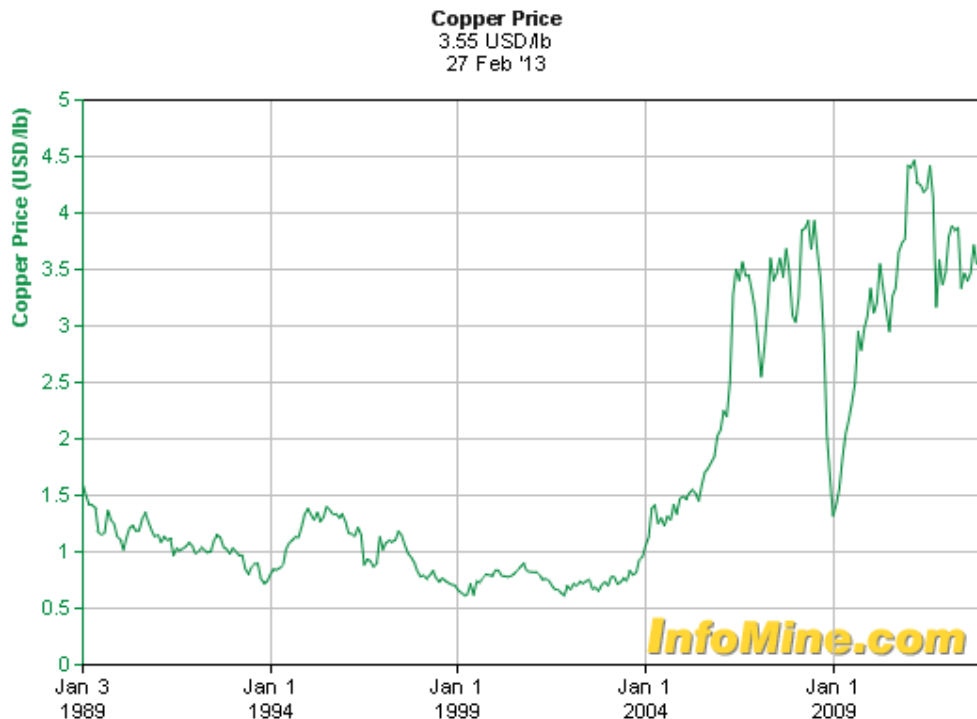
Figure 1: Copper price (InfoMine, 2013)

High copper demand, driving the prices upwards, is fed by urbanisation, industrialisation and prosperity in Asia, China and India in particular. Since China alone accounts for 40% of the world's copper demand, it is justified to focus on this part of the world. The increase of urban population in China will result in 221 cities with more than 1 million inhabitants by 2025. For comparison, the whole European continent only has 35 such cities (White, 2013). The construction of these cities will need high amounts of copper. The prosperity of these urban citizens, if measured as a country's GDP per capita, is catching up rapidly with other Western countries around the world. More and more Chinese want washing machines and electrical applications like computers, tablets and television screens. This increase in power demand requires a more extensive power network, existing of kilometres of copper cables. This urge for construction and electronic consumables is driving the copper industry today. (Rosling, 2013)

Currently, copper is produced mainly from open cut operations, but in general underground mines will start to play a more dominant role in the worldwide ore supply as shown in Figure 2. Developments in block and panel caving methods will contribute to a large extent to this increase in production from underground mines.
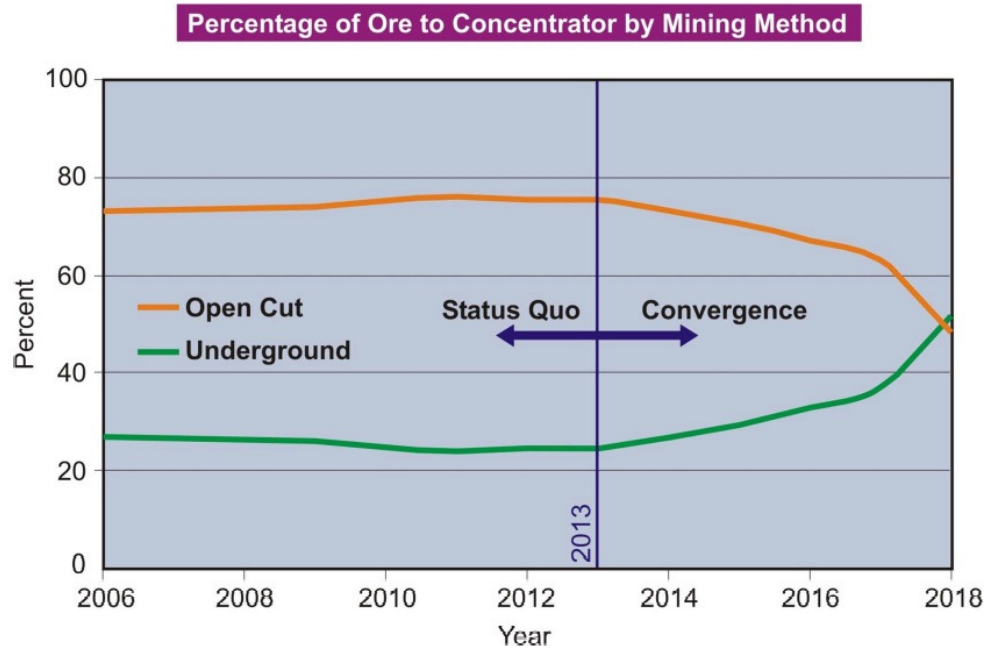
Figure 2: Source of the world ore supply. (Moss, 2011)

Undercutting strategies in the development of caving operations increase the rate of fracturing of the rock mass at the underlying infrastructure due to abutment stresses. Subsequent relaxation of the fractured rock mass results in further damage. Therefore, the geotechnical assessment of the rock mass is essential for a stable and safe design of the extraction and undercut level. Since continuity of production operations is critical, conservative approaches on pillar stability are often adopted. An evaluation of pillar stability may result in improved pillar geometries and new support requirements that will positively influence drawpoint spacing and consequently draw control. Analysis of the extraction level layout should optimize the production rate, enhance the safety performance and find the best trade-off between expenditure and stability.

The current industry standard approach to estimate rock mass strength is the non-linear Hoek-Brown failure criterion (Kaiser, *et al.*, 2010). This failure criterion may underestimate the strength of brittle rock masses in highly confined zones, because the empirical relations rely on observations from relatively unconfined rock with significant stress-relief. An S-shaped failure criterion was more recently proposed by Kaiser *et al* (2010) to illustrate the transition from spalling at low confinement to shear failure at high confinement. Confined pillar cores and spalling at tunnel walls can be incorporated in a single continuum model by applying this failure criterion. However, validated principles to establish the rate of degradation in high confinement zones are currently not available and the approach is therefore not yet ready for engineering purposes. Until it is, numerical codes like FLAC^{3D} are able to indicate differences between the two approaches. The Finite Difference Method used by the program links displacements, strains and forces to simulate the rock mass behaviour.

1.1 Objectives

The aim of this project is to indicate differences in results derived from numerical modelling when either the Hoek-Brown or the S-shaped failure criterion is applied. Infrastructure dimensions and rock mass properties of Northparkes Mines block E48 were used to develop a continuum model. Simulation results are compared to geotechnical data from the mine site. The complexity of simulating a producing block cave goes beyond the scope of this project and thus the focus is put on pillar stability during undercut development. The project objectives are outlined as follows:

1. Develop a model that simulates undercut development using the Finite Difference Method.
2. Implement brittle rock mass behaviour in constitutive laws in FLAC^{3D}.
3. Calibrate the model using extensometer data from Northparkes Mines E48.

1.2 Outline

The accomplishment of these objectives is set out in this report according to the following outline.

Chapter 1: Introduction

Chapter 2: Block cave mining
Explains how a block caving operation is designed, developed and operated.

Chapter 3: Northparkes Mines
Gives an overview of geology, operational aspects, the market and an outlook of Northparkes Mines.

Chapter 4: Rock mass characterisation
Describes four schemes to classify rock masses.

Chapter 5: Rock mass behaviour
Links stress regimes to the geotechnical environment while focussing on brittle rock failure.

Chapter 6: Stress-strain relations
Elaborates on elastic-brittle behaviour at different stress levels in laboratory setups.

Chapter 7: Failure criteria
Discusses three well-known failure criteria and introduces the S-shaped failure criterion.

Chapter 8: Numerical modelling
Describes different modelling methods and introduces FLAC^{3D} and its way of operating.

Chapter 9: Convergence analysis
Explains how relative displacements in the rock mass are measured.

Chapter 10: Simulations
Describes the modelling approach and all aspects of the script used in FLAC^{3D}.

Chapter 11: Results and Interpretation

Chapter 12: Conclusions

Chapter 13: Recommendations

2 Block cave mining

Due to rising welfare in booming industries like the BRIC-countries, worldwide demand for construction materials, electronics and luxury products has risen steeply over the past decade (Rosling, 2013). As set out in the introduction, the demand for copper is dealing with these trends. Porphyry deposits are the most important source of copper. They are present in the earth's crust as large-scale, steeply dipping, low-grade ore bodies and require a non-selective, bulk mining method. Caving or unsupported mining methods intend to create mass failure of the country rock and are most suitable to apply on porphyry deposits (Figure 3). The most selective caving mining method is sublevel caving. It is applied on ore bodies with smaller footprints and rock masses of a high quality. High quality rock masses require development on multiple levels and produce ore by ring blasting from the different levels.
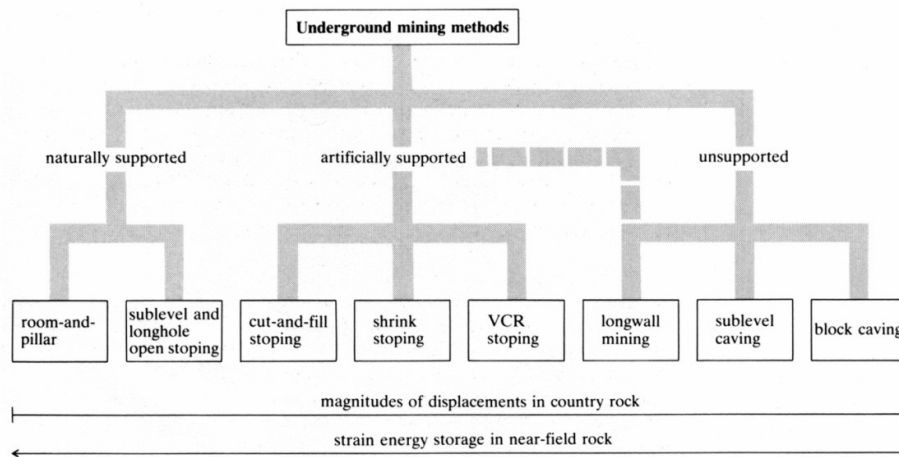
Figure 3: Mining method classification (Brown, 2003).

In general, the production rate of mines using the block caving mining method exceeds the production rate of mines using sublevel caving. Nowadays, several block caves produce over 50,000 tonnes per day and future mines will produce even more (Figure 4).
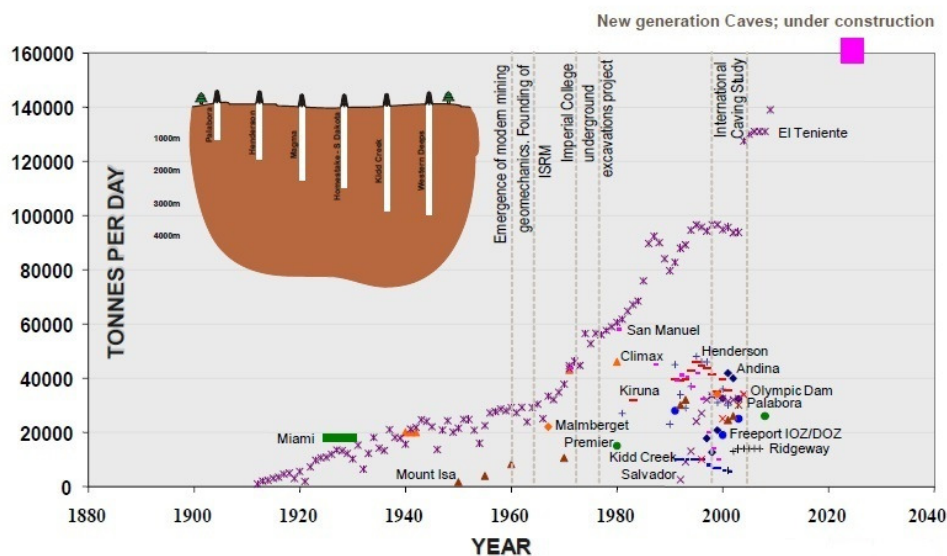
Figure 4: Evolution of daily production rates in block caving (Moss, 2010)

Block caving is an unsupported mining method where the rock mass collapses under its own weight and forms a self-propagating cave once the ore body has been sufficiently undercut. Figure 5 shows a schematic representation of the typical layout of such an operation. The undercut level is used to drill and blast rings in a progressive manner to initiate the caving process. The production or extraction level is located beneath the undercut level and is used by LHDs to haul the broken ore from drawpoints to an ore pass or crushing station. The two levels are connected by funnel-shaped drawbells that guide the broken ore towards the drawpoints.
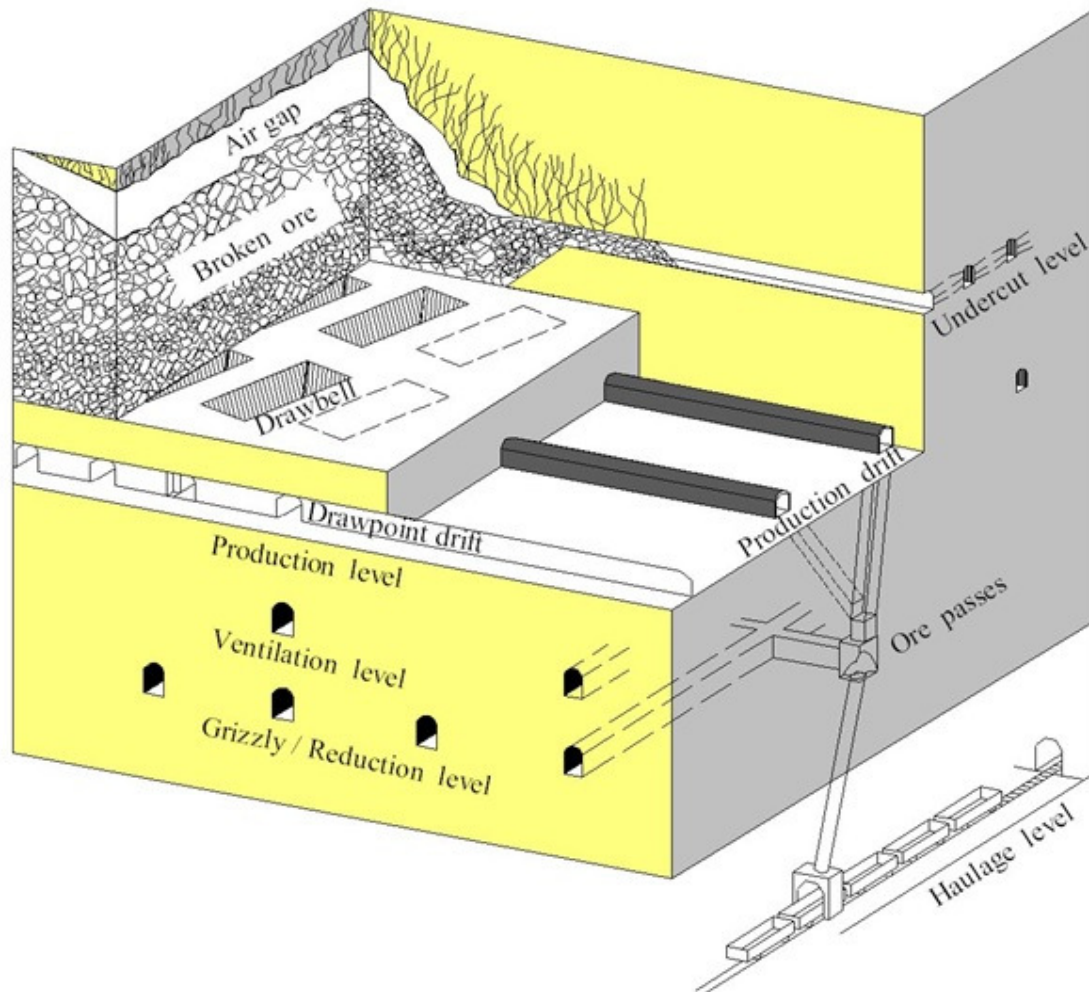
Figure 5: Schematic three-dimensional representation of a block caving operation. (Onederra, 2005)

Panel caving is a variation of the block caving mining method that mines progressively along the panel, while block caves start production from the complete ore body footprint. Both methods tend to have very large, regular footprints. These methods are applied on rock masses that are sufficiently weak to sustain a caving mechanism and, at the same time, are strong enough to ensure that the excavations will last throughout the mine life. The largely fixed infrastructure of a block or panel cave is a perfect environment for partial or full automation. Fully autonomous loading techniques are currently available, but rarely implemented. Extra care on support systems and road pavement benefit the automated tramming and dumping, the loading is often done by tele-remote control. (Lovejoy, 2012)

Block caving operations become increasingly interesting due to higher metal prices, an improvement in knowledge of caving mining methods, lower discovery rates of significant new near-surface deposits and the depletion of current open pit mines. Extensive development of shafts, ramps and the infrastructure beneath the block means that block caving operations have a period of 15 years between discovery and steady state production, making them very capital-intensive. On the other hand, operating costs are so low, approximately US$ 9 per tonne of ore, that they are comparable to open pit mining costs. This is considerably less than room-and-pillar mining or sublevel caving which cost approximately US$21 and US$ 22 per tonne of ore respectively (InfoMine, 2010). Technology moves the block and panel caving operations towards being a 'rock factory'. The remainder of this chapter is primarily based on the Block Caving Geomechanics manual of E. Brown (2003), unless stated otherwise.

2.1 Amenability to caving

A steady, high production rate is necessary to make the payback period on the high capital investment as short as possible. The production rate is highly influenced by the ability of the ore body to cave. The cave can be divided into five zones, which all have distinctive characteristics and behave in a unique way. Figure 6 shows these zones in a cross-section of the cave. The elastic region represents an undisturbed, elastic rock mass. Slip along pre-existing faults and micro-cracks that open up create micro seismicity somewhat closer to the extraction level. The yielded zone is unsupported and severely fractured. A lack of cohesive strength and low stress components cause blocks to fall down into the cave. An air gap should be maintained to encourage the yield, but should be minimised to reduce the risk of an air blast. The mobilised zone contains moving blocks that are drawn downwards due to production at the drawpoints. These zones move laterally and vertically over the life time of the cave as new draw bells come into production and grades at drawpoints drop below a minimum value. (Sainsbury, *et al.*, 2011)
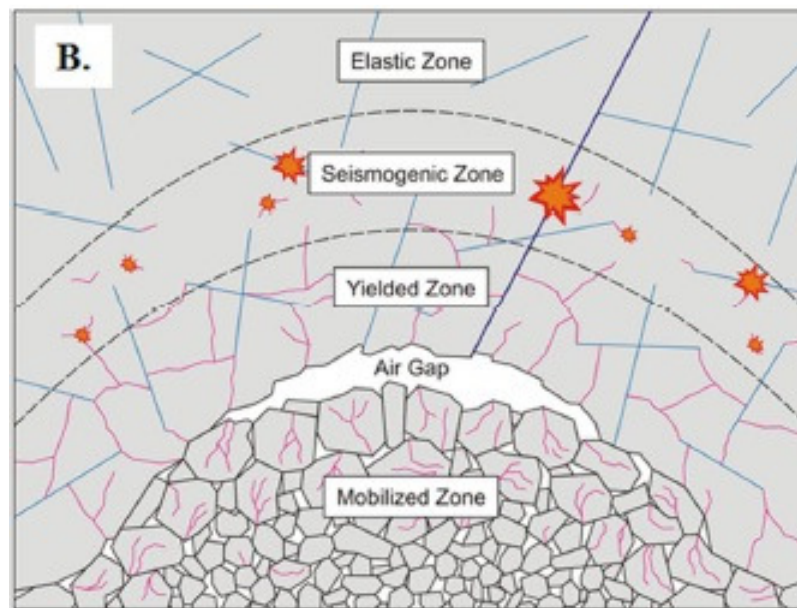
Figure 6: Zones in a vertical cross-section of the cave that indicate the transition from an undisturbed, elastic rock mass to moving blocks in the mobilised zone due to development and production activities. (Sainsbury, *et al.*, 2011)

When the cave reaches a sufficient hydraulic radius (HR), defined in equation 2.1, a self-sustainable propagating cave will develop under the condition that bulked ore is continuously withdrawn. Other factors that play a role in caveability are discontinuity geometry and strength, rock mass strength, ore body geometry, undercut dimensions and induced stresses in the cave. All these topics will be addressed in the remainder of this chapter. (Sainsbury, *et al.*, 2011)

$$HR = \frac{Area}{Perimeter}$$ **2.1**

Laubscher (1994) created a caving chart that is able to predict the amenability to caving of a particular ore body. The chart relates the Mining Rock Mass Rating (MRMR, section 4.2.2) and the hydraulic radius to indicate the likelihood of caving (Figure 7). Most of the factors that contribute to the caving behaviour of the rock mass, as described above, are included in these two parameters. This chart is the industry standard of caveability assessment and is most successful in the weaker and larger ore bodies, since this resembles the origin of most data. The transitional zone in the chart indicates cave initiation with minimal propagation. (Sainsbury, *et al.*, 2011)
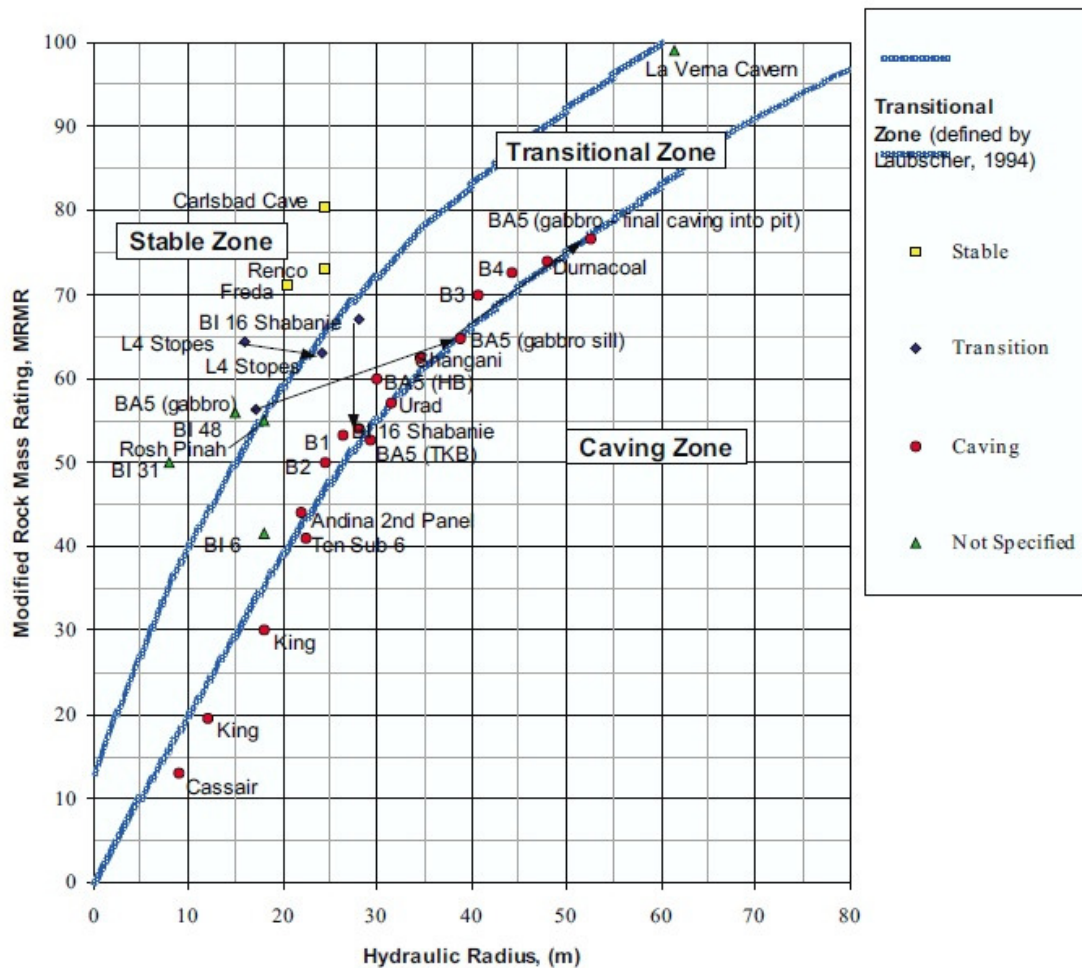
Figure 7: Laubscher's caving chart (Laubscher, 1994).

2.2 Fragmentation

Nowadays, more and more competent rock masses are mined with caving mining methods, thanks to a better understanding of geotechnical conditions and fragmentation and the availability of improved equipment. In some cases the rock mass needs to be preconditioned in order to increase the ability to cave. Holes are drilled and manmade fractures are induced by hydrofracturing or explosives to weaken the rock mass. (Lovejoy, 2012)

Fragmentation influences most essential engineering issues in a caving operation. Factors such as drawpoint spacing, draw bell shape and size, draw control and production rates. Three stages can be distinguished and the first is *in situ* fragmentation, which incorporates all discontinuities present in the rock prior to mining activities. Primary fragmentation is the detachment of rock from the cave back at caving initiation. All subsequent fragmentation until the rock is hauled away from the drawpoints is called secondary fragmentation. The primary fragmentation size is finer than one would expect due to induced stresses which create detachment from the cave back. The secondary fragmentation stage consists of opening of filled and healed discontinuities, extension of pre-existing discontinuities, failure of rock bridges creating new fractures and crushing due to overlying weight. Figure 8 shows that secondary fragmentation processes play a more dominant role as the Height of Draw (HoD) increases, causing finer fragmentation. Thus, the fragmentation does not only dependent on the rock mass quality, but also on the stage of the mine life of the cave.
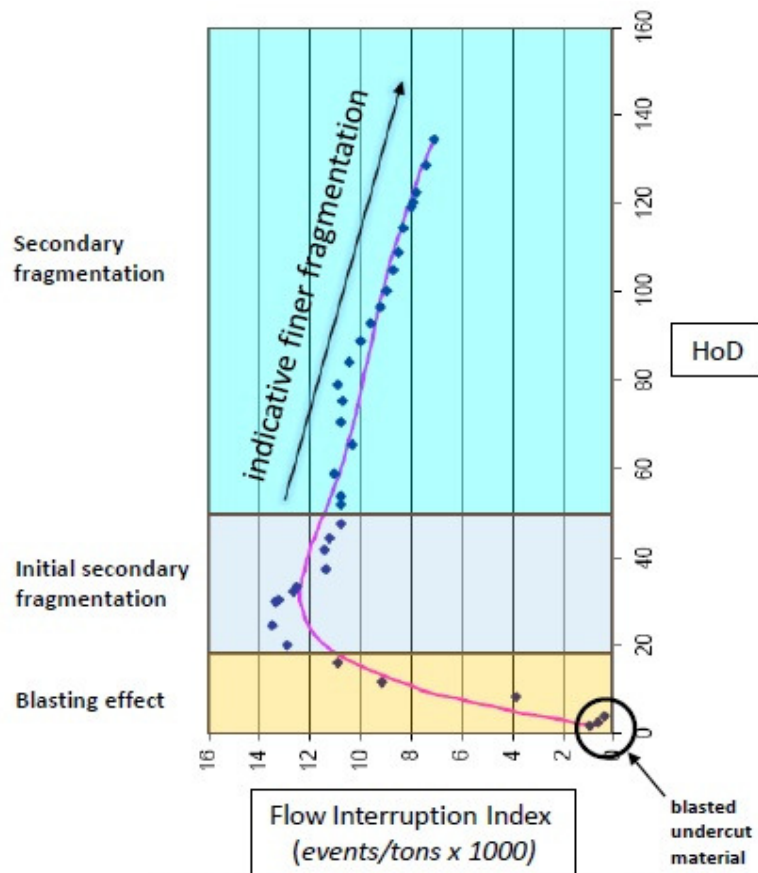
Figure 8: Data gathered at the El Salvador copper mine in Chile shows a trend of finer fragmentation as the Height of Draw increases. (Moss, 2010)

Sieving and physical measurements are accurate yet impractical methods of fragmentation assessment. Other methods are boulder counting and logging of explosive usage in secondary blasting. Secondary blasting needs to be done on hang-ups, oversized blocks that get stuck in draw bells. The state of the art, fast and non-disruptive alternative fragmentation assessment method is Digital Image Processing (DIP). This method consists of sampling, image acquisition and image analysis. Particle outlines can be identified by a human being, but computers can process far more images per time unit. Adequate lighting is an issue for DIP in all underground mining activities. DIP techniques are more effective for block and panel caving mines than for sublevel caving operations due to larger sized fragments produced by natural caving.

2.3 The undercut

A cave is initiated by undercutting the ore from the undercut level or levels. Progressive undercutting increases the hydraulic radius to an extent where caving is initiated. High undercuts generate higher initial production rates at the expense of higher investment costs. The height of undercuts can vary from 3.6 to 42 meters. The undercutting strategy can have a significant effect on the stresses induced on the extraction level excavations and on cave propagation. In addition, Butcher (1999) explained that large irregularities in the undercut front, the cave line, cause local stress accumulations which result in damage as illustrated in Figure 9. Also, damage will occur if the cave reaches the hydraulic radius and undercut development continues, enlarging the hydraulic radius, without drawing of the ore.
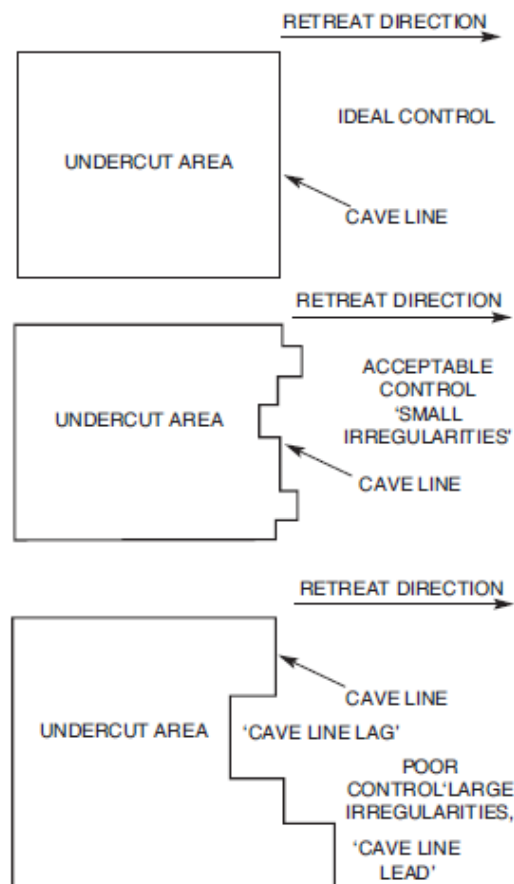
Figure 9: Cave line geometry issues (Butcher, 1999)

An increasing hydraulic radius causes changes in the local stress field and creates abutment stresses. According to Vink (1995) this is: "the vertical stress concentrated around the perimeter of broken rock which no longer supports the mass above". One of the main functions of the undercut is the creation of a stress shadow to relief deeper infrastructure from high stresses as they are developed.

The initial starting point of the cave and the direction of development depend on a huge number of factors. Ideally, in the case of an equi-dimensional ore body, the cave will initiate at the boundary of the ore body and progress diagonally. Or the cave initiates in the centre of the ore body and develops to the boundary. Foremost, the direction of advance should be parallel to the major principal horizontal stress. An undercut advancing towards the major principal horizontal stress results in high abutment stresses and a good fragmentation. An undercut advancing away from the major principal horizontal stress results in lower abutment stresses, but also poorer fragmentation as shown in Figure 10. Another geotechnical factor that influences the initiation point of a cave is the rock mass strength, as cave initiation is easier in weak rock. An economic factor could be a high grade zone.
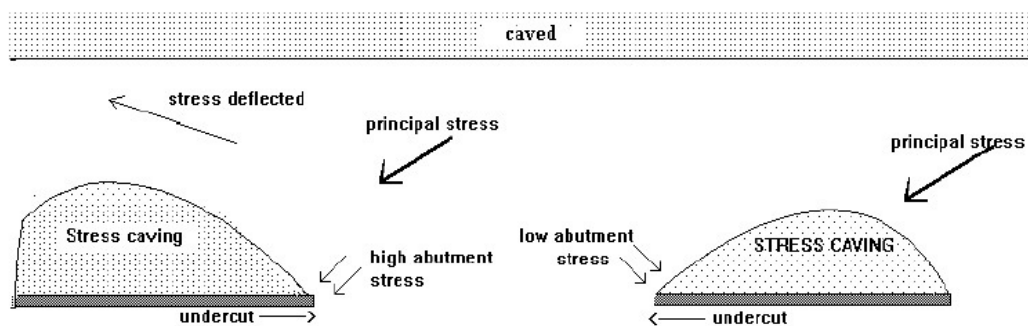
Figure 10: Undercut advance direction and principal stress (Moss, 2010)

2.3.1 Undercutting strategies

There are three general strategies for undercutting. Each of them has its own advantages and disadvantages which are discussed below.

- **Post-undercutting strategy**
  The extraction level is developed completely, including draw bells, before the undercut front advances over that location. Abutment stresses at the undercut front create great stresses on extraction level infrastructure, which can have disastrous consequences in an early stage. On the other hand, a quick ramp-up to full production results in time savings and is positive for the NPV of the project.

- **Pre-undercutting strategy**
  The development of the extraction level lags behind on the undercut development. The '45 degree rule' describes the maximum angle between the undercut and extraction level development front. The main advantage is a de-stressed environment in which the extraction level can be developed. According to Rojas *et al*. (2000), this has remarkable advantages over post-undercutting considering pillar rock mass quality.

- **Advance undercutting strategy**
  This strategy attempts to combine the benefits of the post- and pre-undercutting strategy. The extraction level is partially developed before the undercut at that location is drilled and blasted.

According to Butcher (2000), there are three methods to extract the undercut. The most applied method is fan undercutting, which has great variability of the undercut height. Flat undercuts are more applied at great depth to maximise advance rates. Narrow crinkle cuts prevent arching by the creation of inclined, self-cleaning surfaces on top of the major apex. If the slope is steeper than the angle of friction, approximately 45°, there will not be any residual caved rock on the slopes. Figure 11 shows a typical crinkle cut and relating issues that might arise when development works are not executed properly. Crinkle cuts can also be developed from undercut drifts that are located directly above the extraction drifts.
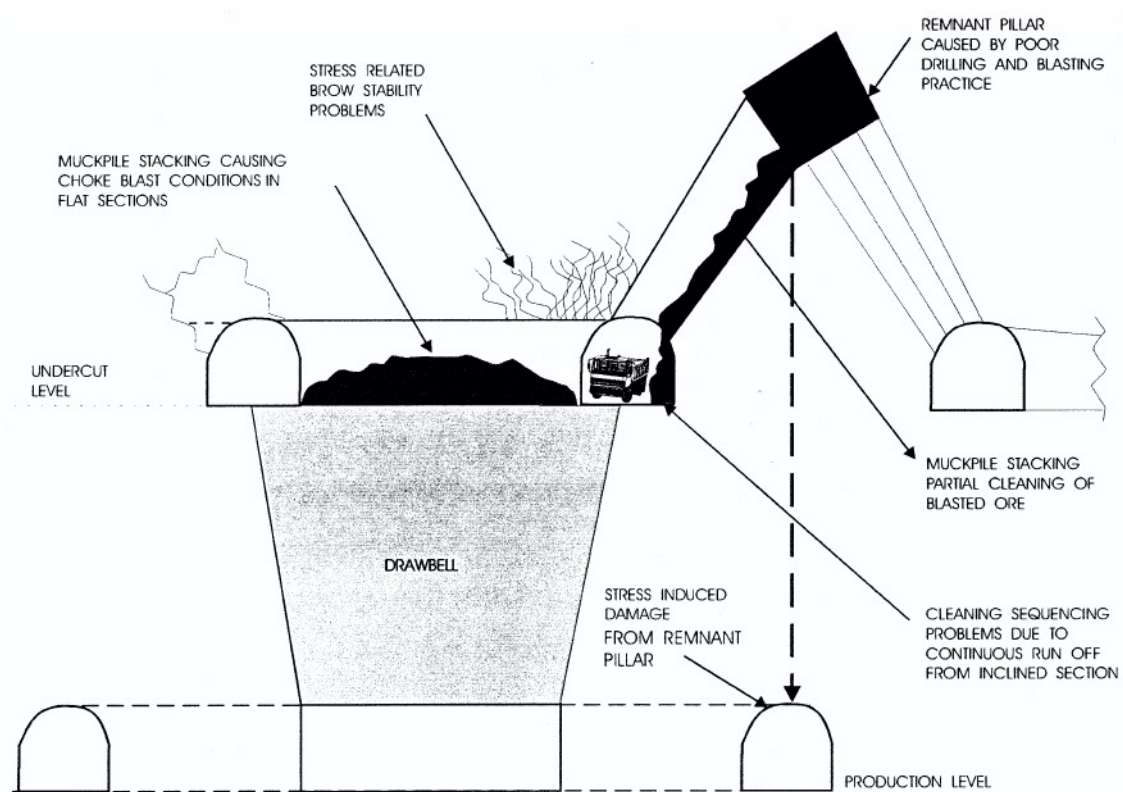
Figure 11: Crinkle cut geometry and possible relating issues (Butcher, 2000).

2.4 Extraction level design

The layout of the extraction level, also called production level, is a result of the degree of fragmentation and the undercutting strategy. Also the ease for equipment to operate and stability of the pillars needs to be considered in the design. Grizzly and slusher systems have been used extensively in the past. They are perfectly able to draw finer fragmented rock by gravity systems. Most of these operations made way for mechanized drawing and haulage performed by Load Haul Dump (LHD) trucks. This is the best solution for more competent rock masses and subsequent coarser fragmented rock. Excavations between the extraction and the undercut level have complex geometries which should stay intact for several years up to over a decade to allow LHDs to operate. The two- and three-dimensional extraction ratios are discussed in Appendix A, together with some additional factors that influence extraction level stability.

Flores and Karzulovic (2002) performed a benchmarking study using data from 45 mines which have undertaken, or will be undertaking, a transition from an open pit operation to an underground mine. They concluded that production drift spacing has increased and drifts have become higher and wider over the past 40 years. Since the launch of the LHD thirty years ago, the relative frequency of the herringbone layout (55%) and the El Teniente layout (40%) transcends all other layouts. Five unique layouts are briefly described on the next page and shown in Figure 12. The abundance of block caving operations with either the herringbone or the El Teniente layout is subject to a detailed comparison in subsection 2.4.1.
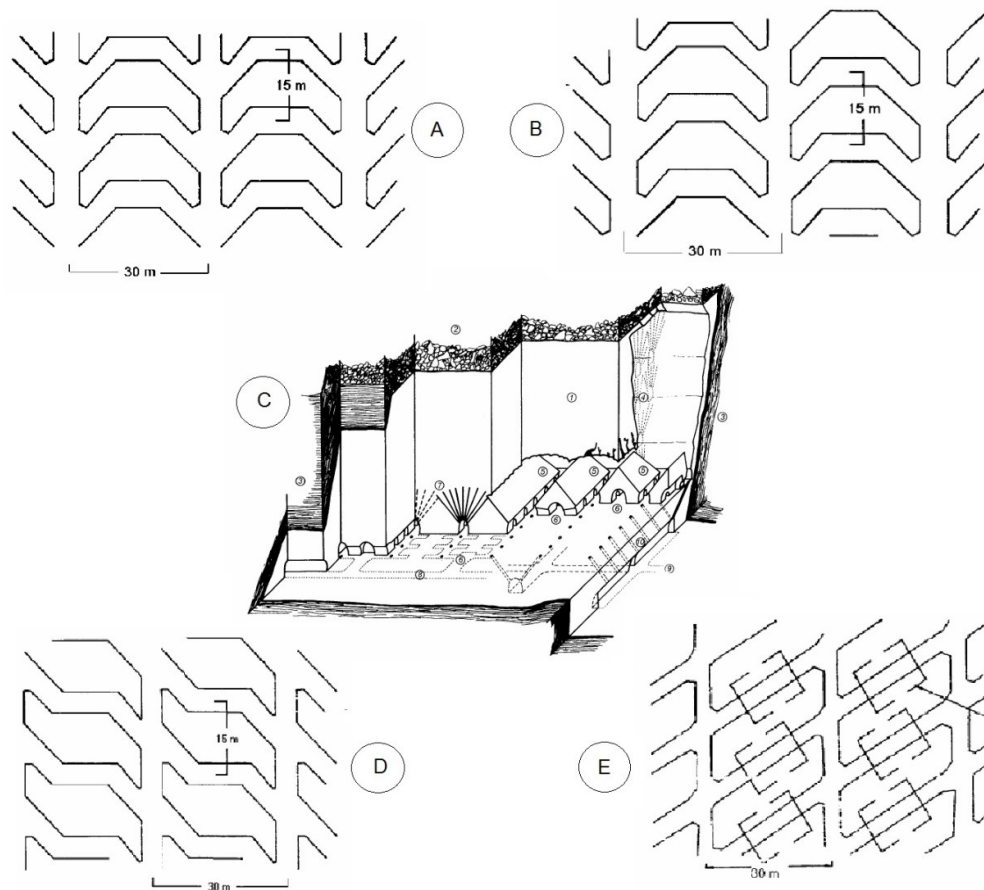
Figure 12: A) Original herringbone - B) Offset herringbone - C) Continuous trough - D) Henderson - E) El Teniente. (modified after Brown (2003))

- **A) Original herringbone layout**

The major and minor apices are diametrically opposed. An inclination in the drawpoint drifts makes it easy for LHD vehicles to turn. The two acute corners in the base of the pillars create unfavourable stability conditions.

- **B) Offset herringbone layout**

The drawpoints are staggered which improves the overall stability and operational efficiency compared to the original layout. Besides that, the span of intersections is minimized in respect to all other layouts. The minor apex is thicker, giving more support, than in the El Teniente layout. This layout is perfectly suitable if there is preferred ventilation or tramming direction.

- **C) Continuous trough or trench layout**

There are no minor apices in this layout, which means that the ore is drawn into longitudinal trenches developed in pre-undercutting. Due to the undisturbed, lateral continuation of the major apices and the absence of minor apices, there is a low two-dimensional extraction ratio at the extraction level compared to other layouts. Furthermore, this design is very suitable in high stress conditions.

- **D) Henderson or Z-layout**

There are many similarities with the original herringbone layout. Only the two acute corners are in this case diagonally opposite.

- **E) Straight through layout (El Teniente)**

The drawpoint drifts are in most cases 60 degrees inclined from the production drifts. Originally the draw bells were right-angled to the drawpoint drift, but operational improvements have changed this over time. LHD vehicles can easily back up into the opposite drawpoint drift to straighten out. All drawpoint drifts have the same orientation, favourable to the *in situ* stress field. It is hard to use electric LHDs, because of cable run overs. Mud rushes will flood into the opposite drift and will have big impacts. This layout is especially favourable in post undercut mines to deal with high abutment loads. Numerical modelling by Laubscher and Esterhuizen (1992) showed the El Teniente layout to be 'stronger' than all other layouts.

The offset herringbone layout is used in the models described in the remainder of this thesis. Figure 13 introduces terms used in the mining industry to refer to certain regions or distances on the extraction level. Drawpoint spacing can be expressed within the same draw bell, across the minor apex or across the major apex. When one of these three is not explicitly quoted, the spacing across the minor apex is intended. Consequences of increased drawpoint spacing would be diminished cost of development, increased pillar size, larger equipment and thus more efficient production. The drawpoint spacing across the major apex is normally the longest of the three and should be kept to a minimum to benefit ore flow.
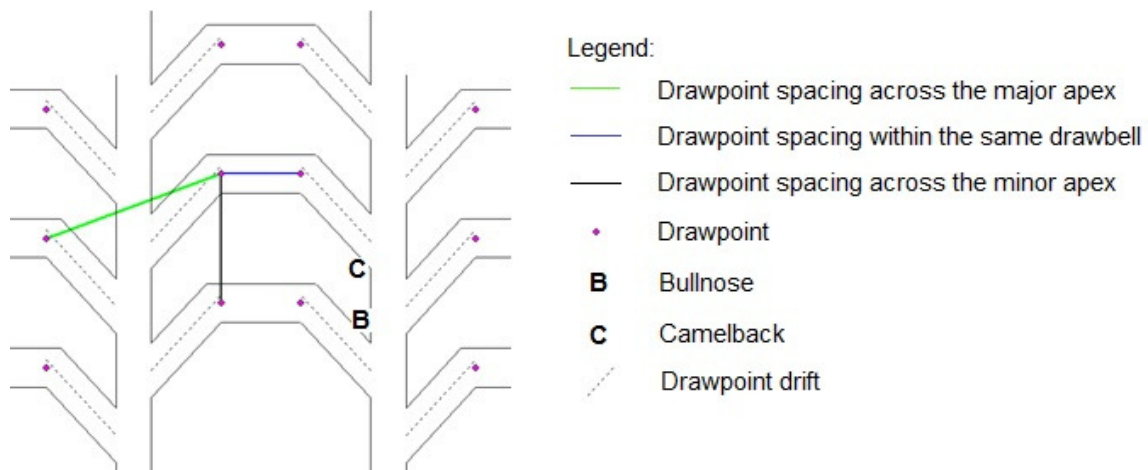
Figure 13: Illustration of industry terms on a plan view of the extraction level with an offset herringbone layout.

Severe consequences from drawpoint spacing on fragmentation and production can be shown with the flow ellipsoid concept. The flow ellipsoid concept describes the movement of ore through the mobilised zone. An ellipsoid of extraction represents all material that will be produced in a given time. Material in the ellipsoid of loosening has been mobilised, but has not been produced. The eccentricity of the ellipsoid depends on the particle sizes and the size of the draw bell amongst other things. If extraction ellipsoids of adjacent draw bells do not intersect, there is a potential loss of ore and excess weight on the major apex (Figure 14). A hexagonal pattern of drawpoints limits the undrawn sections (or "dead" zones) and can limit drawpoint spacing. On the other hand, there is a chance of dilution if extraction ellipsoids do intersect caused by overdraw in the intersecting areas. The flow of broken material towards drawpoints is in reality much more complex than explained above. (Richardson, 1981)
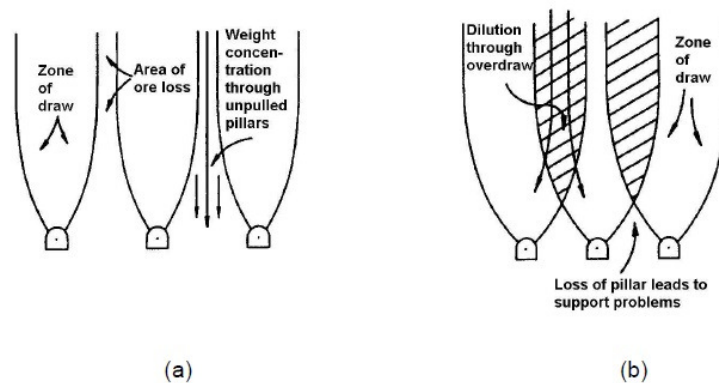
Figure 14: Flow ellipsoid concept showing (a) excessive drawpoint spacing and (b) dilution (Richardson, 1981).

2.4.1   Comparison of El Teniente and offset herringbone

Leach *et al.* (2000) compared the offset herringbone and El Teniente drawpoint layouts using the numerical code FLAC^{3D} 2.00 to assess their performance for a new block at the Premier Diamond Mine, South Africa. They placed the drawpoint drifts on a spacing of 17 meters. The effective pillar width, measured perpendicular to the trough, is significantly larger for the offset herringbone layout than for the El Teniente layout due to the inclination of the drawpoint drifts. Peak stresses occur in both cases near the production drifts and are highest in the bullnoses. They observed an extent of failure of two meters into the pillar and even more around corners. A major difference is the much larger span at intersections for the El Teniente layout. They concluded a slightly better performance of the offset herringbone layout if final extraction ratios are similar. But according to deWolfe (2009), the drawpoint packing, development meters and pillar stability are similar in both cases.

Lavoie and Pierce (2011) recently reported on the stability of a 28 x 15 herringbone layout using FLAC^{3D} and compared it to an El Teniente layout of the same dimensions. It must be emphasized that the models differed in trough length and break-away angle. They concluded that the herringbone layout was subject to slightly more damage, especially in the bullnoses, based on contour plots of the Hoek-Brown *s* parameter, apparent cohesion, plasticity indicators and major principal stress. Furthermore, the El Teniente layout was able to withstand a slightly higher peak load in a compression test.

2.5 Draw control

Scheduling in block caving is referred to as draw control, since the schedule determines the rate of draw at each location over a given time period. The processing plant requires a consistent ore grade which impedes draw control. The goal is to maximize ore recovery while avoiding excessive dilution, damaging load concentrations on the extraction horizon, non-uniform cave propagation, air blasts and mud rushes.

The goal of draw control is to maximize Net Present Value (NPV), minimize costs and allocate the right amount of resources (capital, equipment and labour). The latter is vital to obtain a desirable production strategy. The following aspects need to be addressed in order to correctly plan future production rates per drawpoint; Drawpoint sequence and development rate, active area size, draw rate, draw and geotechnical constraints and the distribution of tonnages within an active block or panel.

Forecasting of production over the whole footprint is not a problem in mine scheduling, but the variances between planned and actual production from drawpoint to drawpoint are significant. A deviation between planned and actual production leads to under or over pull. This leads to early dilution entry and over induced stresses. The variance between planned and actual production can be used to develop an optimised mine plan for the future or to relate variances in production to rock mass properties and thus account for individual reliabilities of drawpoints.

Ore is drawn towards the drawpoints by three different mechanisms. The mass flow is the uniform movement of ore in the upper part of the cave. The particle flow rate for this mechanism is not dependent on single drawpoint production rates and there is no mixing of fine and coarse materials. Gravity flow, or interactive flow, is the second mechanism and describes the lateral migration and mixing of granular material as it moves from slowly producing drawpoints to more active draw columns. The last mechanism consists of larger, angular particles that create voids in between them which can be filled with finer material or can collapse. These less dense zones form 'fingers' pointing in an upward direction rather than ellipsoids. Good draw control of many drawpoints can lead to a favourable mass flow in higher zones of the cave. Hang-ups are most likely in circumstances described by the last 'void' mechanism. In reality, the broken ore will exhibit a composite behaviour.

The volume of rock increases in the process of caving. An *in situ* volume (V) becomes $V \cdot (1 + B)$ where B is called the bulking factor. The bulking factor should not be confused by the swell factor which is represented by $1 + B$. Draw control is performed successfully when the air gap expands due to production in such a way that it does not get too large (accompanied by risk of an air blast or major rock fall from the cave back) and is filled up frequently by the bulking of freshly caved rock. The cave line is moving at all times in panel caving operations, creating an inclined ore-waste contact in the cave (Figure 15). Factors that contribute to good draw control are a well-established communicating system, clear numbering of production and draw bell drifts and individual drawpoint production recordings.
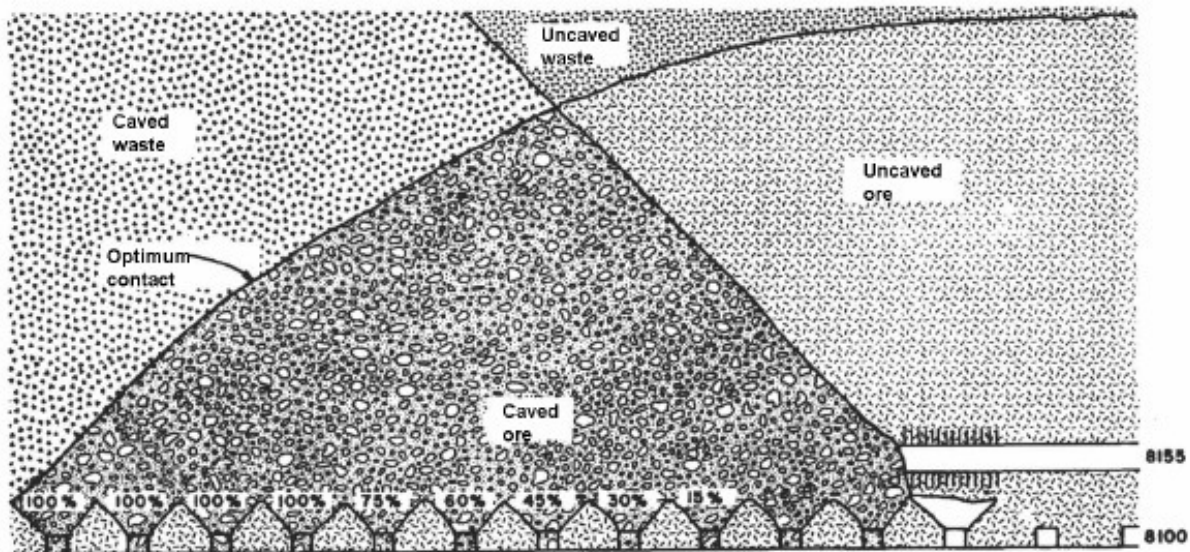
Figure 15: Sketch of the ore-waste contact in a vertical cross-section of a cave. (deWolfe, 1981)

2.6 Geotechnical monitoring

Geotechnical monitoring in caving operations is used to check cave initiation, surface subsidence and the stability of the extraction level. In general, it is preferred to use measurable parameters like displacements or pressure to compare situations instead of parameters calculated by a model. Expensive monitoring instruments and labour-intensive techniques should reduce costs to make geotechnical monitoring profitable on the long run. According to Brady and Brown (2004), geotechnical monitoring has four functions.

1. Ensure safety by the creation of a warning system
2. Record natural values of geotechnical parameters
3. Check the validity of assumptions
4. Control ground treatment workings

2.6.1   Cave initiation and propagation

According to Brown (2003), the advancement of the cave can also be seen from damage at the extraction level. Spalling and initial cracking are caused by loading and unloading of the rock mass between the undercut and extraction level. There are four techniques to monitor cave initiation and propagation and if used in series, they can simulate the shape of the cave back.

1. **Manual methods**
   Devices attached at the end of a measuring cable can be lowered onto the broken ore in the cave and pulled back to get in touch with the cave back. The height of the air gap can be measured in this way.

2. **Time Domain Reflectometry (TDR)**
   Cave growth is measured by deformation of cables installed in the cave back. A TDR unit sends electrical pulses through a co-axial cable. At local extensions and shearing the pulse is reflected. These locations indicate bulking of the cave back and the distance between the cave back and the TDR unit can be calculated from pulse travel times. (Chen, 2000)

3. **Micro-seismic analysis**
   Seismic sensors pick up sound shockwaves of caving rock at the cave back or above and convert them into electrical analogues. This monitoring method is mainly used to manage rock bursts, but can also be applied on cave propagation in three dimensions. The difficulty is that seismic events can also be created by machinery, blasting and movements in the mobilised zone.

4. **Cavity monitoring systems**
   Lasers can be used to obtain a three dimensional image of the cave back and the top of the broken ore pile. This technique can also be used to check for remnant pillars after undercutting. A more old-fashioned monitoring technique makes use of a wheeled weight on the end of a thin steel wire. A loss of tension upon lowering the device marks the location of the top of the muckpile and catching after pulling it back up marks the cave back.

2.6.2 Surface subsidence

Caving operations remove large volumes of supporting material, causing subsidence of the surface overlying the mining area. The surface area affected is even bigger than the mining area and set by the angle of draw. The angle of draw is influenced by many factors such as the *in situ* stress field and geological features amongst others. When the boundary of a vertical ore body is clearly defined, caving will propagate vertically to the surface. The zone of influence is the zone around the cave which will suffer from the redistribution of stresses as the cave progresses. It is a discontinuous form of subsidence, which makes it distinguishable from continuous subsidence caused by longwall mining. Chimney caving can result from excessive drawing from a single drawpoint. It is the progressive migration of fractures through weak overlying rock to the surface. Inclined ore bodies can cause progressive hanging wall caving, but most of the time block caving is characterised by large scale surface subsidence as a result of massive underground production.

2.6.3 Stability of the extraction level

The remainder of this report elaborates on the assessment of the stability of the extraction level. The stability is monitored by damage mapping, carried out to see the evolution of cracks in the shotcrete over time. Relative displacements in the rock mass are measured by Multi-Point Borehole eXtensometers (MPBX) and SMART cables. Tape extensometers measure convergence of the tunnel profile. All these devices record sub millimetre movements and are discussed in detail in chapter 9.

2.7 Major operational risks

Safety is always a priority in multinational mining companies and constant vigilance is necessary to reduce the amount of hazards and minimise risk. Risk is a product of the likelihood and the consequence of events. Risk management tries to minimize, monitor and control risks by the identification, assessment and prioritization of hazards. Appendix B contains tables to define the risk class for each hazard. It is part of a level 2 qualitative risk assessment at Northparkes Mines (Grosvenor, 2013). The operational risks are highlighted in the remainder of this section, because a risk-free mining environment does not exist and caving operations in particular are exposed to several operational hazards. The most severe operational hazards are sketched in Figure 16.
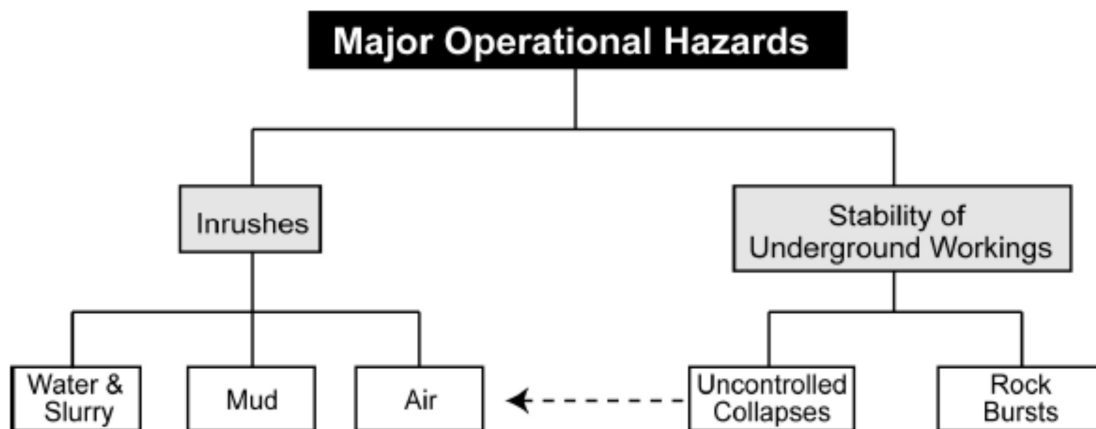
Figure 16: Major operational hazards tree. (Brown, 2003)

Major, uncontrolled collapses cause damage to the undercut and extraction level. It can result in loss of production, infrastructure damage or even loss of life. The average area affected by a single collapse is 3,700 m^2, based on a benchmark study by Flores and Karzulovic (2002). The crown pillar can collapse towards the surface or big blocks from the back of the cave can fall or slide due to induced stresses. These hazards are especially dangerous in combination with big air gaps. The abutment stress created in front of the cave front, strengthened by geological features, can cause very high stresses on extraction level drifts and pillars, potentially causing them to fail. The best measures to remedy these collapses are draw management, adequate support systems and an improvement of geotechnical data. (Flores & Karzulovic, 2002)

A rock burst is a seismic event which causes violent and significant damage to tunnels and other excavations in the mine (Ortlepp, 1997). Caving mining methods are nowadays applied in stronger and more brittle rocks at great depth and so the likelihood of rock bursts increases. Especially in abutment zones the stresses can reach levels where rock bursts are possible. A rock burst can either be caused by unstable slip on faults or unstable brittle fracturing of intact rock. The latter is also termed strain burst and is triggered by bulking, which will be explained later on in this thesis report. Rock bursts occur most likely in the early stage of mining, before the cave has progressed to an overlying void or the surface.

A mud rush is a mixture of fines saturated in water that penetrates the cave or underlying levels quickly at unexpected moments. External mud rushes arise from outside the cave mostly from tailings, back fill or open pit slip failures. Internal mud rushes originate inside the cave from the comminution of clay minerals. When there are sufficient mud-forming minerals and water, a trigger system is needed to initiate the mud rush. Drawing of ore, blasting or seismic activity can all act as a disturbance. The drawpoints are the most common discharge points for mud rushes. Extraction level layouts with opposing drawpoints are vulnerable for these hazards, because more than one drawpoint can be affected by a mud rush.

An air blast is compression of air in underground excavations coupled with rapid airflows up to 500 km/h. It is caused by the sudden fall of large volumes of rock from the cave back or hang-ups. Equipment can be overturned and destroyed, safety doors can be blown away and people can be injured or even killed instantaneously. A side effect is dust creation in the excavations which decreases visibility severely. If air gaps are unavoidable in order to operate efficiently, the gap should be less than 10 meters high and only in circumstances with a horizontal cave back. (Flores & Karzulovic, 2002) According to Laubscher (2000), a finely fragmented caved ore pile of 60 meters, or an equivalent 90 meters of coarse material, can minimise the effects of an air blast from the void in the upper region of the cave.

2.8 Block Cave Mine of the future

The increase in global demand for raw materials, discussed in the introduction, requires an increase in development speed and production capacity. Faster access to the ore body and higher production rates will lead to a higher Net Present Value of the project. Several companies have produced continuous extraction and haulage equipment and are currently performing trials on an industrial scale. One of these systems is the CAT Rock Flow System, described by Steinberg *et al*. (2013). An operation using their continuous system is believed to be able to produce 160,000 tonnes of ore per day which will represent the new generation of block caves (Figure 4).

The extraction rate of a discontinuous LHD haulage system is limited by the traffic stream and the deposit footprint. Less than 10% of the active mining area can be used due to the limitation of one LHD per extraction drift. This results in a mean extraction rate of 0.4 to 0.5 tonnes of ore per day per square meter. The continuous mining system consists of mobile feeders, chain conveyors and primary crushers. The mobile feeders are installed in each drawpoint and push the caved ore on the chain conveyor by means of a dozer plate that is driven by a hydraulic pushing device. Figure 17 illustrates the installation of such a system on an extraction level. A primary crusher is installed at the transition between the chain conveyor and a conventional conveyor belt. Service drifts and production drifts are alternated and used for drawpoints on either side.
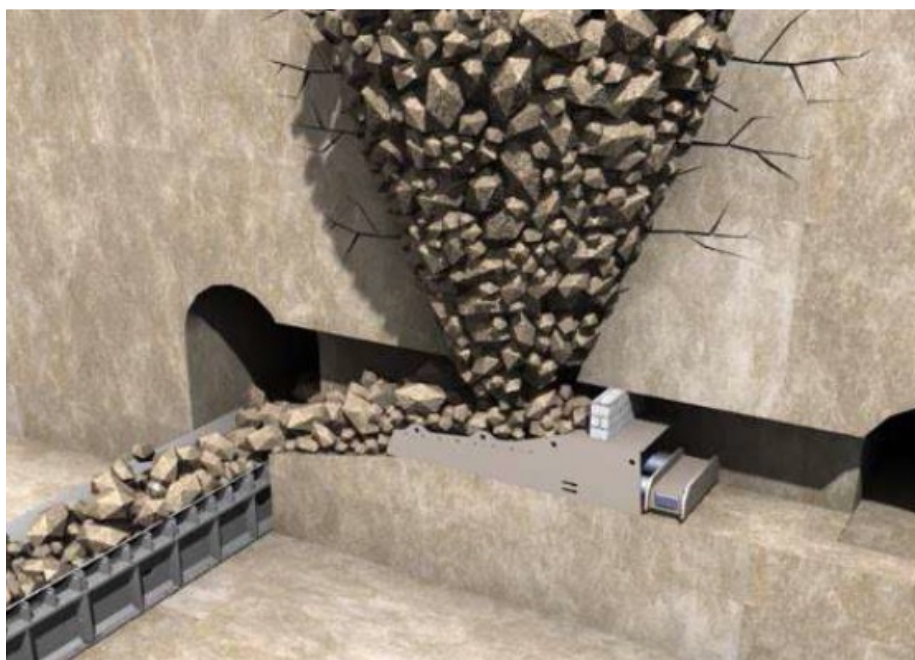
Figure 17: Artist impression of the CAT Rock Flow System (Frenzel, 2012)

Development rates have to increase in order to benefit from this innovation in continuous hard rock production. Hard rock road headers would deliver higher advance rates compared to drill and blast operations and will increase extraction level development. Prototypes are being tested on an industrial scale, such as the Tunnel Boring Machine at Northparkes Mines (Wyllie & Webster, 2012). A fully automated longwall system, adapted for hard rock mining, is planned to be used to undercut the block. The high grade of automation results in a reduction of the operating costs and an increase of safety. First trials in 2008 at the Inca mine showed a six times higher performance. The system has been industrially applied for the first time at the Andina mine in early 2013. (Steinberg, *et al*., 2013)

3   Northparkes Mines

Northparkes Mines (NPM) is a metalliferous block cave mining operation located in a farming-dominated landscape 27 km north of Parkes in New South Wales, Australia (Figure 18). Production commenced in 1993 and since 2000 the operation is an unincorporated Joint Venture between Rio Tinto (80%), Sumitomo Metal Mining Oceania (13.3%) and Sumitomo Corporation (6.7%). North Mining Limited, fully owned by Rio Tinto, is the manager of this Joint Venture. NPM was the first mine in Australia to use block caving techniques.
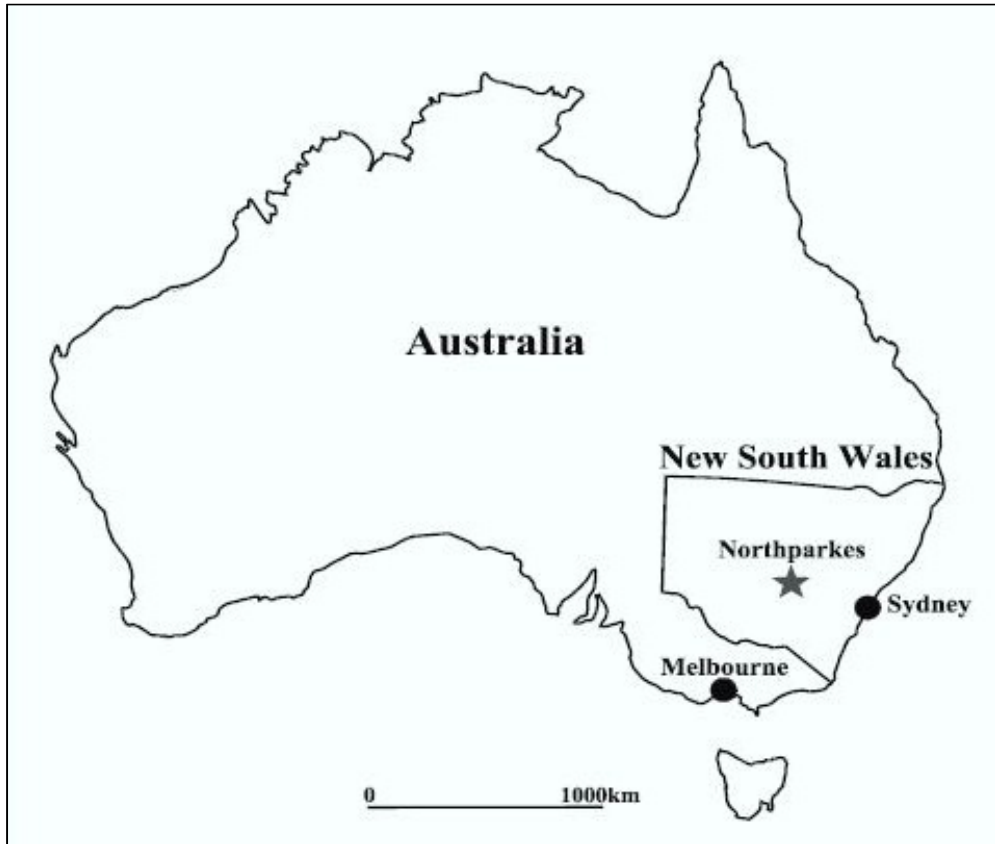
Figure 18: Location of Northparkes Mines. (Duffield, 2000)

NPM produces 5.8 Mt of ore per year, containing 0.82% copper and 0.51 g/t gold. In 2011, they converted this into 146,625 tonnes of copper-gold concentrate. Each tonne of concentrate contains 350 kilograms of copper and 10-20 grams of gold. The concentrate is transported by train to Port Kembla and shipped to custom smelters in Japan (57%) and China (43%) which validates the current Asian-bound copper market set out in the Introduction.

NPM consists of four copper-gold porphyry deposits, named E22, E26, E27 and E48; the 'E' stands for Endeavour. The E22 and E27 are open pits that have been mined by contractors to accelerate ore processing when a new block cave was commissioned. Also the extraction of the E26 deposit started with an open pit. All pits were roughly 600 meter in diameter and reached depths of approximately 220 meters. Because of these relatively shallow depths, the stripping ratios stayed below 2:1 (waste : ore). Figure 19 illustrates the overall mine layout.

The E48 rock mass properties and the extraction level design of lift #1 have been selected as reference case for this thesis project. The rock mass properties are discussed in detail in section 10.3. Rock mass behaviour and tunnel convergence are discussed in chapter 9.

Section 0 briefly discusses the origin of all deposits. Appendix C contains detailed descriptions of the two lifts that have been mined out in the E26 deposit. Currently, the first lift in the E48 deposit is being mined and an extension of the footprint is underway. Section 3.2 describes the current operation and contains background information. The life of mine is until 2024 with reserves of 75.5 Mt and resources of 287.8 Mt. A $115 million pre-feasibility study has been started two years ago to extent the mine life beyond 2024. The so called Step Change Project is explained in further detail in section 3.3. (Northparkes Mines, 2011)

3.1 Regional Geology

According to reconstructions of the supercontinents, Australia-Antarctica was separated from Laurentia, the North American craton, in the early Neoproterozoic (750 Ma). Approximately 520 million years ago the passive margin along eastern Gondwana developed into a convergent margin. This resulted in the Lachlan Orogen in Tasmanides, present-day New South Wales and Victoria. Figure 20 shows the location of the Junee-Narromine Volcanic Belt. The Late Ordovician to Earliest Silurian Goonumbla Volcanic Complex is part of this belt and hosts the porphyry copper-gold deposits which are mined at NPM. (Glen, *et al.*, 1998) The complex is best described as high-potassium calc-alkaline to shoshonitic. (van As, 2011)

The Goonumbla Volcanic Complex is a folded sequence of trachyandesitic to trachytic volcanics and volcaniclastic sediments that is deposited in a deep submarine environment. Quartz monzonite porphyries have penetrated the host lithology as narrow, vertically extensive pipes. Figure 21 shows a geological cross-section of the subsurface at NPM. The lithological units will be discussed in detail in section 10.3.2. Sulphides have mineralised disseminated or as coats on fractures. The core of the porphyries contains different sulphide species than the rock mass at some distance. From the core outwards, one will find in succession bornite, chalcopyrite and pyrite. Bornite contains gold as inclusions and is the dominant ore mineral. (Butcher, *et al.*, 2011)

Figure 20: Lachlan orogeny (Glen, *et al.*, 1998)
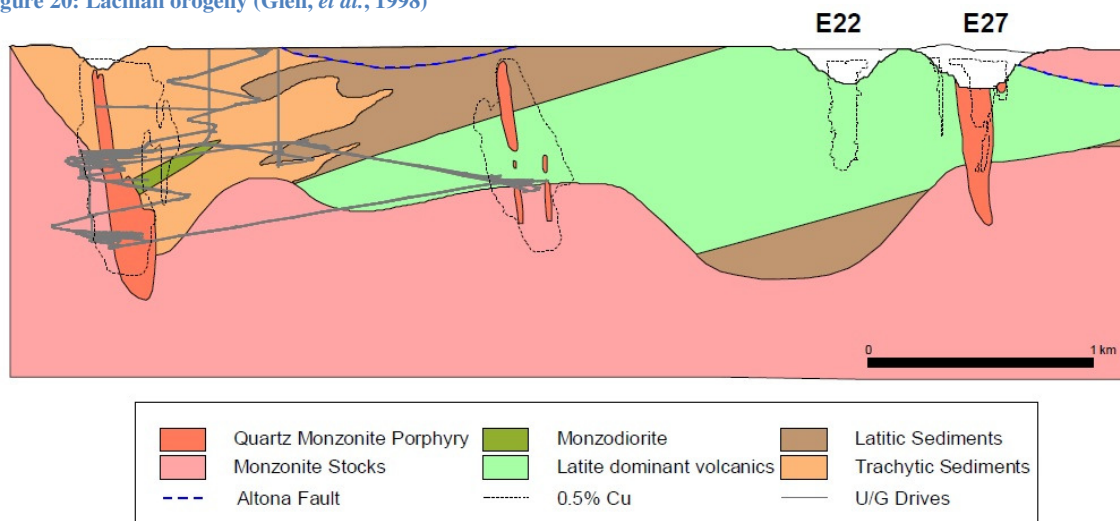
Figure 21: North-south cross-section of local geology. (Butcher, *et al.*, 2011)

3.2 E48 lift #1

Block E48 lift #1 is the main ore source at present, producing 5.8 Mtpa and ramping up to 6.2 Mtpa once the northerner extension is finished. Two extraction drives will complement the footprint to achieve this. High copper grades are associated with quartz veining, showing a correlation between the density of strongly healed fractures and the copper grade. The ore contains relatively high concentrations of tennantite which contains arsenic.

A post-undercut strategy is employed, in contrast to advanced undercut strategies at E26 lift #1 and #2. Some areas were damaged and weakened during undercut blasting activities. The first unstable drawpoints, and adjacent extraction drives, were noticed during initial production in September 2010. Concrete filling was necessary to provide immediate stability of the areas showing average strain rates of 3%. Figure 22 shows the highly converging areas and the concreted drifts. The draw strategy was adjusted to reduce stress loading in the centre of the extraction level. Therefore, draw rates around the concreted zones were high and decreasing radially to the margins of the cave. The cause of this unfortunate event remains under debate, but the most likely hypothesis is rapid cave propagation. This would rapidly increase the caved mass onto the extraction level and subsequent increased loading conditions. This theory was supported by surface cracks. (Peebles, 2012)
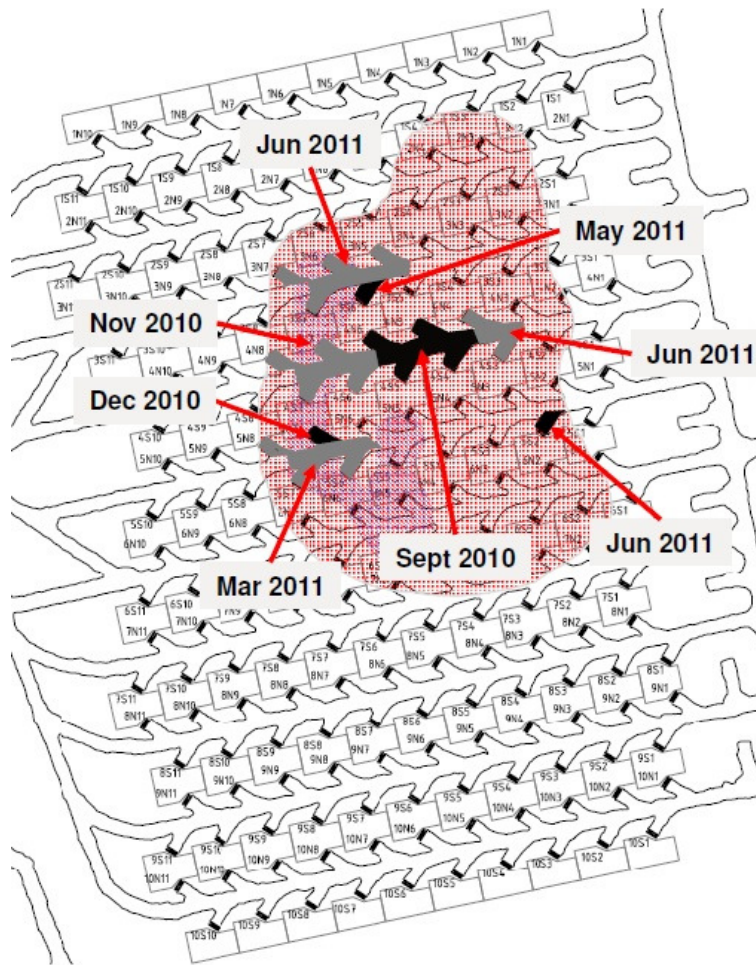
Figure 22: Highly converging area indicated in red and concreted sections in grey or black. (Peebles, 2012)

A project based on several trials was set up in July 2012 to redevelop the concreted parts of the mine. Redevelopment projects on other mines led to lateral cable bolting and polymer resin injection as reinforcement measures to keep horizontal deformation to a minimum after redeveloping. The primary objective was to increase the Life of Mine by recovering lost reserves of ore due to the concreting. Other objectives were decreasing operating costs and improving operational safety by improving the way loaders can operate. The concreting works prevents electric loaders to pass from the east to the west side of the extraction level, resulting in the use of diesel powered loaders and detours causing increased trafficking in adjacent extraction drives. Redevelopment of concreted areas would also benefit the implementation of the loader automation program. All redevelopment workings were finished in early 2013. (Peebles, 2012)

Mine access for the 80 full-time employees working underground and equipment is by decline, while the 6 metre concrete-lined hoisting shaft serves as an emergency escape route and as primary air intake together with the decline. Two exhaust fans of 750 kW suck 400 m^3 of air per second through the mine. Five Load Haul Dump Units (LHDs) with 14 t capacity have to meet a daily production target of 18 kt. They haul the ore into Run-Of-Mine (ROM) bins at the margin of the extraction level. The ore is fed by a plate feeder to a primary jaw-gyratory crusher with a capacity of 1,000 t/h and ends up in another storage facility. The primary crusher can reduce rocks of three cubic metres to a consistent P80 of 120 mm. Hereafter, a high-speed 35° inclined conveyor belt transports the ore to the underground loading station. Now the ore has arrived at the bottleneck of the operation, a hoisting system with two 16 t payload skips. At surface, a secondary crusher reduces the ore to a P80 of 55 mm. Figure 23 shows the primary crushing stage for the currently deployed extraction level. (Butcher, *et al.*, 2011)
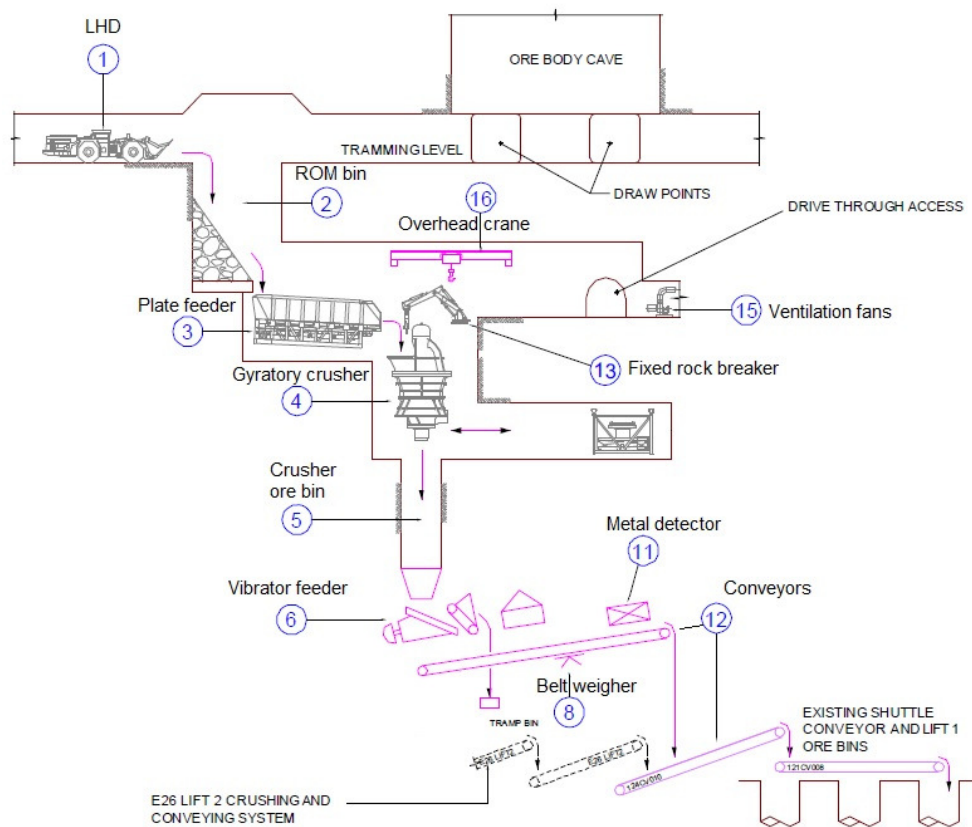
Figure 23: E48 Lift #1 underground material handling system (Butcher, *et al.*, 2011)

3.3 Step Change Project

Exploration within the current concession is done to find new resources and reserves to secure revenues after depletion of block E48 lift #1. An investment of $115 million for a pre-feasibility study assessing large-scale, lower-grade resources was made in the third quarter of 2010. The main task is to prove the presence of sufficient reserves for the mineralisation GRP314 and depth extensions of the E22, E26 and E48 ore bodies by a major evaluation drilling program. The locations of the proposed new caves are displayed in Figure 24. Together they will produce approximately 30 Mtpa, which has been concluded as the optimal production rate. The reported inferred resources before the pre-feasibility study were 271 Mt at 0.55% copper and 0.26 g/t of gold. An updated resource statement will be presented with completion of the pre-feasibility study. Table 1 gives an idea of the potential scale of the Step Change Project. (Wyllie & Webster, 2012)

Table 1: Footprint of the caves in the Step Change Project.

	# Drawpoints	Depth (m)
E22 Lift #1	257	550
E48 Lift #2	883	1080
GRP Lift #1	271	660
GRP Lift #2	615	1160
E26 Lift #3	968	1330
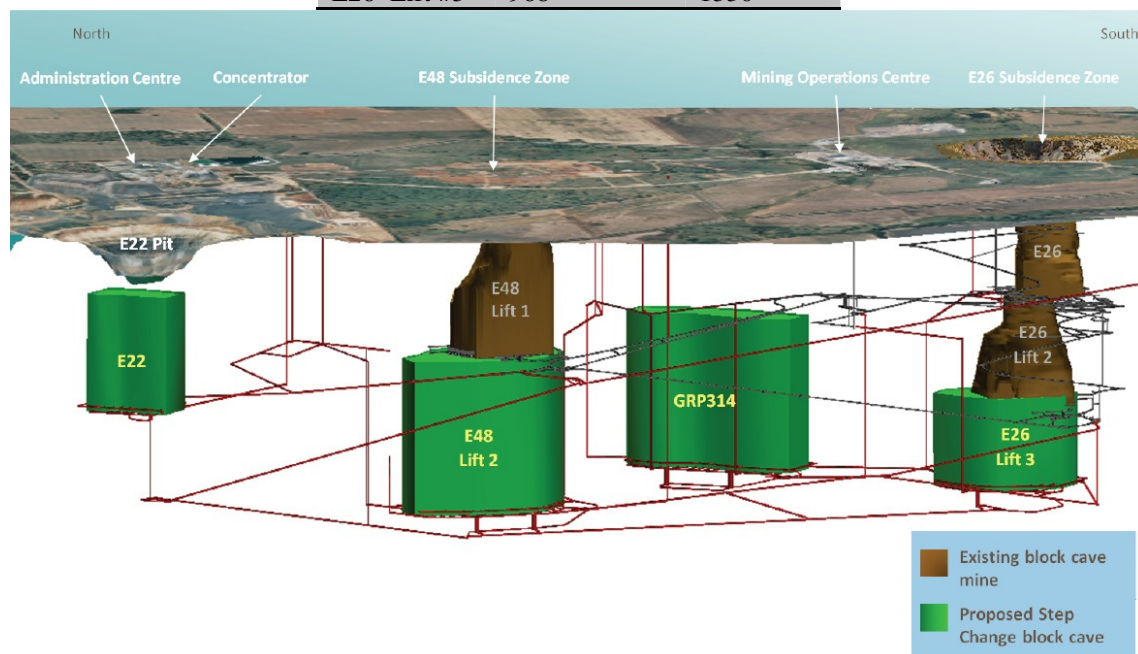
Figure 24: Cross-section showing the proposed mine expansion (Wyllie & Webster, 2012)

The ability to mine multiple caves at the same time provides great flexibility during the operational stage. A Tunnel Boring System (TBS) will greatly beneficiate the efficiency of developing the large amount of tunnels. Rio Tinto Technology & Innovation developed a TBS in conjunction with Aker Wirth that is capable of doubling the industry standard advance rate of 6 meters per day for single headings. It can cut 30 meter radius corners and is fit for purpose of extraction level ground support installation. (Wyllie & Webster, 2012)

4 Rock mass characterisation

Since the underground is not transparent and interesting zones are commonly overlain by hundreds of meters of rock, all data that can be retrieved is of value. Most information comes from geological, hydrological and geotechnical studies. Geological information is gathered through drilling, seismic and electromagnetic surveys. It enables engineers to locate high grade ore zones and deposit boundaries. Geotechnical data allocates physical and mechanical properties to intact rock and discontinuities. Section 4.1 discusses discontinuity parameters and section 4.2 introduces four different rock mass classification schemes.

4.1 Discontinuity modelling

A discontinuity orientation analysis uses statistic modelling to express the arrangement of discontinuities in a rock mass. At first, the number of discontinuity sets needs to be established and their three-dimensional orientation vectors with a 'true' mean and dispersion about the mean. Discontinuity sets are graphically shown as polar projections in an equal-angle lower hemisphere. The Fisher distribution is commonly used to describe the symmetric, angular distribution of the orientation about the mean. It makes use of the Fisher constant k, a larger k-value results in a tighter cluster of poles. The frequency of discontinuities can be expressed as the number of discontinuities within a unit volume, a unit area or a unit length. The latter is most common and practicable and called the linear fracture frequency. Terzaghi's formula corrects the apparent frequency to the true frequency using the angle between the mean discontinuity plane orientation and the sample line direction. Discontinuity spacing is the reciprocal of discontinuity frequency and is the distance between planes. The discontinuity persistence is measured as the one-dimensional lateral extent of the trace length of a discontinuity plane on a sample plane. These parameters and others are visualised in Figure 25 (after Hudson and Harrison (1997) in Brown (2003)).
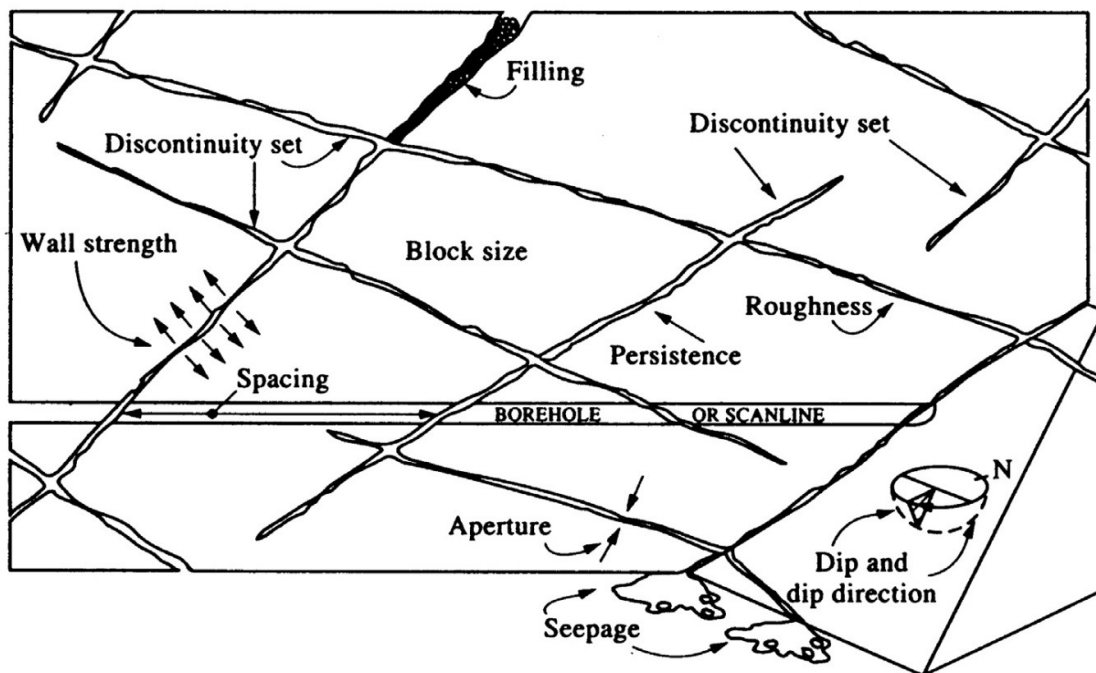
Figure 25: Discontinuity parameters (Hudson & Harrison, 1997)

4.2 Classification schemes

Rock mass classification schemes are used in the early stage of a mining project to estimate support requirements, rock mass strength and deformation properties. The structure of the rock mass has the most influence on rock mass behaviour. Heavily jointed rock masses are typically classified to have low rock mass strengths. A designation that is used in multiple of these schemes is the Rock Quality Designation (RQD). The RQD is the percentage of intact rock pieces over 100 mm in length that can be recovered from a core run. Equation 4.1 expresses this relation mathematically. The drilling orientation may influence the RQD to a great extent. The following four subsections describe different rock mass classification schemes. (Brown, 2003)

$$RQD = 100 \times \frac{\sum core\ pieces > 100\ mm}{total\ length\ of\ core\ run} \qquad \textbf{4.1}$$

4.2.1 Rock Mass Rating (RMR)

Bieniawski (1976) created a measure of the quality of rock masses for the purpose of preliminary support design in tunnelling based on mining experience in South Africa. An enumeration of five ratings results in an overall score for the rock mass between 8 and 100, with 100 being excellent rock quality. The final score is adjusted for discontinuity orientation in respect to the excavation. Due to its simplicity, this classification system is useful for communication between professionals, although modifications have been made over the years.

1. Uniaxial compressive strength of rock material (0 – 15)
2. Rock Quality Designation (3 – 20)
3. The spacing of discontinuities (5 – 30)
4. The condition of discontinuities gives an indication of the shear strength (0 – 25)
5. Groundwater conditions (0 – 10)

Rock masses are divided into regions which are assessed separately. These regions are commonly separated by major discontinuities. Later in his career, Bieniawski (1989) created guidelines for tunnel support. The subscript after 'RMR' indicates the year of publication of the ratings, *e.g.* RMR_{76} or RMR_{89}. Appendix D shows a table which assists in the retrieval of the five ratings listed above.

4.2.2 Mining Rock Mass Rating (MRMR)

Laubscher (1990) adapted Bieniawski's RMR classification scheme to mining conditions by introducing adjustments for weathering, mining-induced stresses, joint orientation and blasting effects. Most of the case histories used to compose the MRMR are derived from caving operations. The term Intact Rock Mass Rating (IRMR) is sometimes used in the industry in the same context. A similar rating principle as the RMR_{76} makes up a rating for the rock mass according to the three factors described below.

1. Rock Block Strength Rating (RBS)
   The intact rock strength, weighted average of the UCS of rock without discontinuities, corrected for the amount of fractures and veins.
2. Joint Spacing Rating (JSR)
   The joint spacing is a function of the discontinuity frequency and the RQD. Joints are considered as "obvious features that are continuous and greater in length than the width of the excavation (or all other joints that form blocks by intersections). Or the joint spacing is the same as the fracture frequency per meter when all discontinuities are measured.

3. Joint Condition Rating (JCR)

   The rating for discontinuity condition is set at a maximum and reduced for joint wall alteration, joint filling, roughness, planarity, groundwater inflow etc.

The enumeration of these ratings is adjusted for weathering, discontinuity orientation, mining-induced stress and blasting. This is done percentage-wise to end up with the MRMR. Laubscher and Jakubec (2001) made some changes to the rating system after a decade to improve the resemblance with reality.

4.2.3 Rock Tunnelling Quality Index (Q)

Barton, *et al*. (1974) developed this classification scheme for tunnel support requirements in hard rock. The Q index, equation 4.2, is a multiplication of three fractions that resemble the relative block size, inter-block shear strength and the active stress respectively. An equivalent dimension (D_e) is needed to select the right support requirements from a chart. The equivalent dimension is the excavation span, diameter or height in meters divided by the Excavation Support Ratio (ESR). All tables and graphs required to use this classification scheme can be found in appendix E. (Hoek, *et al*., 1995)

$$Q = Q' \times \frac{J_w}{SRF} = \frac{RQD}{J_n} \times \frac{J_r}{J_a} \times \frac{J_w}{SRF}$$

4.2

Parameter	Description
RQD	Rock Quality Designation
J_n	Number of discontinuity sets
J_r	Discontinuity roughness
J_a	Discontinuity alteration
J_w	Discontinuity water reduction factor
SRF	Stress Reduction Factor

4.2.4 Geological Strength Index (GSI)

The Geological Strength Index is developed by Hoek (1994) and Hoek *et al*. (1995) to overcome compatibility issues with the Hoek-Brown failure criterion (section 0). It describes the blockiness and degree of interlocking of a rock mass and the condition of discontinuity surfaces. The index shows the reduction in rock mass strength for different geological settings. Figure 26, on the next page, shows an indicative chart with GSI-values.

The main differences with the RMR are a lack of a uniaxial compressive strength value for intact rock pieces and a single parameter for the discontinuity spacing (the RMR includes discontinuity spacing and an RQD-value, which indirectly indicates discontinuity spacing). Equations 4.3 and 4.4 can calculate the GSI value from the RMR_{76} or RMR_{89} if the groundwater rating is set to 15 and the adjustment for joint orientation is set to zero. This is especially handy when blasting damage makes it hard to evaluate a rock face, because the RMR_{89} can be retrieved from a core sample. (Hoek, *et al*., 1995)

$$GSI = RMR_{76} \qquad RMR_{89} \geq 18$$

4.3

$$GSI = RMR_{89} - 5 \qquad RMR_{89} \geq 23$$

4.4

Hoek and Brown (1998) have related the GSI to the Q-classification scheme and came up with equation 4.5. It can be applied for rock masses with an RMR_{89}-value below 23 and only uses the rock mass characteristics from the Q-classification system, denoted by Q' in equation 4.5. This highlights the stress independency of the GSI.

$$GSI = 9 \cdot \ln Q' + 44$$

4.5
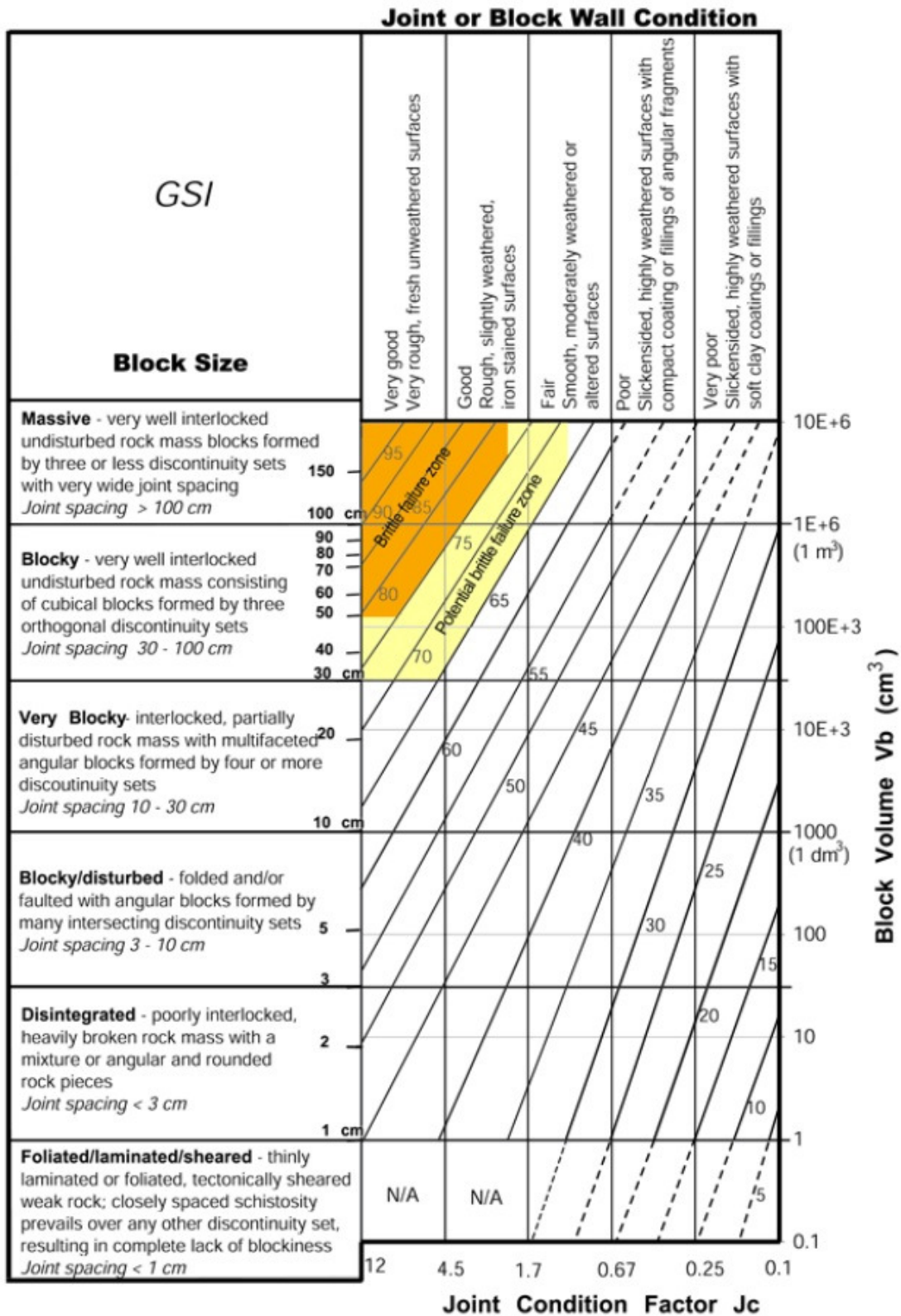
Figure 26: Indicative chart for GSI (Cai, *et al.*, 2004)

5 Rock mass behaviour

Three different modes are able to describe the instability of a rock mass under all conditions. These modes of instability are sketched in Figure 27. The rock mass behaviour depends strongly on the geotechnical environment and the stress field. Squeezing conditions can be observed in weak rock masses and are accompanied by shear failure. Excavations in hard rock lead to two distinct failure processes. The first is a gravity-driven process that leads to wedge type failures from the back and walls, *i.e.* structurally controlled kinematic instability. These conditions only apply in very shallow mines or in mining-induced stress relaxation conditions. Block caving operations are mainly in competent rock masses and in high stress regimes. Brittle rock failure is the most common mode of instability in these geotechnical conditions. (González-Nicieza, *et al.*, 2006)
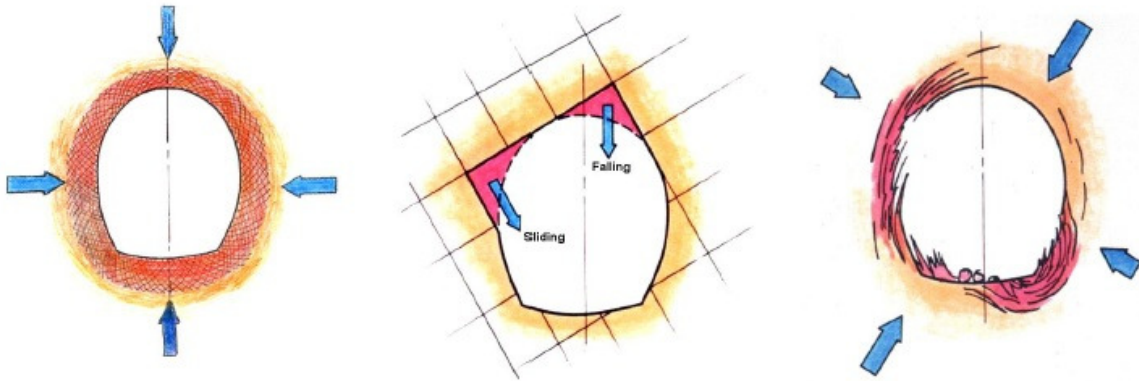
Figure 27: Modes of instability – Weak-rock shear failure (left), structurally controlled kinematic instability (middle), brittle rock failure (right). (Corkum, *et al.*, 2010)

This chapter will introduce the conventions of stress analysis and the change in stress fields from *in situ* to mining conditions. The second section will expand on brittle rock failure. Subsequently, the damage to rock masses due to blasting is discussed and the last section of this chapter describes the shear strength of caved rock.

5.1 Stress analysis

The stress state can be defined by three sets composed of a normal stress and two shear stresses acting on perpendicular planes. Normal stresses act normal and shear stresses act tangentially to a plane. The shear stress components are always stated as stresses acting on planes perpendicular to one of the three coordinate directions. There are no shear stresses present when the stress tensor is built from principal stresses. These three principal stresses are mutual perpendicular stress components and follow the convention denoted in equation 5.1. The complete stress tensor is shown in equation 5.2.

$$\sigma_1 > \sigma_2 > \sigma_3 \qquad\qquad \text{5.1}$$

$$\sigma_{ij} = \begin{pmatrix} \sigma_{xx} & \tau_{xy} & \tau_{xz} \\ \tau_{yx} & \sigma_{yy} & \tau_{yz} \\ \tau_{zx} & \tau_{zy} & \sigma_{zz} \end{pmatrix} \qquad\qquad \text{5.2}$$

The traditional sign convention in rock mechanics is a negative sign for tensile stresses and a positive sign for compressive stresses. This is done in order to avoid frequent use of negative signs. When a positive normal stress is directed parallel to a positive coordinate axis, the shear stresses are positive when directed parallel to one of the remaining two coordinate axes, and vice versa, as shown in Figure 28. The first subscript of the shear stresses denotes the direction the stress acts in, the second subscript denotes the direction of the normal of the plane the shear stress is located on. (Goodman, 1989)
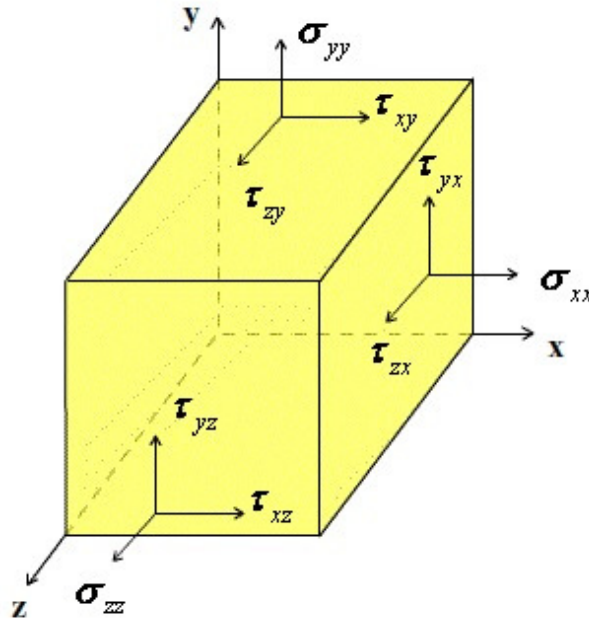
Figure 28: Visualisation of the full stress tensor.
(Department of Materials Science and Metallurgy, University of Cambridge, 2013)

5.1.1 *In situ* stress

The vertical stress is typically consistent with the weight of the overlying rock, a product of depth and unit weight as described in equation 5.3. The industry standard unit for stress is MPa, equal to 100 tonnes per square meter. Measurements of vertical stress levels deviate from a linear relation with depth due to the unique unit weight of each rock mass. Brady and Brown (2004) collected measurements worldwide and derived a linear interpolation as shown in Figure 29.

$$\sigma_v = \gamma \cdot z \qquad\qquad 5.3$$
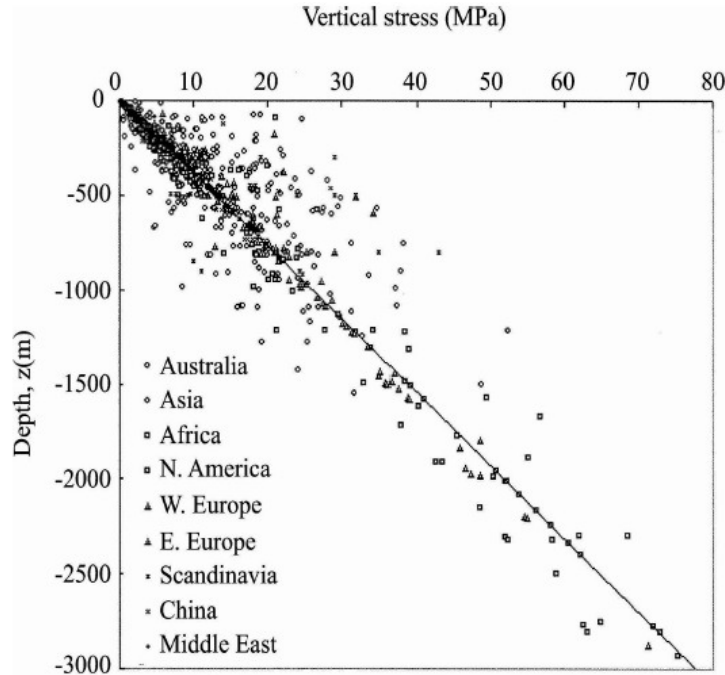
Figure 29: Interpolation of the unit weight of rock masses. (Brady & Brown, 2004)

The calculation of horizontal stresses is more complicated and commonly makes use of the stress ratio k to arrive at equation 5.4. The horizontal to vertical *in situ* stress ratio k is determined in an elasto-static thermal stress model of the earth's crust by Sheorey (1994). Under-calculated vertical stresses, very high horizontal stresses and the differences between directional horizontal stresses cannot be explained by Sheorey (1994), because of the scale of his model. Equation 5.5 states the relation between the stress ratio, depth and the elastic modulus.

$$\sigma_h = k \cdot \gamma \cdot z \qquad\qquad 5.4$$

$$k = 0.25 + 7 \cdot E_h \left(0.001 + \frac{1}{z} \right) \qquad\qquad 5.5$$

Parameter	Unit	Description
σ_v	Pa	Vertical stress
σ_h	Pa	Horizontal stress
k	-	Horizontal-to-vertical *in situ* stress ratio
γ	N/m^3	Unit weight
E_h	GPa	Horizontal elastic modulus
z	m	depth

Higher values for the stress ratio k close to surface are an effect of the curvature of the earth. The formula can be used to predict the average horizontal stress, but actual measurements of stress levels remain advisable. The relation between the parameters in equation 5.5 is shown in Figure 30, together with a plot of worldwide *in situ* stress measurements. The importance of the stress ratio for block caving operations is clarified by Figure 31, which shows the impact of the stress ratio on cave back stability with a Finite Element Model (FEM) of an 80m span excavation (consult section 8.1 for the definition of FEM).
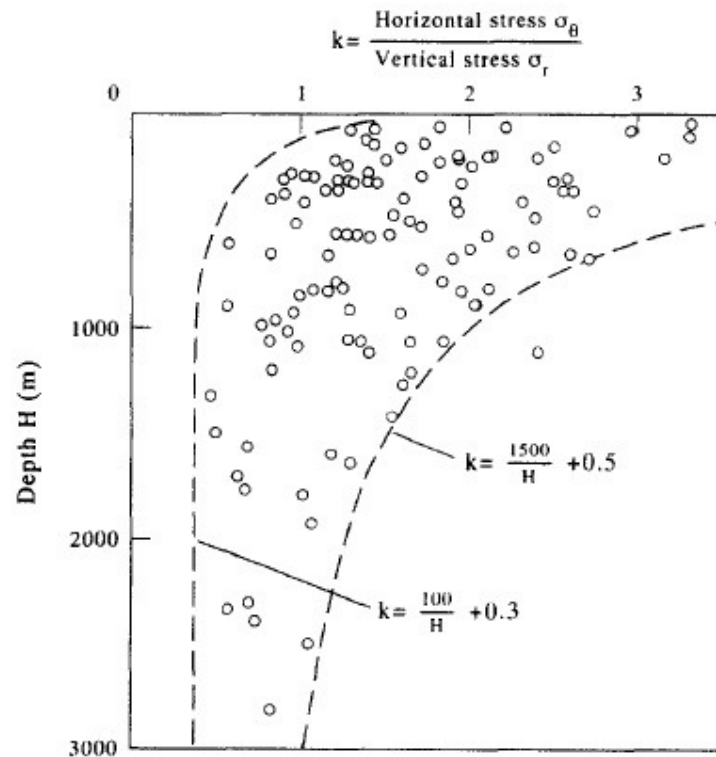
Figure 30: Stress ratio as a function of depth and different deformation moduli. (Sheorey, 1994)

80 m span, k = 1.0   80 m span, k = 1.5   80 m span, k = 1.8
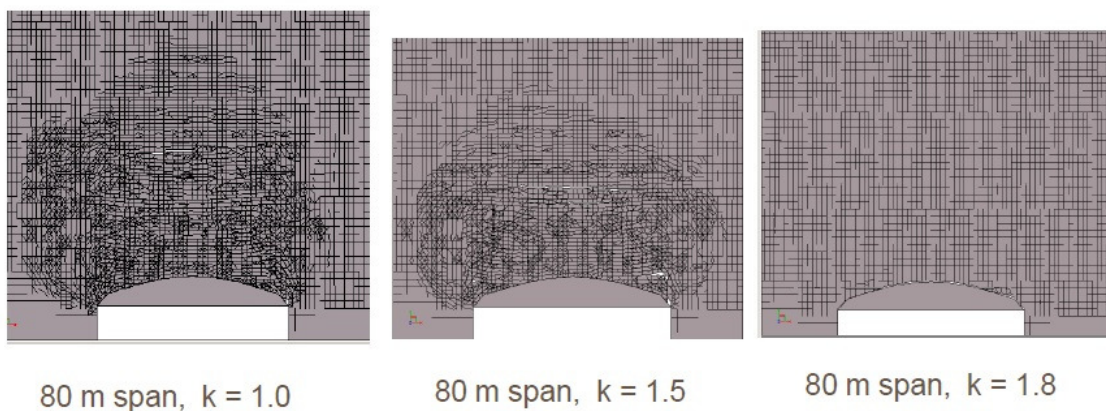
Figure 31: A Finite Element Model of a jointed rock mass shows the influence of the stress ratio k on cave back stability. Stability increases with an increasing horizontal stress relative to the vertical stress. A low stress ratio implies early cave initiation. (Moss, 2010)

5.1.2 Induced stress

Excavations in the rock mass create a re-distribution of the *in situ* stress field. The minor principal stress, *i.e.* confining stress, at excavation boundaries becomes zero and increases at distance from the excavation boundary. The major principal stress varies from place to place and over time due to the geometry and size of the excavation. Figure 32 illustrates the induced stress field during cave initiation. Major principal stress magnitudes are colour coded. Green indicates low stresses (even tensile stress regimes) and red indicates relatively high stresses. The back of the cave is characterised by a tensile stress regime, while the high abutment stresses are acting on the extraction level infrastructure in front of the cave line.
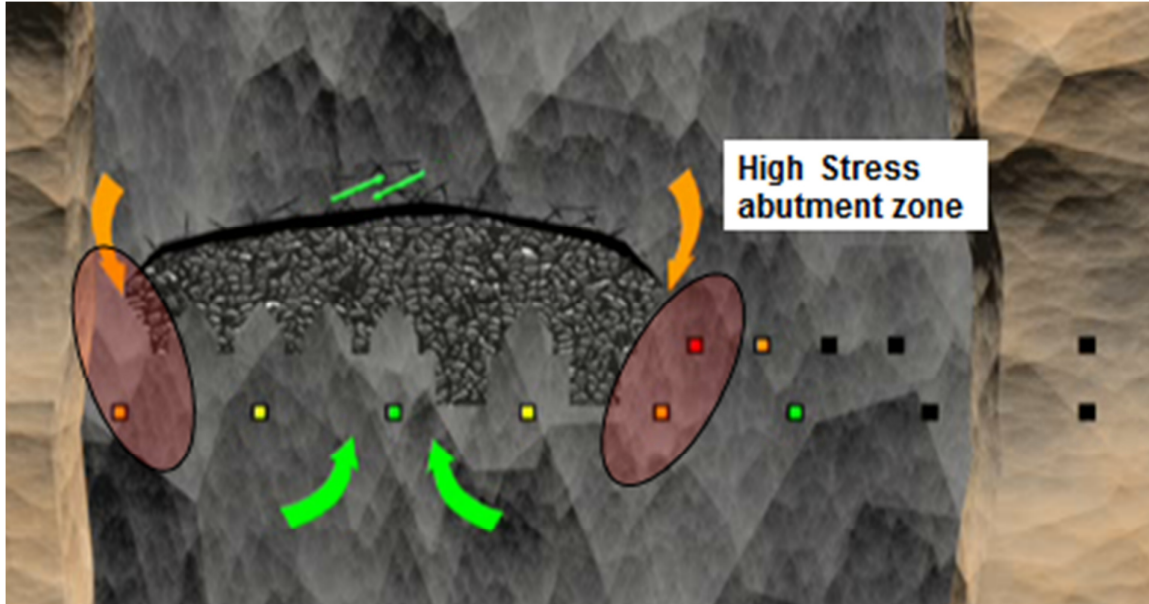
Figure 32: Vertical cross-section of a massive deposit during cave initiation. Green indicates low stresses, red indicates high stresses. (Moss, 2010)

5.1.3 Stress measurements

It is almost impossible to understand all processes involved in local geological history to estimate, in particular the horizontal, stresses. Therefore, an *in situ* stress measurement campaign has to be set up to map the total stress field in three dimensions (σ_{tot}). The total stress is always an addition of initial stresses and induced stresses (σ_{ind}) due to topography, excavations and material properties. The initial stress can be split into a gravitational component (σ_{grav}) and a tectonic component (σ_{tec}) which generally represents the horizontal stresses mentioned before. Equation 5.6 summarises the composition of total stress in a formula. It must be emphasized that the uncertainty of both the direction and the magnitude of stress components after measurements is significant. (Corkum, *et al.*, 2010)

$$\sigma_{tot} = \sigma_{grav} + \sigma_{tec} + \sigma_{ind} \qquad \text{5.6}$$

5.2 Brittle rock failure

A brittle rock mass is competent with relatively large block sizes, high uniaxial compressive strength and a high Geological Strength Index (GSI). Processes driving failure in brittle rock masses differ significantly at high and low confinement (Kaiser, *et al.*, 2010). Micro-defects, built-in planes of weakness, open up parallel to an excavation due to stress release. Together with subsequent fracture propagation this results in brittle failure. This type of tensile failure is called brittle spalling and is depicted in Figure 33. The ratio of intact rock strength to *in situ* stress determines if spalling is limited to small slabs or if it can develop into rock- or strainburst conditions. The general name for this process is bulking, the unidirectional (orientated to lowest confinement) volumetric increase of the rock mass due to brittle failure and to a smaller extent by shearing mechanisms. According to Corkum *et al*. (2010), brittle rock failure takes place around excavations as long as the deviatoric stress $(\sigma_1 - \sigma_3)$ is higher than approximately 30% of the Unconfined Compressive Strength. Kaiser & Kim (2008) point out that degradation near excavations cannot be prevented, but must be managed by appropriate rock reinforcement and retention techniques. In high confinement zones, the propagation of tensile cracks is prevented by confining stresses. Shear bands are the dominant structures causing failure in these elastically behaving zones.
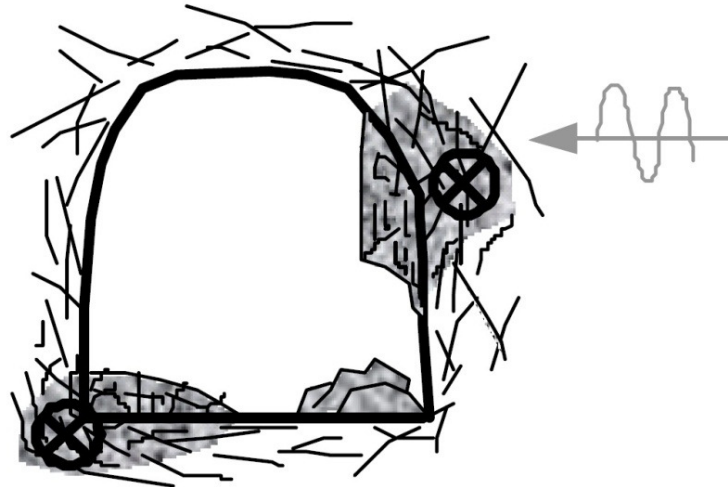
Figure 33: Strain burst or bulking (Kaiser, *et al.*, 2000).

Figure 34 shows a collection of failure modes depending on the rock mass quality and the stress regime. According to Kaiser & Kim (2008), the conditions marked in red are typically accompanied by brittle rock failure.

Figure 34: Tunnel failure modes as a function of the Rock Mass Rating and the ratio of the maximum far-field stress to the unconfined compressive strength of the rock mass. Modified after Kaiser *et al*. (2000).

Zhao & Cai (2010) described the failure process of brittle rock as shown in Figure 35. Initial loading results in crack closure and linear, elastic deformation. Heterogeneities in the rock mass are microcrack sources and cause local tensile stresses. Microcracks start to propagate and new cracks are formed, but the volume of the rock mass is still decreasing. At the crack damage threshold (point B/F), the crack density in a rock mass is sufficient for cracks to coalesce and unstable crack growth is the result. Tensile spalls and shear bands are formed and volumetric strain is reversed. Subsequently, the compaction of initially existing voids equals the volume of newly generated cracks at point G. More information on stress-strain relations and the dilative behaviour of rock masses can be found in chapter 6.
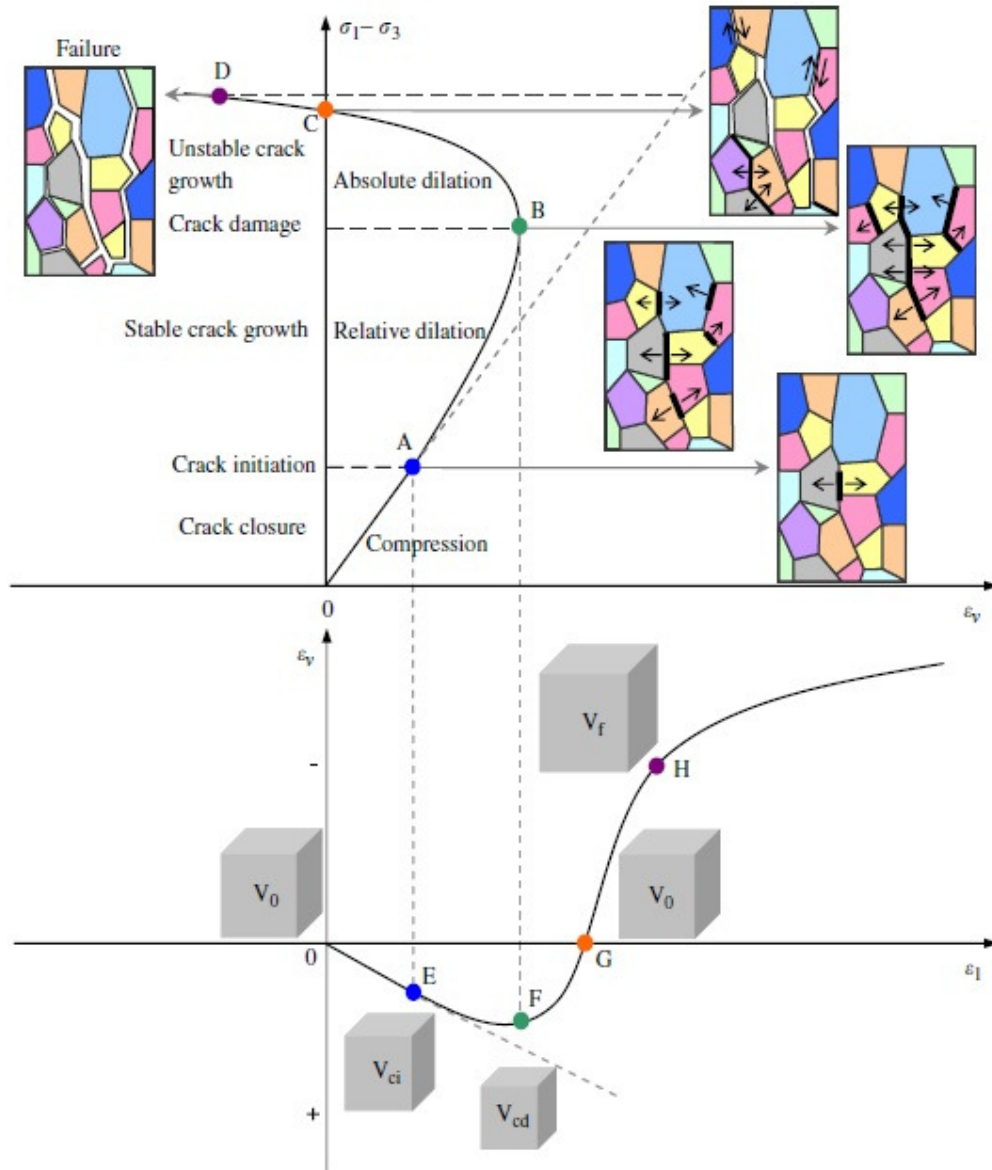
Figure 35: Differential stress versus volumetric strain with illustrations of crack initiation, growth and coalescence (top). Volumetric strain versus axial strain with illustration of the dilation process (bottom). (Zhao & Cai, 2010)

5.3 Damage induced by blasting

Because infrastructure at the extraction level of a block cave is designed to persist most of the lifetime of the mine, damaged induced by blasting should be kept to a minimum. The challenge is to achieve a maximum rock breakage within the drill pattern and minimize damage outside the blast design. This damage results in a decrease in stability and requires an increased amount of support. Besides that, overbreak results in excessive rock to handle during development and operators are therefore always keen to prevent as much blasting damage as possible.

There are two mechanisms dominating fragmentation and thus blasting damage. These are dynamic stresses or vibrations and expanding gasses produced by the explosion. Vibrations are quantified by the peak particle velocity, while fragmentation due to gas fracturing is hard to quantify. According to Hoek (2007), the stability of underground excavations is dependent on the integrity of the rock immediately surrounding the excavation. Incorrect blasting results can be obtained due to preliminary seismic events. Seismicity causes dislocation of the boreholes which prevents the boreholes from being filled completely with explosives. As a result, the rock mass around the last part of the affected boreholes will stay intact. This can be an issue when the inclined surfaces on top of the major apex are drilled from below. If the rock mass surrounding the bottom of the borehole stays intact, remnant pillars of intact rock will support stable arching at the back of the cave. Figure 36 illustrates arch forming on flat major apices as a result of poor undercut design. Measures have to be taken to reinforce production.
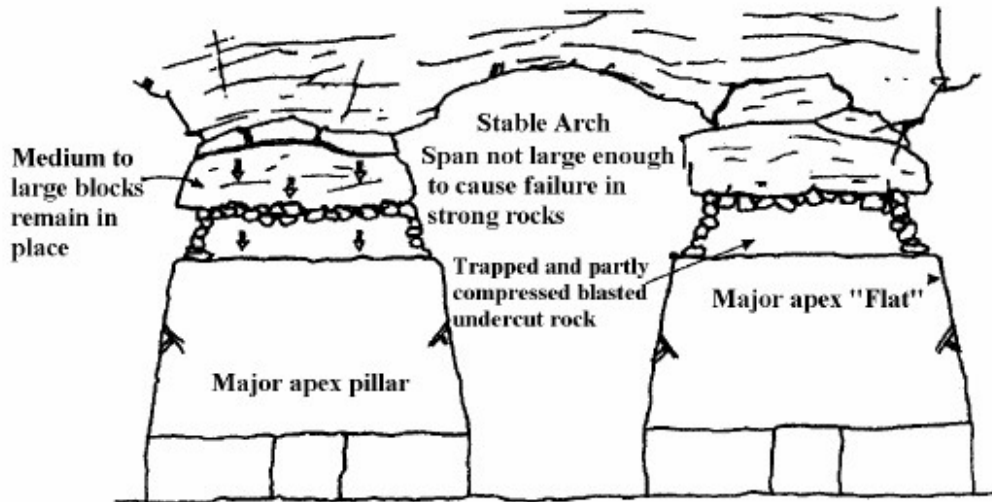
Figure 36: Stable arch forming on flat major apex (Brown, 2003)

There are several methods to prevent or control blasting damages. The most obvious one is to replace drilling and blasting by mechanical excavation whenever possible. The best way to ensure minimised blast damage is stress relief by undercutting, as discussed in section 2.3. Drilling accuracy can be improved significantly by reducing the spacing of perimeter boreholes and the burden between rings. Smooth blasting techniques use less powerful explosives in these perimeter boreholes and result in a less fractured rock boundary when detonated simultaneously. Pre-splitting is a similar technique where the perimeter boreholes are detonated before the rest. Specified tolerances with contractors help to minimise overbreak and deviation from the centre line of tunnels. Furthermore, ground support can assist in the ability of rock to withstand stresses and wear throughout the lifetime of the infrastructure. The result of a well performed drill and blast campaign in combination with a suitable support mechanism is reduced maintenance on initial ground support and major and minor apices that can withstand forces from arching.

5.4 Shear strength of caved rock

Barton and Kjaernsli (1981) have studied the stability of dams and reported on rock fill, rock joint and interface strength. In essence, these situations all are point-contact stress states and they therefore show very similar behaviour. Figure 37 clearly shows the resemblance with caved rock in a block caving operation. The remainder of this subsection will focus on the frictional strength of rock fill.
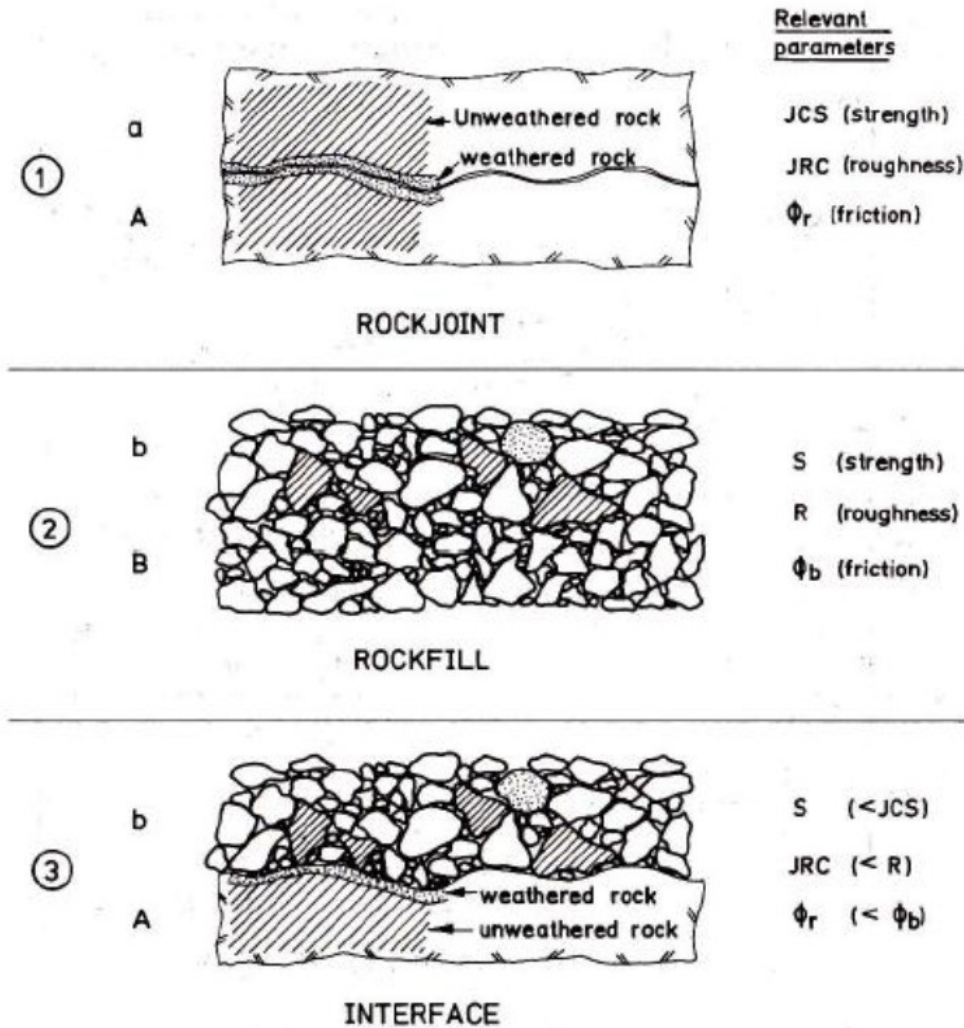
Figure 37: Empirical shear strength estimates (Barton & Kjaernsli, 1981)

The complicated behaviour of rock fill is best described by equation 5.7. The peak drained friction angle (ϕ') is a summation of the basic friction angle (ϕ_b) and the structural component of strength (i) which is strongly stress dependent. The peak drained friction angle can be used in the Mohr-Coulomb constitutive law (section 7.1) to analytically retrieve the peak shear strength of rock fill. The basic angle of friction can be estimated from a simple tilt test on a dry, flat, non-dilatant surface and typically ranges between 25° and 30°. Conservative, long-term designs of permanent rock fill use the residual angle of friction (ϕ_r) instead of the basic friction angle. The residual angle of friction can be calculated from the basic angle of friction together with the results of a Schmidt hammer test.

$$\phi' = \phi_b + i \qquad\qquad 5.7$$

The empirical approach to establish the structural component of strength makes use of a size-dependent equivalent particle strength factor (S) and an equivalent roughness factor (R). The factor S depends on the UCS of the rock and the mean particle size according to Figure 38. The factor R depends on the origin, roundness and smoothness of the particles and on the porosity, according to Figure 39. Together with the effective normal stress they form the structural component of strength according to equation 5.8.

$$i = R \cdot \log\left(\frac{S}{\sigma'_n}\right) \qquad\qquad 5.8$$
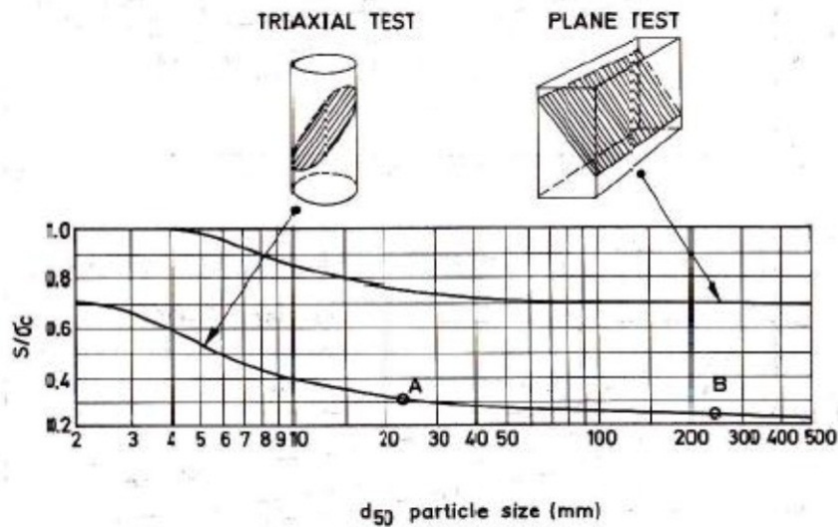
Figure 38: Dependencies of the S-factor (Barton & Kjaernsli, 1981)
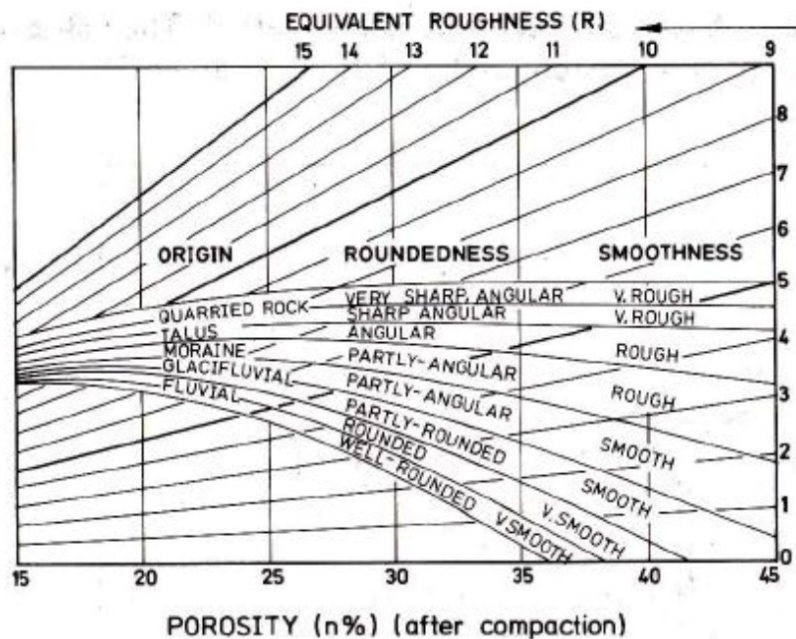
Figure 39: Dependencies of the R-factor (Barton & Kjaernsli, 1981)

High stresses localise at positions where particles in rock fill are in contact. These local stresses are called contact normal stresses (σ_{cn}) and are illustrated in Figure 40. The ratio between the contact normal stress and the particle strength (S) is assumed to be equal to the ratio of true contact area (A_0) to assumed contact area (A_1) according to equation 5.9. These asperities can easily wear off as a result of local failure, resulting in a smoother and more round contact surface. This process results in lower shear strength of the rock fill. (Barton, 2008)

$$\frac{\sigma_{cn}}{S} = \frac{A_0}{A_1} \qquad\qquad 5.9$$
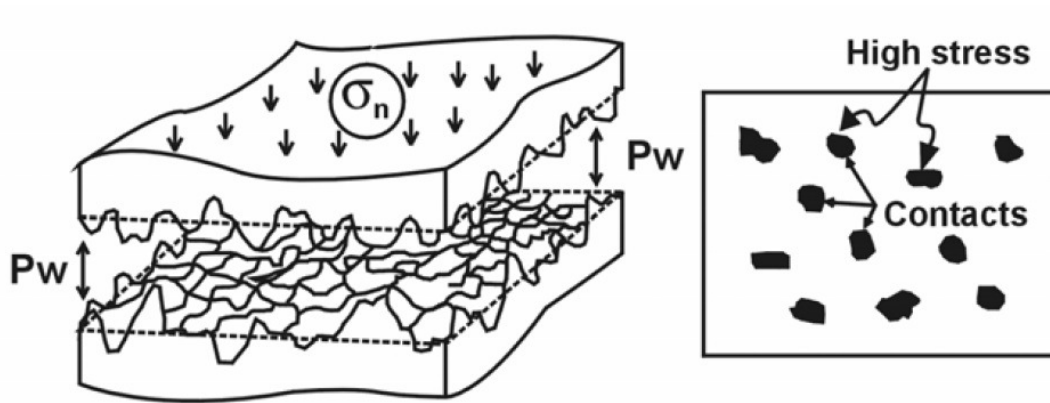
Figure 40: Concept of contact normal stress (Barton, 2008)

6 Stress-strain relations

The stress-strain behaviour usually dominates the mechanical properties of a rock mass. Stress and strain constants in the elastic range, stress levels at which yield, fracturing or slip occur and post-peak stress-strain behaviour of failed rock are important aspects of this behaviour according to Brady and Brown (1993). Rock failure in nature takes place on a big scale and is therefore hard to study. Scientific research provides small scale and fast processes in laboratories. A stress-strain curve can be created by performing laboratory strength tests like the direct or triaxial shear test, the uniaxial or triaxial compressive test and the Brazilian test which measures tensile strength. The triaxial compressive test has become the industry standard. Figure 41 shows a triaxial cell designed by Hoek and Franklin (1968). In this test, the rock is strengthened by applying a confining pressure realised by an impervious jacket. Strain gauges measure the amount of axial and radial strain. Hoek *et al*. (2002) recommend performing triaxial tests with confining pressures up to 50% of the Uniaxial Compressive Strength (UCS) of the intact rock. The UCS index can be obtained from a compression test on a cylindrical rock specimen without any confining pressure and is therefore also called the Unconfined Compressive Strength.
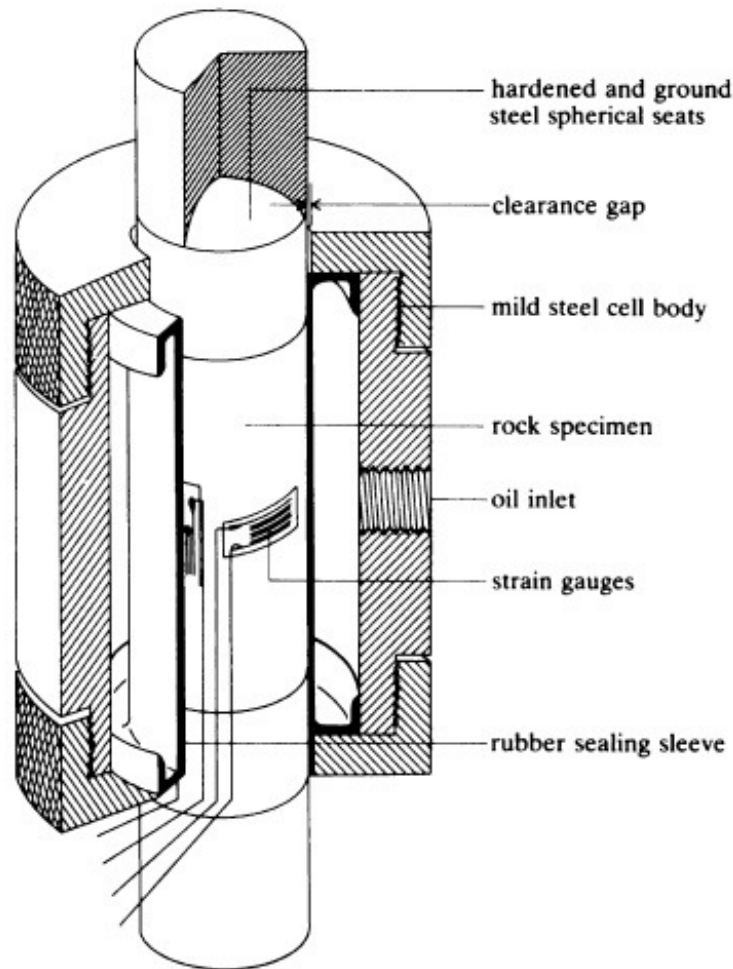
Figure 41: Schematic cut-away of a triaxial cell (Brady & Brown, 2004)

6.1 The elastic range

The initial response of a rock mass to an increase of stress is elastic. The results of an ideal triaxial test on brittle intact rock are plotted in Figure 42. Only the stress-strain relation until peak-load is shown at this stage. The following descriptions give some extra information on the processes that take place according to Cai *et al.* (2004).

I.   Fissures and pores begin to close in an inelastic way.
II. The axial and lateral strain react linear-elastic on axial stress according to Hooke's Law. The constant slope angle in the stress-strain curve is called Young's modulus (or elastic modulus). The amount of recoverable strain as a result to an applied stress is every time the same according to differential equation 6.1.

$$E = \frac{d\sigma}{d\epsilon} \qquad\qquad 6.1$$

III. The lateral strain starts to increase at a faster rate relative to the axial strain. This means that the so called Poisson's ratio is increasing according to equation 6.2. This ratio describes the extension in a direction perpendicular to a compression. Each stress increment is accompanied by a finite crack length growth. Crack initiation and stable propagation are associated with "rock noise".

$$\upsilon = -\frac{d\varepsilon_{lateral}}{d\varepsilon_{axial}} \qquad\qquad 6.2$$

IV. Coalescence of micro-cracks and unstable crack growth form faults and cause the rock to fail at peak load (point D).
V.   Macro-cracks or shear bands are formed after the peak strength is reached.
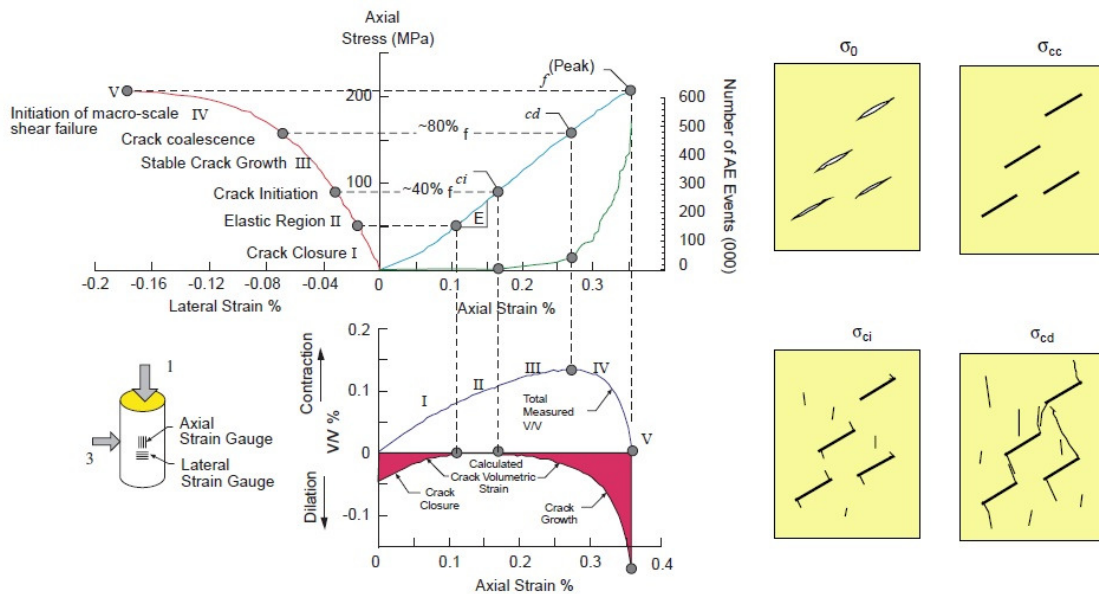
Figure 42: Stress-strain diagram with stages of crack development. (Cai, *et al.*, 2004)

The isotropic, elastic behaviour in the elastic range can be described by two different pairs of parameters. These coupled coefficients of proportionality are either the bulk modulus (K) and shear modulus (G) or the discussed Young's modulus (E) and Poisson's ratio (v). The mathematical relation between these pairs of parameters is expressed in equation 6.3 and 6.4.

$$K = \frac{E}{3(1 - 2v)}$$ 6.3

$$G = \frac{E}{2(1 + v)}$$ 6.4

There are multiple ways to measure the Young's modulus, since the initial slope of a stress-strain curve is not exactly linear. The Tangent Young's Modulus (E_t) is the slope of the curve at 50% of peak strength. The Average Young's Modulus (E_{av}) is the average slope of the linear section of the curve and the Secant Young's Modulus (E_s) is the slope of a line through the origin and a point on the curve, mostly taken at peak strength. (Brady & Brown, 2004)

By convention, all isotropic, linear elastic materials have a Poisson's ratio between -1 and 0.5. Negative Poisson's ratios have never been observed in nature, this would imply lateral extension upon longitudinal extension, but are not ruled out mathematically. The extremes represent limiting cases in the equations above. The use of Young's modulus and Poisson's ratio would imply an arbitrarily large bulk modulus or a Young's modulus that tends to zero. Since compressibility is limited and the principal mode of elastic resistance does not change, the use of the bulk and shear moduli is desirable in numerical modelling and hence the importance of the formulas above.
(Itasca Consulting Group, Inc., 2013)

Non-deviatoric stresses, *i.e.* hydrostatic pressure, do not destruct or distort the rock. They produce a volume decrease and can change the rock fabric permanently. This elastic bulk rock compression consists of pore deformation and grain compression and is denoted by the bulk modulus, mathematically expressed in equation 6.5. (Goodman, 1989)

$$K = \frac{d\sigma_{mean}}{d\epsilon_v}$$ 6.5

6.1.1 Empirical fitting of elastic parameters

Serafim and Pereira (1983) were one of the first to empirically relate the elastic modulus of rock masses to a rock mass classification scheme, namely the RMR_{76} (equation 6.6). Their relation only holds for isotropic rock masses with a UCS above 100 MPa. Hoek and Brown (1997) made a relation for poor quality, isotropic rock masses and incorporated the disturbance factor and the GSI (equation 6.7). Barton (2002) used a third power curve and his Tunneling Quality Index Q to relate the elastic modulus and the quality of the rock mass for rock masses with a UCS of approximately 100 MPa (equation 6.8). After three decades of research in this field, the most recent and widely accepted relation is established by Hoek and Diederichs (2006). Equation 6.9 can be applied when reliable estimates of the elastic tangent modulus of intact rock are available and equation 6.10 is a simplified version that does not use the intact rock elastic modulus.

$$E_{rm} = 10^{\frac{RMR-10}{40}} \qquad \text{6.6}$$

$$E_{rm} = \left(1 - \frac{D}{2}\right)\sqrt{\frac{\sigma_{UCS}}{100}} \cdot 10^{\frac{GSI-10}{40}} \qquad \text{6.7}$$

$$E_{rm} = 10\left(\frac{Q \cdot \sigma_{UCS}}{100}\right)^{1/3} \qquad \text{6.8}$$

$$E_{rm} = E_i\left(0.02 + \frac{1 - D/2}{1 + e^{\frac{60+15 \cdot D - GSI}{11}}}\right) \qquad \text{6.9}$$

$$E_{rm} = 10^5 \cdot \left(\frac{1 - D/2}{1 + e^{\frac{75+25 \cdot D - GSI}{11}}}\right) \qquad \text{6.10}$$

Parameter	Unit	Description
E_{rm}	GPa	Modulus of rock mass
RMR	-	Rock Mass Rating
σ_{UCS}	MPa	Uniaxial Compressive Strength
GSI	-	Geological Strength Index
D	-	Disturbance factor
Q	-	Tunneling Quality Index
E_i	GPa	Intact rock modulus

Gercek (2007) created a table with ranges of the Poisson ratio of intact rock for several rock types (appendix F). Unfortunately, there is no empirical relation that correlates the Poisson's ratio for intact rock and rock masses. *In situ* determination of Poisson's ratio can be done with cylindrical and flat hydraulic borehole pressure cells or with large flat jacks. The involved rock mass volume ranges from a cubic meter to significantly large volumes. There is however a correlation between Poisson's ratio and the Geological Strength Index. Equation 6.11 is formulated by Lorig and Pierce (2000) after data from Hoek *et al.* (1995).

$$v_{rm} = 0.32 - 0.0015 \cdot GSI \qquad \text{6.11}$$

6.2 Peak strength

The elastic behaviour transforms to plastic behaviour, at the yield point. Any deformation beyond the yield point is non-recoverable. The rock mass parameters have different values before and after peak strength. The peak strength of a rock specimen without any confining pressure is termed the Uniaxial Compressive Strength or Unconfined Compressive Strength (UCS). The UCS is, by convention, retrieved from rock samples with a diameter of 50 mm. Equation 6.12 can be used to scale strength values of other sample sizes. Figure 43 shows a diagram with all rock masses used to create the relation between sample size and peak strength. The ratio of UCS to tensile strength is indicative for the brittleness of the rock.

$$\sigma_{UCSd} = \sigma_{UCS50} \left(\frac{50}{d}\right)^{0.18} \hspace{3cm} 6.12$$
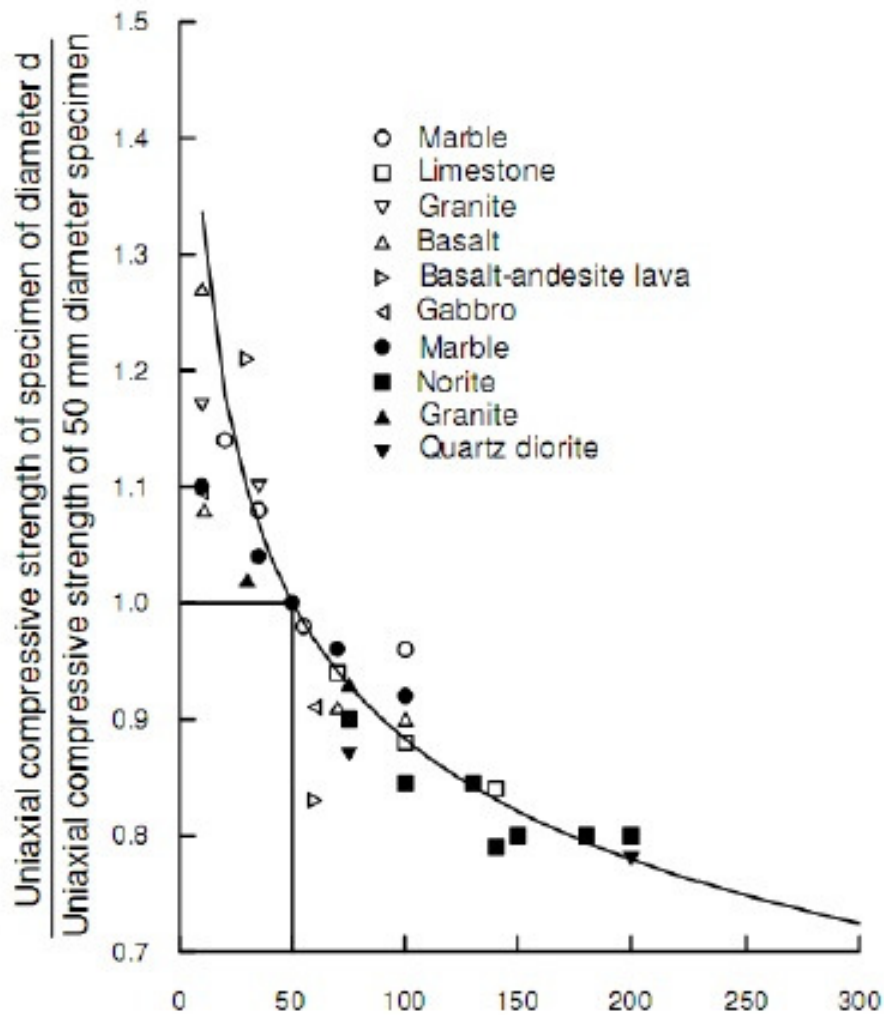
Figure 43: Scaling of UCS for different sample diameters (Hoek, *et al.*, 1995).

6.3 Post-peak behaviour

Rock masses generally exhibit post-peak strain-softening behaviour, *i.e.* strength-weakening, which is the gradual loss of load-bearing capacity from a peak load condition to a residual one. Figure 44 illustrates the difference in post-peak behaviour related to confinement. A rock mass behaves increasingly ductile with increasing confining pressure until the brittle-ductile transition pressure is reached. Mogi (1966) terms this transition as $\sigma_3/\sigma_1 = 1/3.4$. Beyond this point, strain-hardening of the rock mass, instead of strain-softening takes place. Thus, the rock mass becomes stronger as strain increases.

Besides confinement, the quality of the rock mass determines its post-peak behaviour. Very good quality rock masses behave elastic-brittle, average quality rock masses show strain-softening and very poor quality rock masses behave elastic-perfect plastic. It must be emphasised that not only the material properties determine the failure characteristics, but also the state of stress.
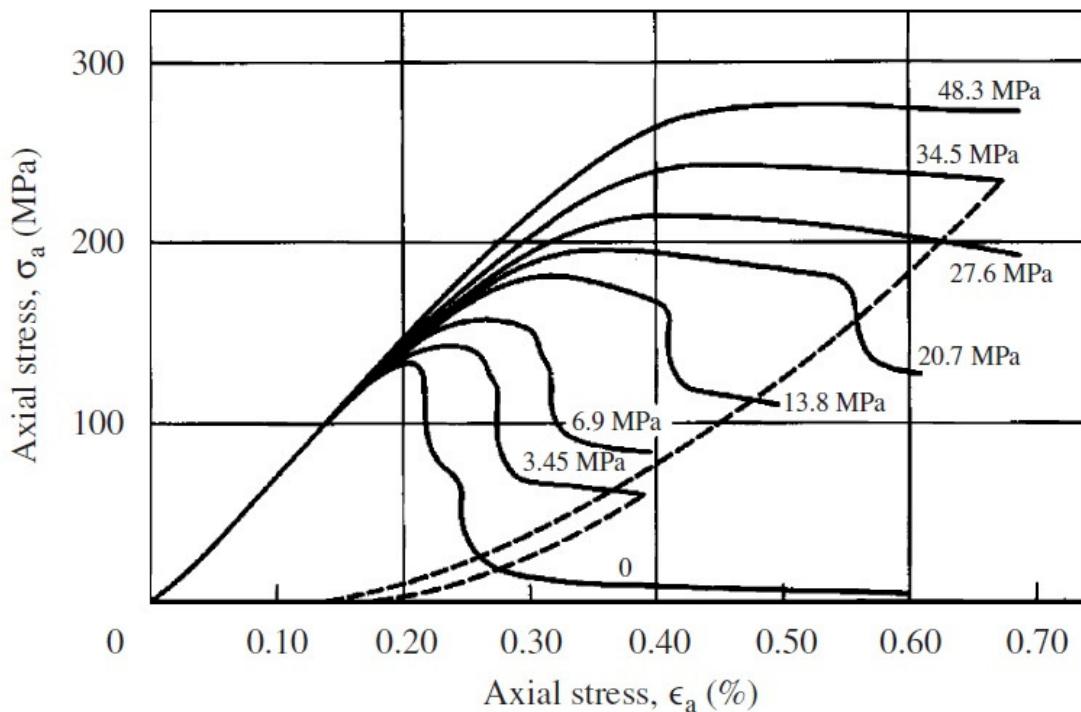
Figure 44: Post-peak behaviour at different confining pressures (Cai, *et al.***, 2007)**

The critical plastic strain indicates the transition from peak to residual strength. The amount of critical plastic strain increases with decreasing rock quality and increasing confinement. Thus, the sudden drop in the load-bearing capacity of a brittle failing rock mass is accompanied by a small amount of critical plastic strain (Zhao & Cai, 2010). The following two subsections discuss the relation between plastic strain and cohesion, friction and dilation. Subsection 8.4.3 elaborates on the relation between rock mass quality and critical plastic strain in numerical modelling.

6.3.1 Cohesion Weakening and Frictional Strengthening (CWFS)

Traditional failure criteria like the linear Mohr-Coulomb and the nonlinear Hoek-Brown criterion are based on the simultaneous and instantaneous mobilization of cohesive and frictional strength components as sketched in Figure 45. Continuum models based on these traditional failure criteria have not been able to successfully predict the extent and depth of brittle failure. A fundamental aspect of brittle failure is that the formation of tensile cracks precedes failure in shear. Therefore, Hajiabdolmajid *et al.* (2002) developed a modelling approach called Cohesion Weakening and Frictional Strengthening (CWFS).
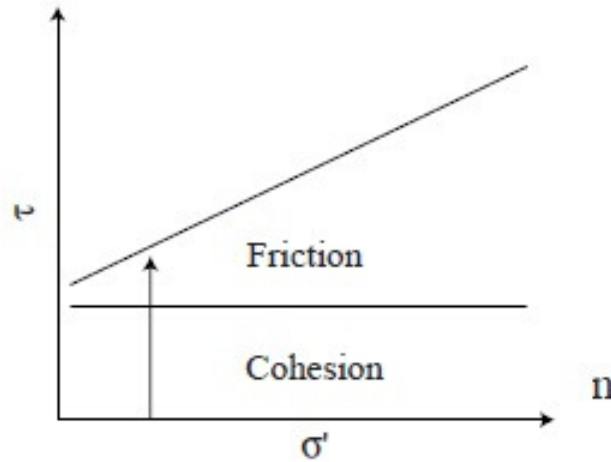
Figure 45: Simultaneous mobilization of cohesive and frictional strength (Hajiabdolmajid, *et al.*, 2002)

The CWFS approach incorporates the initiation, growth and accumulation of micro-cracks and progressive slabbing around excavations by considering plastic strain-dependencies of cohesive and frictional strength. Cohesion loss, in the early stage of brittle failure, is the predominant driving mechanism of observed brittle behaviour. The cohesive strength is gradually destroyed by tensile cracking and crack coalescence, while the frictional strength is mobilised at a later stage due to delayed internal normal stress development. Figure 46, on the next page, illustrates the CWFS approach and Figure 47, on the next page, emphasizes the delay in frictional strength mobilisation with respect to the mobilisation of cohesive strength ($\varepsilon_f^p > \varepsilon_c^p$).
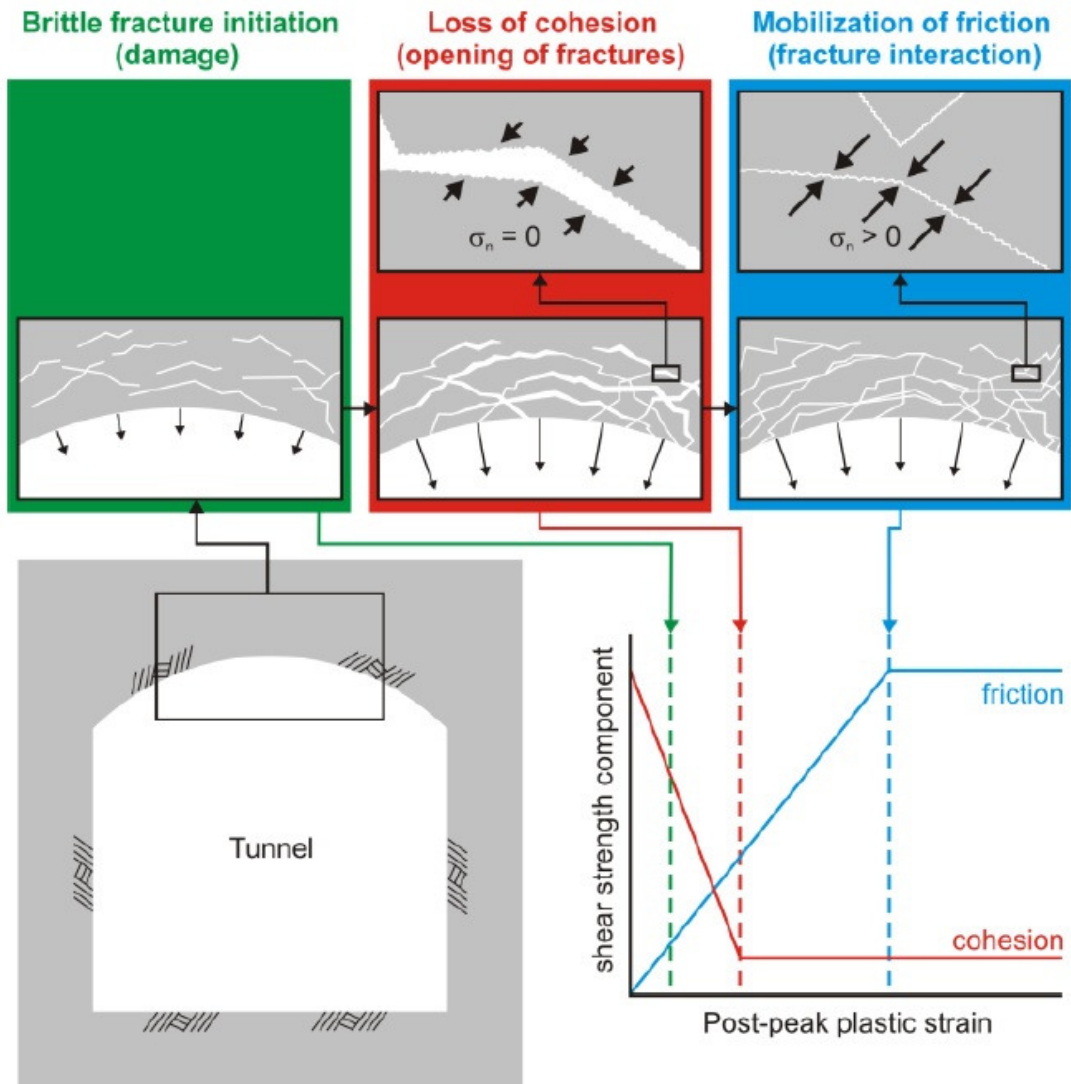
Figure 46: Cohesion Weakening and Frictional Strengthening (Corkum, *et al.*, 2010)
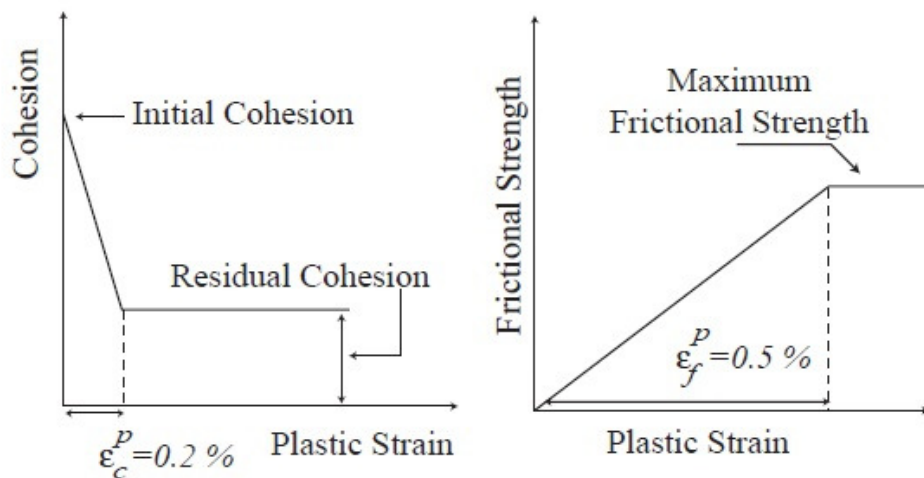
Figure 47: Cohesion and frictional strength versus plastic strain (Hajiabdolmajid, *et al.*, 2002)

6.3.2　Dilatancy

Dilation is best described by Sturm (2012) as a concise definition compiled from multiple papers: *"Dilatancy is the volumetric increase of rock caused by an increase in void space as result of shear distortion and by micro-crack initiation and propagation under compression."* The physical meaning can be understood by considering a frictional sliding along micro-cracks or particles as shown in Figure 48.
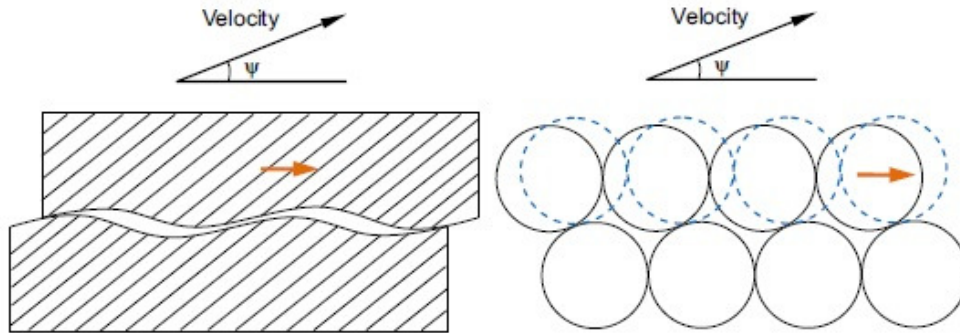
Figure 48: Frictional sliding along micro-cracks (left) or particles (right). (Zhao & Cai, 2010)

Dilatancy is described by the dilation angle (ψ), a ratio between plastic volume change and plastic shear strain. A positive dilation angle stands for an irreversible volume increase and a negative dilation angle accompanies plastic contraction. The dilation angle varies from zero to the friction angle ($0 \leq \psi \leq \phi$). Vermeer and de Borst (1984) believed that the dilation angle is a constant around peak strength values and is at least 20° lower than the friction angle, commonly between 0° - 20°. Hoek and Brown (1997) suggested a constant dilation angle based on the rock mass quality. They used a dilation angle of one fourth of the friction angle for very good rock qualities and a negligible dilation angle for poor rock qualities. Corkum *et al*. (2010) produced Figure 49 to provide a starting point in establishing the dilation angle.
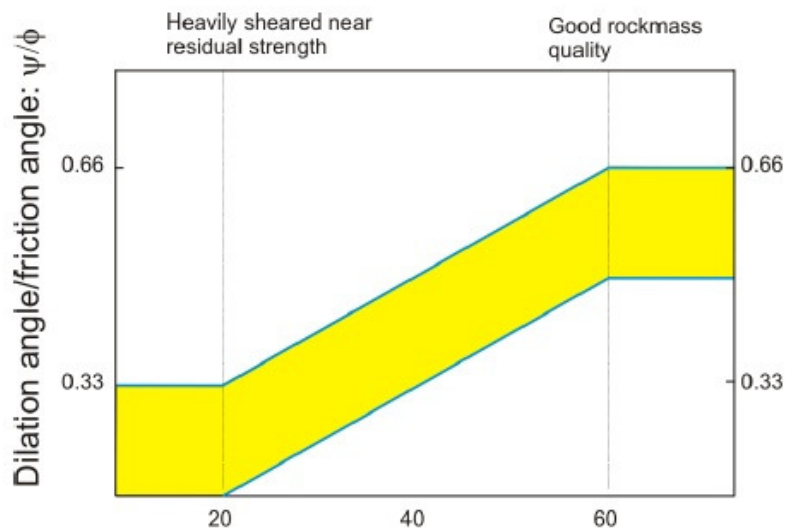
Figure 49: Dilation angle as a function of the GSI and friction angle (Corkum, *et al.*, 2010)

Research by Zhao and Cai (2010), amongst others, have shown that the mobilisation of the dilation angle is influenced by plastic shear strain and confinement. Therefore, it is not realistic to assume that the dilation angle is constant. Figure 50 shows a correlation between a stress-strain curve and a volumetric strain versus axial strain curve. The blue dots correspond to the same axial strain level in both graphs. It is clear that confining stresses delay the onset of dilation. Furthermore, the maximum rate of dilation is at the strain-softening stage after which dilation reaches a constant value.
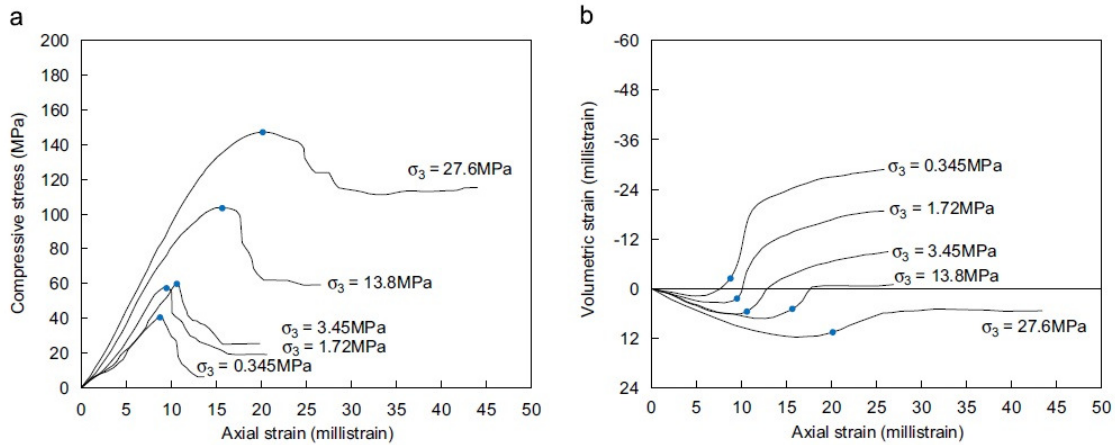
Figure 50: Stress-strain curves for various confining stresses with blue dots to indicate peak strength (left). Volumetric-axial strain curve with blue dots that match the axial strain level of the stress-strain curve for various confining stresses (right). (Zhao & Cai, 2010)

The plastic shear strain is the irrecoverable deformation of rock along a face. Equation 6.13 describes the plastic shear strain as a function of the major and minor principal plastic strain.

$$\gamma_p = \varepsilon_1^p - \varepsilon_3^p = \varepsilon_1^p - \frac{\varepsilon_v^p - \varepsilon_1^p}{2} \qquad 6.13$$

Parameter	Description
γ_p	plastic shear strain
ε_1^p	plastic major principal strain
ε_3^p	plastic minor principal strain
ε_v^p	plastic volumetric strain

Alejano and Alonso (2005) developed a method of average strain to calculate the dilation angle. The subscripts a, b and c in the following equations refer to positions in Figure 51b, on the next page. The subscript i represents 1 or 3, *i.e.* the major or minor principal strain direction. Equation 6.14 and 6.15 calculate the plastic strain components of the corresponding intervals and equation 6.16 calculates the plastic strain increment for their combined interval. Equation 6.17 formulates the average volumetric plastic strain increment from the major and minor average plastic strain increments. The dilation angle can now be calculated according to equation 6.18. The result is graphically depicted in Figure 51c. The plastic shear strain is considered to start from null, resulting in a shift of all dilation angles. This way, calculated negative dilation angles are ignored.

$$\varepsilon^p_{i,v\_ab} = \frac{\varepsilon^p_{i,v\_a} + \varepsilon^p_{i,v\_b}}{2} \qquad\qquad 6.14$$

$$\varepsilon^p_{i,v\_bc} = \frac{\varepsilon^p_{i,v\_b} + \varepsilon^p_{i,v\_c}}{2} \qquad\qquad 6.15$$

$$\dot{\varepsilon}^p_{i,v\_ac} = \varepsilon^p_{i,v\_bc} - \varepsilon^p_{i,v\_ab} \qquad\qquad 6.16$$

$$\dot{\varepsilon}^p_{v\_ac} = \dot{\varepsilon}^p_{1,v\_ac} + 2 \cdot \dot{\varepsilon}^p_{3,v\_ac} \qquad\qquad 6.17$$

$$\psi = \sin^{-1}\left(\frac{\dot{\varepsilon}^p_{v\_ac}}{-2 \cdot \dot{\varepsilon}^p_{1\_ac} + \dot{\varepsilon}^p_{v\_ac}}\right) \qquad\qquad 6.18$$

Parameter	Unit	Description
ψ	°	Dilation angle
$\dot{\varepsilon}^p_v$	-	Volumetric plastic strain increment
$\dot{\varepsilon}^p_1$	-	Axial plastic strain increment
$\dot{\varepsilon}^p_3$		Lateral plastic strain increment

In practice, the dilation angle can be obtained from triaxial tests by recording the plastic axial and volumetric strain increments and the use of equation 6.18. Crouch (1970) developed a technique to monitor the amount of fluid required to maintain a constant pressure on the specimen conducted to a triaxial test to measure the average volumetric change over the specimen. Recoverable and irrecoverable strain can be observed by performing loading-unloading cycles. The assumed "memory" of the sample causes the stress-strain curve to return at the initial loading point for every cycle.
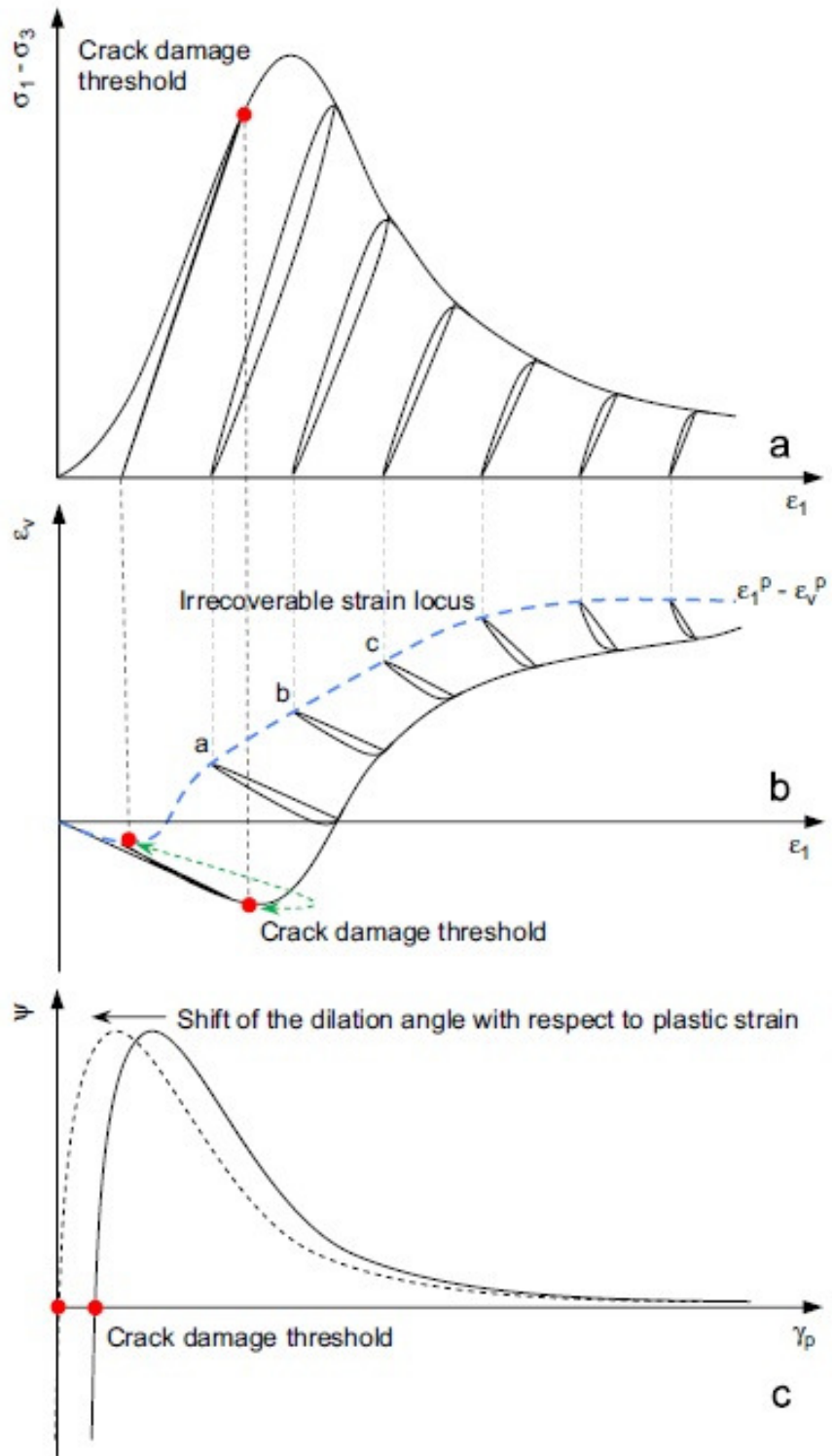
Figure 51: Mobilisation of the dilation angle as a function of plastic shear strain. (Zhao & Cai, 2010)

7 Failure criteria

Estimation of the mechanical properties of a jointed rock mass on the scale of support problems has always been a major concern. Failure criteria help to assess if stress levels in the rock are intolerable. Various empirical failure criteria are retrieved from pillar stability assessments in the past. Appendix G elaborates on the historical development of these empirical pillar formulae. The failure envelopes indicate the border between equilibrium and failure. These criteria can be expressed as the relationship between normal and shear stresses or, more commonly, as the relationship between the major and minor effective principal stresses. This chapter discusses three well-known failure criteria and introduces the S-shaped failure criterion, which is the most recently developed hypothesis in this field of work.

7.1 Griffith's theory

Griffith (1921) proposed that the failure of brittle materials is governed by the initial presence of microcracks. These cracks will propagate if they can lower their total potential energy under uniaxial tension. The cracks are modelled as ellipses in a uniform tensile stress field where failure will occur if their tensile strength is overcome. The tensile strength can be calculated by equation 7.1, where E' is substituted by equation 7.2 in plane stress problems and by equation 7.3 in plane strain problems.

$$\sigma_t = \sqrt{\frac{2}{\pi} \cdot \frac{E' \cdot \gamma_s}{c_l}}$$

7.1

$$E' = E$$

7.2

$$E' = \frac{E}{1 - v^2}$$

7.3

Parameter	Unit	Description
σ_t	MPa	Tensile strength
E	GPa	Young's modulus
v	-	Poisson's ratio
γ_s	N/m	Specific surface energy
c_l	m	Half crack length

Griffith extended his theory for compressive domains three years later. He stated that the compressive strength of a rock equals eight times its tensile strength. Friction on closed cracks was neglected in his biaxial, compressional model. These assumptions can be formulated as equation 7.4 and 7.5, illustrated in Figure 52 as a non-linear failure envelope.

$$(\sigma_1 - \sigma_3)^2 - 8 \cdot \sigma_t(\sigma_1 + \sigma_3) = 0 \quad if \quad \sigma_1 + 3 \cdot \sigma_3 > 0 \qquad \text{7.4}$$

$$\sigma_3 + \sigma_t = 0 \quad if \quad \sigma_1 + 3 \cdot \sigma_3 < 0 \qquad \text{7.5}$$
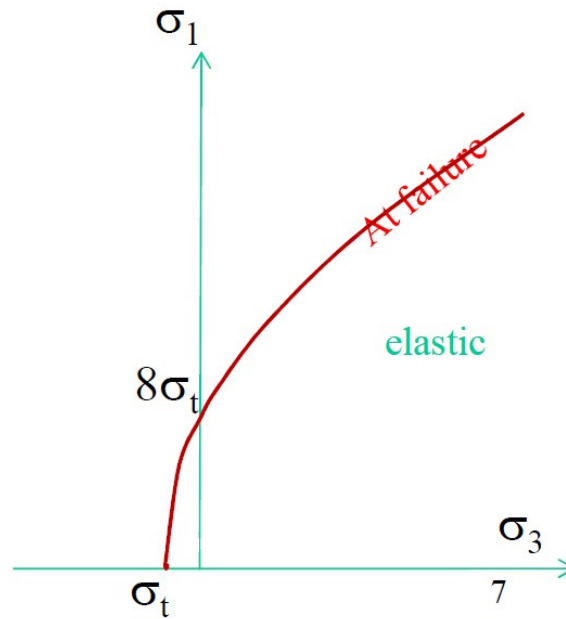
Figure 52: Failure envelope based on Griffith's theory for a biaxial, compressive stress state.

The criterion was modified by McClintock and Walsh (1962) and Murrell (1964) to cover triaxial stress conditions. The compressive strength of the rock equals twelve times the tensile strength in the modified criterion described by equation 7.6. But both the classical and the modified theories fail to predict the observed UCS to tensile strength ratio, because they only deal with crack initiation and not with macroscopic failure.

$$(\sigma_1 - \sigma_3)^2 + (\sigma_2 - \sigma_3)^2 + (\sigma_3 - \sigma_1)^2 - 24 \cdot \sigma_t(\sigma_1 + \sigma_2 + \sigma_3) = 0 \qquad \text{7.6}$$

7.2 Mohr-Coulomb failure criterion

The fundamental work on the Mohr-Coulomb failure criterion was undertaken by Coulomb (1773). The current version describes a linear envelope which relates shear strength and normal stress. The criterion is formulated in equation 7.7 and shown graphically in Figure 53. Note that the intermediate principal stress plays no role in the criterion. Shear failure occurs when the difference between shear stress and frictional resistance becomes less than the cohesion of the rock. Frictional resistance is dependent on the normal stress while cohesional strength is not. The criterion has several shortcomings, like the inability to describe the behaviour of intact rock material properly in the tensile and low stress domain and the lack of flattening of the failure envelope at high stresses. The simultaneous mobilisation of cohesion and frictional resistance has already been proven wrong in subsection 6.3.1. According to Zhao & Cai (2010), the dilation angle is taken as a constant in conventional Mohr-Coulomb models, but in reality it is dependent on confinement and plastic shear strain as discussed previously in subsection 6.3.2.

$$\tau = c + \sigma_n' \cdot \tan \phi \qquad \qquad 7.7$$

Parameter	Unit	Description
τ	MPa	Shear stress
c	MPa	Cohesion
σ_n'	MPa	Effective normal stress
ϕ	degrees	Angle of internal friction
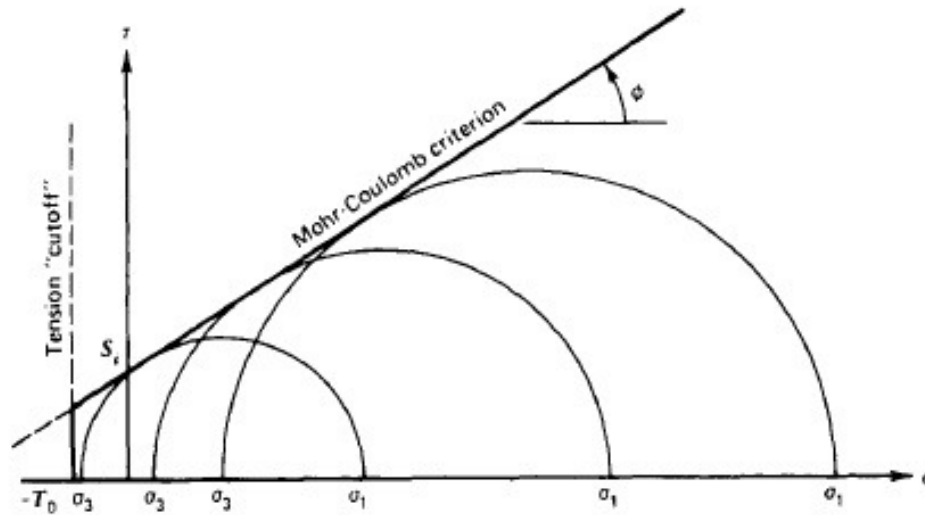
Figure 53: The Mohr-Coulomb criterion as a tangent to serveral Mohr circles. (Goodman, 1989)

59

The relation between shear stress and normal stress can be translated to a formula comparing major and minor principal stress by equation 7.8. The minor principal stress cannot exceed the tensile strength. Tensile yield is detected when equation 7.9 is satisfied. The angle of internal friction and cohesion are derived from triaxial tests. Strength is commonly described in terms of the UCS, according to equation 7.10. (Goodman, 1989)

$$\sigma'_1 = \sigma_{UCS} + \sigma'_3 \cdot \tan^2\left(45 + \frac{\phi'}{2}\right) \qquad 7.8$$

$$\sigma_t < -\frac{2 \cdot c \cdot \cos\phi}{1 + \sin\phi} \qquad 7.9$$

$$\sigma_{UCS} = 2 \cdot c' \cdot \tan\left(45 + \frac{\phi'}{2}\right) \qquad 7.10$$

Parameter	Unit	Description
c'	MPa	Effective cohesion of the rock mass
ϕ	°	Friction angle of the rock mass
σ_1'	MPa	Major principal effective stress at peak strength
σ_3'	Mpa	Minor principal effective stress at peak strength
σ_{UCS}	Mpa	Uniaxial compressive strength
σ_t	Mpa	Tensile strength

7.3 Hoek-Brown failure criterion

Hoek and Brown (1980) developed an empirical failure criterion to estimate the resistance to shear failure of intact rock or jointed to heavily jointed rock masses. At least three joint sets should be present in order for the criterion to be applicable in its generalised format. Figure 54 illustrates the range of applicability for underground and open pit mining. A simplification of the criterion, expressed by equation 7.11, is applicable on intact rock specimens. The Hoek-Brown failure criterion takes the intact rock strength as a starting point and reduces its value by means of degradation rates to obtain the rock mass strength. It assumes a homogeneous, isotropic rock mass with randomly oriented discontinuities.

$$\sigma_1' = \sigma_3' + \sigma_{UCS} \left(m_i \frac{\sigma_3'}{\sigma_{UCS}} + 1 \right)^{0.5} \qquad\qquad 7.11$$
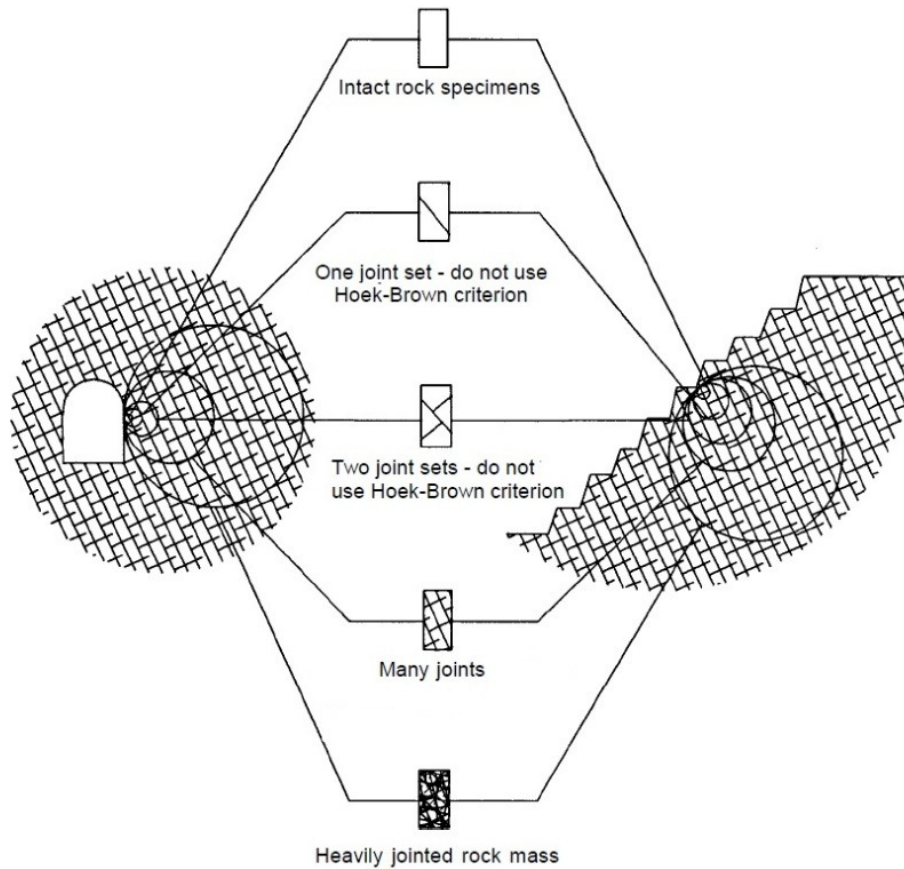
Figure 54: Range of applicability of the Hoek-Brown failure criterion (Hoek, *et al.*, 1995).

There are some other limitations to the Hoek-Brown failure criterion besides the amount of discontinuity sets. The Hoek-Brown parameters, explained on the next page, are not valid at both extremities of the rock competence scale as illustrated in Figure 55. Other concerns should be tectonically disturbed environments and extreme heterogeneity. (Carter, *et al.*, 2008)
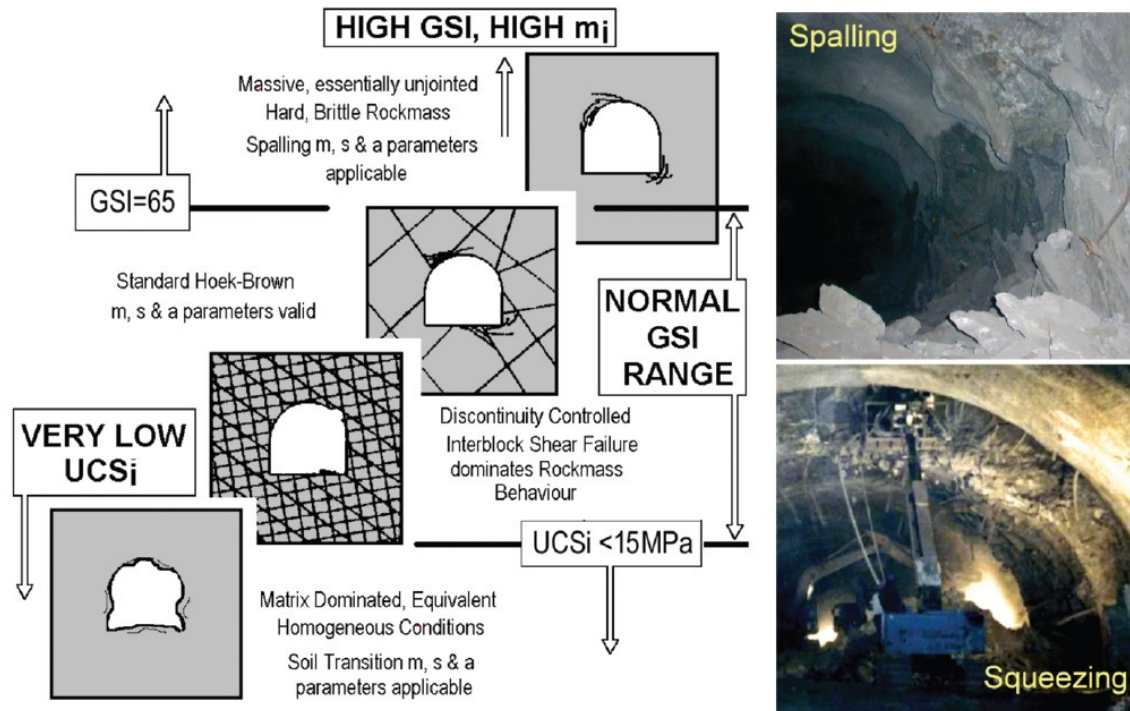
Figure 55: Rock competency and failure modes (Carter, *et al.*, 2008)

The initial criterion is based on the RMR_{76} and was designed for preliminary studies on underground excavations. The RMR was found to be unpractical as classification scheme. So, Hoek and Brown (1997) developed the Geological Strength Index, see section 4.2.4, to overcome compatibility issues. Since the criterion started to be used on a wide range of problems in practice, Hoek *et al.* (2002) adapted the criterion to the cases not accounted for yet. They also introduced the disturbance factor D. This is the degree in which the rock mass has been subjected to blast damage and stress relaxation. Undisturbed rock masses are rated 0 and very disturbed rock masses 1. The disturbance factor can be selected in appendix H. Equations 7.12 to 7.17 show the generalised Hoek-Brown criterion for rock masses. (Hoek, *et al.*, 2002)

$$\sigma_1' = \sigma_3' + \sigma_{UCS}\left(m_b\frac{\sigma_3'}{\sigma_{UCS}} + s\right)^a \qquad \text{7.12}$$

$$m_b = m_i \cdot e^{\left(\frac{GSI-100}{C_m}\right)} \qquad \text{7.13}$$

$$s = e^{\left(\frac{GSI-100}{C_s}\right)} \qquad \text{7.14}$$

$$a = \frac{1}{2} + \frac{1}{6}\left(e^{-GSI/15} - e^{-20/3}\right) \qquad \text{7.15}$$

$$C_s = 9 - 3 \cdot D \qquad \text{7.16}$$

$$C_m = 28 - 14 \cdot D \qquad \text{7.17}$$

Parameter	Unit	Description
σ_1'	MPa	Major principal effective stress at peak strength
σ_3'	MPa	Minor principal effective stress at peak strength
σ_{UCS}	MPa	Uniaxial compressive strength of intact rock
m_b	-	'Friction' parameter of the rock mass
m_i	-	'Friction' parameter of intact rock, see appendix I
s	-	Hoek-Brown parameter
a	-	Curvature parameter of the criterion
GSI	-	Geological Strength Index
D	-	Disturbance factor, see appendix H
C_m	-	Degradation factor, typically 28
C_s	-	Degradation factor, typically 9

The material constant m_i is a measure for the quality of the composition, structure and surface conditions of the rock, just like s and a. The m_i-value for brittle rock behaviour is typically above 15 and corresponds with relatively high internal friction angles. Relatively low m_i-values can be associated with ductile rock behaviour. Figure 56 shows the change of the failure envelope for different m_i-values and appendix I shows typical m_i-values for igneous, metamorphic and sedimentary rocks. The m_i-value can be approximated by the ratio between the UCS of intact rock and the tensile strength. (Carter, *et al.*, 2008).
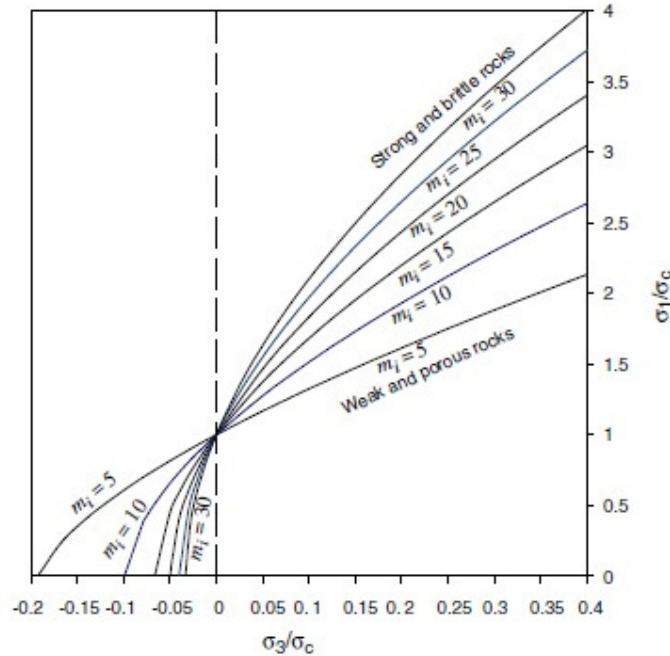
Figure 56: Influence of m_i-value on the shape of the Hoek-Brown failure envelope for intact rock. In this diagram, σ_c is the UCS at peak strength. (Cai, 2010)

Martin and Maybee (2000) emphasize that four parameters have to be known in order to apply the generalised Hoek-Brown criterion. The first two parameters relate to the intact rock material and the last two parameters characterize the quality of the in-situ rock mass.

1. Uniaxial compressive strength of intact rock material (σ_{UCS})
2. Petrographic constant or "friction" parameter (m_i)
3. Geological Strength Index (GSI)
4. Disturbance factor (D)

The continuously convex, nonlinear failure envelop for rock material is derived from a great amount of triaxial tests and represents a non-linear increase in strength with increasing confinement. The criterion is only applicable for isotropic rock, where rock masses in nature are often anisotropic. The criterion is most suitable in the design of pillars at the extraction level, the design of crown pillars and the analysis of surface subsidence according to Brown (2003).

7.3.1 Adaptation to brittle failure

Traditional Hoek-Brown parameters are designed to represent shear failure. The criterion has trouble to represent brittle failure in low confinement zones. Hoek and Brown (1997) suggest brittle parameters to be used to resemble elastic-brittle behaviour in these zones. Martin and Maybee (2000) propose that pre-peak spalling is fundamentally a cohesion-loss process. They used the brittle parameters in equations 7.18 and 7.19 to produce a function that is non-linearly increasing with an increasing width-height ratio of pillars. It increases with an upward curvature in contrast to all previously mentioned empirical pillar formulae in appendix G, see Figure 57. The fact that other empirical pillar formulae all have horizontal asymptotes far below their confined rock mass strength advocates their theory.

$$m_b{}^{brittle} = 0 \qquad\qquad \textbf{7.18}$$

$$s^{brittle} = 0.11 - 0.25 \qquad\qquad \textbf{7.19}$$
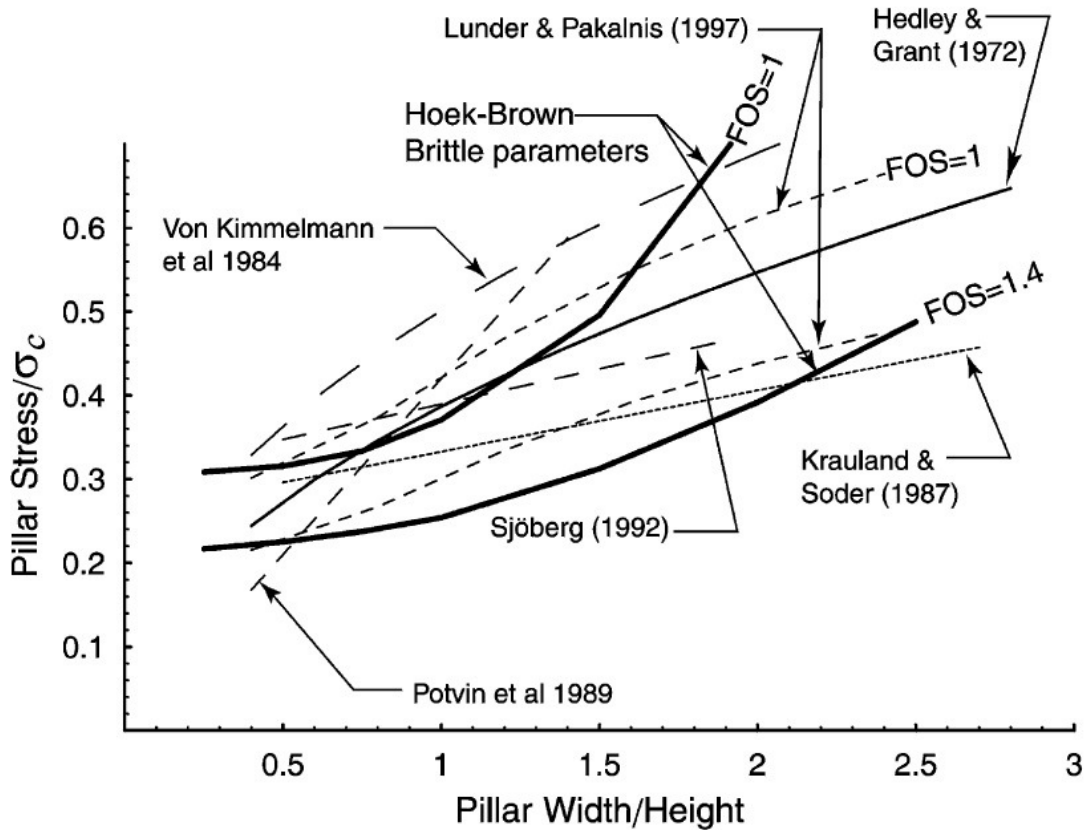
Figure 57: Hoek-Brown criterion with brittle parameters for low confinements expressed among historical pillar formulae from Appendix G. (Martin & Maybee, 2000)

7.3.2 Adaptation to post-peak behaviour

Most parameters from the generalised Hoek-Brown criterion change to a residual value after peak strength. The unconfined compressive strength (σ_{UCS}) is the only fixed parameter and should be determined from intact rock specimens. Since the Hoek-Brown parameter m_b resembles the friction angle, the residual value drops significantly in brittle failing rock whereas perfect plastic behaviour shows no reduction of the residual value. The Hoek-Brown parameter s represents the cohesive strength of the rock mass and has a residual value of zero. The value of the disturbance factor D remains constant since the damage this factor represents is not due to failure, but due to blasting or other disturbances. The GSI is used to calculate peak strength parameters and should therefore not be altered for post-peak behaviour. Values for post-peak Hoek-Brown parameters have been assigned by Crowder & Bawden (2004) in Table 2.

Table 2: Post-peak behaviour guidelines based on rock type (Crowder & Bawden, 2004)

GSI range	s_r	m_r	Behaviour
< 30	s	m_b	Elastic-perfectly plastic
40 – 50	0	$0.5 \cdot m_b$	Strain softening, loss of tensile strength, retains shear strength
50 - 65	0	15	Rock fails to a 'gravel'
70 - 90	0	1	All strength lost at failure

7.3.3 Conversion from Hoek-Brown to Mohr-Coulomb parameters

Most geotechnical modelling software is based on the Mohr-Coulomb criterion parameters cohesion (c) and friction (ϕ), although it does not adequately describe the behaviour of jointed rock masses. Linear regression of the Hoek-Brown failure envelope is the preferred method to obtain these parameters. Hoek *et al.* (2002) created two equations to transform the Hoek-Brown parameters into the effective internal friction angle and effective cohesion according to equations 7.20 and 7.21.

The upper limit of the confining stress, σ'_{3max}, is determined by equation 7.23. The horizontal stress should be used instead of $\gamma \cdot H$ if its value is higher than the vertical stress. The global rock mass strength, σ'_{cm}, represents the overall strength of a rock mass and is represented by equation 7.24. Hoek *et al.* (2002) state that these transitions should not be used in block caving operations, because the cave extends to surface and forms a subsidence trough. They recommend determining and analysing material properties based on either the Mohr-Coulomb or the Hoek-Brown criterion.

$$\phi' = \sin^{-1}\left(\frac{6 \cdot a \cdot m_b(s + m_b \cdot \sigma'_{3n})^{a-1}}{2(1+a)(2+a) + 6 \cdot a \cdot m_b(s + m_b \cdot \sigma'_{3n})^{a-1}}\right) \qquad 7.20$$

$$c' = \sigma_{ci}\frac{\left((1+2a) \cdot s + (1-a) \cdot m_b \cdot \sigma'_{3n}\right)(s + m_b \cdot \sigma'_{3n})^{a-1}}{(1+a)(2+a)\sqrt{1 + m_b(s + m_b \cdot \sigma'_{3n})^{a-1}/\left((1+a) \cdot (2+a)\right)}} \qquad 7.21$$

$$\sigma'_{3n} = \sigma'_{3max}/\sigma_{UCS} \qquad 7.22$$

$$\frac{\sigma'_{3max}}{\sigma'_{cm}} = 0.47\left(\frac{\sigma'_{cm}}{\gamma \cdot H}\right)^{-0.94} \qquad 7.23$$

$$\sigma'_{cm} = \sigma_{ci}\frac{\left(m_b + 4 \cdot s - a(m_b - 8 \cdot s)\right)(m_b/4 + s)^{a-1}}{2(1+a)(2+a)} \qquad 7.24$$

7.4 The S-shaped failure criterion

Kaiser *et al.* (2010) proposed a hypothesis to counter conservative pillar design due to erroneous interpretation of confined, brittle rock masses. Brittle failure by tensile spalling occurs when tangential stresses reach the damage initiation threshold, *i.e.* stage III in section 6.1. The hypothesis assumes an inhibition of tensile failure processes at relatively high confinements, where shear failure is the dominant failure process. Figure 58 indicates the difference in failure processes at low and high confinement. The inhibition of tensile failure suggests a lower degradation at relatively high confinements and thus superior strength of confined rock masses compared to the Mohr-Coulomb and Hoek-Brown failure criteria. Bahrani *et al.* (2011) also state that the confined strength may be significantly underestimated for moderately jointed, hard rock masses. Carter *et al.* (2008) describe the same phenomena in a slightly different way. They state that in highly competent rock ($\sigma_{UCS} \gg 65$ and $m_i \gg 15$) the intact material behaviour, instead of the discontinuities, dominates the rock mass strength instead of the discontinuities. Therefore, the standard generalised Hoek-Brown parameters are not valid for these rock masses.

Figure 58: Spalling at unconfined tunnel walls and shear failure in confined zones. (Kaiser, *et al.*, 2010)

7.4.1   Explanation of the S-shape

Kaiser *et al.* (2010) suggest an S-shape of the failure envelope for the entire confinement range which describes both failure processes. It is vital for pillar design to understand shear failure in the confined zone as well as spalling at tunnel walls. Figure 59 is a schematic representation of the S-shaped failure envelope explaining brittle failure processes in different stress regimes. (Kaiser & Kim, 2008)

7.4.1.a Tension cut-off

Failure criteria predict a negative confinement, tension, which is higher than the tensional strength of the rock mass. The rock mass is assumed to fail when the tensional strength is reached. Therefore, the failure criterion is cut-off vertically at the tensional strength of the material.

7.4.1.b Damage initiation threshold

The initial rise of the envelope indicates the damage initiation threshold, indicated in red in Figure 59. It depicts the stress at which small cracks are initiated and grow in the direction of maximum applied stress. The threshold is a function of the condition and density of internal flaws and heterogeneities and can be approximated using the Hoek-Brown brittle parameters, see subsection 7.3.1. Field studies show that failure is initiated when tangential stresses at excavation boundaries reach the damage

initiation threshold. For igneous rocks this threshold is one third of the UCS of intact rock, but it can be as high as halve of the UCS of intact rock (Esterhuizen, 2006). The onset of systematic cracking is defined by this threshold and can be retrieved from acoustic emissions or radial strain data. Stable cracks accumulate and interact upon increasing applied stress. The reason for the difference in strength perceived from laboratory and field tests remains uncertain until today. (Valley, *et al.*, 2012)

7.4.1.c Spalling limit
Spalling is constrained as confinement increases, since initiated cracks do not propagate under sufficient confinement. The rock mass behaviour for the confinement range between spalling and shear failure is a topic of discussion up to today. This transition zone between low and high confinement is better known as the spalling limit. It can be approximated as a linear transition defined as a ratio between major and minor principal stress (σ_1/σ_3). Common values for this ratio are between 5 and 20. Diederichs *et al.* (2007) state that the spalling limit is below 10 for very heterogeneous rock masses and above 10 in more homogeneous rocks. Kaiser *et al.* (2010) define the transition at a fixed confinement level of $\sigma_3 = \sigma_{UCS}/10$ with a sigmoid function. Details of the function connecting the envelope at low and high confinement are still unknown. (Kaiser, *et al.*, 2010)

7.4.1.d Long term strength
Crack accumulation is recorded as acoustic emissions or micro-seismic events. Accumulated cracks will coalesce and ultimately propagate into shear bands under sufficient confinement. Therefore, shear failure is the dominating failure type in the high confinement range. The rock mass behaves elastically below the failure envelope. The Mohr-Coulomb or Hoek-Brown criterion can therefore describe the part of the envelope to the right of the spalling limit. It depicts long term strength of intact rock samples. According to Martin (1997), the cohesional strength of the rock is lost at this stage and the frictional strength is mobilised.
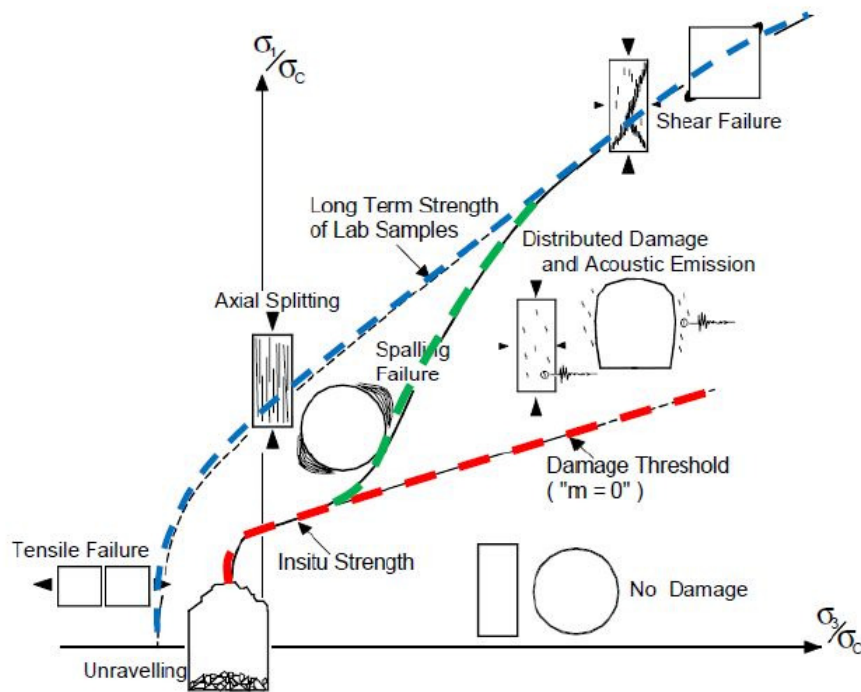
Figure 59: Schematic of the S-shaped failure envelope for brittle failure. (Diederichs, 1999)

7.4.2 Formulation

The constant rate of degradation in the Hoek-Brown failure criterion is empirical and only supported with data near excavations in low confinement zones for the purpose of support design. Furthermore, the degradation constants were calibrated on rock masses with $GSI < 65$ and might not be representable for all brittle rock masses. A constant rate of degradation results in Figure 60 and resembles the Hoek-Brown failure criterion where strength reduction, in absolute terms, is larger for confined rock masses. Kaiser *et al.* (2010) used lower degradation rates, higher values for C_s and C_m, at high confinement to come up with the S-shaped failure envelope shown in Figure 61. Figure 62 shows an S-shaped failure envelope of a Quartzite with $C_s = 9$ at low confinements and $C_s = 50$ for confined rock. The effects of this parameter become clear when it is raised to infinity for confined rock, illustrated in Figure 63.
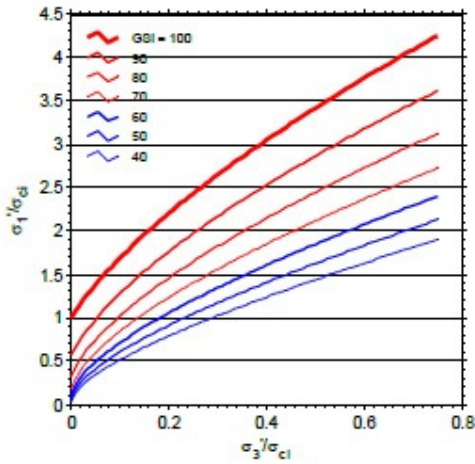
Figure 60: Hoek-Brown failure envelope (Kaiser, *et al.*, 2010)
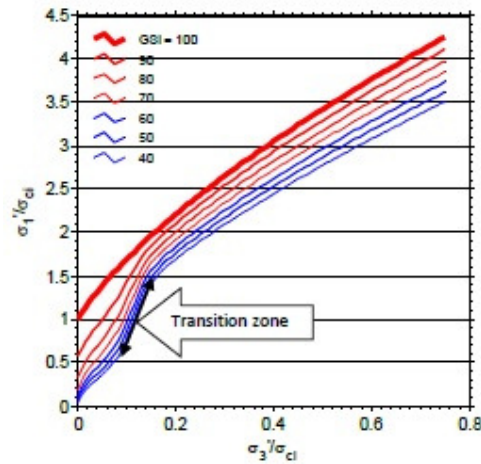
Figure 61: S-shaped failure envelope (Kaiser, *et al.*, 2010)
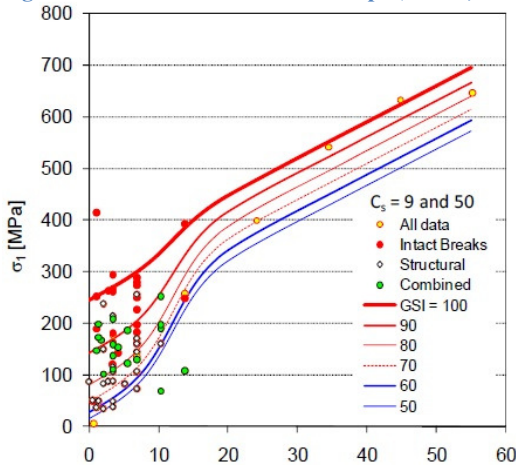
Figure 62: S-shaped failure envelope with two different degradation factors. (Kaiser, 2010)
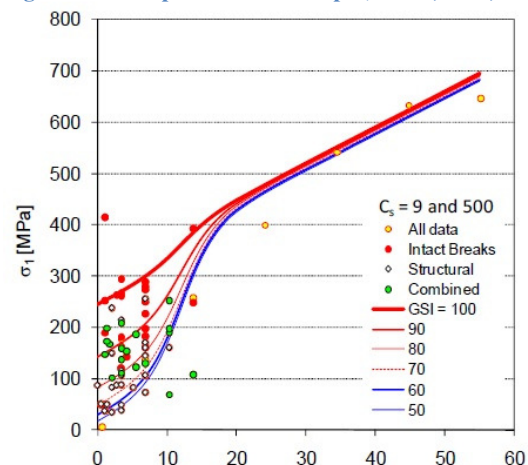
Figure 63: The effects of an increased degradation factor for confined rock on the S-shaped failure envelope. (Kaiser, 2010)

The envelope can be modelled using Hoek-Brown parameters with a confinement dependent version of the GSI as described by equation 7.25. With the GSI', confinement dependent versions of the Hoek-Brown parameters m_b, s and a will control degradation. Typical degradation rates are applicable at low confinement, making the envelope identical to the Hoek-Brown criterion. The parameter M controls the degradation rate above the spalling limit. It can be varied between 0, the GSI' is kept constant at all confinement levels, and 100, the GSI' is capped at 100 for confining stresses well above the spalling limit. Intermediate values of M indicate a maximum GSI' according to a linear course. Figure 64, created by the author, shows the range of GSI' versus confinement for different values of M, the sigmoidal function around the spalling limit is clearly visible. A limited data set was best matched by an S-shaped failure criterion with M=80. It has to be emphasised that this approach is not suitable for rock masses with low intact rock strengths or very weak joints. (Kaiser, *et al.*, 2010)

$$GSI' = \frac{M - (M/100) \cdot GSI}{1 + e^{-\sigma'_3 + \sigma_{UCS}/10}} + GSI \qquad \text{7.25}$$

Parameter	Unit	Description
GSI'	-	Confinement dependent GSI
M	-	Constant to determine degradation above the spalling limit (assumption: 80)
GSI	-	Geological Strength Index
σ'_3	MPa	Minor principal effective stress at peak strength
σ_{UCS}	MPa	Uniaxial compressive strength of intact rock
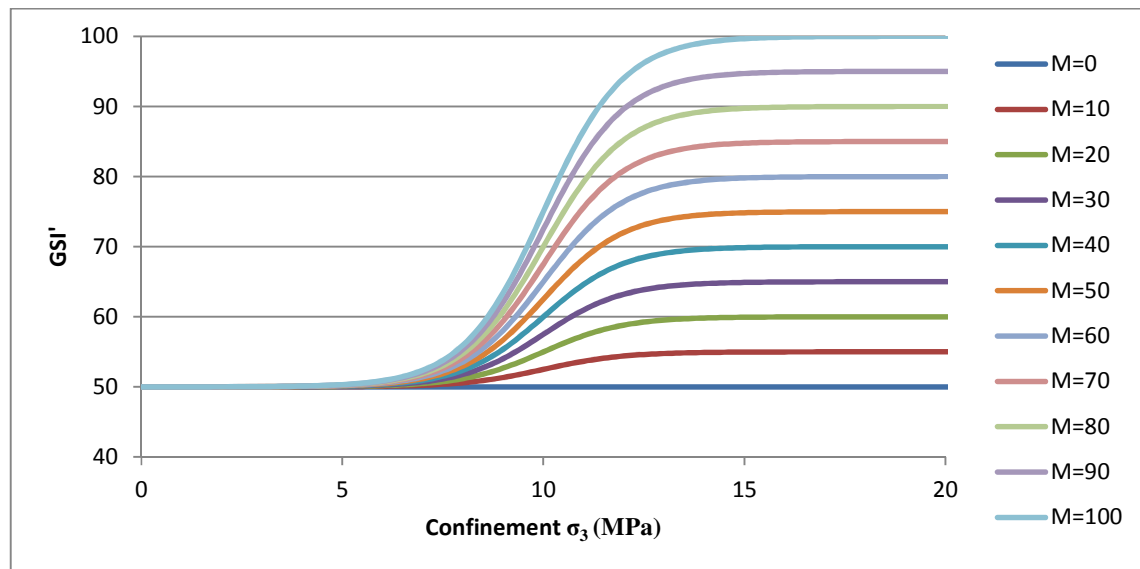
Figure 64: Sensitivity of M for the confinement dependent parameter GSI' (UCS=100 , GSI=50)

According to Valley, *et al.* (2012), a degradation constant of $C_s = 50$ should be used for confined conditions. These conditions can be simulated by keeping $C_s = 9$ and exchanging the GSI for GSI' to find the value for M that matches this statement. The goal seek function in EXCEL is extremely useful in this case and results in $M = 82$. This validates the findings of Kaiser, *et al.* (2010).

7.5 Comparison of failure criteria

The Mohr-Coulomb and Hoek-Brown criteria assume that cohesion and frictional strength components contribute simultaneously to peak strength, whereas the modified S-shaped criterion assumes cohesion to make up pre-peak strength and frictional components to make up residual strength. According to Kaiser (2010), the conventional criteria tend to over predict rock mass strength in low confinement regions due to the ignorance of spalling. In high confinement regions the strength is underestimated by the conventional shear failure criteria. This is due to the use of identical degradation factors on both sides of the spalling limit, whereas the modified S-shaped criterion lowers the degradation rate at high confinement.

The economical and operational impact of the S-shaped failure criterion is far-reaching. Since pillar design is based on field observations and back-analysis from near wall-behaviour, the strength of the confined core of a pillar is underestimated. A re-design of pillars in a block cave would result in significantly reduced width / height ratios, a different drawpoint spacing and fragmentation. *(Kaiser, et al.*, 2010)

8 Numerical modelling

Numerical modelling is a tool to simulate processes that are too complex to understand in the real world. It does not help if the model itself is too complex and therefore generalisations and assumptions will always be present to some extent. Nevertheless, numerical approaches are more accurate in describing complex mechanics than empirical methods. Therefore, they are applied in a wide range of inhomogeneous problem domains with non-linear partial differential and constitutive equations. An example of such a domain is a block caving operation which is characterised by its self-propagating disintegration of the rock mass due to a redistribution of stresses. Typical input data for a geotechnical, numerical models are in-situ stress conditions, mining geometry and rock mass characteristics. The numerical caveability assessment is then able to include induced stresses, rock mass strength and brittleness. (Brown, 2003)

This chapter describes in succession the different modelling methods, a brief history in geotechnical, numerical modelling, the numerical code used for this thesis and different constitutive models within this numerical code.

8.1 Modelling methods

All numerical modelling methods used in stress driven problems in rock mechanics can be divided into three classes; integral, differential and hybrid methods. The integral (or "boundary") methods divide only the boundary of excavations into elements and treat the interior as an infinite continuum, while the differential (or "domain") methods also divides the interior into elements and assigns properties to them. The outer boundaries of the model must be placed sufficiently far away to prevent interaction with the excavations. The hybrid methods are a combination of as many advantageous features and as little disadvantageous features as possible of the integral and differential methods. Table 3 shows the subdivision of all numerical methods.

Table 3: Classification of numerical modelling methods (Flores, *et al.*, 2004)

Method	Description	Media Modelling	Numerical Method	Characteristics
Integral	Divides the boundary of excavations into elements and the interior of the rock mass is represented mathematically as an infinite continuum.	Continuum	• Indirect (boundary element) • Direct (boundary integral equation)	• Elastic material behaviour • Limited number of material types • Static analysis • Two-dimensional problems are fast to set up and run • Three-dimensional problems are large due to fully populated matrices
		Discontinuum	• Displacement discontinuity	
Differential	Divides the interior of the rock mass into geometrically simple elements, and solves the problem by considering each element and the whole set of elements.	Continuum	• Finite elements • Finite differences	• Linear and non-linear material behaviour • Multiple material types • Static and dynamic analysis • Mesh generators necessary to reduce set-up time • Far-field boundary location/condition determined by user
		Discontinuum	• Distinct elements	
Hybrid	Combines boundary and domain methods to form hybrid methods, which are designed to maximize the advantages and minimize the disadvantages of each of the former two methods.	Continuum	• Direct or indirect boundary elements and finite elements	• Linear and non-linear material behaviour • Multiple material types • Static and dynamic analysis • Mesh generators necessary to reduce set-up time
		Discontinuum	• Displacement discontinuity boundary elements and finite element	

Each of these classes has continuum and discontinuum numerical methods. Continuum models do not contain joints and discontinuities. The intact rock strength is decreased by a certain amount (by means of the GSI) to resemble the rock mass strength. Continuous and homogenous properties are allocated to the rock mass although these properties are of discontinuous and heterogeneous nature. Discontinuum models value the key role of joints and discontinuities with respect to excavations and model them as interfaces between discrete blocks.

The indirect and direct methods are hard to distinguish. The only difference is that the indirect method uses a set of fictitious stresses that satisfy the boundary conditions to calculate actual stresses and displacements, while the direct method solves the displacements for the boundaries directly. The displacement discontinuity method represents an elongated slit being pulled apart in a continuum. An application is in the modelling of tabular ore bodies where the entire ore body is modelled as a 'discontinuity'. (Hoek, *et al.*, 1995)

The finite element and finite difference methods are again very similar. The detailed mathematical differences go beyond the scope of this thesis, but are described by Jing (2003). The finite difference method is more suitable for problems that consist of several stages, large displacements and strains and non-linear material behaviour. The methods relate the condition of nodal points to the state of the elements they enclose. They are excellent in solving heterogeneous and non-linear material properties. A disadvantage is the difficulty of modelling 'infinite' boundaries. The distinct element method, also called Discrete Element Method (DEM), best describes blocky rock masses. The model assumes that deformation at the contact between 'wedges' and 'blocks' is far more significant than deformation of the intact rock. Joints are explicitly modelled to create a discontinuum. (Hoek, *et al.*, 1995)

The hybrid method combines boundary element methods with finite element or distinct element methods. This way the numerical model can handle stresses in close proximity of the excavation while boundary conditions are being maintained. Table 4 shows an overview of available numerical codes on the market. The numerical code used for this thesis project is FLAC^{3D}.

Table 4: Commercially available numerical codes

	Continuum Codes								
	FLAC	*FLAC^{3D}*	*PLAXIS*	*ADINA*	*ABAQUS*	*PHASE^2*	*MAP3D*	*EXAMINE^{3D}*	*BEFE*
Formulation	Finite differences (*FDM*)		Finite elements (*FEM*)				Boundary element (*BEM*)		*BEM + FEM*
Dimensions	Two	Three	Two and Three			Two	Three		Two and Three
Interfaces	YES								
Water pressure in interfaces	YES		(?)	YES		NO	(?)		NO
Water pressure in rock mass	YES					NO	YES		NO
Inelastic material models	Mohr-Coulomb Hoek-Brown Ubiquitous joints Strain softening Creep		Mohr-Coulomb Strain softening Creep	Mohr-Coulomb Ubiquitous joints Strain softening Creep		Mohr-Coulomb Hoek-Brown	(?)	NO	Mohr-Coulomb Ubiquitous joints Strain softening Creep
Ability to customize constitutive relations	YES		NO	YES		NO			
Time-domain dynamic analysis	YES					NO			

FLAC: Fast Lagrangian Analysis of Discontinua, Itasca Consulting Group, USA
FLAC^{3D}: Fast Lagrangian Analysis of Discontinua in 3 Dimensions, Itasca Consulting Group, USA
PLAXIS: Plasticity Axisymmetry, PLAXIS BV, Netherlands
ADINA: Automatic Dynamic Incremental Nonlinear Analysis, ADINA R & D, Inc. USA
ABAQUS: Superior Finite Element Analysis Solutions, ABAQUS, Inc., USA
PHASE^2: Finite Element Analysis and Support Design for Excavations, Rocscience 2002, Canada
MAP3D: Is a fully Three-Dimensional Boundary Element Program, Mine Modelling Pty Ltd, Australia
EXAMINE^{3D}: Three-dimensional Stress Analysis and Data Visualization for Underground Excavations in Rock, Rocscience 2002, Canada
BEFE: Boundary Element and Finite Element, Computer Software & Services, Austria

8.2 History in geotechnical, numerical modelling

The first numerical study on caveability was a two dimensional, elastic Finite Element Model applied on the El Teniente mine in Chile (Palma & Agarwal, 1973). This model assumed that caving was only a result of tensile failure and therefore simulated a fracture network with zero tensile strength assigned to all fractures. They were the first to indicate the principal stress field during undercutting (Figure 65). Their model was improved by Barla & Boshkov (1980) who implied that caving is the result of tensile failure and a compressional yielding mechanism. The softening behaviour of the rock was expressed in a reduction of the strength, density and stiffness.
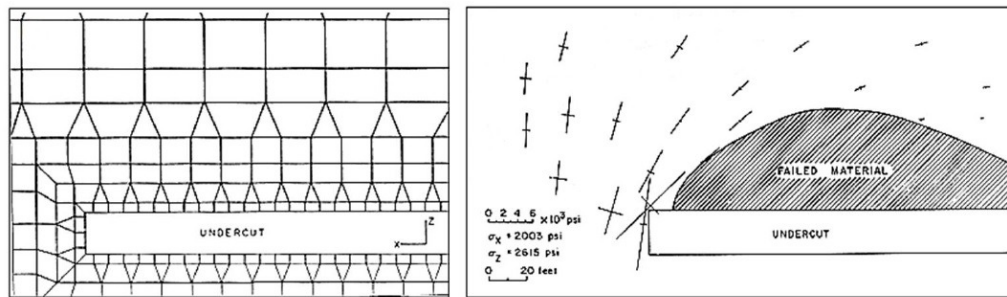
Figure 65: First FEM results showing principal stress orientations in relation to the undercutting process. (Palma & Agarwal, 1973)

Rech and Lorig (1992) used the two-dimensional numerical code *FLAC* developed by Itasca to correlate the planned amount of production with the advance of the cave at the Henderson Mine in Colorado, USA. Lorig (2000) then used a strain-softening material in *FLAC* to assess the extension of the yielding rock mass by monotonically reducing the support pressure in the roof of the undercut. He was able to make predictions of the hydraulic radius associated with cave initiation and propagation that were in line with Laubscher's caving chart. Furthermore, he showed that cave height increased when post-peak brittleness of the rock mass was increased. Pierce and Lorig (1998) used an axis-symmetric approach to simulate an increasing hydraulic radius with sequential undercuts of constant width in FLAC^{3D}. The addition of a velocity controlled production draw algorithm eight years later made it possible to simulate the evolving cave behaviour.

The Synthetic Rock Mass (SRM) approach uses a smooth joint contact model and the application of strain paths to simulate rock as intact rock bridges between particles with intersecting disc-shaped joints and is an example of a Distinct Element Model. The first SRM study was a back-analysis of Northparkes' E26 Lift 2 block (Pierce, *et al.*, 2006). The biggest challenge was to create a Discrete Fracture Network (DFN) from joint orientation, joint spacing and joint size distribution data and link mechanical properties to these discontinuities. The DFN is then embedded in an intact rock matrix. Micro-properties can be calibrated to the synthetic rock mass based on field measurements and laboratory tests. Real-life stress fields can be simulated to retrieve elastic behaviour, strength and brittleness. SRM enables the observation of deformation, fracturing, brittleness, the full stiffness matrix, the peak strength envelope and primary fragmentation. The methodology uses PFC^{3D}, another numerical code developed by Itasca in 2007. Retrieved data can be used in continuum models on cave-scale using a FLAC^{3D} testing environment and has high potential for future applications. However, it was impossible to apply the SRM approach on a case study at the Palabora Mine in South Africa due to very low fracture frequency and very large fracture persistence. The Ubiquitous Joint Rock Mass technique was developed to account for this anisotropy and scale effects in FLAC^{3D}. This technique is very suitable for cave-scale modelling and proved itself as a good cave management tool. (Ivars, *et al.*, 2008)

The advances in three-dimensional numerical modelling of extraction level stability have been significant in the past decade. Models like in Figure 66 were created only ten years ago while recent analyses produce results like in Figure 67. The improvement in the level of detail in the mesh is evident.
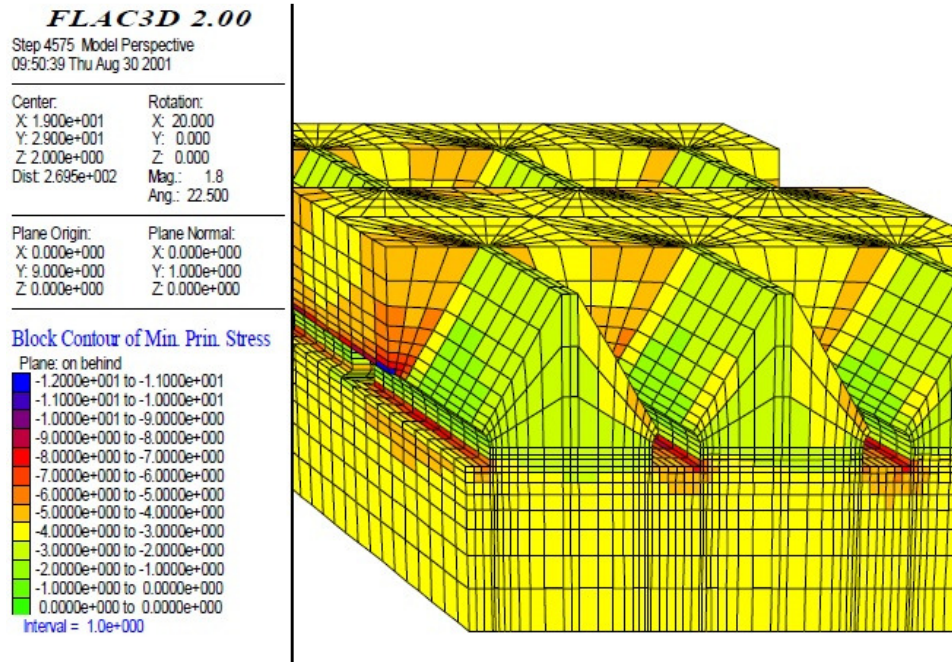
Figure 66: Extraction level stability analysis over a decade ago. Block contour plot of the minor principal stress. (Wattimena, 2003)
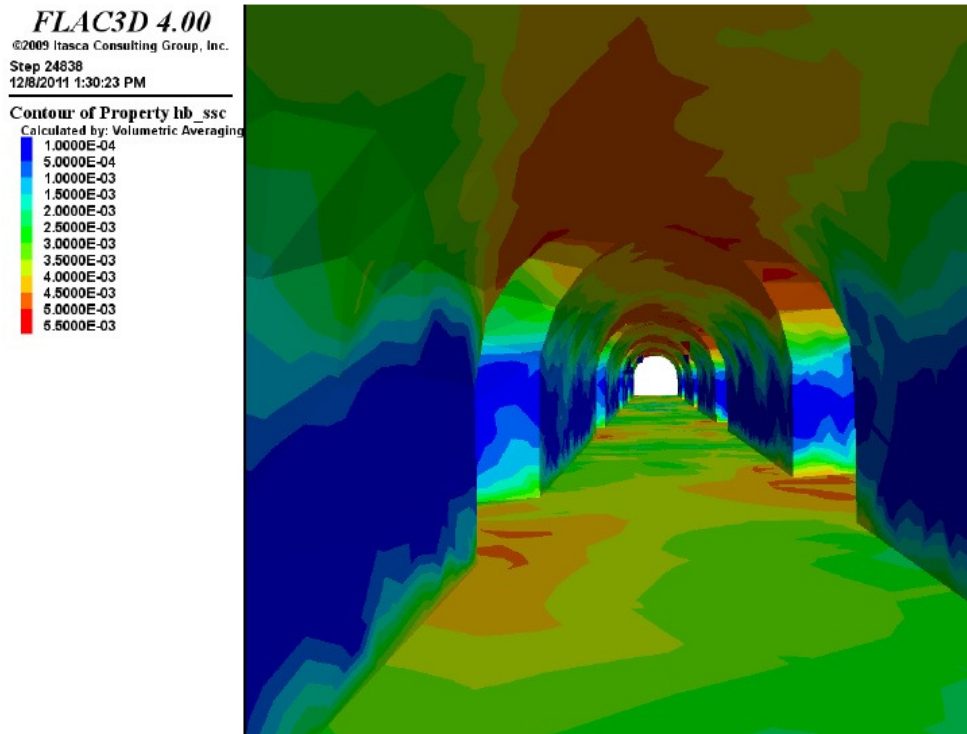
Figure 67: Recent extraction level stability analysis of the El Teniente layout. Contour plot of the Hoek-Brown property s. (Lavoie & Pierce, 2011b)

8.3 FLAC³ᴰ: Fast Lagrangian Analysis of Continua in 3 Dimensions

FLAC³ᴰ is a three-dimensional explicit finite-difference program for advanced geotechnical analysis of soil, rock and structural support. It was developed primarily for geotechnical engineering applications. Fields of application include mechanical analyses of underground excavations with complex phases, modelling of non-linear behaviour and large deformations, the evolution of progressive failure and collapse in hard rock mines, stability analyses of slopes and embankments and many more.

FLAC³ᴰ is operated in a command-driven mode. There are over 40 main commands and over 400 command modifiers, called keywords. *FISH* is the programming language that enables the user to define new variables and functions. The input files must be in standard ASCII format. The default calculation mode in FLAC³ᴰ is for static mechanical analysis.

8.3.1   Main calculation steps

The numerical code is mathematically expressed as a set of partial differential equations, relating mechanical (stress) and kinematic (strain rate, velocity) variables. These equations have to be solved for materials that are represented by polyhedral elements, hexahedra or tetrahedra, within a three-dimensional grid. Each element behaves according to a prescribed linear or nonlinear stress-strain law in response to applied body forces or boundary conditions. These conditions consist of surface tractions, concentrated loads at surface nodes and displacements in terms of nodal velocities. All stresses and nodal velocities are initially set to zero, initial stresses are specified thereafter.

Hexahedra are discretized automatically by the code into five tetrahedra. The combination of two overlays, depicted in Figure 68, gives the best results for nodal force calculations out of strain rates and stresses when high stress gradients and deformations are expected. The mixed discretization scheme averages the volumetric behaviour of zones over neighbouring zones. The technique is applied to overcome the over-stiff behaviour of these zones during plastic flow, when their yield limit is reached. This approach ensures a symmetric zone response for symmetric loading (Itasca Consulting Group, Inc., 2013).
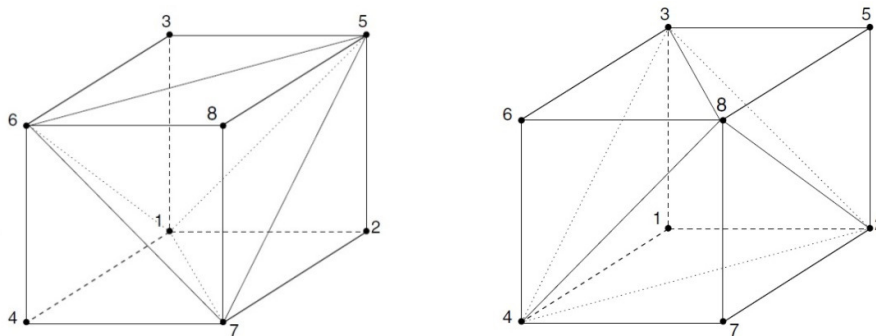
Figure 68: Two ways in which FLAC³ᴰ discretises hexahedra into five tetrahedral elements. (Itasca Consulting Group, Inc., 2013)

FLAC^{3D} translates a set of differential equations into matrix equations for each element, relating forces at nodes to displacements at nodes. It uses the full dynamic equations of motion, even when the modelling system is essentially static. The explicit solution scheme of the code is included in the flow chart in appendix J and can be summarised by the following sequence:

1. The strain-rate tensor for each tetrahedron in a zone is computed out of nodal velocities. Mixed discretization results in new diagonal strain-rate tensor components.
2. Stress increments for each tetrahedron in a zone are derived from these strain rates by invoking the constitutive equations. Addition of the stress increments results in new stress values. Mixed discretization techniques adjust the diagonal components of the stress-tensor.
3. The new stresses, applied loads and body forces create unbalanced forces at nodal points.
4. The equations of motion are invoked to derive new nodal velocities and displacements from the unbalanced forces.

This sequence is repeated at every calculation step. The unbalanced force history can be used to check if the system is at a steady-state flow of material (constant, nonzero value) or if it reaches an equilibrium state (approaching zero). Unbalanced loads can be redistributed with implicit or explicit techniques to retrieve a solution. Implicit techniques solve linear equations by standard matrix reduction. Moderate non-linearity can be handled by modifying stiffness coefficients or initial stress and / or strain iteratively. A non-linear system requires a load-path that mimics reality to a great extent and is best solved explicitly. Implicit techniques are generally faster than explicit techniques unless there is a high degree of non-linearity. (Hoek, *et al.*, 1995)

8.4 Constitutive model

The numerical code FLAC^{3D} has built-in constitutive models like the "null" model, three elasticity models and nine plasticity models, such as the Mohr-Coulomb, Hoek-Brown and ubiquitous-joint model. They all have the same incremental numerical algorithm that uses the stress state and the total strain increment for a time step to determine the corresponding stress increment and the resulting new stress state. The description of plastic flow in FLAC^{3D} is a combination of relations. The failure criterion, *i.e.* the yield function, specifies the limiting stress combination for which plastic flow takes place. Strain increments can be split into elastic and plastic parts. The elastic strain increment is linearly related with the stress increment. The direction of the plastic strain increment vector is specified by the flow rule, see subsection 8.4.1. The constitutive model used for simulations in this project is a User-Defined Model (UDM) by Itasca Consulting Group, Inc. It is a modified version of the Hoek-Brown model and is described in section 8.4.2.

8.4.1 Flow rules

A flow rule describes the volumetric behaviour of the material during yield. It gives the plastic strains after differentiating the plastic potential with respect to the stresses. The plastic potential function describes the kinematics of motion at yield. The associated flow rule, equation 8.1, has a plastic potential function which is identical to the plastic yield stress function (better known as the failure criterion, the stress combination at which plastic flow takes place). The dilation angle is associated with a particular yield criterion. The flow rule specifies the direction of the plastic strain increment vector, which is normal to the yield surface for the associated flow rule.

The non-associated flow rule, equation 8.2, has a plastic potential function that differs from the plastic yield stress function and assumes a constant dilation angle. The non-associated flow rule is effective in using a limited amount of coefficients to represent anisotropy. (Clausen, 2007)

$$d\varepsilon_{ij}^{p} = -\gamma_f \frac{\partial F}{\partial \sigma_{ij}}$$
8.1

$$d\varepsilon_{ij}^{p} = -\gamma_f \frac{\partial g}{\partial \sigma_{ij}}$$
8.2

ε_{ij}^{p}	Component of the plastic strain tensor
σ_{ij}	Component of the stress tensor
γ_f	Flow parameter
F	Plastic yield stress function
g	Plastic potential function

8.4.2 The vHoek model

The vHoek constitutive model is a modified version of the Hoek-Brown model, created with Microsoft Visual C++ and used internally by Itasca employees. The model is provided as a Dynamic Link Library file (DDL) which is loaded automatically by FLAC^{3D} if placed in the right sub-directory. This UDM is an exact implementation of the Hoek-Brown criterion and makes use of the non-associated plastic flow rule. Clausen (2007) believes that a non-associated flow rule better captures the dilative behaviour of the rock mass. The rock mass behaviour is assumed to show perfect plasticity and isotropic linear elasticity. The plastic potential is a scalar function according to equation 8.3 and assumes a constant dilation angle if the curvature parameter a_g is set to unity. The dilation angle is then controlled by the parameter m_g according to equation 8.4.

$$g = \sigma_1 - \sigma_3 - \sigma_{UCS} \left(s_g - m_g \frac{\sigma_1}{\sigma_{UCS}} \right)^{a_g}$$
8.3

$$1 + m_g = \frac{1 + \sin \psi}{1 - \sin \psi}$$
8.4

g	Plastic potential function
σ_1	Major principal stress (MPa)
σ_3	Minor principal stress (MPa)
σ_{UCS}	Uniaxial Compressive Stress of intact rock (MPa)
s_g	H-B plastic potential parameter
m_g	"dilation" parameter of the rock mass
a_g	Curvature parameter in the H-B plastic potential
ψ	Dilation angle (°)

8.4.3 Strain-softening

The degree of strain softening is embedded in the relation between the Hoek-Brown parameters and the plastic shear strain. It is assumed that the Hoek-Brown parameters linearly decrease from peak load to residual values over the range of the critical strain, defined in section 6.3. Published information on critical strain values is scarce and there is a controversy within the industry on critical strain determination. It is widely accepted that critical strain and zone size are inversely related, although the exact relation is subject to discussion. The initial critical strain suggestion for average quality rock masses is approximately 0.0005. The Northparkes caveability study of ore body E26 resulted in a critical plastic strain of 0.075 for a 1-metre zone size. Since zone sizes vary between and within models, these values should be corrected by dividing these critical strains by a representative length scale for the zones of interest. (Lorig & Pierce, 2000)

Table 5: Typical equivalent strain-softening rates for a 1-metre zone size (Lorig & Pierce, 2000)

UCS (MPa)	GSI	Critical plastic strain (%)	Material	Analysis
20-50 (?)	100	0.06	Concrete	Concrete tunnel liner Performance at Wesselton Mine
34	100	0.06	Concrete	Concrete tunnel liner performance at Premier Mine
90	70-85	0.012	Primary Andesite	Extraction-level pillar performance at El Teniente Sub-6
95	63.4	5	Tuffistic Kimberlite Breccia	Extraction-level tunnel performance at Premier Mine
na	60	5	Primary Andesite	El Salvador cavability study
70-130	59-79	7.5	Volcanic rock, including Quartz Monzonite	Northparkes cavability study

It is hard to establish the zone size of tetrahedra and hexahedra. Therefore, each zone is represented by a cube with the same volume in order to calculate the zone size according to equation 8.5. Since FLAC^{3D} runs in small strain mode, and thus coordinates of grid points are not recalculated, it is sufficient to calculate the critical strain for each zone once at the start of the simulation. The approach to establish the critical strain in this report is adopted from the recently published Feasibility Study on Oyu Tolgoi's Hugo North Lift 1 (Pierce, *et al.*, 2011). This approach is mathematically expressed by Equation 8.6 as a linear decrease of critical strain versus the GSI.

$$zone\ size = \sqrt[3]{zone\ volume} \qquad \text{8.5}$$

$$cr\ strain = \frac{12.5 - 0.125 \cdot GSI}{100 \cdot zone\ size} \qquad \text{8.6}$$

An alternative determination of the critical strain is expressed by the exponential equation 8.7 and is compiled of numerical back-analysis of case histories by Corkum *et al*. (2010). It is a relation between the critical minimum principal plastic strain and the GSI. Values for the critical minimum principal strain (e_3^{p*}) and the critical shear plastic strain (e_s^{p*}) can be used interchangeably based on experience. Equation 8.7 is valid for 1-metre zone sizes.

$$e_3^{p*} = 370 \cdot e^{-0.1 \cdot GSI} \qquad\qquad \text{8.7}$$

Figure 69 shows a plot of both equations, created by the author. This plot shows that data used to derive these trend lines is concentrated in the middle of the GSI range. Corkum *et al*. (2010) used an exponential trend line and Pierce *et al*. (2011) used a linear trend line. Itasca Consulting Group, Inc. is currently working on a simple regularization technique to address the issue of grid dependency on softening behaviour. They derived a property that resembles the grid zone size used to calibrate model properties; the calibration length '*hb_len*'. The input softening rate, amongst others, is then adjusted automatically to account for a different zone size. However, this technique is still experimental (Itasca Consulting Group, Inc., 2013).
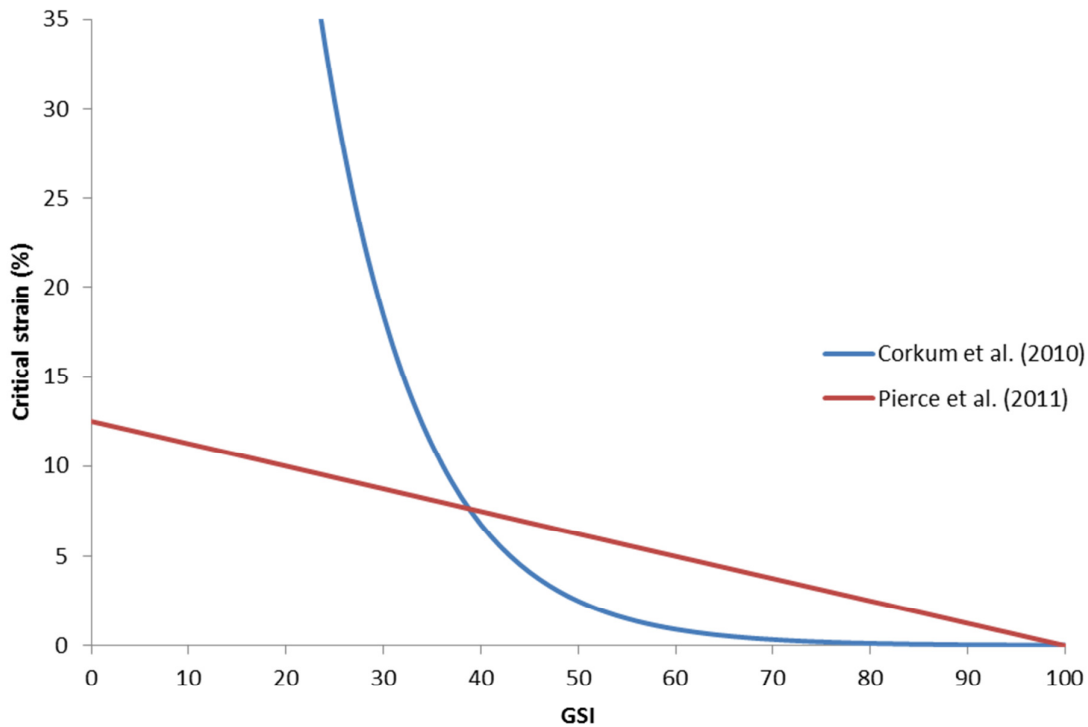
Figure 69: Comparison between two approaches to retrieve an estimate of the critical strain.

9 Convergence analysis

Displacements in the rock mass are monitored closely throughout the life of a block cave in order to guarantee the safety of employees and optimal productivity. Data are gathered by multi-point borehole extensometers (MPBX), SMART cable bolts and tape extensometers amongst other instruments. Data are presented as tunnel convergence or displacement profiles along boreholes and are very useful to adjust and verify numerical models. Section 9.1 describes the state-of-the-art real-time monitoring system currently deployed at Northparkes Mines. Section 9.2 and 9.3 discuss the selection of data used to check displacements in the numerical model. Section 9.4 discusses a theoretical analysis tool that is able to make quick estimates of wall displacements and support design.

9.1 Real-time monitoring system

The real-time monitoring system at Northparkes' block E48 lift 1 was established shortly after development of the block cave in the third quarter of 2011. As of February 2013, 72 'Stretch Measurement to Assess Reinforcement Tension' or SMART instruments have been installed either horizontal or vertical. Most of these devices are SMART MPBX (Figure 70).

Figure 70: MPBX (left) and SMART Cable (right). (Mine Design Technologies, 2013)

These instruments measure drift closure and deformation of brows as movement within the rock mass along a borehole. They provide a profile of movement based on data from six anchor points, also called nodes or targets. All anchor points are connected to an integrated 33mm diameter electronic readout head by fibreglass rods. Most MPBX at Northparkes are 10 m in length, although the length of some instruments differs. An MPBX is grouted into a borehole to prevent any slip between the anchor points and the rock mass.

The displacement of each anchor point is translated into a voltage by a linear potentiometer. This small, variable resistor is a well-known application in volume controls (Figure 71). The maximum detectable displacement is 127 mm which is represented by 2 Volts in intervals of 0.0001 V. This results in a resolution of 0.00635 mm per digit. Nine out of the 72 instruments are SMART cable bolts, a combination of the extensometer and a standard 7-strand cable bolt (Figure 70). Their maximum detectable displacement is 63.5 mm, resulting in a resolution of 0.003175 mm per digit. (Powell, pers. comm., 2013)
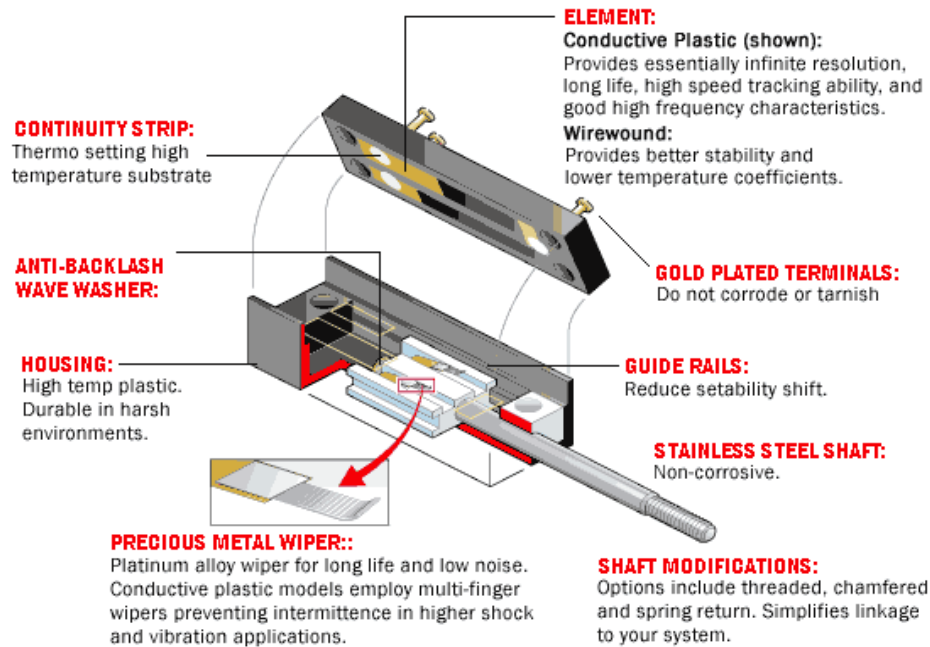
Figure 71: Example of a linear potentiometer. (ETI Systems, 2013)

The instruments are connected to automatic loggers per three instruments. A voltage reading of each potentiometer is recorded by these loggers every 5 minutes. Data are stored on the network and downloaded daily as text files, one for each instrument. This high level of automation and computerisation comes with new digital issues. The next section highlights several errors that can be observed in data. (Powell, pers. comm., 2013)

9.1.1 Troubleshooting

Vertical stations are hard to grout, because gravitational forces cause drainage of the bore hole during settlement of the grout. An air bubble will arise at the top of the hole if sufficient grout leaks at installation. This causes delayed responses to rock mass displacement from the deepest anchor point or points. Small compressions detected by the MPBX shortly after installation can be caused by shrinkage of the grout.

If a particular node of the extensometer suddenly reads 0 V, it means the circuit is open. If one or more nodes read the maximum voltage while they were not before, there is a short circuit. Both issues are caused by damaged or pinched leadwires due to flyrock or external impacts. The most common external impact is reckless driving of the LHD vehicles. The horizontal MPBX or SMART Cable stations are installed, without a recess, at two meters height in the camelback (Figure 72). This location makes the instruments vulnerable for damage. Wireless instruments are developed and for sale on the market and would greatly benefit the quality of data.

Figure 72: Scrape marks of an LHD on the camelback of the pillar next to drawpoint 5N9 (left) and an example of a resulting breakage in the leadwires (right). This particular section of leadwire was taken at station EXT-02S03-HM.

Damaged leadwires will still give a random voltage at every reading called a 'floating voltage'. It is easy to mistake these readings for actual rock mass displacements as can be seen in Figure 73. This graph illustrates the displacement of the rock mass at station EXT-02S03-HM and is typical for data as a result of floating voltages.
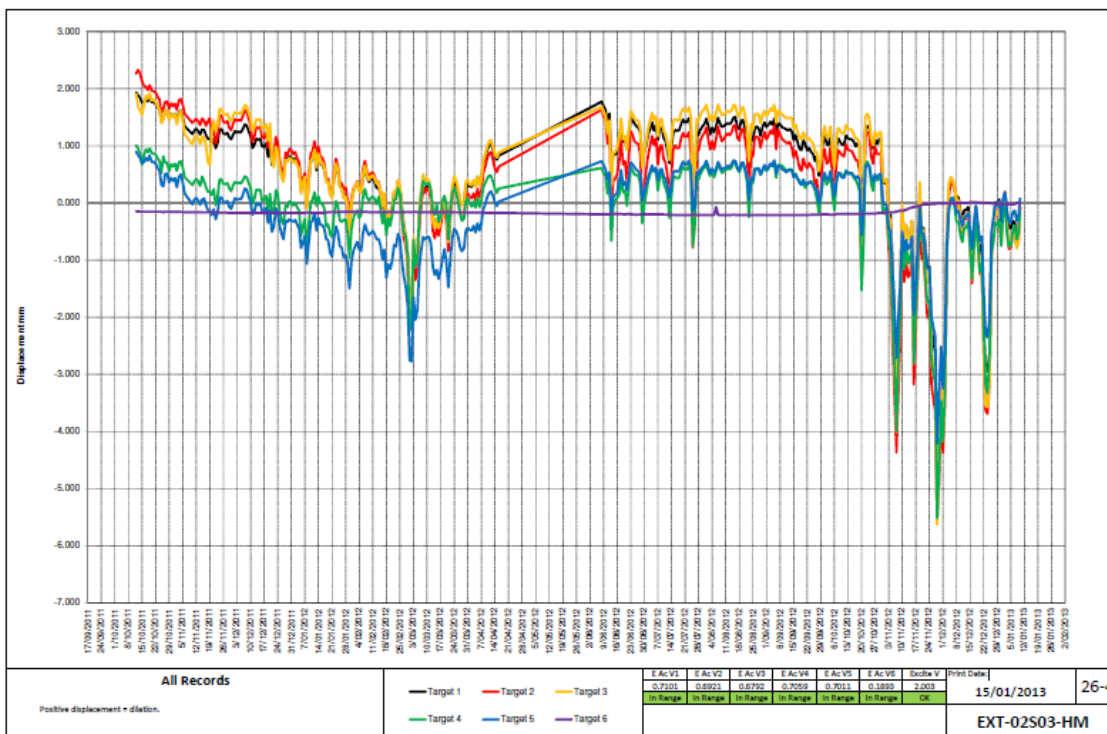
Figure 73: Floating voltages caused by breakage of the leadwires.

Other common errors in data include (but are not limited to) data jumps, symbols, date and / or time issues, blanks and outliers. Table 6 clarifies these errors in the same order, from top to bottom. The numbers used in this table are random and not linked to any graph or conclusion. The causes for these errors remain speculative.

Table 6: Typical errors, indicated in yellow, in real-time monitoring data.

12/11/2011 08:50	0.1849	0.1199	0.1439	0.1918	0.1655	0.1285
12/11/2011 08:55	0.1849	0.119	0.91439	0.1918	0.1655	0.1285
12/11/2011 09:00	0.1849	0.1199	0.1439	0.1918	0.1655	0.1285
13/07/2012 14:00	0.2744	0.2887	0.2934	0.2924	0.2866	0.2352
	0.2744	0.2887	0.293	r4Æ⊥ÆJ~LIó┬▓J>&IÜ▓¬J~LióÆÆJ~LÿÿL┬14:30:00		
13/07/2012	0.2744	0.2887	0.2934	0.2924	0.2866	0.2352
03/02/2012 08:45	0.0004	0.0005	0.0005	0.0004	0.0004	0.0004

9.1.2 Resulting graphs

True geotechnical trends only become visible after removing or altering erroneous data. An error-free factual report has been created by the author on the 1st of February 2013 where displacement data is correlated to draw rates. These draw-rates are categorised in intervals of radial distance towards the relevant station. This is done in order to support the hypothesis of causality between relative high draw rates close to the station and a decline in rock mass dilation. Production of ore should result in stress relief of surrounding infrastructure. An optimised production schedule is the ultimate goal. Yet more knowledge about the correlation between draw rates and displacements in the rock mass has to be gathered.

Appendix K shows an as-built record with all MPBX and SMART Cable stations in block E48 lift 1. A digital attachment contains a factual report of six graphs per station that correlate production rates to relative displacements at MPBX stations. Each graph contains a number in the lower right corner which refers to the as-built record. The extension of this number matches the legend in Table 7 and denotes the time-span over which data is shown.

Table 7: Legend of the factual report.

-0	24 hours
-1	07 days
-2	07 days (automatic stiction adjustment applied)
-3	05 weeks daily average
-4	All records
-5	All records (combined)

9.2 Undercut development MPBX data

A great number of MPBX have been installed during the undercutting of block E48 lift 1 during the first half of 2010. Each Extraction Drive was allocated three stations; one at each end of the drive and one in the middle. Data was gathered with handheld readout units (Figure 74) since they were installed before the real-time monitoring system was set up. The readings of these devices indicate a voltage and range between 000 and 500. The maximum presents 5 V and means that the extensometer is fully extended (127 mm). This results in a resolution of 0.254 mm per digit, which is significantly less than the resolution of the real-time monitoring system used nowadays. All MPBX were installed vertically with the head located in the collar of the borehole, *i.e.* in unstable ground, as shown in Figure 75. The deepest target (T1) was assumed to be in stable rock mass. (Powell, pers. comm., 2013)

Figure 74: Handheld readout unit (Tod & Lausch, 2003)
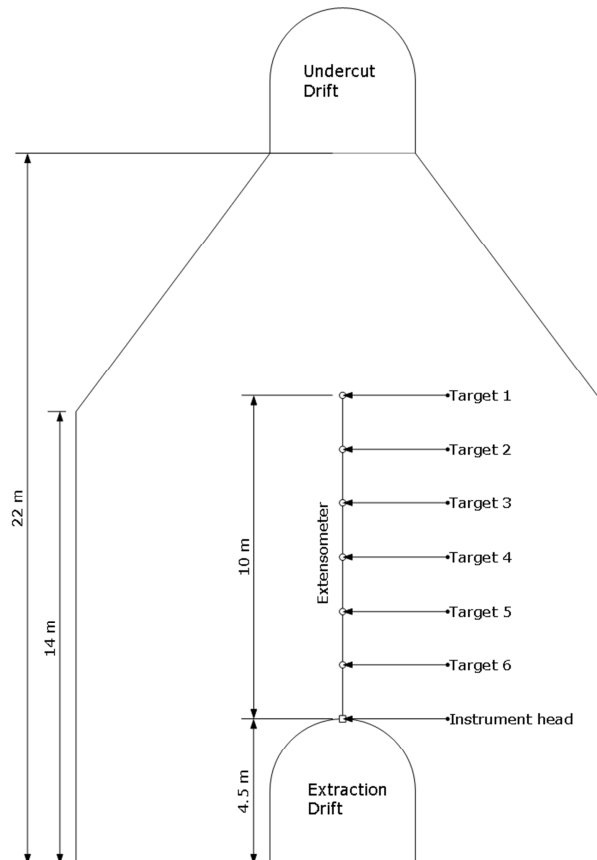
Figure 75: Illustrative sketch showing the location of a vertical extensometer in a cross-section of the major apex.

Equation 9.1 compensates for the movement of the instrument head which changes the reading for all anchor nodes. The reference node is the anchor node closest to the instrument head. Some SMART Cable bolts are installed with the instrument head in stable ground in order to plate and tension the cable. In other words, they are installed reversed. Equation 9.2 gives the displacement change for instruments installed this way. (Tod & Lausch, 2003)

$$Displacement = \left(\left(Rdg_{actual} - Rdg_{prev} \right) - \left(Ref_{actual} - Ref_{prev} \right) \right) \cdot \frac{Pot.Length}{500} \qquad \mathbf{9.1}$$

$$Displacement\ Change = \left(Rdg_{actual} - Rdg_{prev} \right) \cdot \frac{Pot.Length}{500} \qquad \mathbf{9.2}$$

$\mathbf{Rdg_{actual}}$	$\frac{1}{100}V$	Current handheld reading
$\mathbf{Rdg_{prev}}$	$\frac{1}{100}V$	Previous handheld reading
$\mathbf{Pot.Length}$	mm	Length of potentiometer
$\mathbf{Ref_{actual}}$	$\frac{1}{100}V$	Current reading of reference point
$\mathbf{Ref_{prev}}$	$\frac{1}{100}V$	Previous reading of reference point

The displacement graphs of all stations that were measured with the handheld reading unit in the past are attached digitally. This includes some stations above the crusher, the workshop and the crib room as well as some horizontal MPBX installed later. The map in appendix L shows the location of each station. The displacement plot versus time is linked to the position of the cave line in respect to the MPBX station. The plot also includes a graph of each station showing displacement versus distance along the cable.

9.2.1 Data selection

The extensometers at the west and east end of the extraction level are unfit for purpose, because they are installed relatively close to barrier pillars. These pillars are substantially bigger than regular pillars and cause increased stability compared to the layout in the numerical model. Appendix N shows a lithological plan of the extraction level and indicates the dominant lithological unit at the extraction level. This map is the result of a geological block model after input from diamond core drillings. Table 8 links the ten remaining MPBX stations with the local dominant lithological unit.

Table 8: Dominant lithological unit per MPBX station

ED01-EXTO2	VSS / POR
ED02-EXTO2	VSS / LTE / POR
ED03-EXTO2	POR / LTE
ED04-EXTO2	LTE
ED05-EXTO2	LTE
ED06-EXTO2	LTE / POR
ED07-EXTO2	LTE
ED08-EXTO2	LTE
ED09-EXTO2	LTE
ED10-EXTO2	LTE

At first sight, there is no clear relation between the dominant lithology and the displacement profile at the MPBX stations. This is in accordance with the findings of an evaluation study performed in 2004 (van As, 2004). Van As (2004) concluded that the rock mass variability is not lithologically controlled, since variation in discontinuity frequency and characteristics between lithological units are not significant. Therefore, domains within the rock mass must be described by classification schemes.

Three MPBX stations have been deemed not representative of the NPM rock mass at the extraction level based on their displacement profile and were not selected. ED02-EXTO2 and ED04-EXTO2 did not show any significant movement and ED07-EXTO2 showed only compression while all other MPBX stations show dilation of the back of the extraction drive. Figure 76 shows the location of the remaining seven MPBX stations which are selected to represent the overall rock mass behaviour in the major apex. Especially ED09-EXTO2 in Figure 77, on the next page, shows a clear response to the approaching undercut front which starts when the cave line is approximately 40 m away from the MPBX station.
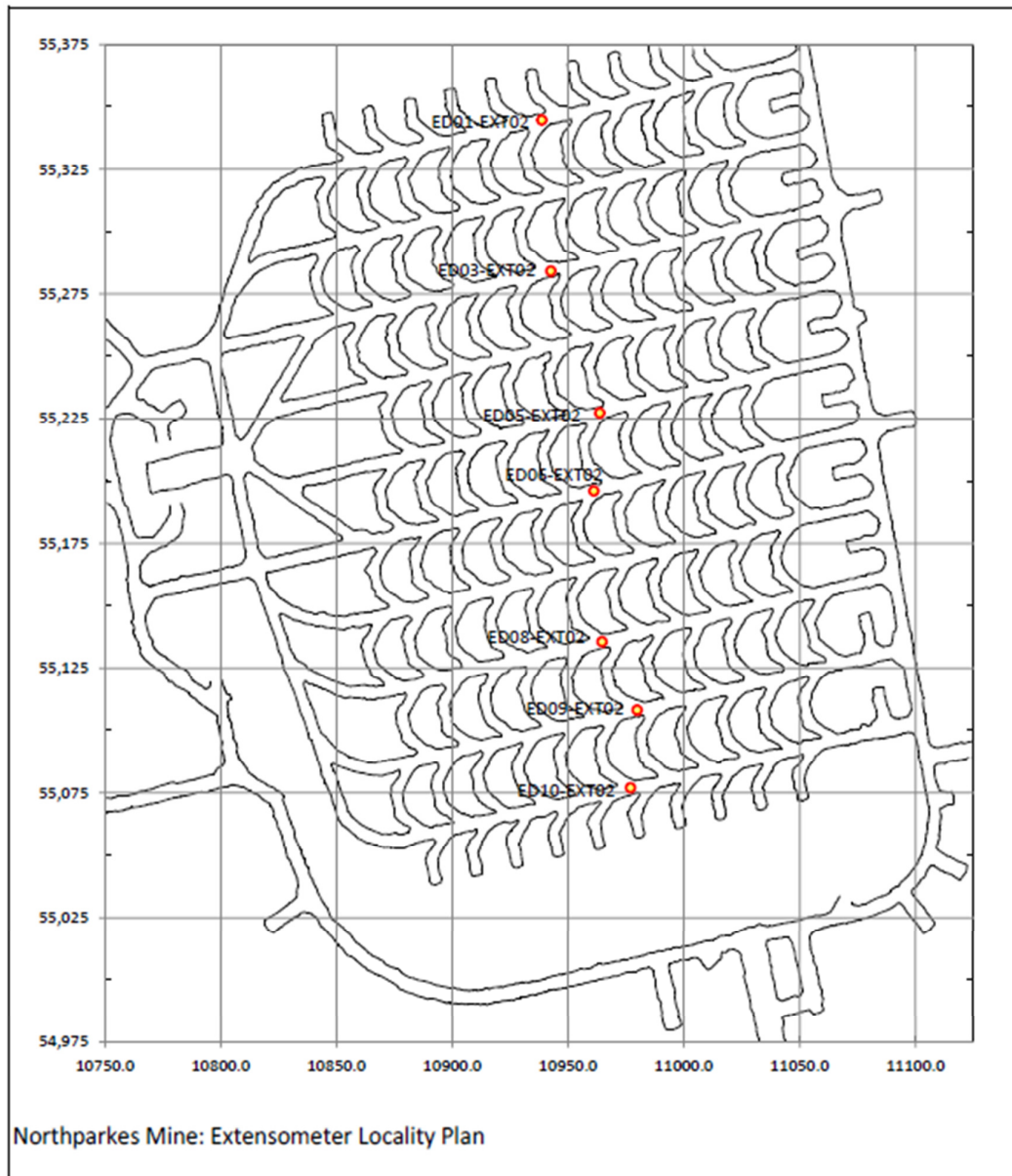
Figure 76: Plan of the extraction level with the location of the seven MPBX selected for calibration purposes.
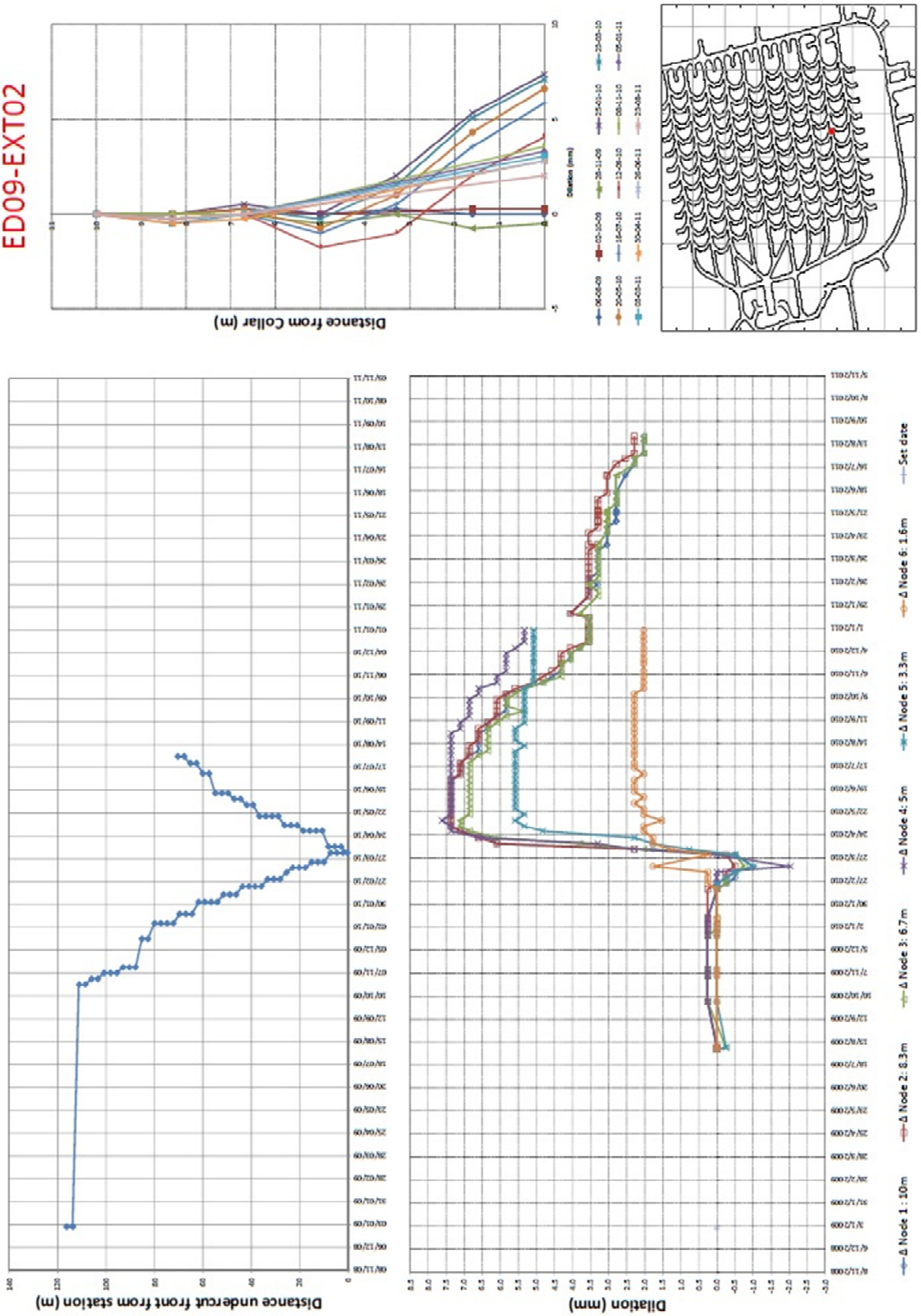
Figure 77: Relative displacements of the rock mass correlated to the approaching undercut front in extraction drive 9.

9.2.2   Data processing

The seven selected displacement profiles have to be combined into one graph in order to come up with a 'single' rock mass response that can be compared with the simulation of a continuum in FLAC^{3D}. Blast dates of drill drive rings, manual voltage readouts from extensometers and FLAC^{3D} history files have to be processed in order to correlate the simulation to reality.

Firstly, all dates that MPBX measurements were taken have to be stated relative to the distance of the undercut front to the respective MPBX station. The graphs cannot be simply plotted against time, because rock mass contraction or dilation is correlated to abutment stress instead. Abutment stress, in turn, depends on the distance from the undercut front and the initial *in situ* stress field. It is common that multiple undercut rings are blasted at the same time. If this is the case, the distance between the MPBX station and the undercut ring with the highest rank number is used. The rings are numbered in ascending order from West to East. The VLOOKUP function in excel is used to link the tables with voltage readings from the MPBX with the undercut ring blast records by the date. When there is not an exact match, the next most recent date that is older than the requested date is used. In other words, an MPBX reading taking place in between two blasts is coupled to the last blast and not to the next one. The lateral distance between the MPBX station and the undercut front is calculated from the difference in location based on coordinates (equation 9.3). Hereby, it is assumed that there is no influence of rings that are blasted in neighboring drill drives.

$$\sqrt{\left(x_{ring} - x_{MPBX}\right)^2 + \left(y_{ring} - y_{MPBX}\right)^2} \qquad\qquad \textbf{9.3}$$

Occasionally, multiple readings (on different dates) are taken before the undercut is advanced. In this study, the latest reading is used since the rock had more time to adapt to the induced stress field and the displacement represents the stress state better. The handheld measurements continued after the respective undercut drift had been developed. The maximum displacement for target 1 is selected as measurement for this period. If there are multiple readings with the same displacement at target 1 after the undercut drift has been developed, the reading with the maximum displacement at target 2 is selected, and so on. The readings in this distance range do not differ significantly from each other, so the impact of this assumption is relatively small. A minus sign is added manually to the values that represent the distance before the undercut front has passed the MPBX location. The displacements of each 'Target 1', located at ten meters from the instrument head in a rock mass that is assumed to be stable, of all selected MPBX stations is plotted against the distance from the undercut front in appendix N.

Not all MPBX measurements were taken on the same day in the week. This is expressed by a seemingly random data acquisition caused by limited human resources and priority of other tasks at the mine site. In order to combine data, all data gathered in a week are averaged and displayed as a single value per MPBX station per anchor. These seven data points, one per week per MPBX, are again averaged to represent a single data point for each anchor every week. Some stations were monitored for a longer period of time after undercut development than others. This creates a decrease of involved MPBX stations as the time since the passing of the undercut front increases, causing biased averaged results. The two combined displacement profiles in appendix N show the two extremes, one plot where all stations need to supply data to create a data point and one plot where all averages are plotted regardless of the amount of stations involved.

The stress relief once the undercut front has passed causes relaxation of the rock mass. Relaxation is a combination of elastic behaviour and the initiation and opening of cracks and fractures. The negative trends of deeply located targets with respect to shallow targets in Figure N-2, *i.e.* contraction, should not be interpreted as creep. The main reason for this phenomenon is a biased change in the selection of data as described in the previous paragraph, although some of this contraction is visible in the individual plots of stations in ED03, ED05 and ED09. The compaction of the rock mass is local (deeper than 5m from the tunnel wall) and can be attributed to the closure of cracks and fractures. It takes place when the undercut front has long passed. (van Hout, pers. comm., 2013a)

The fractured rock is subject to increased stress levels, abutment stress versus *in situ* stress, as the undercut front approaches the MPBX station location. These stresses are acting mainly on the pillars and are not clearly seen in displacement data of the back of the extraction drives. The whole major apex, including the MPBX, will move when the pillars show a lot of displacement or even fail. This movement cannot be visualised by the extensometer since the device only shows relative displacement. It assumes that the deepest target, *i.e.* 10 meters into the major apex, is located in stable rock and does not move. This would be true if the target was 10 meter away from an isolated tunnel boundary, but is questionable when it is located in the centre of the major apex. (van Hout, pers. comm., 2013a)

9.3 Convergence analysis

The simplest way to measure convergence in any direction is by using a tape extensometer. This device measures the distance between pairs of eyebolts that are fixed in the walls and back of a tunnel. Extensometers measure the relative displacements inside the rock mass while tape extensometers measure the distance between pairs of eyebolts relative to the previous measurement. A displacement profile over time can be constructed with sufficient measurements and eyebolts in place. Measurements are taken manually with a calibrated tape extensometer that consists of a stainless steel measuring tape wound upon a reel with a tape tensioning device and a digital LCD readout unit (Figure 78). The tape extensometers measure the distance with an accuracy of 0.01 mm. The measurements are directly entered in a specially developed application on an iPad, which is linked to the local network, by the operator. The frequency of measuring is determined based on the activity in the area due to development, production or geotechnical hazards. Northparkes Mine uses three eyebolts at each convergence station. The stations are spread across the extraction level and concentrated around 'problem areas'. Data can be used to create colour coded convergence maps of the extraction level as shown in Figure 79 on the next page. Software packages like CaveCad, a state-of-the-art integrated cave management system of Rio Tinto, are able to combine all monitoring data. Subsection 9.3.1 discusses convergence data of the extraction drifts since the start of development.

Figure 78: Digital tape extensometer (ITM-Soil Pty Ltd., 2009)

Figure 79: Example of an Extraction Level plan with convergence stations and colour coding to indicate weekly convergence rates.

9.3.1   Northparkes data

Horizontal convergence can be measured directly by connecting the tape extensometer between eyebolt B and C in Figure 80. The line along which the horizontal convergence is measured is not exactly perpendicular to the extraction drift walls. The initial distance between eyebolt B and C is mostly 5-6 meters with outliers as high as 7.5 meters. The reason is a lack of space along the extraction drift in an offset herringbone layout for the anchors to be placed on opposite walls at the exact same location along the Extraction Drift. Therefore, horizontal closure strains should be treated with caution when they are expressed as percentages of the tunnel width. These percentages are always an overestimate of the real convergence.
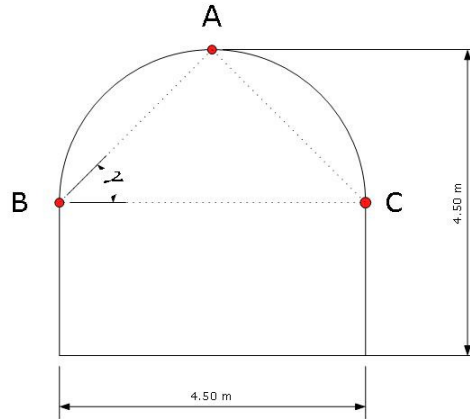
Figure 80: Sketch of a typical convergence station in an extraction drift of E48 lift #1.

Vertical convergence has to be calculated from the three measured distances, because a reference eyebolt at the floor of the extraction drift is not practical considering all equipment and safety of personnel. The Law of cosines (equation 9.4) relates the three sides of a triangle to one of its angles (equation 9.5). This triangle can be drawn in between the anchor nodes of the tape extensometer station like in Figure 80. The vertical distance ($VERT$), from anchor A downwards, can now be calculated with angle γ and side AB. The vertical distance will be overestimated when anchor C is installed lower than anchor B and it will be underestimated when anchor B is installed lower than anchor C. This has to do with the squareness of $VERT$ and BC.

$$AC^2 = AB^2 + BC^2 - 2 \cdot AB \cdot BC \cdot \cos \gamma \qquad \text{9.4}$$

$$\gamma = \cos^{-1}\left(\frac{AB^2 + BC^2 - AC^2}{2 \cdot AB \cdot BC}\right) \qquad \text{9.5}$$

$$VERT = AB \cdot \sin \gamma \qquad \text{9.6}$$

Appendix O contains a graph of vertical convergence over time and a graph of horizontal convergence over time. The vertical dashed lines in both graphs indicate the period of undercut development. The convergence stations that were not installed prior to undercut development are excluded from these graphs. Furthermore, it is evident from the vertical convergence graph that eyebolt A is installed significantly later than the two eyebolts on the sidewalls. This is most likely caused by the availability of scissor lifts, the installation of support or the installation of auxiliary objects (*e.g.*, ventilation tubes, pipes, data cables, etc.). Replacements of eyebolts are done multiple times a year for many reasons. One of the causes is damage due to the collision of LHDs.

9.3.2 Pre-development numerical modelling

Sainsbury (2007) investigated the integrity of the extraction level at block E48 during undercut development with the numerical code FLAC^{3D}. The geometry of his grid for the post-undercut sequence was created with generic FLAC^{3D} commands and matches the final designs to a great extent. He segmented the undercut into nine increments of advance approximately along the undercut drives (Figure 81). The northeast and southwest corners of the extraction level are subject to the highest abutment stresses due to the orientation of the major principal stress. As expected, a post-undercut sequence resulted in an increase in damage compared to an advance-undercut sequence.
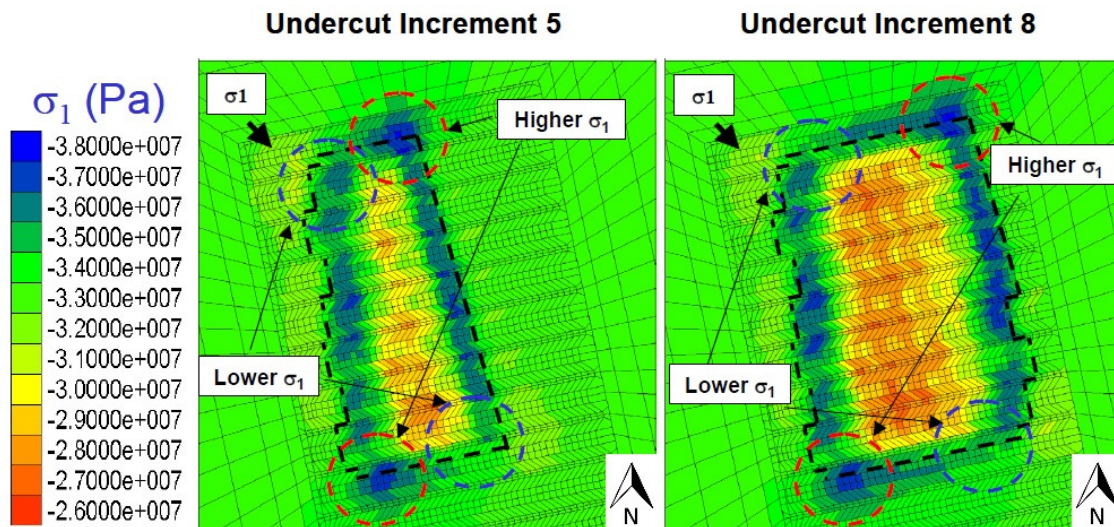
Figure 81: Abutment stress during undercut development according to Sainsbury (2007).

The horizontal and vertical closure strains of the extraction drives, stubs and drawpoint brows were assessed during simulation of the undercut development. The most significant damage was observed at the stubs and drawpoint brows. Closure strain is the relative decrease of the distance between two history points since the start of the simulation (pre-excavation). Horizontal strain precedes vertical strain since vertical stresses are diverted around the tunnels, causing tunnel walls to succumb prior to large deformations in the back. The results of the horizontal convergence assessment in appendix O are more explicit than the results of the vertical convergence assessment and eyebolt A, essential to measure vertical closure strain, is installed relatively late after the start of undercut development. For these reasons, the horizontal closure strain at the extraction drives is selected as a stage control parameter. The predicted horizontal closure strain at the extraction drive in a post-undercut sequence is slightly more than 1% and is illustrated in Figure 82. A closure strain of 1% coincides with a wall displacement of 21 millimetres on each side, because Sainsbury (2007) used a tunnel width of 4.2 meters instead of 4.5 meters. The thick black line in appendix O indicates this threshold of 1% horizontal closure strain. The threshold for vertical closure strain is approximately 0.8% according to Sainsbury (2007) and is also indicated in appendix O.
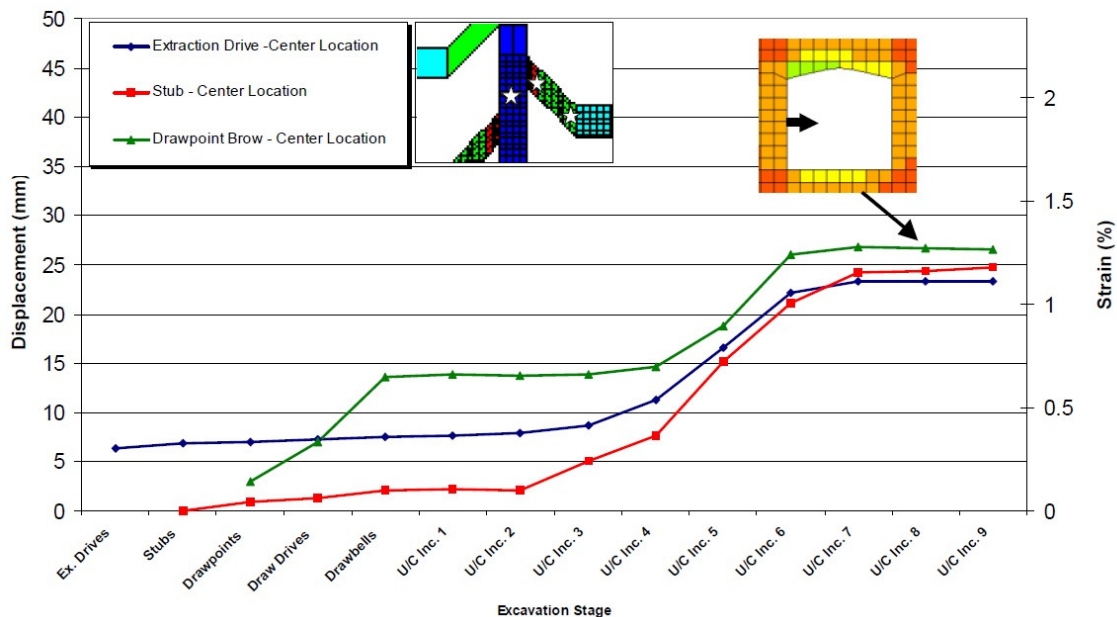
Figure 82: Horizontal closure strain (right vertical axis) and horizontal displacement (left vertical axis) after development of a post-undercut sequence. (Sainsbury, 2007)

9.3.3   Comparison

The analysis of horizontal convergence during undercut development at Northparkes Mines E48 included 28 convergence stations. 11 out of the 28 convergence stations showed a closure strain above the threshold of 1%, within or immediately after the undercutting process. This shallow rock mass response verifies the simulation results of Sainsbury (2007) to a fair extent. In reality, heterogeneity of the rock mass will always cause a larger spread of displacements than simulated results of a continuum model.

9.4 Convergence - Confinement

The convergence-confinement method is an analysis tool to make a quick estimate of anticipated wall deformation and support design. It shows how the support or reinforcement helps mobilise and conserve the inherent strength of the rock mass surrounding the excavation. The analysis is performed using the analytical solution for the elasto-plastic response of a cylindrical opening in isotropic, homogeneous material subjected to hydrostatic *in situ* stress and supported axi-symmetric. It is a two-dimensional simplistic approach of a three-dimensional problem. The analysis could also be performed by a plane strain numerical model. (Carranza-Torres & Fairhurst, 2000)

Figure 83 illustrates the Longitudinal Deformation Profile (LDP), Ground Reaction Curve (GRC) and Support Reaction Curve (SRC) which describe the convergence-confinement method graphically (Vlachopoulos & Diederichs, 2009). It shows that the load on the support segment will increase when the face is moving away from the tunnel segment of subject. Thus, the further the support is installed away from the face, the lower the final load on the support is going to be. Early installation of support is important, since the strength of recently exposed rock can deteriorate rapidly.

- The LDP relates the normalized distance from the tunnel face to the normalized wall displacement and is essential when specifying the appropriate installation distance from the face for tunnel support. Subsection 9.4.1 discusses its details.
- The GRC relates the normalized internal pressure to the normalized wall displacement. The internal pressure is a surrogate for the effect of gradual radial resistance reduction from intact rock to an exposed boundary as the tunnel face passes the location. This internal pressure is normalized by the far field stress. Subsection 9.4.2 discusses its details.
- The SRC relates the normalized external pressure to the normalized wall displacement. The external pressure is the pressure the rock mass exercises on the support. Subsection 9.4.3 discusses its details.
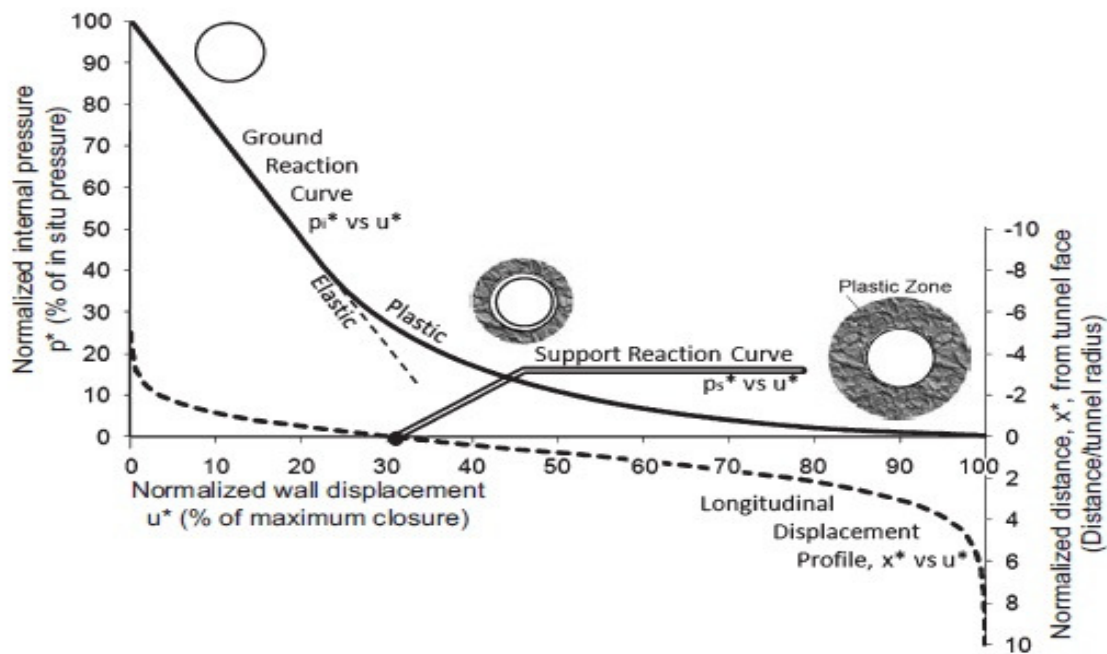
Figure 83: Convergence-confinement theory. (Vlachopoulos & Diederichs, 2009)

9.4.1 Construction of the LDP

A portion of the radial displacement at the tunnel wall takes place before the face advances. The radial displacement continues as the face advances further away of the segment of interest. Figure 84 shows the Longitudinal Displacement Profile as a function of the normalized ultimate plastic radius. This is the ratio between the maximum radius of the plastic (yielding) zone and the tunnel radius. This stereotype displacement profile is correct for civil industry applications, but in mining environments tunnels are often in close proximity to other excavations and mining-induced stresses can cause displacements long after the face of the tunnel has advanced (see Figure 85). (Vlachopoulos & Diederichs, 2009)
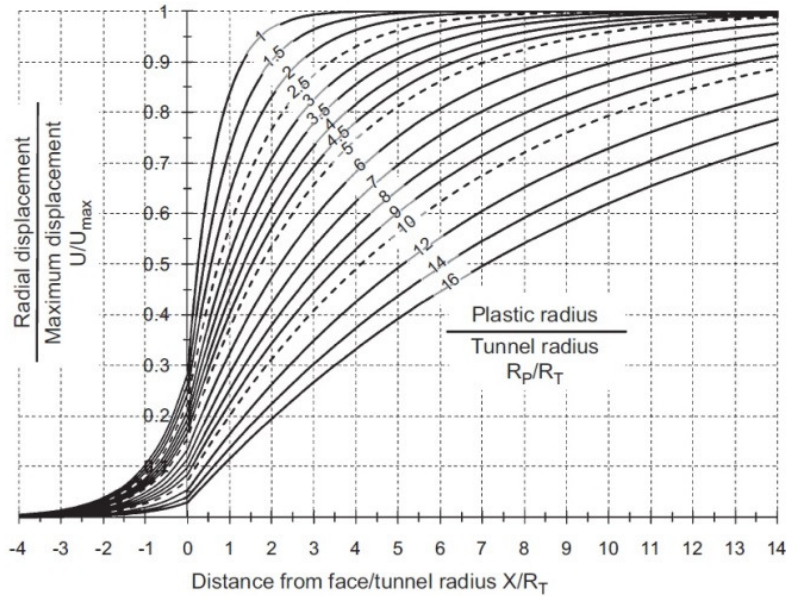
Figure 84: The LDP as a function of the normalized ultimate plastic radius, radial displacement and distance from the face. (Vlachopoulos & Diederichs, 2009)
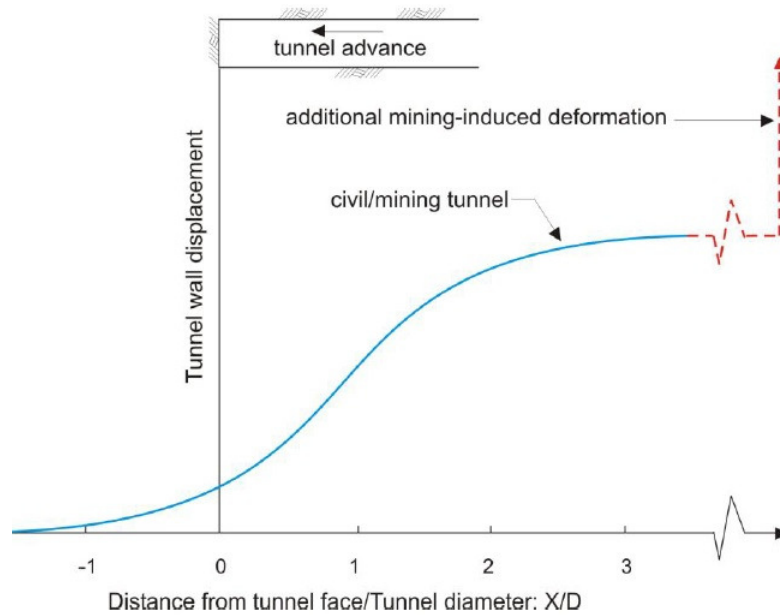
Figure 85: The LDP adapted to mining conditions. (Corkum, *et al.*, 2010)

9.4.2   Construction of the GRC

The Ground Reaction Curve (GRC) shows the relationship between radial convergence and internal pressure. A circular tunnel, excavated in an elasto-plastic medium, is subject to a hydrostatic far-field stress σ_0. Plastic failure is accompanied by a faster increase of radial tunnel displacement and occurs when the internal pressure drops beneath the critical internal pressure p_i^{cr} as illustrated in Figure 86. The graph can be constructed using a numerical code by decreasing values of internal pressure while monitoring radial wall displacement. (Carranza-Torres & Labuz, 2006)
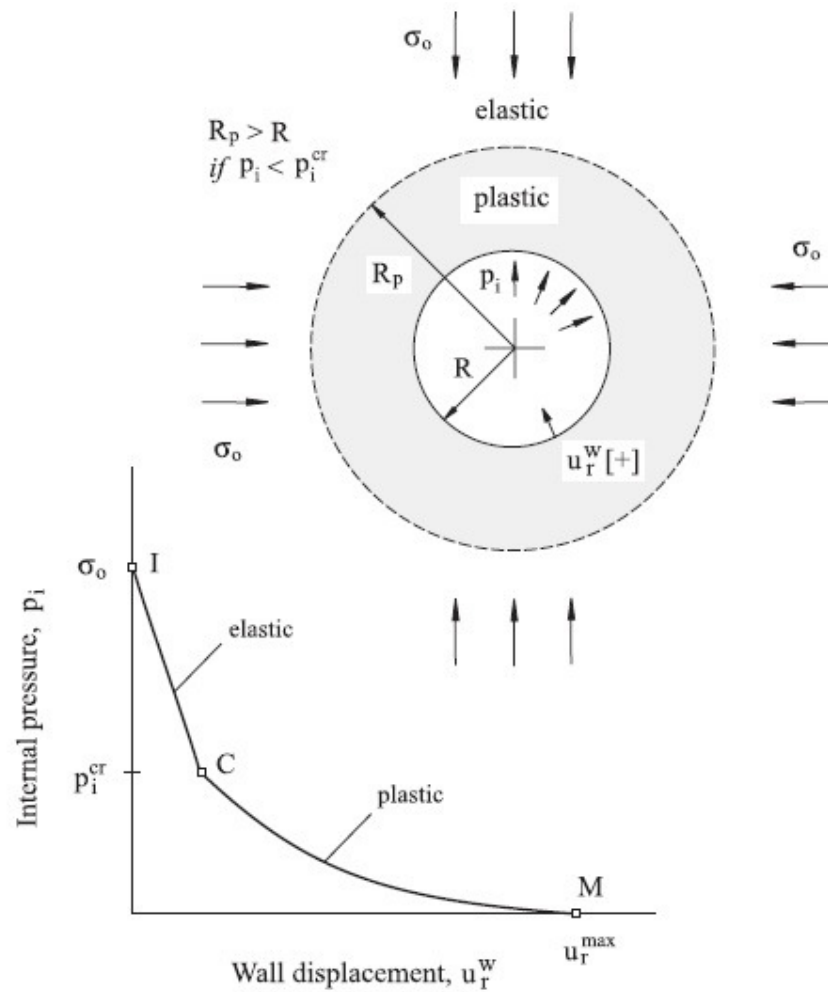
Figure 86: Characteristics of the Ground Reaction Curve (GRC) where positive radial displacement means inward radial displacement. (Carranza-Torres & Labuz, 2006).

9.4.3 Construction of the SRC

The Support Reaction Curve (SRC) is defined by the maximum support pressure (p_s^{max}) and the elastic stiffness of the support (K_s). Equation 9.7 defines the slope of the SRC and equation 9.8 defines the final level of supporting pressure.

$$K_s = \frac{\Delta p_s}{\Delta u_r^s} \qquad\qquad 9.7$$

$$p_s^{max} = \frac{t_s}{R_{tun}} \cdot \sigma_s^{max} \qquad\qquad 9.8$$

Parameter	Unit	Meaning
K_s		Stiffness
p_s^{max}	MPa	Maximum support pressure
Δp_s	MPa	Difference in support pressure
Δu_r^s	mm	Difference in radial displacement of support
t_s	m	Thickness of support
R_{tun}	m	Tunnel radius
σ_s^{max}	MPa	Ultimate compressive strength of support

10 Simulations

Lorig & Pierce (2000) suggest a three dimensional model when the investigated geotechnical component is nearly equi-dimensional and multiple openings cross each other, such that the interaction between adjacent openings is significant near the intersection. This perfectly applies to the stability analysis of the extraction level of a block cave. An unsupported model, *i.e.* opening without rock support, is justified if the support in reality is light, meaning it allows displacement.

A common three-dimensional model of the extraction level of a caving operation is made up out of several pillars. A model of only one pillar can be used if the rock material is homogeneous and isotropic and if applied stresses are uniform and vertical. These strong assumptions have been applied on a simplified model that served as a practice environment with relatively low computation times and is described in section 10.1. A more complicated parameterized environment is required in order to mimic reality. Section 10.2 discusses the way this environment is build up and section 10.3 describes the methods used to acquire input parameters for this comprehensive model.

10.1   Simplified model

The simplified model is based on the three-dimensional model of Wattimena (2003) (Figure 66). The script is set up, by the author of this thesis, in such a way that one can change all dimensions, rock mass parameters and model controls in one data file, while another data file is used to run the simulation by calling all data files that execute specific parts of the simulation at the appropriate time. The purpose of this section is to show all preparations for the comprehensive model. Each following subsection explains the procedures in one of the data files called upon by the execution file.

10.1.1 Input parameters

This data file contains 37 parameters which fully control the model. Some required parameters can be calculated out of several of these input parameters. This approach enhances the ability to quickly review results after changes. The input parameters describe amongst others the extent of the model, the dimensions of excavations, the density of meshing, the stress field, rock mass properties (elastic, peak, post-peak and caved) and the direction of incremental undercut development.

10.1.2 Mesh generation

Attempts to create a mesh with generic FLAC^{3D} functions and *KUBRIX* Geo tetrahedral and hexahedral meshing were compared to evaluate intrinsic differences and limitations. Also the interaction around interfaces between FLAC^{3D} and *KUBRIX Geo* meshes were assessed. These trials provided a basis for meshing procedures to be used in the comprehensive model, section 0. Figure 87 illustrates the geometry of half a drawbell on either side of an extraction drift. The model is 30 x 9 meters in plan view and has been extended in the vertical direction on both sides. The drawpoint drifts are right angled with the extraction drift to enable true symmetry planes in both the X- and Y-direction. The simplified model represents a partial off-set herringbone layout with a break-away angle of 90°.
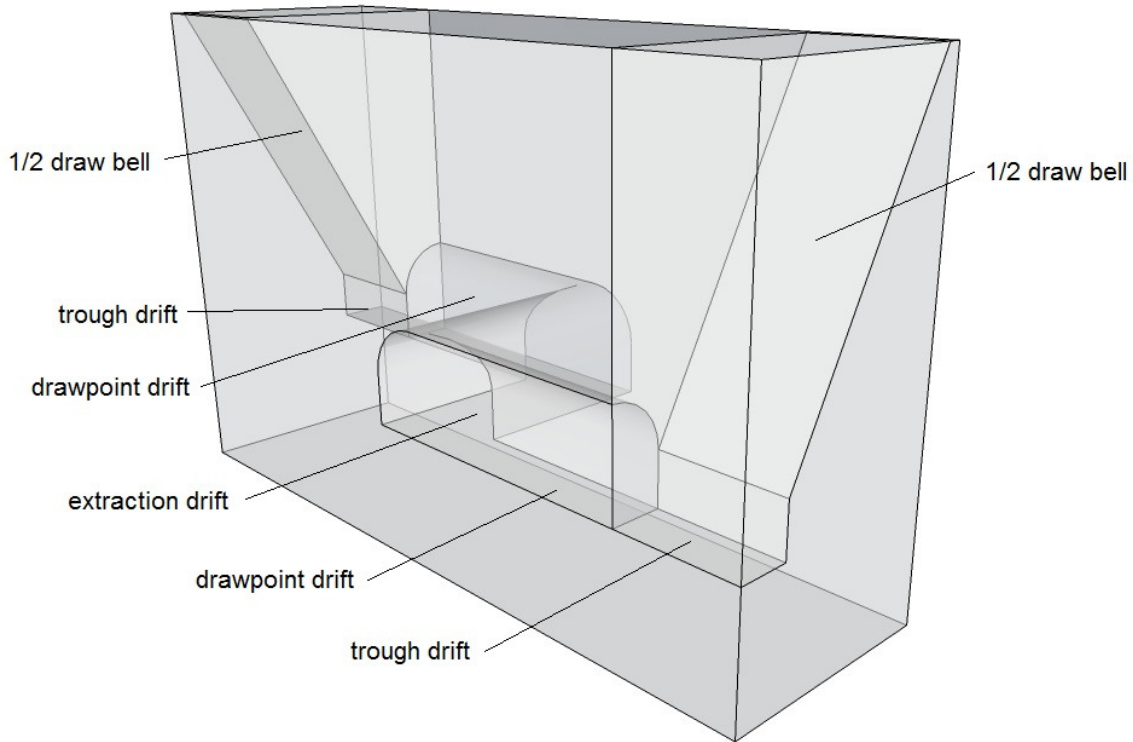
Figure 87: Zone of interest of the simplified model

10.1.3 Initial and boundary conditions

Boundaries on all sides, except the top, are fixed in their normal direction. The initial stresses are principal stresses aligned with the Cartesian axes. An elastic constitutive model is used to reach a static equilibrium state. Displacements at the tunnel boundary are monitored to evaluate the effects of excavations.

10.1.4 Constitutive model and rock mass properties

Additional rock mass properties are calculated from input parameters. The differences between the 'Hoek-Brown', 'modified Hoek-Brown' and 'vHoek' constitutive model and the importance of individual properties have been explored. The functionality of these models has been discussed in section 8.4 and finally the vHoek constitutive model has been selected for further use.

10.1.5 Assign caved rock properties

Additional caved rock properties are calculated from input parameters and the Mohr-Coulomb constitutive model is used to describe the caved rock in the drawbells. Stresses are reset to zero upon excavation of the drawbells. The gravitational force of the caved rock in the drawbells is applied as a gradational stress from the top of the drawbells downwards to check if a natural flow of material would occur. This natural flow of caved rock would verify the caved rock properties. Figure 88 shows this flow as displacement of gridpoints in the drawbells.
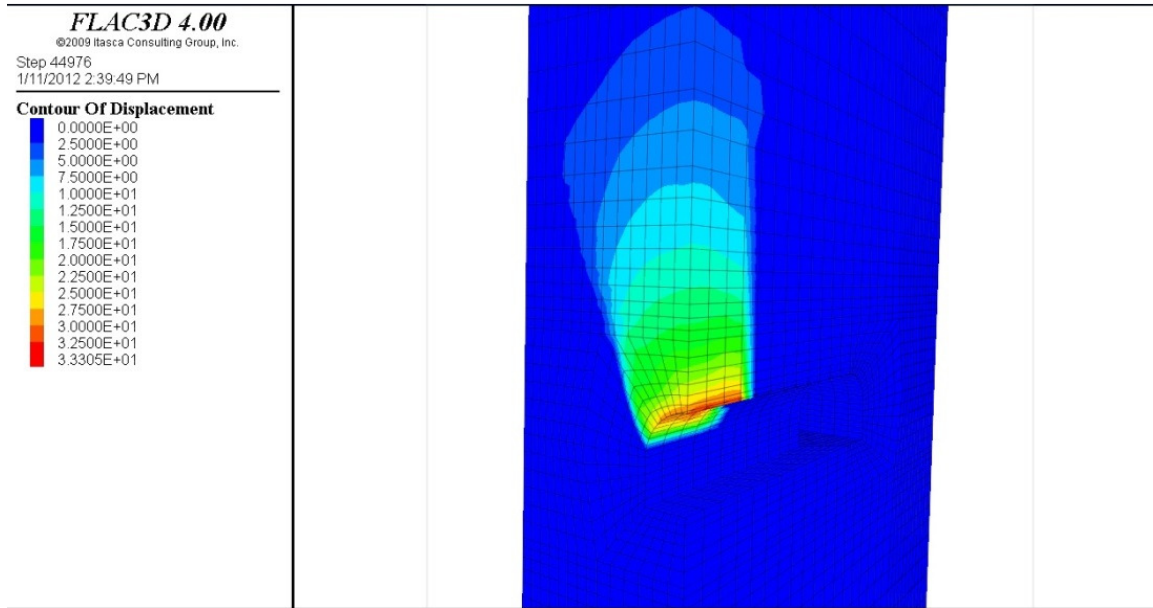
Figure 88: Natural flow of caved rock from the drawbell due to gravitational forces, indicated by displacement (m).

10.1.6 Incremental undercut development

The rock mass above the infrastructure is incrementally transformed into caved rock in an attempt to mimic the undercut development process. The model is converged to a static state solution after each incremental undercutting step and the rock mass behind the cave line is changed into caved rock. Similar caved rock properties and stresses as the caved rock in the drawbells, described in the previous subsection, are allocated to these groups. The changes in abutment stresses in front of the cave line are not assessed, since the scale of this undercut development is not realistic.

Equations 10.1 and 10.2 indicate the shortest distance between the sides of the model, pivoting around two opposite corners. This distance resembles the line along which the advance of the undercut front takes place and can be used to calculate increments of undercut advance. Figure 89 shows the dependency of this distance to the angular difference between the production tunnel and the cave line for this particular model.

$$dist = \frac{\_ymax}{\cos \alpha} + \sin \alpha \cdot \left(\_xmax - (\tan \alpha \cdot \_ymax)\right) \quad if \quad \beta > \tan^{-1}\left(\frac{\_ymax}{\_xmax}\right) \qquad \text{10.1}$$

$$dist = \frac{\_xmax}{\cos \beta} + \sin \beta \cdot \left(\_ymax - (\tan \beta \cdot \_xmax)\right) \quad if \quad \beta < \tan^{-1}\left(\frac{\_ymax}{\_xmax}\right) \qquad \text{10.2}$$

dist	Total distance along which the undercut advances
_xmax	Half of the drawbell spacing across the minor apex
_ymax	Production tunnel spacing
α	Angular difference between the production tunnel and the cave line
β	$90 - \alpha$
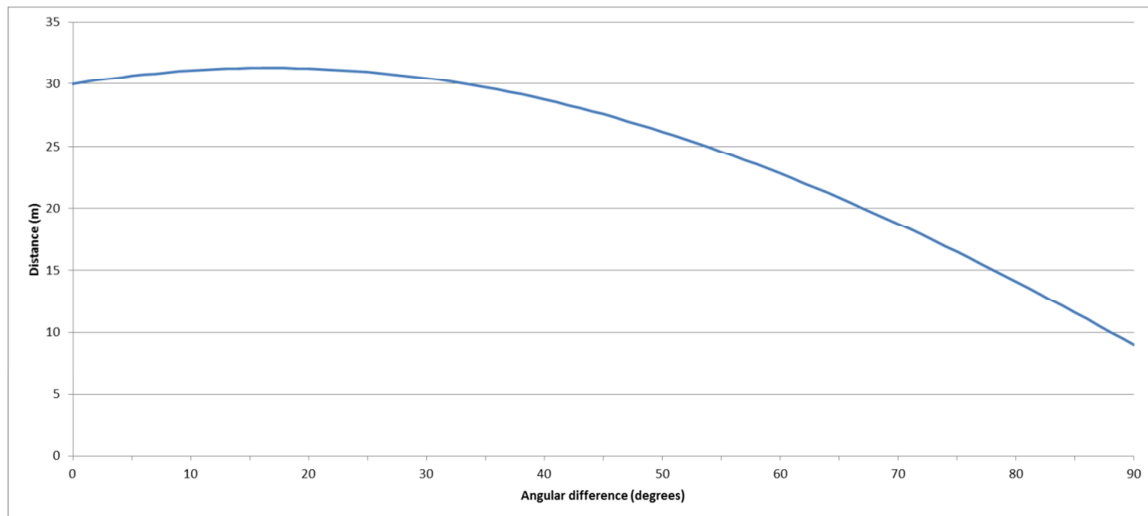
Figure 89: Change in distance along which the undercut front advances versus the angular difference between the cave line and the extraction drift.

The maximum distance is resembled by a horizontal asymptote in Figure 89 and represents the diagonal of the plan view of this simplified model. Equation 10.3 validates this approach. At angular differences of 0° and 90°, the cave line is parallel to the extraction drift and the trough drift respectively.

$$\sqrt{\_xmax^2 + \_ymax^2} = 32.321 \qquad \text{10.3}$$

The model was unable to converge to an equilibrium state upon execution of the last undercut increment. Due to boundary conditions, all sides of the model are acting as symmetry planes. Modelling a cave line that advances oblique into one direction is interpreted by the simulation as four cave lines advancing towards one point. The issue only becomes obvious upon 'blasting' of the last intact rock mass group, which can be seen as a diamond-shaped pillar on top of the infrastructure surrounded by caved rock on all sides.

10.1.7 Implementation of S-shape failure criterion

The stress state varies significantly during development and production of block and panel caving operations. Unexpected failure due to variations in the magnitude and orientation of induced stresses can result in unmanageable situations. Therefore, all rock mass properties should be up-to-date in order to determine the failure status of each zone in the numerical model. (Brown, 2012)

A user-defined *FISH*-function (see appendix P) was created by the author to apply the S-shaped failure criterion. The script tracks down every element in the model that is not a void and still has its original density. This approach will exclude caved rock and excavations. The GSI is replaced by the GSI' based on the modelled minor principal stress. Since the GSI' is highly variable throughout the simulation, it should be updated preferentially after each calculation step. The user must make a consideration between the level of detail and computation time by setting the amount of calculation steps prior to recalculations of the GSI' manually. The Hoek-Brown parameters m_b, s and a and the elastic modulus are altered according to the new GSI' value in each cycle of this loop and the process is repeated until a steady-state solution is achieved. Figure 90 shows the result of this application. The computation time of the model does not increase significantly with respect to the '*solve'* command.
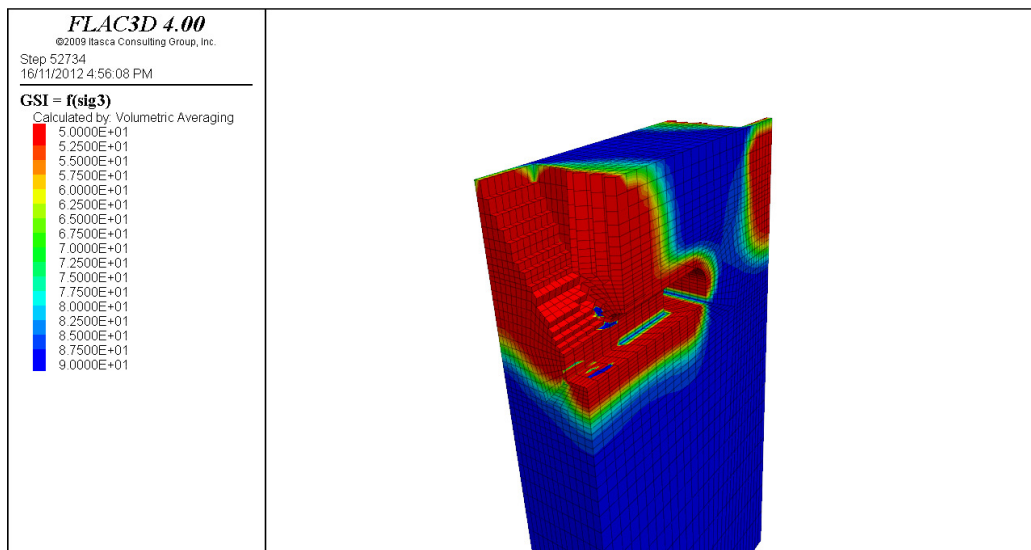
Figure 90: A contour plot of the GSI' (M=80) after drawbell development. The caved rock inside the drawbell and the top of the model are not plotted to increase visibility.

10.1.8 Gradual reduction of stiffness and stresses in excavated zones

The easiest way to simulate excavation in FLAC^{3D} is by changing the constitutive model of a certain range to the "null" model. This might cause numerical instability. Stresses will have to be diverted suddenly and this instability could result in overestimates of displacements. A solution for this issue is the use of zonk-stages. These stages simulate an advancing face by decreasing the normalized internal pressure gradually from 100 to 0 per cent (Figure 86). The accuracy of the resulting Ground Reaction Curve increases as more zonk-stages are used to simulate the tunnelling process. It is recommended to use 10 or more zonk-stages. (Sturm, 2012)

The script uses a user-defined *FISH* function to gradually reduce the bulk modulus, shear modulus and stress tensor in a group of elements assigned by the user. Firstly, the constitutive model of this group is changed to an elastic model. Subsequently, all parameters mentioned previously are reduced by a factor which is set by the user. The next zonk-stage starts when the model is in a state of equilibrium. This process is looped until a user-defined threshold is reached.

10.2 Comprehensive model

The simplified model provided insights into the operation of FLAC^{3D}, experience with programming in *FISH* language and it showed the functionality of the approach to implement the S-shaped failure criterion. A more sophisticated model is required to simulate the changing state of stress during undercut development. There is no correct solution to this nonlinear and inelastic system unless the stress path is specified. The model should mimic the way the system evolves to satisfy this path-dependence. Therefore, an exact replica of the final design of block E48 lift 1 has to be used in order to investigate its stability during and after undercut development. The mesh required for this model is far too complex to be created with generic FLAC^{3D} functions, so the mesh generator *KUBRIX* Geo is applied on a Computer-Aided Design (CAD) of the extraction level. Itasca Consulting Group, Inc. assessed the stability of different extraction level designs as part of the Resolution Copper Mine (RCM) feasibility study (Lavoie & Pierce, 2011b). Their way of building a parameterized environment and evaluating infrastructure performance has been used as a foundation for the comprehensive model applied in this thesis. The last part of this section discusses features of the *FISH* script that controls the simulation of all development stages. Appendix J contains a flow chart that describes the modelling procedures graphically.

10.2.1 Infrastructure design

High computation times and an outrageous amount of memory prohibit the modelling of the entire extraction level. The model is five drawbells long and two extraction drives wide. It has a footprint of 90 x 60 meters. Symmetry along the extraction drives prevents any boundary effects in the x-direction and a length of five drawbells in the y-direction is sufficient to protect the central pillar from boundary effects. The infrastructure is created from scratch with Rhino3D, a three-dimensional modelling software package using the Non-Uniform Rational Basis Spline (NURBS) mathematical model. The NURBS object needs to be meshed before it can be exported as an ASCII Stereo Lithography file (STL). The STL file only describes the triangulated surface geometry by the unit normal and vertices of its triangles. Appendix Q contains two cross-sections and a perspective view of the triangulated design. The essential dimensions and angles, matching the final design, are displayed in the figures. The tunnel profile is assumed to have vertical walls up to half the tunnel height and a semi-circle connecting these walls to form the tunnel back. The height of the trough drift (connecting two drawpoint drifts and filled with broken rock after drawbell development) is 5.00 meters in the final design. The design for this thesis uses a height of only 4.00 meters to avoid serious meshing complications at the locations where trough drift, drawpoint drift and drawbell meet. This change in design has a negligible effect since the drawbell overlaps with the top half of this drift. The other dimensions are an exact match to the final design.

10.2.2 Grid generation

KUBRIX Geo is an automatic grid generator used along the CAD software Rhinocerus. The combination of Rhinoceros and *KUBRIX* Geo is the preferred package for FLAC^{3D} modelling. It can handle complex non-manifold geometries which is frequently required in mining geomechanics. Tetrahedral meshing creates an unstructured grid; a tessellation of tetrahedra. This is required to handle the irregular shape of the infrastructure. Each tetrahedral element is then split into four hexahedral elements to create an all-hexahedra mesh as displayed in Figure 91. Such structures are known to capture plasticity in the best way. The non-manifold nature of the design is retained throughout the automatic meshing process and results in unique groups recognized by FLAC^{3D}.
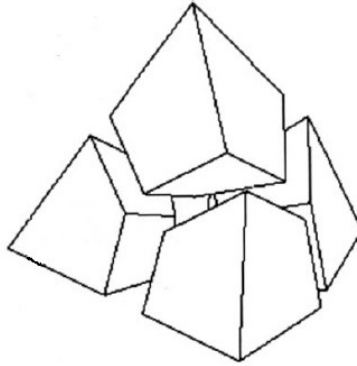
Figure 91: A visualisation of a tetrahedral element that is split into four hexahedral elements (Zuo, *et al.*, 1999)

The input parameters used in the study by Lavoie & Pierce (2011b) are listed in Table 9. They have used these input parameters on 30 x 15 and 30 x 20 off-set herringbone layouts amongst others. This resulted in a grid of 2,885,980 and 2,838,068 elements respectively.

Table 9: Standard input parameters KUBRIX Geo
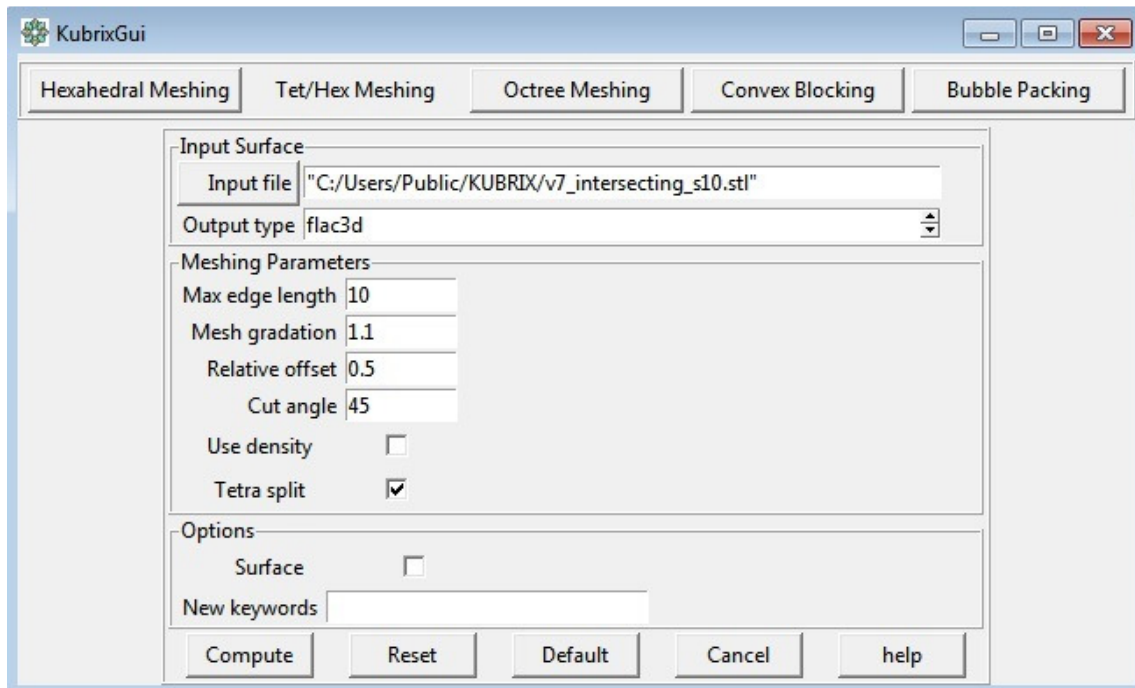
The initial settings did not give satisfying results for the infrastructure of E48 lift #1. Figure 92 shows the unsmooth surface on the sides of the drawbells. Thus, the initial input parameters have been altered by the author of this thesis. It is favourable to simulate the three-dimensional layout of the infrastructure in great detail, but on the other hand it is important to keep the total number of elements as low as possible to minimise computation time. The relation between an increase in the amount of elements and computation time is approximately linear. The cut angle is a threshold angle for the capture of surface features and should be modified in order to smoothen the surface of the drawbell. Table 10 summarizes the effect of the variation of the cut angle on the total number of elements. Changing the cut angle from 45° to 44° has an enormous impact on the total number of elements, but is necessary to remove the unwanted surface features displayed in Figure 92. Not all the unwanted surface features are gone at this stage and a further decrease of the cut angle to 40° is necessary. At this stage, the total number of elements is still lower than the total number of elements of grids used in the RCM study (Lavoie & Pierce, 2011b).
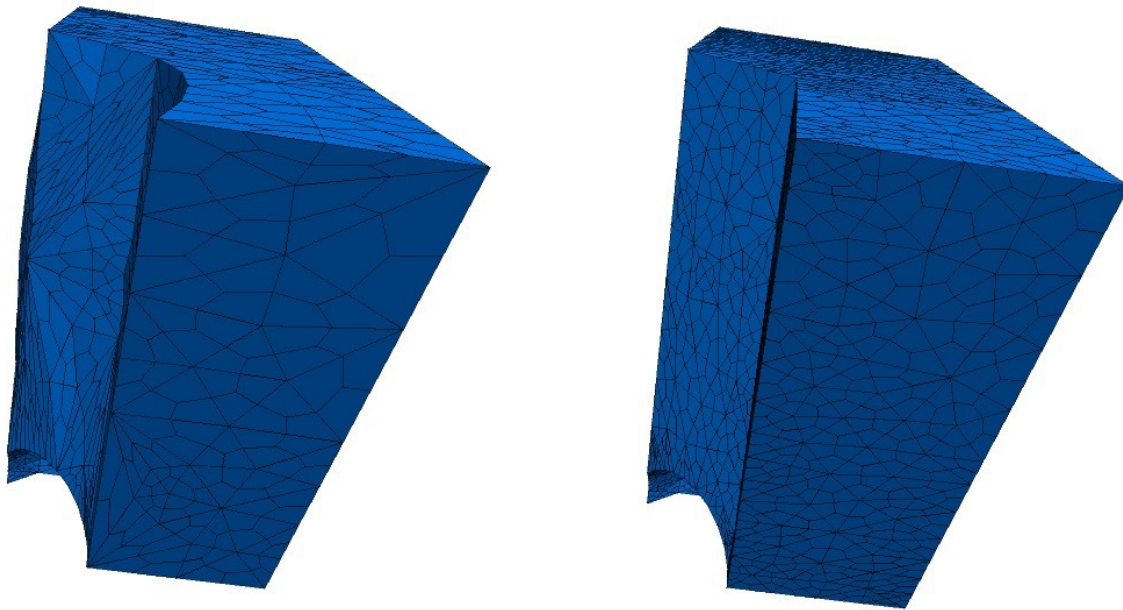
Figure 92: Half drawbell after tetrahedral meshing with a cut angle of 45° (left) and 40° (right).

Table 10: Variation of the cut angle.

Cut angle	Elements
35	2,442,708
40	2,442,708
44	2,116,424
45	727,548
60	793,956
180	930,868

The mesh gradation is the rate at which, at the surface of the tetrahedral mesh, neighbouring triangle sizes vary as triangles increase or decrease in size due to local size adaption. A higher rate of change will result in a lower resolution away from group boundaries. Hence, a lower total amount of elements and higher computation speed. The surface detail is not affected by changing this parameter. Table 11 summarizes the effect of the variation of the mesh gradation on the total number of elements. Figure 93 illustrates that the initial mesh gradation of 1.1 is well chosen, but the best trade-off between the amount of elements and the level of detail is around 1.15.

Table 11: Variation of the mesh gradation.

Mesh gradation	Elements
1.05	4,782,064
1.10	2,442,708
1.15	1,598,272
1.25	1,054,472
1.50	717,996
2.00	547,480
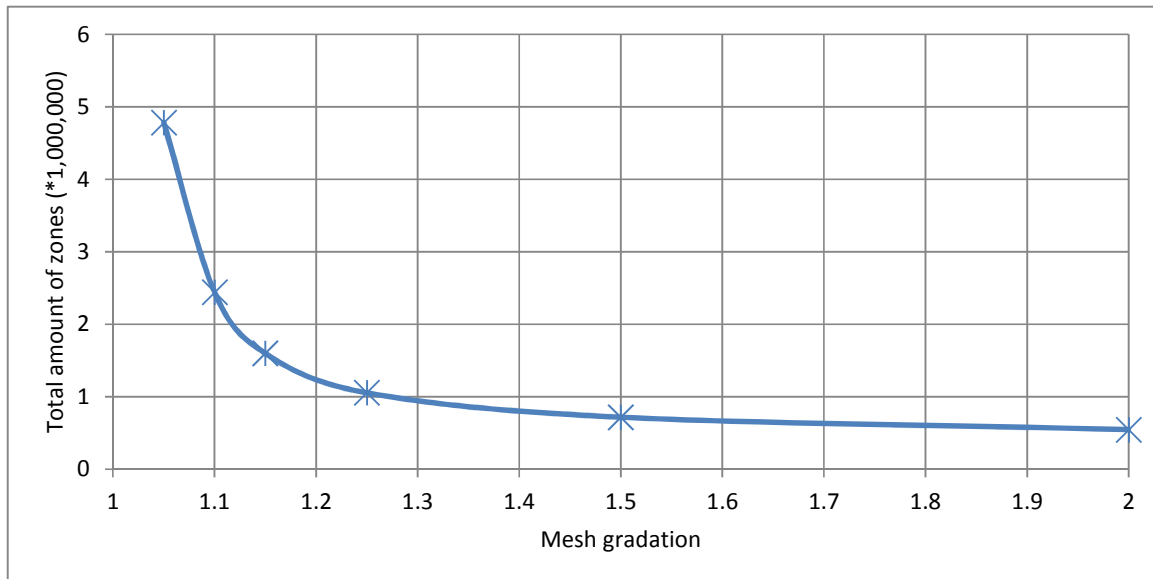
Figure 93: Variation in mesh gradation.

Figure 94 shows the resulting grid after it is imported in FLAC[3D]. Only the major infrastructure group is illustrated to enhance visibility. The histogram on the right hand side shows the spread of zone sizes and associated critical strains of the elements in the major infrastructure group. Table 12 shows the average and the extremes.
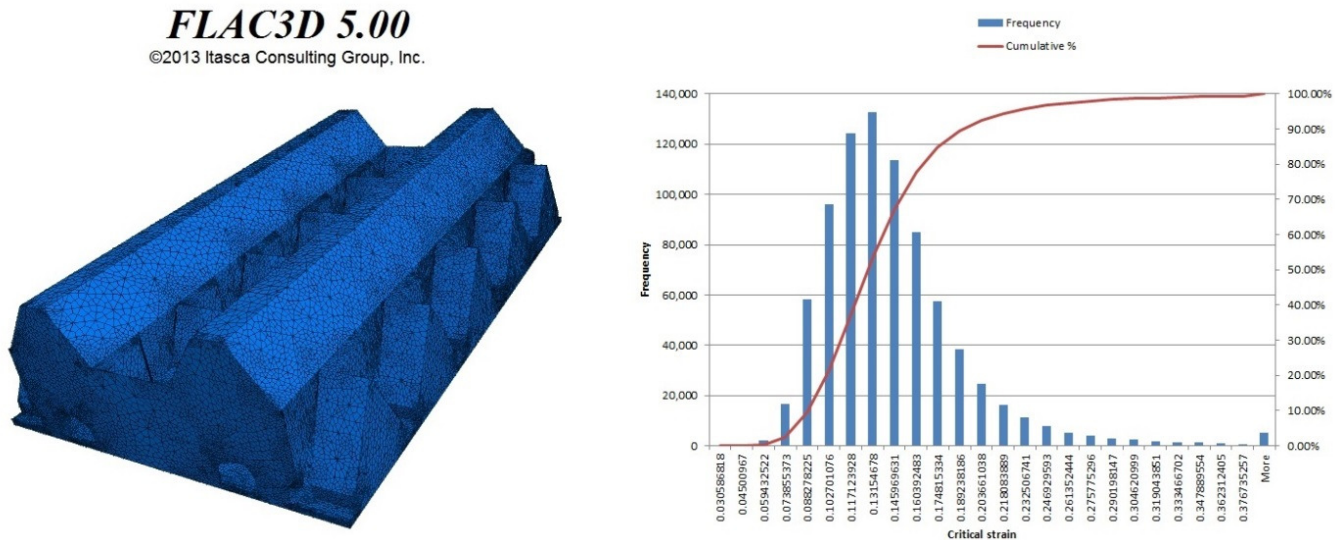
Figure 94: Zone of interest of the final grid (representing 811,140 elements) and a histogram of critical strain values for these elements. (GSI = 59)

Table 12: Spread of zone sizes and related critical strain data ($GSI = 59$)

	Zone size (m)	Critical strain (%)
Minimum	0.012	427.7
Average	0.437	11.7
Maximum	3.115	0.2

10.2.3 Initial stress equilibrium

Two rectangular grids with a relative low zone density are generated in FLAC[3D] and attached, at the top and the bottom, to the *KUBRIX* Geo grid when it is imported in FLAC[3D]. The limits of the grid are automatically detected with the 'get_limits' function. Boundary conditions and initial stresses are assigned to the model to simulate the *in situ* stress regime. Initial stresses are assigned to the centroid of a zone, where after forces are equally divided over the nodes that make up this zone. The model has to be in an equilibrium state, *i.e.* a balance of forces at each node, before any further changes to the mechanical model of elements can be made. An equilibrium state is obtained by damping the equations of motion to a negligible rate of change of kinetic energy, *i.e.* a sufficiently low ratio of unbalanced force at a grid point to the mean of the set of absolute forces acting at that grid point. The maximum unbalanced force can easily be monitored with an intrinsic FLAC[3D]-function. An elastic model is required to obtain the initial equilibrium state without any failure in the rock mass. Displacements should be reset after initial equilibrium to monitor the rock mass response to any changes made afterwards. (Itasca Consulting Group, Inc., 2013).

FLAC^{3D} prefers cubical-shaped elements to perform its calculations described in section 8.3.1. When the grid is build up out of these ideally shaped elements and the boundary conditions have been chosen carefully, FLAC^{3D} is able to reach the equilibrium state within several or even a single calculation step. An all-hexahedral grid created with KUBRIX Geo consists of non-uniform elements with a wide variety of zone sizes and therefore the numerical code requires more calculation steps to cycle to an equilibrium state. According to Itasca, a model with approximately 600,000 elements requires 4,000-6,000 calculation steps to reach an equilibrium state (Sturm, pers. comm., 2013). The grid used in this thesis consists of 1,614,464 elements and requires 2,090 calculation steps before it reaches the initial equilibrium state.

10.2.4 Script explanation

Mine development changes the in-situ stress field into a mine-induced stress field. This process from an unimpaired rock mass to the start-up phase of production is simulated by a script that consists of two data files. The 'function' file contains user-defined *FISH* functions that are executed when called by the 'parameter' file. The 'parameter' file contains information related to the stress path, excavation sequence, model dimensions and rock mass properties. The original files are coming from the RCM feasibility study by Lavoie and Pierce (2011). The author of this thesis has modified these files significantly and made several additions to be able to meet the goals of this projects. This section describes the processes in these files stepwise. The complete script is written down in appendix R.

Arrays are created to easily give commands to a number of groups that represent the same feature. There are arrays for the stubs, draw drifts, drawbells, extraction drifts, undercut drifts, the top of the model and the bottom of the model. Each group has to be assigned to one of these arrays manually. The model controls define the end of a loading or unloading stage and have to be introduced as horizontal closure strain or abutment stress thresholds. Subsequently, data describing model dimensions, rock mass properties and the interfaces are introduced. Other required parameters are calculated from the input parameters.

A choice between the Hoek-Brown constitutive model and the S-shape variant has to be made at the start of the script. This choice determines if a 'solve' command suffices to reach a static state solution or if Hoek-Brown parameters have to be altered during stepping. History variables are introduced to the simulation before any group is excavated. The constitutive model is changed from the elastic model, used to acquire the initial stress equilibrium, to the vHoek model and the associated properties are assigned to all elements. At this stage, the rock mass prior to mine development is fully simulated and a series of excavations can be started. Each of the following excavation series is followed by a static state solution.

1. Excavation of the extraction drifts and undercut drifts
2. Excavation of the stubs and the drawpoint drifts
3. Excavation of the drawbells and subsequent assignment of caved rock properties to the drawbells and the drawpoint drifts.

The simulation now represents a mine prior to undercut development. Initial relative displacements between the history points that represent anchors of the simulated extensometers are calculated. These displacements will be subtracted from relative displacements monitored during undercut development in order to simulate installation of the extensometers at this moment. The model will now be exposed to the stress-path felt by the extraction level during undercut development. The stress-path can be characterised as a loading–unloading-loading sequence (Figure 95), representing the abutment stress, the stress shadow and cave load.
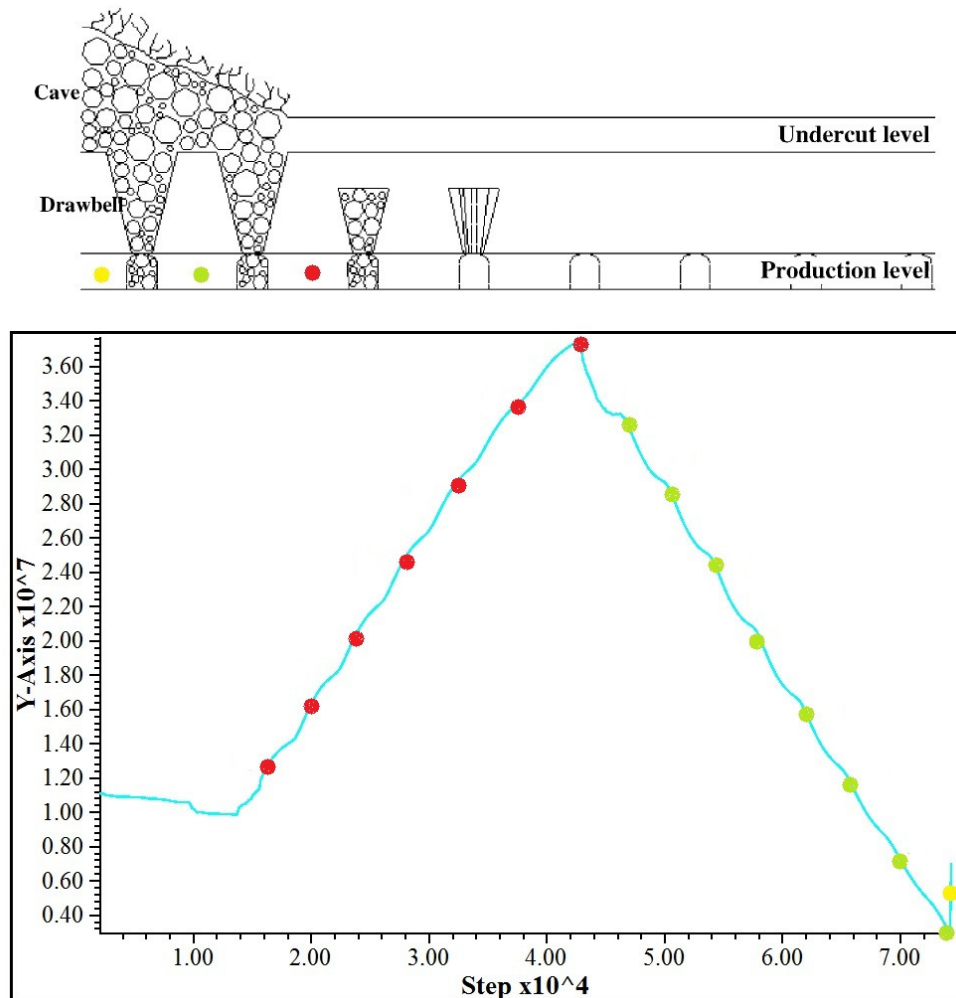
Figure 95: The loading-unloading-loading sequence - The abutment stress increases (red) when the cave line approaches. Vertical stress suddenly drops in the stress shadow (green), *i.e.* when the cave line has passed, and builds up slightly due to cave load (yellow).

The model is loaded by applying a downwards velocity to grid points at the top of the model. Since this simulation is time independent, the velocity represents displacement per calculation step. The velocity is slowly increased from a very small number to 10^{-5} in order to minimize shocks to the system. This results in an increase in abutment stress. This loading continues until the abutment stress at the top of the model reaches the user-defined threshold, *i.e.* expected abutment stress right before passing of the undercut front, or the horizontal closure strain reaches the user-defined threshold at 4 out of 8 continuous monitoring stations along the extraction drifts. Either one of the thresholds can be enabled or both at the same time.

The unloading stage simulates the stress shadow after passing of the undercut front. Ideally, this stage continuous until there is no abutment stress at all at the top of the model. Major parts of the top of the model failed due to tensile conditions when the abutment stress approach zero and caused unrealistic displacements and stress distributions. Therefore, the minimum abutment stress and threshold for the unloading stage is set at 3 MPa.

The last stage simulates a small increase in vertical stress due to broken rock that is piling up on the extraction level infrastructure, *i.e.* cave load. Caved rock properties are assigned to the top of the model and the undercut drifts before this final stage commences. This stage requires a relative small amount of calculation steps and stops when the abutment stress reaches 5 MPa. The thresholds of the last two stages are higher compared to assumptions made by Lavoie & Pierce (2011b), 0.5 and 1.2 MPa respectively.

10.3 Input parameters

In order to compare simulation results with observations at Northparkes Mines block E48 lift 1, the modelled rock mass must resemble the E48 rock mass by selecting the right input parameters. The ore body has been classified by three distinctive classification schemes to assess caveability, fragmentation and support requirements. During the E48 Evaluation Study in 2004 (van As, 2004), over 35 km of core were logged to assess the rock parameters. Point load strength tests were performed on every 10m of core drilled. Additional strength tests included 127 UCS tests and 23 triaxial tests. Stress measurements were obtained through Hollow Inclusion (HI) cell measurements by the overcoring method. All testing confirmed a fairly isotropic rock mass, consisting of poor quality shear zones and fair quality 'host' rock according to the Laubscher system.

10.3.1 Depth

Northparkes Mines uses a New South Wales annotation to indicate heights, which is termed 'RL'. The extraction level of E48 lift 1 is located at 9700m RL. The height of the topography cannot be fixed by a single number due to hilly terrain, waste dumps, stock piles and large engineered structures on surface. The height used by most engineers on site for the topography above the E48 ore body is 10,280m RL. This results in a depth of 580 meters for the extraction level.

10.3.2 Lithology

The lithology of the E48 ore body consists of gently SSE dipping (30°) volcanic sandstones (VSS), latitic lavas and sills (LTE) and minor breccias. The latite lavas and sills have only been recognized since 2006, in previous reports they are annotated as volcaniclastic units. The dark grey to black LTE unit contains submarine latites parallel to the volcanic sequence that contain primary coarse grained magnetite. The crystalline lavas show flow foliations of the feldspar and amphibole phenocrysts. The dark grey VSS unit is a sedimentary volcanic rock deposited below sea level. It contains primary disseminated magnetite and can be distinguished from the LTE unit by its sub-rounded latitic feldspar and mafic crystals. These lithological units combine into two distinctive stratigraphic units at the 9700m RL extraction level. The oldest and lower unit is a submarine latite lava with common intercalations of volcanic sandstone lenses or boulders. The second unit lies above the previous stratigraphic unit and consists of massive crystalline latite lavas with minor thin lenses of volcanic breccia. Figure 96, on the next page, shows the location of these lithological units and the copper grade cut-off in two cross-sections. (Hendrawan, 2011)
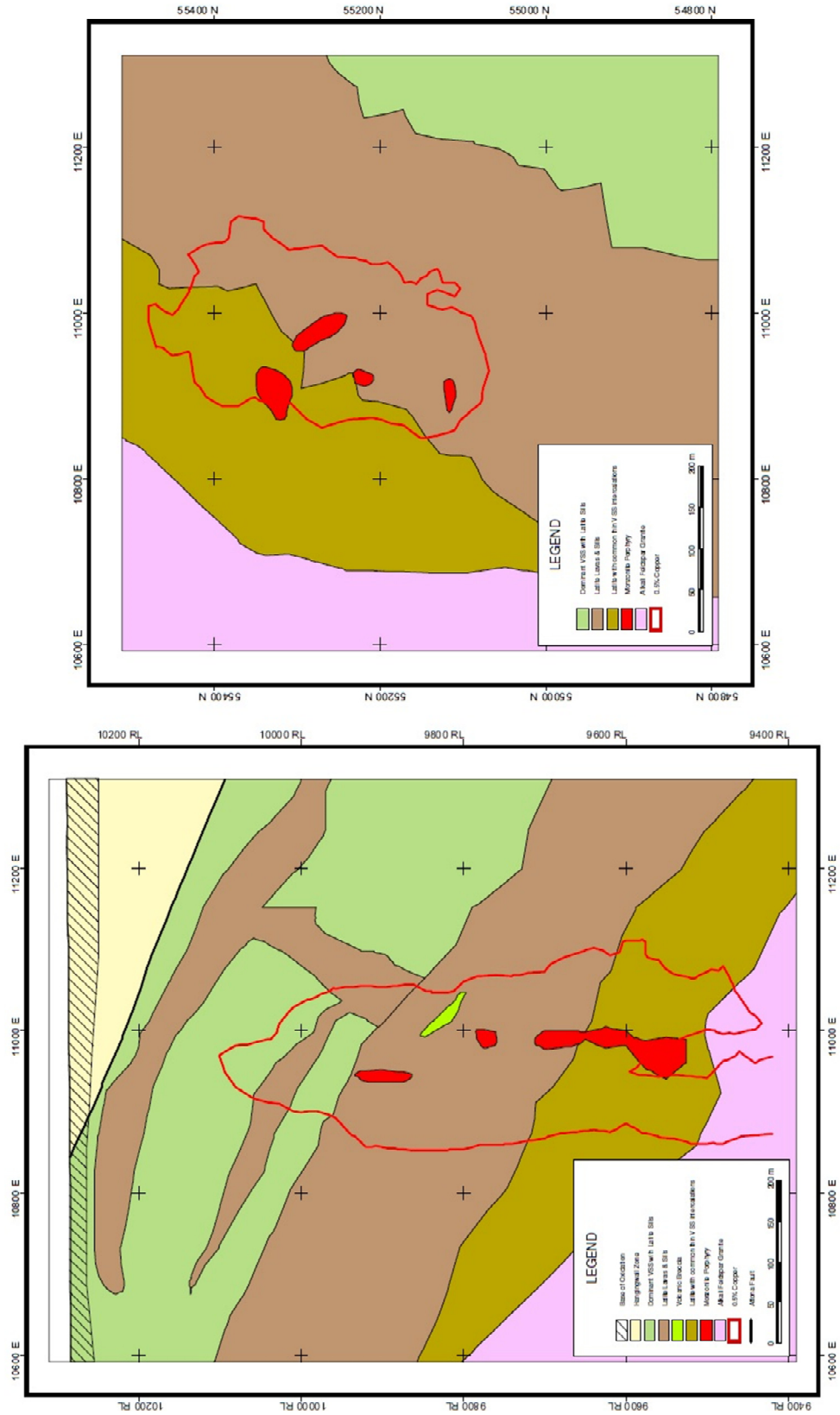
Figure 96: West-East section (left) and plan view at 9700m RL of the geology of E48 (Hendrawan, 2011)

The volcanic sequence is vertically intruded by a multistage, finger-like, light-pink to cream-yellow Quartz Monzonite Porphory (POR) of up to 20m wide in a north south plane and 50m wide in the east west direction. Most porphyries have sheared and faulted margins and can be indicated by the presence of bornite and / or quartz clots. Figure 97 shows a POR core sample retrieved from the extraction level.

Figure 97: Quartz Monzonite Porphyry core sample from a depth of 575.15m (Hendrawan, 2011)

The faulted, quartz-sericite shear zones (FQS) overprint all lithologies. They are narrow and steeply-dipping with a strike of approximately 75°, sub-parallel to the extraction drives. They can be characterised by a central crushed, brecciated zone surrounded by numerous shears and joints and quartz-sericite-carbonate-pyrite alteration. The shear zones were believed to be up to 15 m wide (van As, 2004), with an even wider area of influence, but re-logging revealed that they were only 0.5 to 1 metre wide. (Hendrawan, 2011) The true spacing of the shear zones is 60 – 90 m outside the mineralised zone and 10 – 30 m inside the mineralised zone.

10.3.3 Rock Mass Characterisation

The scope of this thesis project requires a GSI rock mass classification in order to work with the Hoek-Brown and the S-shaped failure criterion. The E48 rock mass has not been classified by the GSI classification system, because it is less preferable than Laubscher's MRMR, the Q-system and Bieniawski's RMR_{76} when quickly estimating support requirements (Talu, pers. comm., 2013). It is considered very useful though to obtain input parameters for modelling purposes.

There have been three small drilling campaigns in the 1990's and a more recent campaign in 2004 which resulted in high quality logging. Figure 98 shows the cumulative frequency distribution of RQD values of four lithology units, with the lowest values in the FQS domain. The average RQD from the 2004 campaign was approximately 91%. There are five dominant fracture sets, three sub-vertical and two sub-horizontal sets. A Fracture Frequency of 3-20 fractures per meter indicates a highly jointed rock mass. (van As, 2004)
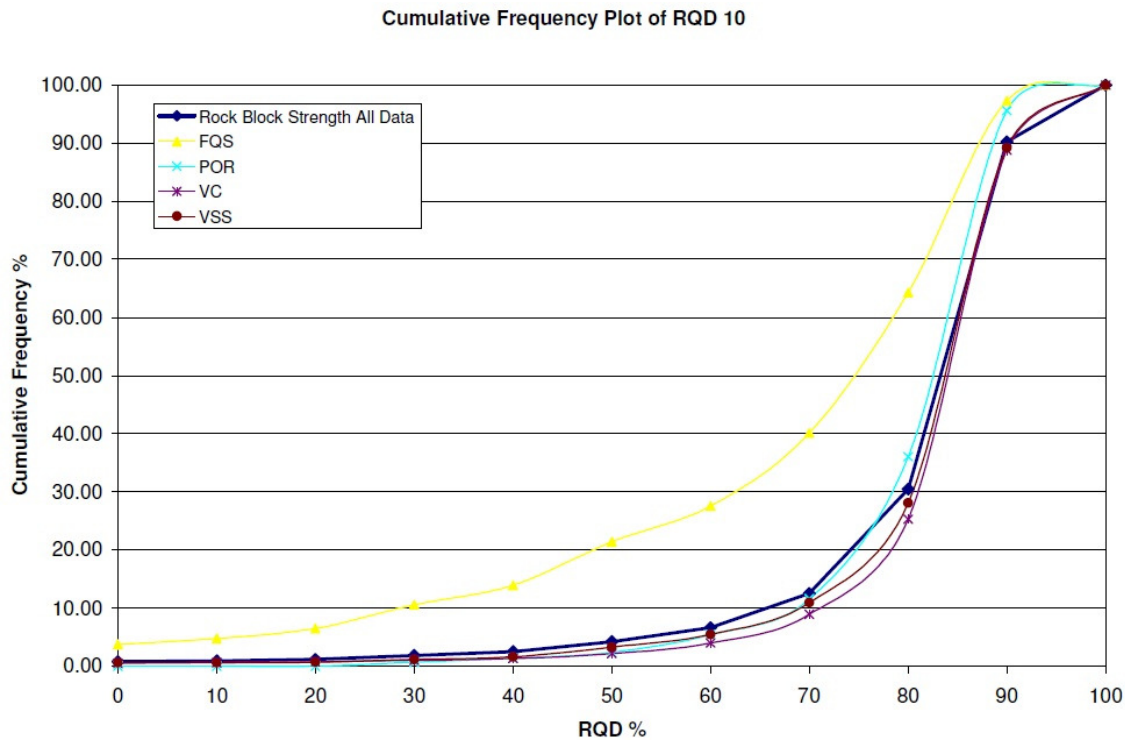
Figure 98: RQD Cumulative frequency plot (van As, 2004)

Statistical data, derived from thorough drill core analysis, was used in geotechnical block models. These block models used the three previously described classification schemes as rating parameters. There was small variance in data and the results of the different geotechnical block models corresponded. The block model that uses the MRMR classification scheme was performed in great detail and resulted in two geotechnical domains. A fairly isotropic host rock (containing LTE, VSS and POR) and FQM shear zones. At Northparkes, the RMR_{76} system was used exclusively to retrieve input parameters for $FLAC^{3D}$. The GSI used as initial input for the $FLAC^{3D}$ model will be based solely on the RMR_{76} study that was designed for this purpose. Table 13 shows the rock mass classification and its spread as a result of the block modelling. According to equation 4.3, a GSI value of 59 will be selected as an input parameter for $FLAC^{3D}$. Equation 4.5 verifies the correspondence between the Q-index and RMR_{76} results when Q-values from the block model are used. (van As, 2011)

Table 13: Geotechnical block modelling results

	Q	MRMR	RMR_{76}
Minimum	1	38	49
Maximum	15	70	70
Mean	4	56	59

10.3.4 *In situ* stress field

Five HI cell measurements were done in the access decline towards E48 lift 1. At a later stage, two ANZI stress cell measurements and other overcoring methods were used to define the *in situ* rock stress in Extraction Drive 6. All methods verified findings from earlier studies and showed a sub-horizontal major principal stress. The principal stresses have lower magnitudes than stresses in the E26 ore body. Table 14 depicts the current principal stress components.

Table 14: Principal stress components E48 lift 1 (van As, 2011)

	Magnitude	Dip	Bearing
σ_1	41 MPa	08°	290°
σ_2	20 MPa	11°	022°
σ_3	12 MPa	76°	165°

The geotechnical team at NPM confirms these principal *in situ* stresses and uses the exact same values for modelling purposes nowadays (Samosir, pers. comm., 2013). Principal stress components are mutually perpendicular and can describe the combined stress state without any shear stress components. The pre-mining stress state has to be converted to a Cartesian system in order to set initial and boundary conditions in FLAC^{3D}. The same stress state as in Table 14 can be represented by Cauchy's 3 x 3 stress tensor, equation 10.4. The conservation of angular momentum implies symmetry and thus equation 10.5 is valid.

$$\begin{bmatrix} \sigma_{xx} & \tau_{xy} & \tau_{xz} \\ \tau_{yx} & \sigma_{yy} & \tau_{yz} \\ \tau_{zx} & \tau_{zy} & \sigma_{zz} \end{bmatrix} \qquad\qquad 10.4$$

$$\tau_{xy} = \tau_{yx} \quad ; \quad \tau_{xz} = \tau_{zx} \quad ; \quad \tau_{yz} = \tau_{zy} \qquad\qquad 10.5$$

The extraction drives are orientated east-west, approximately in the direction of 78° (visible in appendix M). An in-house function of the numerical code Map^{3D} (Table 4 in section 8.1) is used to transform the principal stresses to the Cartesian system (Samosir, pers. comm., 2013). However, the model used in Map^{3D} is turned 90° around the z-axis compared to the coordinate system of FLAC^{3D}. For example, in Map^{3D} σ_{xx} is orientated parallel to the Extraction Drives and σ_{yy} is orientated perpendicular to the Extraction Drives. While in FLAC^{3D} σ_{yy} is orientated parallel to the Extraction Drives and σ_{xx} is orientated perpendicular to the Extraction Drives. Figure 99, on the next page, can be used to inspect the transformation of units while the model (in this case the cube) remains on its position and the coordinate system along with all the stress units is turned 90° counter-clockwise around the z-axis when looking down upon the x-y plane. A positive shear stress points in the positive direction of the coordinate axis of the second subscript if it acts on a surface with an outward normal in the positive direction. Conversely, if the outward normal of the surface is in the negative direction, then the positive shear stress points in the negative direction of the coordinate axis of the second subscript.
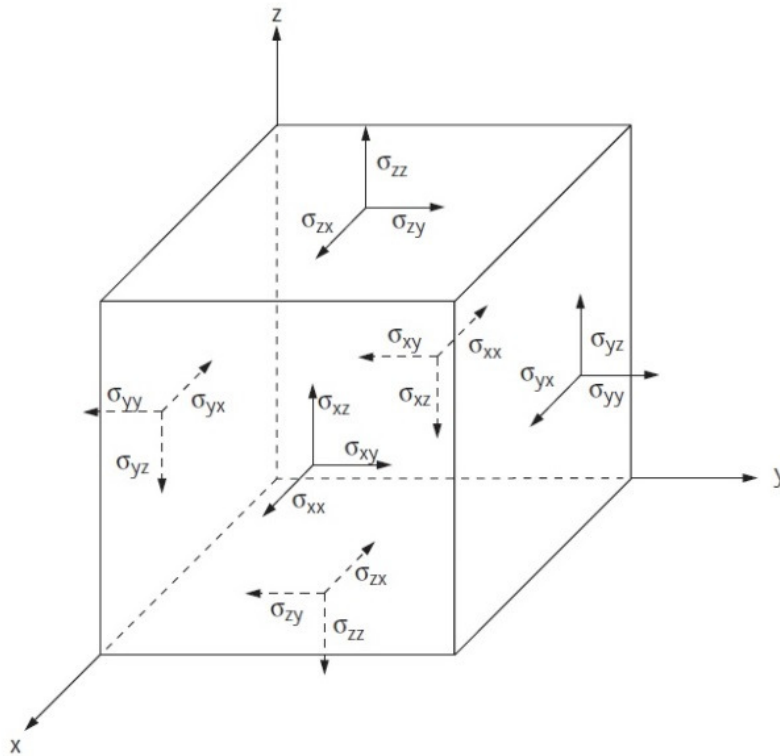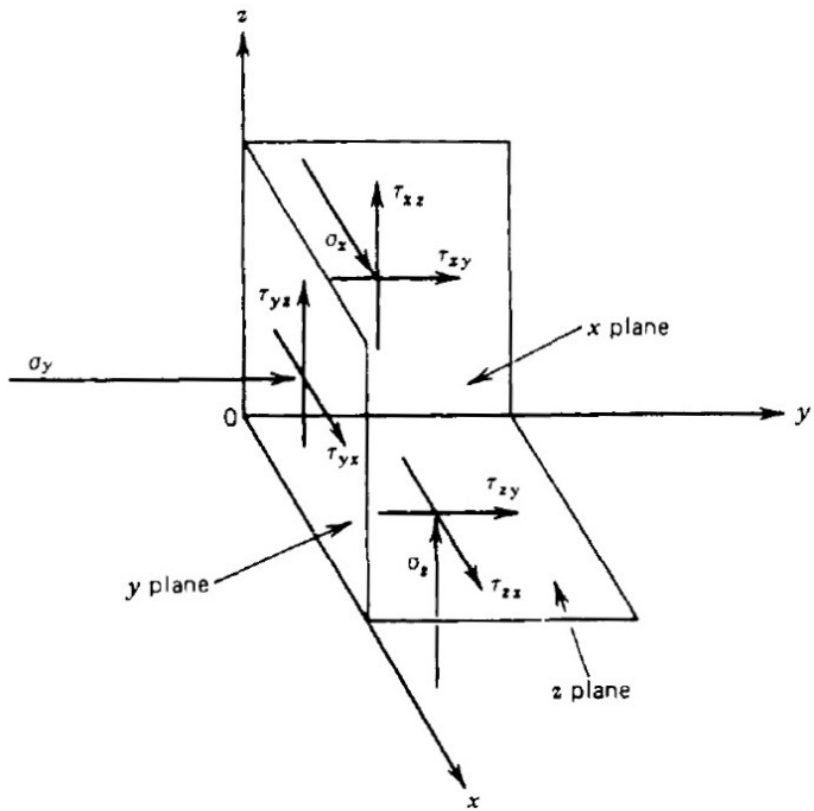
Figure 99: Illustrations of Cauchy's stress tensor in MAP³ᴰ (top) and FLAC³ᴰ (bottom). (Itasca Consulting Group, Inc., 2013)

Another difficulty is that MAP³ᴰ indicates compression with positive stresses while FLAC³ᴰ indicates compression with negative stresses. This applies on normal stresses and shear stresses. Table 15 shows the Cartesian stress state in both software packages.

Table 15: Cartesian stress state E48 lift 1

	Map³ᴰ		FLAC³ᴰ
σ_{xx}	38.2 MPa	σ_{yy}	-38.2 MPa
σ_{yy}	22.0 MPa	σ_{xx}	-22.0 MPa
σ_{zz}	12.9 MPa	σ_{zz}	-12.9 MPa
τ_{xy}	-6.5 MPa	τ_{yx}	-6.5 MPa
τ_{yz}	-2.8 MPa	τ_{xz}	2.8 MPa
τ_{xz}	3.2 MPa	τ_{yz}	3.2 MPa
$\Delta\sigma_{xx}$	-0.063656 MPa / m	$\Delta\sigma_{yy}$	0.063656 MPa / m
$\Delta\sigma_{yy}$	-0.036706 MPa / m	$\Delta\sigma_{xx}$	0.036706 MPa / m
$\Delta\sigma_{zz}$	-0.021438 MPa / m	$\Delta\sigma_{zz}$	0.021438 MPa / m
$\Delta\tau_{xy}$	0.010842 MPa / m	$\Delta\tau_{yx}$	0.010842 MPa / m
$\Delta\tau_{yz}$	0.004641 MPa / m	$\Delta\tau_{xz}$	-0.004641 MPa / m
$\Delta\tau_{xz}$	-0.005334 MPa / m	$\Delta\tau_{yz}$	-0.005334 MPa / m

As shown in equation 10.6, the vertical stress is not consistent with the overburden pressure.

$$\rho \cdot g \cdot h = 2710 \cdot 9.8 \cdot 580 = 15.4 \, MPa \qquad \text{10.6}$$

The density of overlying strata is assumed to be equal to the rock mass density at the extraction level. This assumption is supported by the vertical cross-section in Figure 96. This figure shows that rock of similar density overlies the extraction level. A back-calculation from the vertical stress stated in Table 15 results in a rock mass density of 2,267 kg/m^3. This value is too low to be representative of the overlying strata (Strata Testing Services, 2004). The difference cannot be subscribed fully to a Poisson's effect of sub-horizontal tectonic stresses 'pushing' up the rock mass, because of the relative shallow depth of the extraction level. If the resulting upward stress was this high, the ground surface would rise slightly (Bertotti, pers. comm., 2013).

Multiple attempts have been made to initialize the *in situ* stress according to the full stress tensor, but results were unsatisfying time after time. The relatively close spacing of the boundaries causes significant displacements which develop unrealistic stresses at the initial equilibrium stage or while excavating. A true representation of the full stress state is still considered a challenge throughout the industry. Besides, stress measurements contain significant margins of error in both magnitude and orientation. (Lavoie, pers. comm., 2013b)

Finally, the vertical stress is represented by the lithostatic stress to overcome issues mentioned in the paragraphs above. The two horizontal stress components are calculated using stress ratios, see equations 10.7 and 10.8, taken from Table 15.

$$X_{\text{kfac}} = \frac{\sigma_{xx}}{\sigma_{zz}} = 1.7054 \qquad \text{10.7}$$

$$y_{\text{kfac}} = \frac{\sigma_{yy}}{\sigma_{zz}} = 2.9612 \qquad \text{10.8}$$

10.3.5 Intact rock properties

The intact rock strength, Young's modulus and Poisson's ratio are summarised in Table 16. Hoek-Brown m_i values have been obtained by triaxial testing and are listed in Table 17. These parameters have been successfully applied in a Synthetic Rock Mass study performed by Itasca Consulting Group, Inc. (Pierce, 2006)

Table 16: Intact rock properties per lithological unit (van As, 2004)

	LTE	FQS	VSS	POR
Mean measured UCSi (MPa)	90	90	120	120
Young's Modulus E_s (GPa)	55	55	55	55
Poisson's ratio v	0.11	0.11	0.22	0.17

Table 17: Hoek-Brown m_i values per lithological unit (van As, 2004)

	Min (MPa)	Max (MPa)	Median (MPa)	Mean (MPa)	S. Dev. (MPa)
POR	4.04	49.30	25.00	25.70	17.72
LTE	18.13	37.50	26.30	27.00	13.98
VSS	10.86	28.05	20.20	20.50	11.97
FQS	12.34	21.06	18.99	17.46	4.56

Intact rock properties from an evaluation report of undercut and drawbell blast designs are in line with the tables above (Onederra, 2008). The average properties used in their evaluation (Table 18) give a good indication of the input parameters for the numerical model to be created.

Table 18: Parameters used in evaluation of undercut blasting (Onederra, 2008)

Strength *UCS*	90-120 MPa
Tensile strength T_s	8-10 MPa
Young's modulus E_s	55 GPa
Density ρ	2710 kg/m^3

10.3.6 Residual rock properties

The GSI value, and thus the Hoek-Brown strength parameters, are related to the block volume of the rock mass (V_b) and the joint condition (J_c) by equation 10.9. This function is based on surface fitting techniques and is visualised in Figure 100. (Cai & Kaiser, 2006)

$$GSI = \frac{26.5 + 8.79 \cdot \ln J_C + 0.9 \cdot \ln V_b}{1 + 0.0151 \cdot \ln J_C - 0.0253 \cdot \ln V_b} \qquad \text{10.9}$$
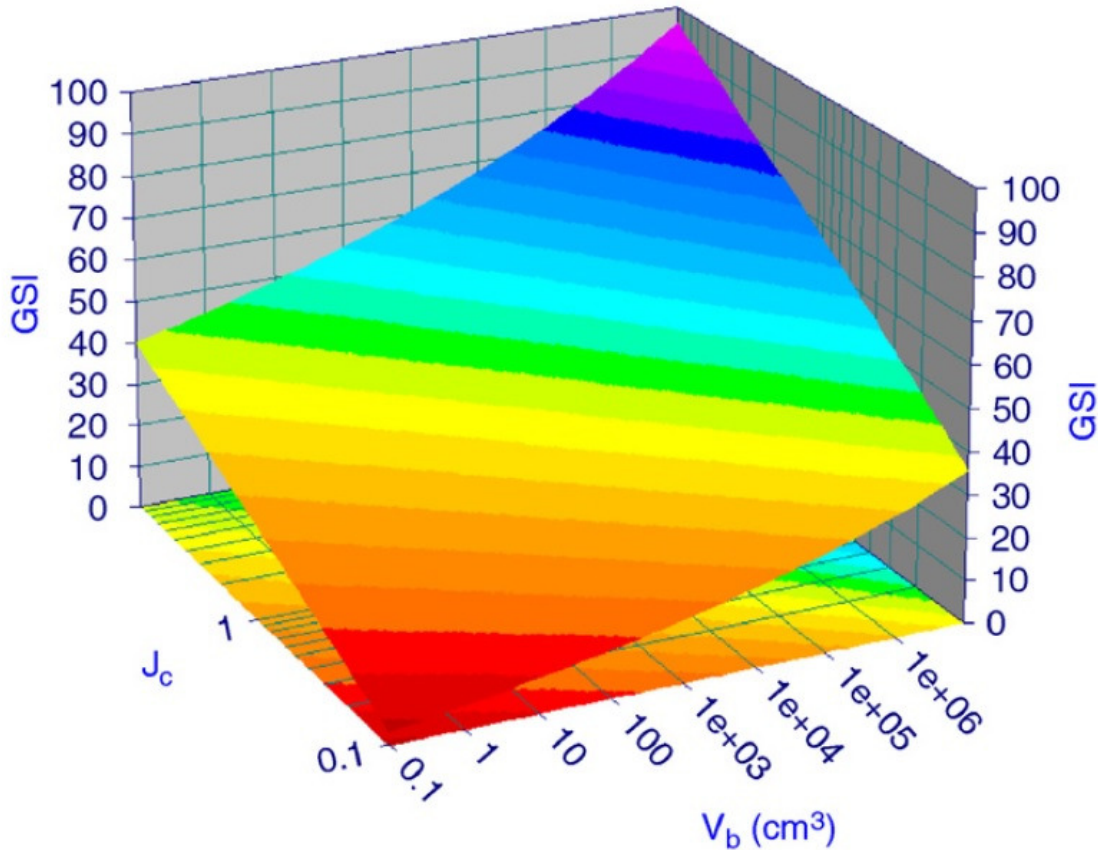
Figure 100: Graphical representation of equation 10.9. (Cai & Kaiser, 2006)

The GSI value reduces gradually from its peak value to a residual GSI_r value. The actual behaviour related to plastic strain is currently unknown, but it is commonly termed strain softening of the rock mass. This behaviour describes the gradual loss of load-bearing capacity of a material and is referred to as strength weakening in hard rocks. The relation between the peak GSI and the residual GSI_r is dependent on the quality of the rock mass. An empirical relation between the two parameters is shown in equation 10.10 where the assumption is made that for very weak rock masses $GSI_{r\ emp} = GSI$. It should be noted that this equation is designed for rock masses dominated by shear failure mechanisms and that the rock mass at Northparkes exhibits brittle failure at low confining pressures and shear failure at higher confinement. (Cai & Kaiser, 2006)

$$GSI_{r\ emp} = GSI \cdot e^{-0.0134 \cdot GSI} \qquad \text{10.10}$$

A more geotechnical approach would be to obtain the GSI_r from post-peak block volume (V_b^r) and joint conditions (J_c^r). These parameters can be obtained from field mapping and borehole logging data. The residual strength range is reached between 5 to 10 times the strain at peak load (ε_{peak}). The residual $GSI_{r\,geotech}$ can be used to calculate residual values for the generalised Hoek-Brown parameters m_r, s_r and a. Equations 10.11 to 10.14 show that the way of calculating these values is similar to functions for peak load conditions.

$$GSI_{r\,geotech} = \frac{26.5 + 8.79 \cdot \ln J_c^r + 0.9 \cdot \ln V_b^r}{1 + 0.0151 \cdot \ln J_c^r - 0.0253 \cdot \ln V_b^r} \qquad \text{10.11}$$

$$m_r = m_i \cdot e^{\left(\frac{GSI_r - 100}{C_m}\right)} \qquad \text{10.12}$$

$$s_r = e^{\left(\frac{GSI_r - 100}{C_s}\right)} \qquad \text{10.13}$$

$$a_r = \frac{1}{2} + \frac{1}{6}\left(e^{-GSI_r/15} - e^{-20/3}\right) \qquad \text{10.14}$$

Block size is determined by joint spacing, joint orientation, the number of joint sets and joint persistence. In other words, it is a volumetric expression of joint density. Fracture frequency rates of 3 – 20 fractures per meter indicate a joint spacing of 5 – 33 cm. Thus, the E48 rock mass can be described as very blocky according to Figure 26 in section 4.2.4. The relating block volumes are in the order of 100 to 30,000 cm^3. In general, the residual block volumes are independent of the original block volumes. If peak block volumes are greater than 10 cm^3, the residual block volume of the disintegrated rock mass is always 10 cm^3. (Cai & Kaiser, 2006)

The residual joint surface condition factor (J_c^r) is defined as in equation 10.15 as a function of residual large-scale waviness (J_W^r), residual small-scale smoothness (J_S^r) and the residual joint alteration factor (J_A^r).

$$J_c^r = \frac{J_W^r \cdot J_S^r}{J_A^r} \qquad \text{10.15}$$

Appendix S contains three tables that list the ratings for the parameters in equation 10.15 at peak load. Most discontinuities are planar or slightly undulating structures and the joint surfaces are smooth or slightly rough, indicating low frictional resistance. The majority of infill is quartz, sericite or carbonate. The last two are fairly weak minerals, but the quartz veins can also act as planes of weakness due to secondary infill. The infill thickness is between $1 - 5$ mm. This is interpreted by the author as a coating / thin filling of frictional material without clay. (van As, 2004) Table 19 shows the resulting values for the three parameters at peak load and their residual parameters calculated with equations 10.16 to 10.18 (Cai & Kaiser, 2006). The values of J_W and J_S fall below their threshold, any variances would have a minimal impact on J_c^r. On the other hand, the value of J_A has a big impact on J_c^r and thus on the residual Hoek-Brown parameters. Therefore, the interpretation of the joint alteration has been verified by Atkins (pers. comm., 2013). The resulting value for the residual joint surface condition factor is 0.25.

$$ if \ \frac{J_W}{2} < 1 \quad J_W^r = 1 \quad else \quad J_W^r = \frac{J_W}{2} \qquad \text{10.16} $$

$$ if \ \frac{J_S}{2} < 0.75 \quad J_S^r = 0.75 \quad else \quad J_S^r = \frac{J_S}{2} \qquad \text{10.17} $$

$$ J_A = J_A^r \qquad \text{10.18} $$

Table 19: Peak and residual values for parameters of the Joint Surface Condition.

	Peak	Residual
J_W	1.0-1.5	1
J_S	1.0-1.5	0.75
J_A	3	3

The $GSI_{r \ geotech}$ value based on the above calculations is 18, a significantly lower number than the $GSI_{r \ emp}$ value of 27. The resulting residual Hoek-Brown strength parameters are listed in Table 20. It is recommended to use the $GSI_{r \ geotech}$ value over the $GSI_{r \ emp}$ value. (Cai, *et al.*, 2007)

Table 20: Results of residual rock mass properties

	Geotechnical	Empirical
GSI_r	18	27
m_r	1.283	1.755
s_r	0.0001	0.0003
a_r	0.550	0.528

10.3.7 Rock mass properties

The best estimate of the Young's modulus for the rock mass is based on the Young's modulus of intact rock samples and the quality of the rock mass (equation 6.9). The rock mass is undisturbed at this stage and its Young's modulus can be calculated as in equation 10.19.

$$ E_{rm} = 55 \cdot \left(0.02 + \frac{1}{1 + e^{\frac{60-59}{11}}} \right) = 27.35 \ GPa \qquad \text{10.19} $$

The average Fracture Frequency is 4.5, representing a mean joint spacing of approximately 20 cm. The rock samples tested for the E48 Evaluation Study were 50 mm in diameter. Therefore, the σ_{UCS} values obtained in the laboratory should be corrected according to Figure 43. $\sigma_c = 80\%$ (200 mm 'specimens') of the values listed in Table 16 and thus will be in the range of 72 – 96 MPa. (Pierce, 2006)

The Poisson's ratios of the lithological units (Table 16) are relatively low in comparison with calculation results from equation 6.11 ($v = 0.23$). Nevertheless, the initial Poisson's ratio will be based upon the laboratory test results in Table 16.

Hoek & Brown (1997) indicate that the dilation angle is one eighth of the friction angle for average quality rock masses of approximately GSI = 50. The use of software package RocLab results in $\phi = 40.8°$ when a Mohr-Coulomb curve is fitted to the Hoek-Brown failure criterion in the range of $0 < \sigma_3 < 22.5\ MPa$. This indicates a dilation angle of 5°. According to Figure 49, the dilation angle should be half of the friction angle, around 20°. After an analysis of similar rock types, the author chose for a value of $\psi = 10°$. This is in accordance with estimates of Sainsbury (2007) for his comparison between post- and advanced undercutting strategies for E48; of $\psi = 9.3°$.

10.3.8 Caved rock

Bulking and dilation accompany softening of the rock. To ensure mass conservation, the corresponding decrease in density and elastic modulus must be accounted for. The dry density of caved rock depends on the porosity and the solid density of *in situ* rock. Areas in the cave that move frequently due to production from the drawbells are lower in density than stagnant areas, but an averaged bulk density as described by equation 10.20 is safe to assume.

$$\rho_d = \frac{\rho_s}{BF}$$

10.20

Parameter	Unit	Meaning
ρ_d	Kg/m3	Dry density of caved rock
ρ_s	Kg/m3	Solid density of *in situ* rock
$BF = 1 + \dfrac{n}{(1-n)}$	-	Bulking Factor
n	-	Porosity

This formula expresses the volumetric changes that accompany bulking. Dilatancy depends on the plastic shear strain, confining stress, porosity and particle size. These relations are discussed in detail in section 6.3.2. Dilation angles are commonly in the range of 5° to 15°, 10° is considered the best starting value for caved rock. The best estimate of Poisson's ratio for caved rock is 0.25 (Lorig & Pierce, 2000). Board and Pierce (2009) supported these findings and attributed zero cohesion and an internal friction angle of 42° for the caved rock. The friction angle decreases with increasing particle size and at a decreasing rate with increasing confining pressure.

Multiple regression analysis is a tool to select independent variables that determine the value of a dependent variable. Pappas & Mark (1993) established a relation for the Elastic Modulus (tangent and secant) of caved rock after reviewing longwall gob material. The general format of the relation is expressed in equation 10.21. The elastic Modulus is a function of the rock strength in psi (x_1) and the thickness-to-width shape ratio of the caved rock (x_2) for a range of Bulking Factors (BF). The Elastic Modulus is positively correlated to x_1 and x_2 and negatively correlated to the Bulking Factor. The Bulking Factor used by Pappas & Mark (1993) differs from the general industry Bulking (B) factor ($BF = 1 + B$). The thickness-to-width shape ratio can be obtained from Figure 101, 0.5 is a suitable value for caved rock in block caving operations. (Lavoie & Pierce, 2011a)

$$E = c_{x1} \cdot x_1 + c_{x2} \cdot x_2 - c_{x3} \qquad \text{10.21}$$
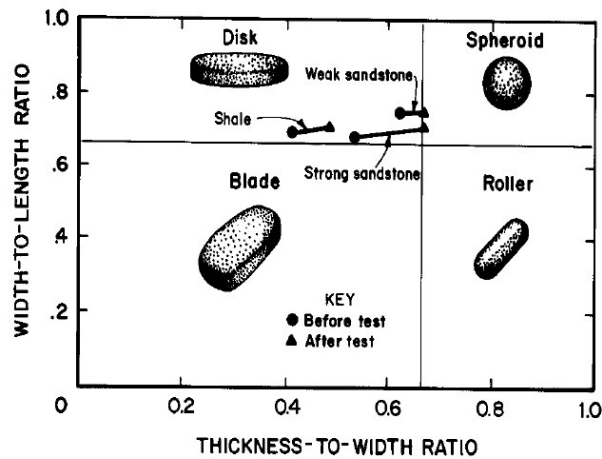
Figure 101: Thickness-to-Width ratio (X_2) (Pappas & Mark, 1993)

Another multiple regression analysis should be performed to link the Bulking Factor to overburden pressure. The independent variables selected by the analysis are again the rock strength and the thickness-to-width shape ratio. The overburden pressure is 15.4 MPa (equation 10.6) which is equivalent to 2,234 psi according to equation 10.22. Since the vertical stress is lower than the overburden pressure (section 10.3.4), the equation for 2,000 psi is selected from Table 21. The resulting Bulking Factor $BF = 1.30$. (Pappas & Mark, 1993)

$$1 \, psi = 6894.8 \, Pa \qquad \qquad \text{10.22}$$

Level	Multiple regression equations
BULKING FACTOR (BF) AT VARIOUS STRESS LEVELS (σ)	
σ = 400 psi	BF = 0.0000184X1 + 0.267X2 + 1.16
σ = 600 psi	BF = 0.0000203X1 + 0.274X2 + 1.06
σ = 800 psi	BF = 0.0000187X1 + 0.262X2 + 1.04
σ = 1,000 psi	BF = 0.0000185X1 + 0.269X2 + 0.992
σ = 1,500 psi	BF = 0.0000160X1 + 0.209X2 + 1.00
σ = 2,000 psi	BF = 0.0000150X1 + 0.221X2 + 0.963
σ = 2,500 psi	BF = 0.0000136X1 + 0.247X2 + 0.931
TANGENT (E_t) MODULUS AT VARIOUS BULKING FACTORS (BF)	
BF = 1.25	E_t = 2.49X1 + 41,200X2 − 24,800
BF = 1.30	E_t = 1.76X1 + 23,800X2 − 15,700
BF = 1.35	E_t = 1.32X1 + 16,300X2 − 11,400
BF = 1.40	E_t = 0.933X1 + 11,300X2 − 7,900
BF = 1.50	E_t = 0.568X1 + 6,900X2 − 5,000
SECANT MODULUS (E_s) AT VARIOUS BULKING FACTORS (BF)	
BF = 1.25	E_s = 0.539X1 + 10,400X2 − 5,340
BF = 1.30	E_s = 0.445X1 + 7,760X2 − 4,160
BF = 1.35	E_s = 0.348X1 + 5,580X2 − 2,750
BF = 1.40	E_s = 0.283X1 + 4,900X2 − 2,300
BF = 1.50	E_s = 0.348X1 + 5,580X2 − 2,750

The estimates of the porosity of caved rock have changed since a decade ago. Lorig & Pierce (2000) reckoned the porosity of caved rock to be between 0.2 and 0.4. Recently, Pierce (2010) conducted a literature review and suggests that the maximum porosity of angular rock fill is in the range of 0.4 to 0.5. These maximum porosities are typical in caving simulations and lead to a Bulking Factor in the range of $BF = 1.67 - 2.0$. New analyses had to express the relation between the elastic Modulus, rock strength and thickness-to-width ratio since there are no multiple regression equations for this range in Table 21. The analysis showed that the constants in equation 10.21 are functions of the Volumetric Strain Increment (VSI). The new constants in equation 10.23 to 10.25 make sense if the trends in Table 21 are followed for increasing Bulking Factors. Based on past experience, $VSI = 0.67$ is used for all rock masses. (Lavoie, pers. comm., 2013a)

$$c_{x1} = 0.1316 \cdot VSI^{-2.145} = 0.31 \qquad \qquad \text{10.23}$$

$$c_{x2} = 1110.5 \cdot VSI^{-2.574} = 3,113 \qquad \qquad \text{10.24}$$

$$c_{x3} = 981.14 \cdot VSI^{-2.318} = 2,483 \qquad \qquad \text{10.25}$$

The resulting rock mass elastic Modulus is depicted in equation 10.26. The value is lower than elastic moduli of rockfill in references by Lorig & Pierce (2000), Ortiz *et al.* (1986), Duncan *et al.* (1980) and Marachi *et al.* (1972) which are typically in the range of $E_{CR} = 50 - 250\ MPa$ and related to confinement.

$$E_{CR} = \left(0.31 \cdot \frac{102 \cdot 10^6}{6894.8} + 3{,}113 \cdot 0.5 - 2{,}483\right) \cdot 6894.8 = 25.2\ MPa \qquad 10.26$$

10.3.9 Results

The continuum model in FLAC[3D] does not contain domains based on lithology or rock mass classification. Every grid cell has the same input parameter and therefore each input parameter does not represent a lithological or stratigraphic unit, but represents the average rock mass response. The dominance of latite will be translated into the initial input parameters by assigning a double weight when calculating the weighted average of all lithological units. Table 22 and Table 23 contain the initial input parameters for the E48 rock mass at 9700m RL.

Table 22: Rock mass properties

Density (kg/m³)	Dilation (°)	Poisson Ratio	$m_{bresidual}$	$s_{residual}$	$a_{residual}$	GSI	mi	UCSi (MPa)	Ei (GPa)
2710	10	0.14	1.283	0.0001	0.55	59	24	81.6	27.35

Table 23: Caved rock properties

Density (kg/m³)	Dilation (°)	Poisson Ratio	Volumetric Strain Increment	$E_{CR}\ (MPa)$
1491	10	0.25	0.67	25.2

10.4 Scenarios

An unbiased comparison between the generalised Hoek-Brown (HB) and the S-shaped (S) failure criterion is one that relies on identical input parameters. Two base case scenarios are built with the input parameters from subsection 10.3.9 and a threshold of 1% horizontal closure strain at half of the monitoring stations to stop the loading stage and start unloading of the model. The only extra parameter that is needed for the S-shaped failure criterion is a value for the parameter M, which controls the degradation rate above the spalling limit. The base case scenario uses $M = 80$, argued in subsection 7.4.2. A sensitivity analysis is performed on this parameter in section 11.4. The parameter M is increased and decreased by 20% to show its effect on the rock mass response in the model.

The two base case scenarios might result in different abutment stresses. It would be interesting to see how the rock mass behaves according to the S-shaped failure criterion when the abutment stress is similar to the HB base case. Therefore, the abutment stress from the HB base case is used as stage control in a simulation of the rock mass according to the S-shaped failure criterion. All scenarios are summarised in Table 24.

Table 24: Summary of simulation scenarios

Indication	Stage control	M
HB base case	Horizontal closure strain	-
S base case	Horizontal closure strain	80
S_{abut}	Abutment stress	80
S_{64}	Horizontal closure strain	64
S_{96}	Horizontal closure strain	96

11 Results and Interpretation

This chapter discusses all modelling results and compares the different scenarios, previously discussed, with each other. The first section of this chapter shows the results, and methods used to acquire them, of simulated relative displacements in the back of the extraction drifts for each scenario. Appendix U should be consulted for all the relative displacement graphs. The significance of these results is discussed in the remaining sections. Section 11.2 compares the two base case scenarios and includes a simulated triaxial test in FLAC^{3D}. Section 11.3 shows the results of a comparison between the two scenarios that use the same abutment stress threshold as stage control, *i.e.* the HB base case scenario versus the S_{abut} scenario. Section 11.4 shows the sensitivity of the results to the value of the parameter M. Finally, the vertical and major principal stresses at the top of the model, the centre of the major apex and the centre of the minor apex are plotted versus the horizontal closure strain in section 11.5. The most important results will be summarized and formulated as concise conclusions in chapter 0.

All graphical modelling results, except the simulated relative displacement plots, are put together in Appendix T. It contains horizontal cross-sections of the model showing the Hoek-Brown s parameter, apparent cohesion, plasticity state and major principal stress. These parameters indicate the damaged and stressed zone in the pillar for each scenario. According to Lavoie and Pierce (2011), the Hoek-Brown s parameter normally shows cohesion-weakening of the rock mass that is independent of confinement. However, the Hoek-Brown s parameter in the S-shaped failure criterion has been made dependent of confinement. The apparent cohesion is always dependent of confinement and obtained by fitting a tangent to the failure envelope at the local confinement level. The meaning of the plasticity state speaks for itself and the major principal stress indicates the magnitude and concentration of stress in the pillar. The left side of the figures show the model state after the loading stage, *i.e.* at the maximum abutment stress, while the right side of the figures shows the model state after the unloading stage, *i.e.* in the stress-shadow. Unfortunately, the colours on both sides indicate different values, so the legends should be used at all times. In between the unloading and re-loading stage, *i.e.* the cave load, no changes were made to the excavations, because a post undercut strategy is applied. The differences in results between these stages were minimal and modelling results after re-loading are therefore not included. Furthermore, plots of the abutment stress and horizontal closure strain versus calculation steps are included for all scenarios, as well as major principle stress magnitudes in the major and minor apex versus the horizontal closure strain.

11.1 Relative displacements

The MPBX stations at block E48 were installed relatively shortly before or during undercut development. Displacements that are the effect of the development of tunnels at the extraction level are therefore not measured, since the MPBX are installed afterwards. The measured displacement is what is referred to as 'mining-induced deformation' in Figure 85. The 'timing' of MPBX installation during mine development has to be adopted in the simulation in order to compare them. This explains the lack of data in the first thousands of calculation steps in all relative displacement plots in appendix U. These initial calculation steps represent development of the drifts and draw bells.

There are two locations where extensometers are virtually installed to investigate the importance of the position of the instrument along the extraction drift. They are installed vertically in the centre of the back, 4.5 meters above the extraction level floor. Figure 102 shows the location of the two virtual extensometers in a horizontal cross-section of the numerical model. Location 'MPBX1' is at the cross-section of the centre line of the extraction drift and the centre line of a drawpoint drift. Location 'MPBX2' is right in between such a cross-section and the next cross-section with the centre line of a drawpoint drift on the opposite side of the extraction drift. These two locations represent the extremities of spans along the extraction drift and should indicate the degree in which the span at the location of the extensometer influences the relative displacements. The results are discussed in subsection 11.1.4.
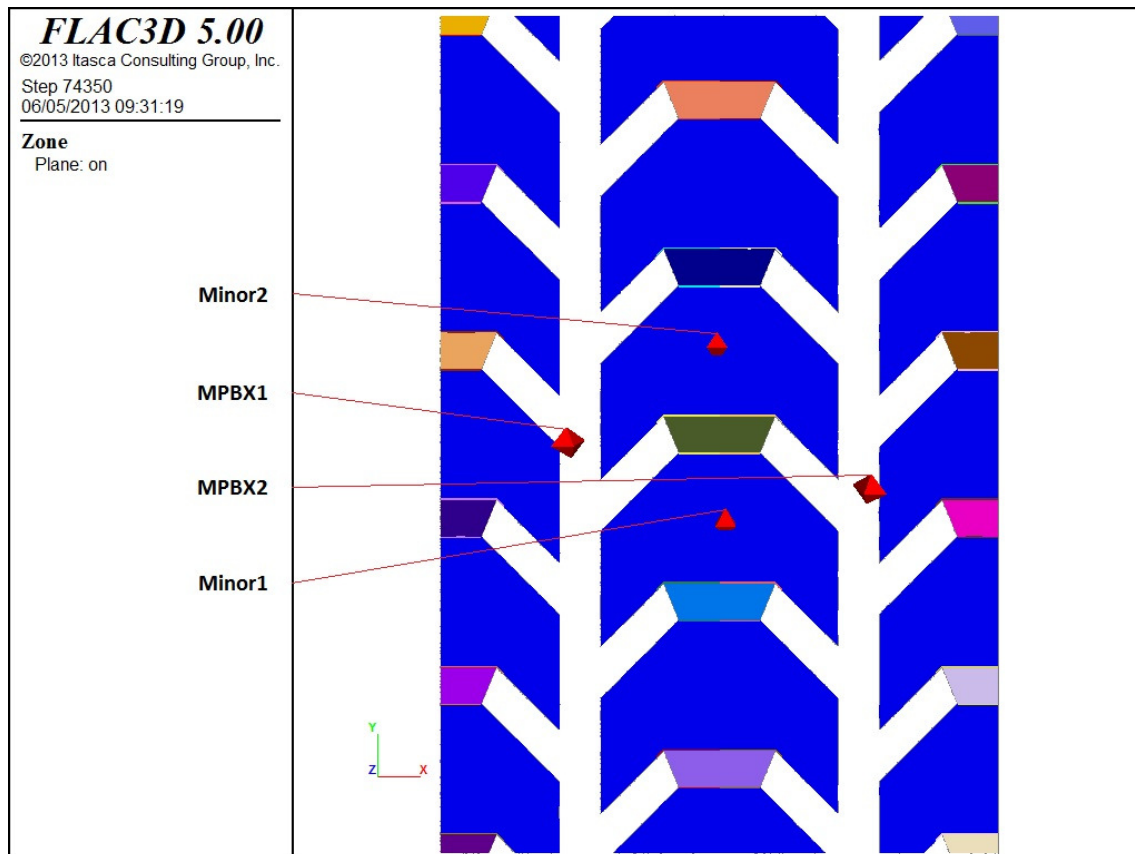
Figure 102: Location of 'MPBX1', 'MPBX2' and history points in the minor and major apices.

11.1.1 Initial calculation

The relative displacement between the instrument head H and target T was calculated according to equation 11.1. The relative displacement at the moment of installation was subtracted to exclude displacements of the history points until the moment of installation. It has to be emphasized that the distance between the anchors is not exactly $10/6$ meter, because the nearest grid point at that location has to be used as a history point. Therefore, the anchors are also not located along an exact vertical line. However, this does not affect relative displacements to a significant extent.

$$rdisp = \sqrt{(xdisp_h - xdisp_T)^2 + (ydisp_h - ydisp_T)^2 + (zdisp_h - zdisp_T)^2} \quad \text{11.1}$$

The result from equation 11.1 is an absolute value, making it impossible to distinguish contraction and dilation in contrast to the working of linear potentiometers in real extensometers, section 9.1. The resulting displacement graphs were therefore not representative of the actual simulated behaviour. The simulated relative displacements of MPBX1 in scenario S_{96} (Figure 103 on the next page) are used to explain the shortcomings of the initial calculations. A positive slope indicates dilation and a negative slope indicates contraction. All targets show contraction at the start of the loading phase. The three deepest located targets start to show dilation before calculation step 20,000. This sudden change is peculiar, because the loading stage continuous until calculation step 31,400 and contraction is still expected at this stage. The reason is an artificial minimum in the calculation. Equation 11.1 cannot result in negative values and thus is the relative displacement at the moment of installation the minimum value. This initial relative displacement is different for each target.

It is assumed that the vertical relative displacement is controlling the dilating or contracting behaviour of the rock mass around vertical extensometers that are loaded vertically. Section 11.1.2 will ratify this assumption. Hence, the relative displacement in the x- and y-direction is negligible. Equation 11.1 is accordingly simplified to equation 11.2. Equation 11.2 results in zero when the absolute displacement in the z-direction at the head of the instrument equals the absolute displacement in the z-direction at a target. The negative slope will be changed in a positive slope due to the absolute nature of the calculation. The slope direction of the graph should only switch when the difference between both absolute values becomes greater when the slope is negative or smaller when the slope is positive. The next subsection discusses the solution for this issue.

$$\sqrt{(zdisp_h - zdisp_T)^2} \quad \text{11.2}$$
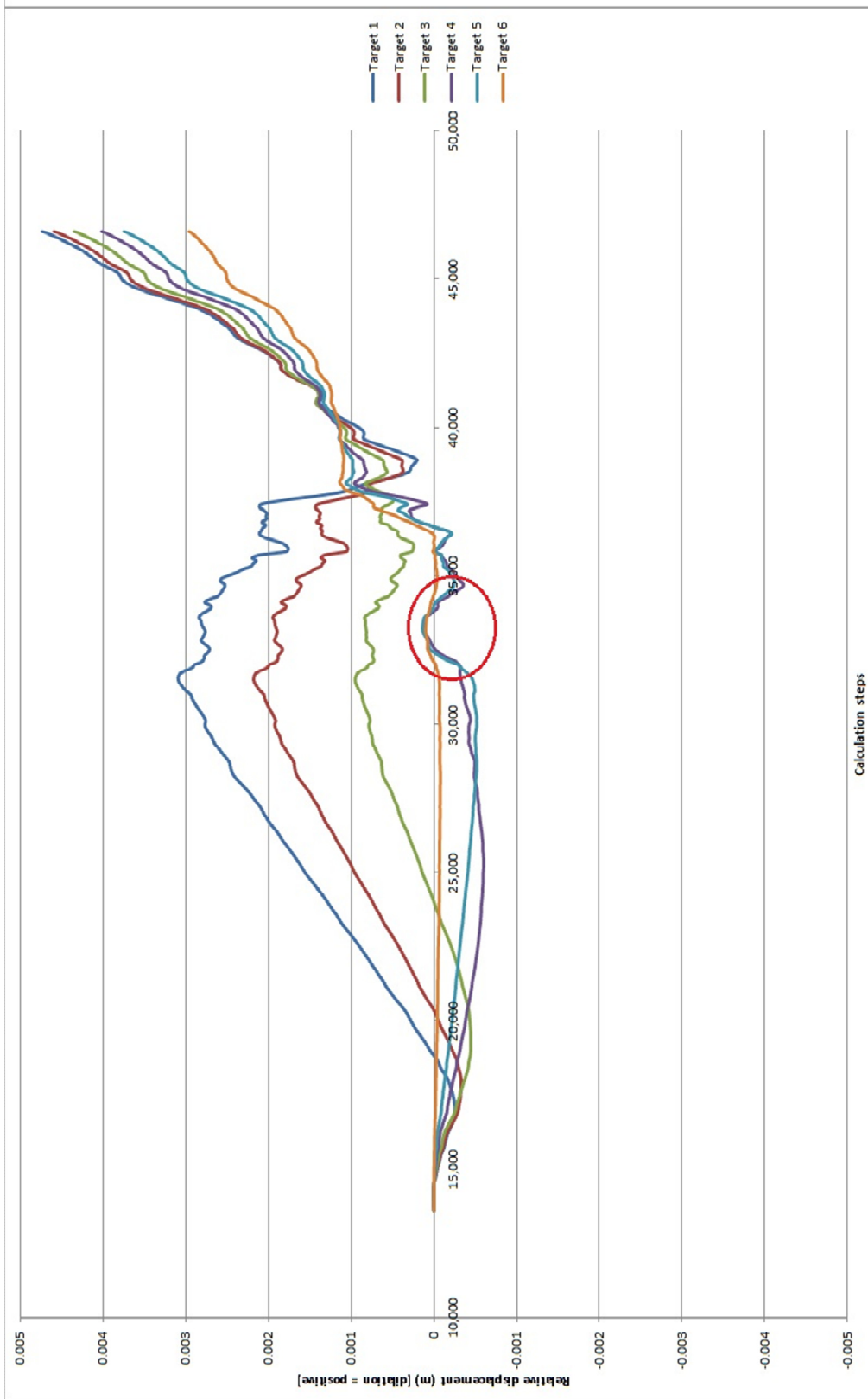
Figure 103: Initial calculations of relative displacements for MPBX1 in scenario S$_{96}$.

11.1.2 Correction

Correct displacement plots can be constructed when the z-displacement of all targets and the instrument head are recorded as histories in FLAC^{3D}. Negative values for z-displacement indicate downward movement. The difference between the z-displacement of a target and the z-displacement of the head at the start of monitoring, *e.g.* at calculation step 13,600 for MPBX1 in scenario S$_{96}$, is used to calibrate all the other measurements. Data points end up beneath the x-axis if history points moved closer together since the start of monitoring and vice versa. Equation 11.3 expresses the calculation for the relative displacement between target T and the head at calculation step i.

$$(zdisp_T - zdisp_H)_i - (zdisp_T - zdisp_H)_{start} \qquad \text{11.3}$$

This method is able to distinguish dilation from contraction and does not have an artificial minimum or maximum. Figure 104, on the next page, shows the corrected relative displacement plot. The loading stage is accompanied by a contracting trend and the unloading stage is accompanied by a dilative trend, according to expectations. The little bump at the transition from the loading stage to the unloading stage is due to the abrupt change in z-velocity of the grid points at the top of the model. The numerical model is slightly off-balance for a moment, but recovers quickly. The ultimate relative displacements at the last calculation step are similar to the results from the initial calculations. This verifies that displacements in horizontal direction can be neglected. The red circle in Figure 103 highlights a rock mass response in the horizontal direction that is not visible anymore in Figure 104.

11.1.3 Alternative correction

New simulations were needed to acquire the histories of z-displacements. Due to long computation times and time constraints at the end of this thesis project, the correct relative displacement plots of scenario S base case and S$_{64}$ are lacking. The correct results can be approached from the initial calculations by the following method.

The slope of the relative displacement graph is forced to be negative during the loading stage by applying equation 11.4. During the unloading stage, the graph is forced to be positive by applying equation 11.5. This results in an overestimate of contraction during the loading stage and an overestimate of dilation during the unloading stage. Since these two overestimates oppose one another and the equations force the graph into a shape that is characteristic for the rock mass behaviour, the final relative displacements at the last calculation step are still indicative of the correct relative displacements.

$$rdisp_i = rdisp_{i-1} - abs(rdisp_i - rdisp_{i-1}) \qquad \text{11.4}$$

$$rdisp_i = rdisp_{i-1} + abs(rdisp_i - rdisp_{i-1}) \qquad \text{11.5}$$

11.1.4 Comparison between MPBX1 & MPBX2

The final amount of dilation at MPBX1 is in every scenario bigger than the final amount of dilation at MPBX2. The difference in relative displacement between the deepest targets of the virtual extensometer stations is 0.0 – 1.0 mm. The scenario S base case is an exception. Here, the difference is approximately 7.0 mm. The span at the location of virtual extensometer MPBX1 is bigger than the span at the location of virtual extensometer MPBX2. This proves that the observed relative displacements are related to the location of an extensometer along the centre line of the extraction drift in an off-set herringbone layout.
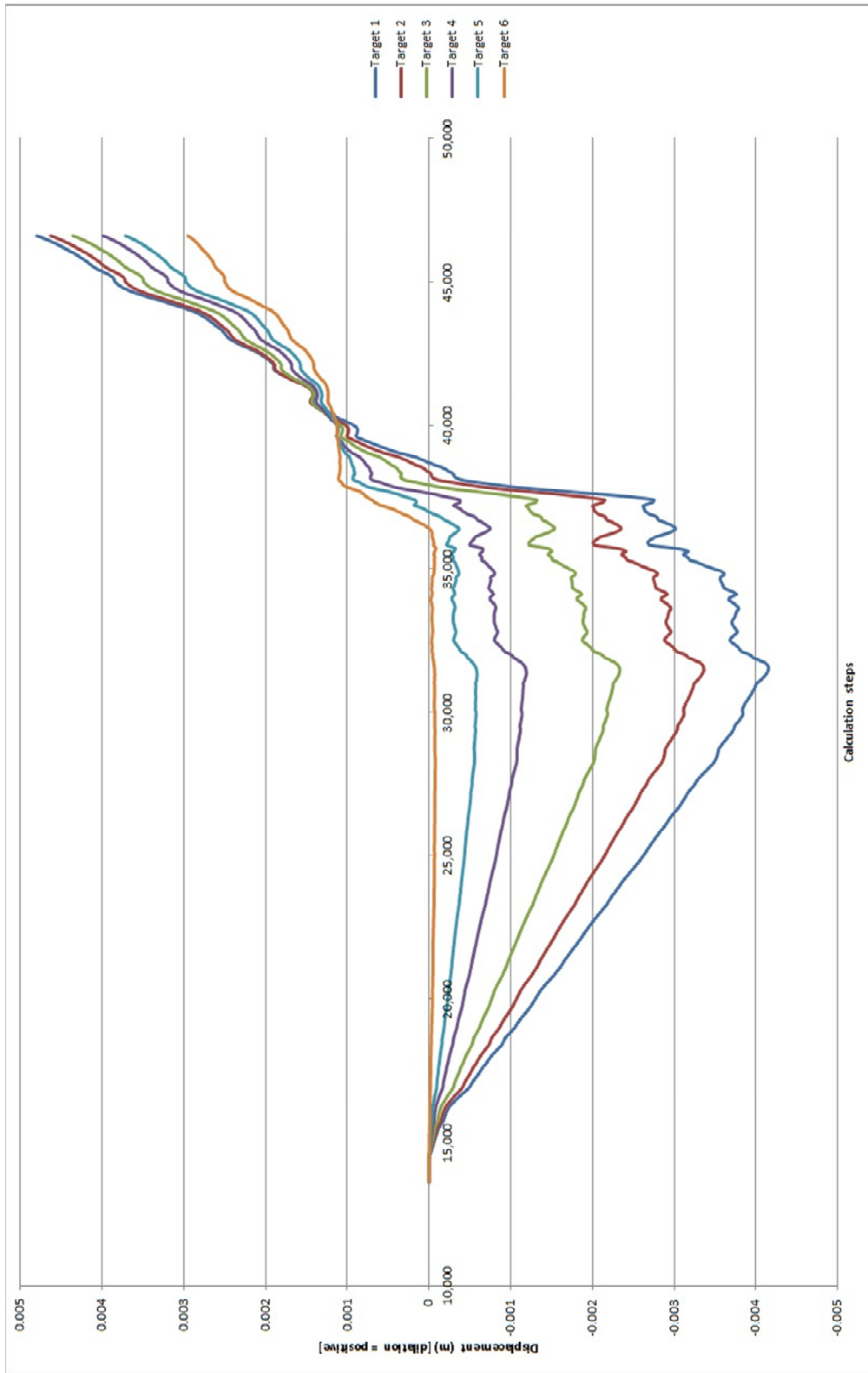
Figure 104: Correct calculations of relative displacements for MPBX1 in scenario S_{96}.

11.2 HB vs S base case

The abutment stress associated with 1% horizontal closure strain in the HB base case scenario is approximately 38 MPa. This is in accordance with the abutment stress observed by Sainsbury (2007) in Figure 81 and with typical abutment stress values, which are 2-3 times the initial vertical stress (van Hout, pers. comm., 2013b). Sainsbury (2007) used a bi-linear Mohr-Coulomb failure criterion instead of the Hoek-Brown failure criterion used in the HB base case, a slightly different set of input parameters indicated in Table 25 and a different modelling approach.

Table 25: Difference in key rock mass parameters.

	Sainsbury (2007)	This thesis project
GSI	55	59
UCS	90 MPa	81.6 MPa
ψ	9.3°	10°

The similarities in the results obtained by two different numerical modelling studies demonstrate the extent of similarity between the model used in this thesis and the real rock mass behaviour of Northparkes Mines block E48 lift #1. It must be emphasized though, that none of the models is calibrated. The S base case scenario requires an abutment stress which is almost twice as high, *i.e.* 72 MPa, before 1% horizontal closure strain can be observed at the extraction drifts. This proves that the application of the S-shaped failure criterion results in a stronger and stiffer rock mass.

In the S base case scenario, the amount of horizontal closure strain during the unloading stage is three times higher than the amount of horizontal closure strain during the loading stage. The HB base case shows not even half the amount of horizontal closure strain in the unloading stage relative to its loading stage. The destabilisation of the rock mass during stress-relief is indicative for failure of brittle rock masses. (van Hout, pers. comm., 2013b)

The apparent cohesion and stress magnitudes in the S base case scenario are approximately twice as high after the loading stage compared to the HB base case scenario. Concentrations of both parameters are distributed across the pillar in a similar fashion in both scenarios. After the loading stage, the de-stressed zone and damage skin are very similar in both cases although the S base case scenario shows more damage at the bullnoses. After the unloading stage, the difference in values of the apparent cohesion and major principal stress between the scenarios has become less.

The plasticity state plot shows a bigger elastic core in the S base case scenario at maximum abutment stress. After unloading, the elastic core in the S base case has diminished to a great extent. Projections of the Hoek-Brown s parameter on the horizontal cross-section of the extraction level show independence of confinement in the HB base case scenario and dependence of confinement in the S base case scenario. This validates the implementation of the rock mass parameters depending on confinement.

The virtual extensometer results show a similar amount of contraction during the loading stage in both scenarios and show relative displacements which are evenly distributed along the instruments. This contractive behaviour is not observed in the real MPBX data due to the relative late installation of the instruments during undercut development. Dilative displacements occur at approximately twice the rate of contractive displacements in the HB scenario. The final relative displacement of the deepest target in this scenario corresponds well to the observed relative displacements at the extraction level of E48 at Northparkes Mines. Half of the final relative displacement can be allocated to the first 1.5 meters of the rock mass surrounding the excavation. The rest of the final relative displacement is equally spread along the remaining 8.5 m of the virtual extensometer.

The S base case scenario shows the biggest final relative displacement of all scenarios and matches observed extensometer data at NPM to a lesser extent. However, the abrupt dilative behaviour observed at all targets is characteristic for brittle rock failure in a de-stressing environment, as discussed before. Especially the pattern of the relative displacement graph at MPBX1 is an excellent match with the average rock mass response of the selected extensometers at E48. The graph shows a very stable rock mass at 6.5 m from the excavation which is expected to coincide with the confinement level of the spalling limit.

A simulation of a triaxial test in FLAC^{3D} increases the axial stress on a cylindrical grid from both sides, while applying a confining stress. The confining stress is changed for each run to investigate the rock mass behaviour in different stress regimes. Figure 105 to 108 show the results of these simulations and highlight differences between the HB and S base case scenario. The black dots indicate peak strength and are a tool to correlate the axial stress – axial strain graph with the volumetric stain – axial strain graph. Notable observations from these plots are a significant stronger rock mass at higher confinements in the S base case scenario, the absence of a transition from brittle towards ductile behaviour upon increasing confining stress in the S base case scenario and similar volumetric-axial strain plots for both scenarios.

Bulking is recognisable as a steep slope of the volumetric-axial strain curve directly after peak strength. This can be interpreted as a relative high amount of radial strain, which is in the direction of the minor principal stress. The dilation angle is a constant input parameter in both scenarios and is responsible for the slope of the volumetric-axial strain curve after peak strength. In reality, dilatancy decreases with increasing confinement as has been shown before in Figure 50.
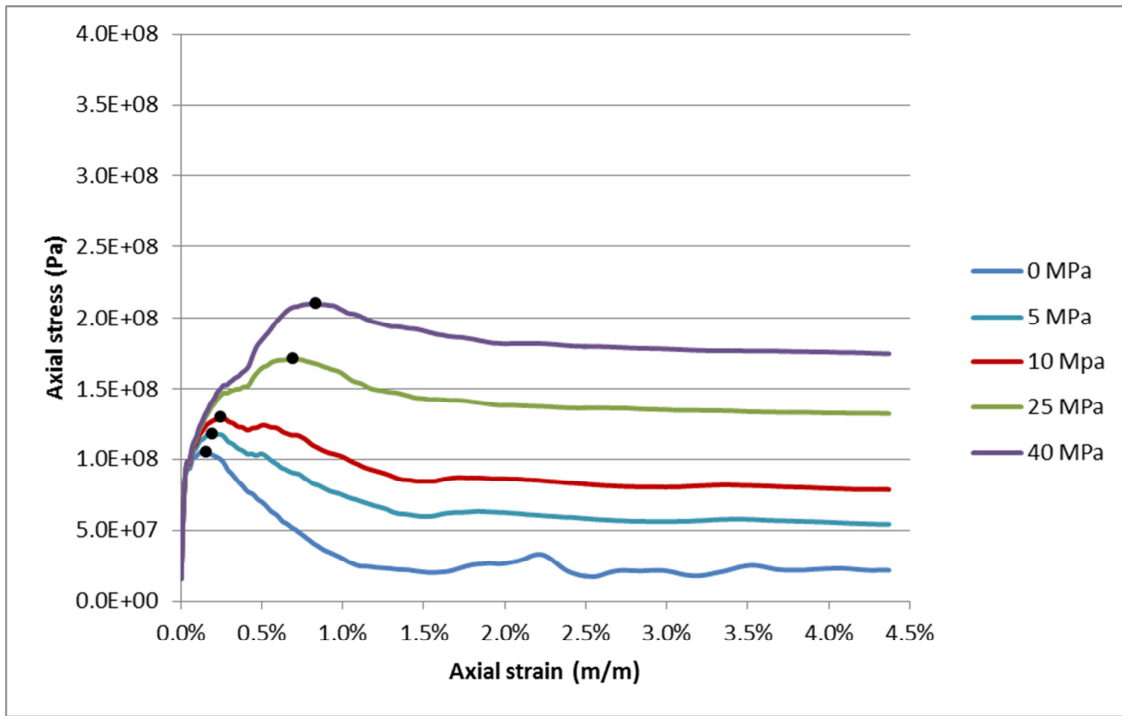
Figure 105: Results of a simulated triaxial test in the HB base case scenario; axial stress versus axial strain plots for different confining stresses. The black dots indicate peak strength and are in correspondence with Figure 106.
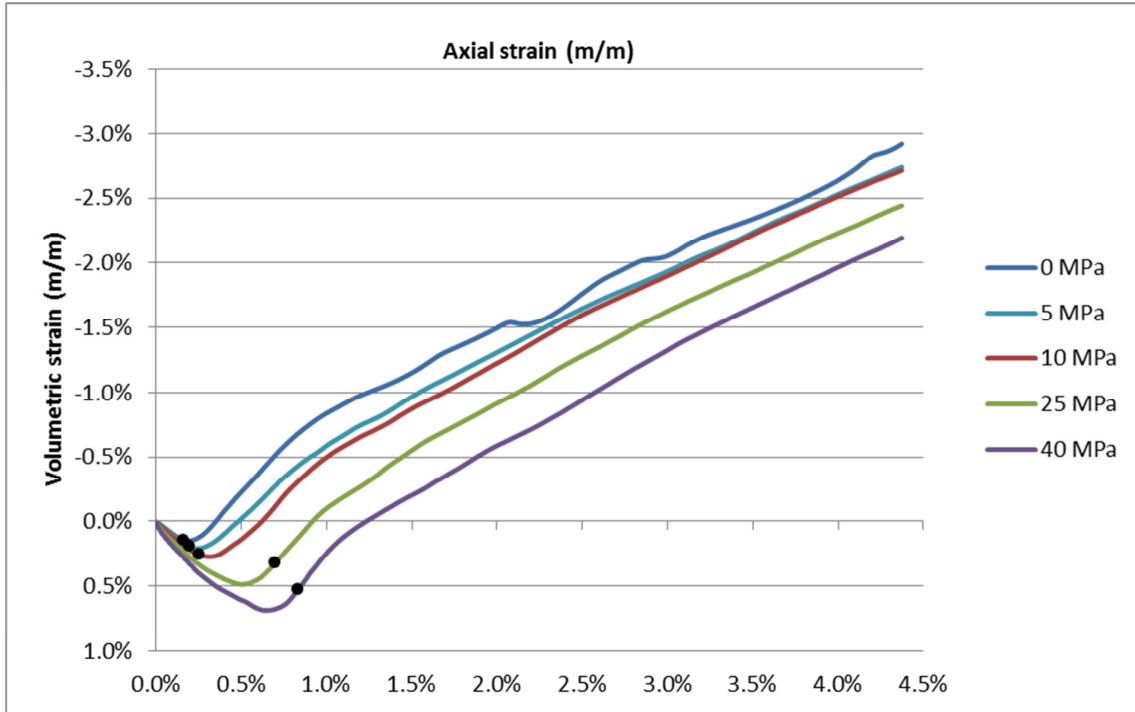
Figure 106: Results of a simulated triaxial test in the HB base case scenario; volumetric strain versus axial strain plots for different confining stresses. The black dots indicate peak strength and are in correspondence with Figure 105.
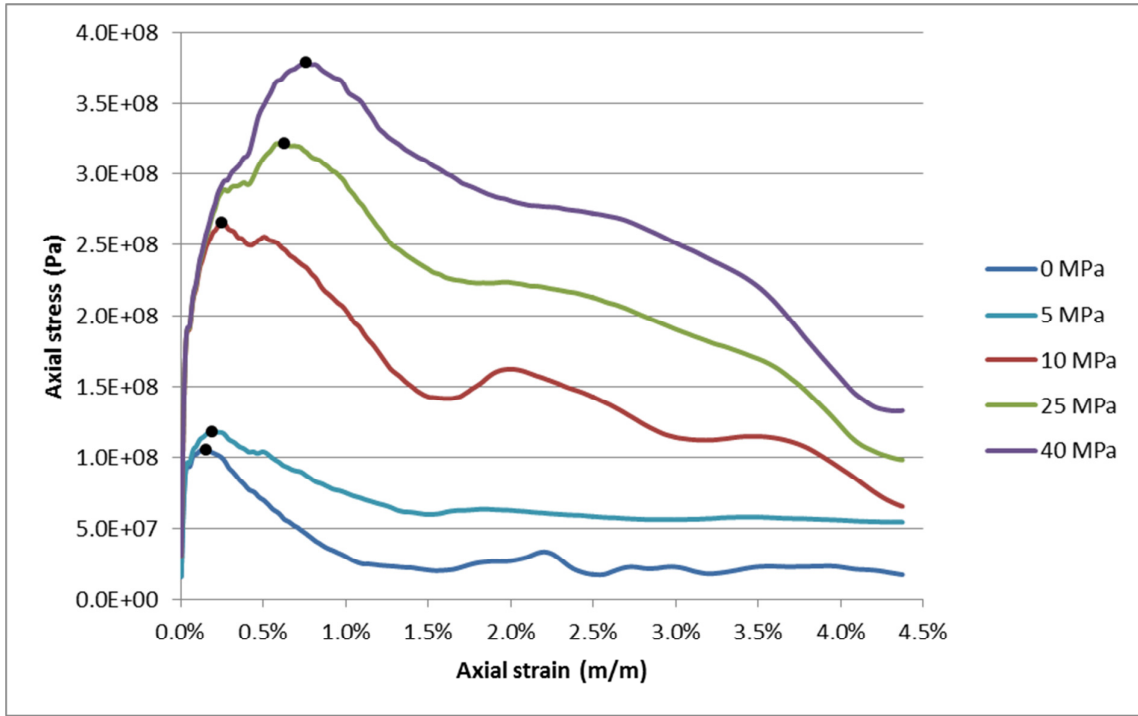
Figure 107: Results of a simulated triaxial test in the S base case scenario; axial stress versus axial strain plots for different confining stresses. The black dots indicate peak strength and are in correspondence with Figure 108.
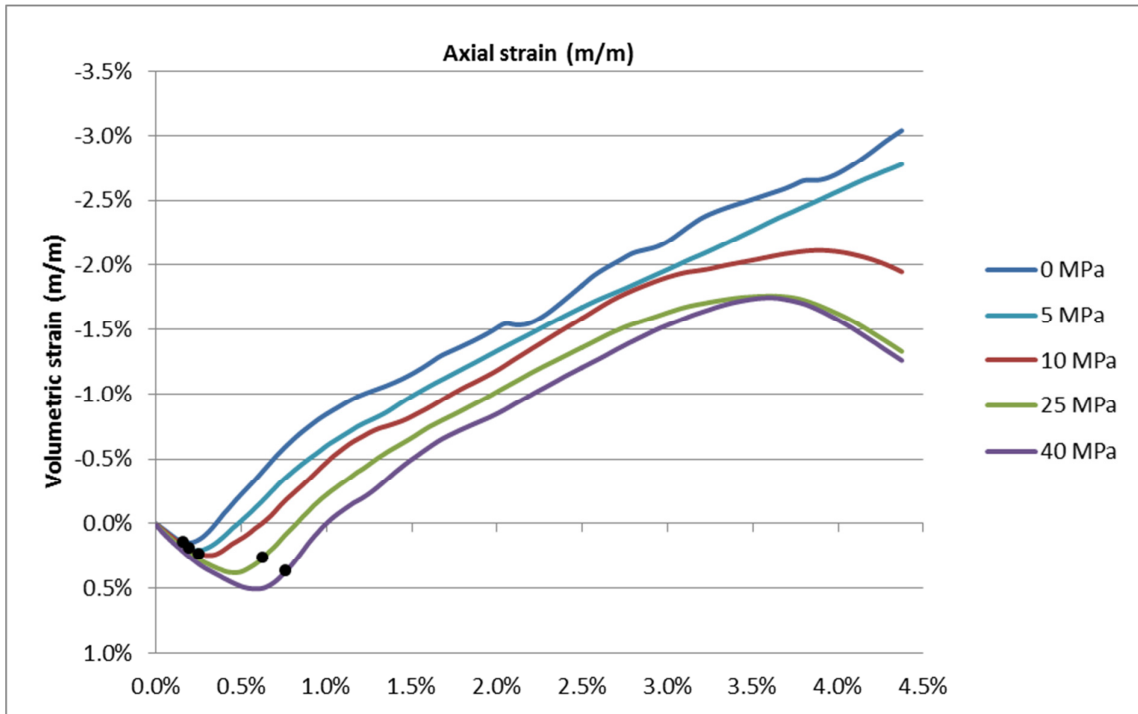
Figure 108: Results of a simulated triaxial test in the S base case scenario; volumetric strain versus axial strain plots for different confining stresses. The black dots indicate peak strength and are in correspondence with Figure 107.

11.3   HB vs S_{abut}

The abutment stress of the two scenarios in the previous section differs due to the choice of the stage control parameter, the horizontal closure strain. The difference in horizontal closure strain between the two approaches can be observed when the S-shaped failure criterion is used in a simulation with the abutment stress as stage control. This new scenario is called the S_{abut} scenario and its rock mass is expected to be stronger and stiffer than the rock mass in the HB base case scenario, because the quality of the rock mass of confined regions is enhanced while both scenarios are subjected to identical stress levels.

Now, the horizontal closure strain in the S_{abut} scenario seems to increase linearly from the start of the loading stage and continuous without a change of slope in the unloading stage. The total horizontal closure strain in the S_{abut} scenario is ten times smaller than the horizontal closure strain in the HB base case scenario which is prove of enhanced pillar stability. It is striking that FLAC^{3D} only needs half of the calculation steps of the HB base case scenario to simulate the loading and unloading stage for the S_{abut} scenario. Stress-strain curves at the top of the model and in the minor and major apex have identical trends. The amount of stress that is concentrated in the major apex is similar in both scenarios, but the HB scenario has much higher concentrations of stress in the minor apex. These stress concentrations are also visible in the horizontal cross-section after the unloading stage. It is obvious that the damage skin of the HB base case scenario extents further into the pillar compared to the S_{abut} scenario. It can be concluded that the stress concentrations are higher in smaller pillars due to their smaller volume. Apparent cohesion and plasticity state plots confirm a bigger damage skin for the HB base case scenario. The differences in damage skin area have become bigger after the unloading stage.

The S_{abut} scenario shows very small relative displacements at all targets. Besides, the contractive and dilative displacements are evenly spaced along the virtual extensometer. The abrupt dilation, observed in the S base case scenario, is absent. Furthermore, the final relative displacements do not match observed extensometer data at NPM. Simulated relative displacements indicate that the rock mass in the S_{abut} scenario is stronger than the rock mass in the HB base case scenario.

11.4 Sensitivity analysis of parameter M

The parameter M in equation 7.25 controls the degradation rate of the rock mass above the spalling limit. A limited data set, mostly consisting of triaxial tests performed in low confinement, was best matched by an S-shaped failure criterion with $M = 80$ (Kaiser, *et al.*, 2010; Valley, *et al.*, 2012). This section discusses the effects of a 20% increase or decrease of the parameter M. The S-shaped failure criterion shows more similarities with the generalised Hoek-Brown failure criterion when the parameter M is decreased, because the quality of confined rock is enhanced to a lesser extent. Indications of enhanced pillar stability are expected when the parameter M is increased.

An increase in the parameter M leads to a bigger de-stressed zone around the pillars at maximum abutment stress. The plasticity state and the apparent cohesion plots confirm that the de-stressed zone is damaged; especially the bullnoses are subject to instability. After unloading, the damage zones of scenario S_{64} and S base case have increased and are now similar. The damage zone of S_{96} only increased slightly and has become smaller relative to the other two scenarios. This indicates a bigger change in the size of the de-stressed zone during unloading, if M is decreased. The value of the Hoek-Brown s parameter for confined rock increases when the parameter M is increased. This observation is intrinsic to equation 7.25.

The abutment stress is reduced faster during the unloading stage, *i.e.* using less calculation steps, when the parameter M is relatively high. Also, the inflection points at the start and end of an increasingly steep section of the horizontal strain curve are more precise. The standard deviation of horizontal closure strain values of individual monitoring stations in the model is smaller when the parameter M is relatively low.

Abrupt dilative behaviour during the unloading stage, which is characteristic for brittle failing rock, is observed at all targets of virtual extensometers in scenario S base case and S_{96}. However, this behaviour is absent in scenario S_{64}. It has to be emphasized that relative displacement results for this sensitivity analysis are slightly compromised, because four out of the six virtual MPBX have been calculated using an alternative correction in subsection 11.1.3.

The next section compares stress-strain curves of all scenarios and includes additional comparative results of the sensitivity analysis of parameter M.

11.5 Stress-strain plots

Figure 109 to 112 plot the vertical stress at the top of the model, the centre of the major apex and the centre of the minor apex. Figure 112 plots the major principal stress at the centre of the major and minor apex. All these stresses are plotted against the horizontal closure strain in the extraction drifts. It must be emphasized that these plots should not be compared directly to stress-strain curves obtained from triaxial testing. The geometry of the three-dimensional model contains excavations and differs significantly from a cylindrical core. Moreover, the strain is measured within these excavations instead of radially outwards from a core.

Figure 109 combines all scenarios by plotting the vertical stress at the top of the model, termed abutment stress, versus horizontal closure strain in the extraction drifts. Scenario S base case and S_{96} show the most horizontal closure strain during the unloading stage, while scenario S_{64} shows the most horizontal closure strain during the loading stage, thus acting similar to the HB base case scenario. Counter-intuitively, the 1% horizontal closure strain in the extraction drift is reached at a significantly lower abutment stress when the parameter M is increased with 20%. A decrease of the parameter M by 20% is accompanied by a small decrease in the abutment stress at the top of the model and in the major and minor apex. The reason for this unexpected behaviour remains speculative, but it can be concluded that an increase of the parameter M does not necessarily mean increased overall pillar strength. The differing behaviour of these three scenarios makes it impossible to identify typical S-shaped behaviour. Furthermore, there is no data to validate any of these curves.

Figure 110 combines all scenarios by showing the vertical stress in the centre of the major and minor apex versus the horizontal closure strain. A comparison with Figure 109 shows that the vertical stress in the major apex is always greater than the abutment stress and the vertical stress in the minor apex is always smaller than the abutment stress.

By comparing Figure 111 and Figure 112, it is evident that the vertical stress in the major apex is equal to the major principal stress. The differences between the peak stress values for each scenario is maximum 3 MPa. On the other hand, major principal stresses in the minor apex have greater magnitudes than the vertical stress at those locations (1.5 – 2.1 times). It is obvious that the major principal stress direction in the major apex is vertical, while the vertical stress in the minor apex is not the major principal stress direction. The maximum major principal stress in the minor apices is reached at a higher horizontal closure strain value than the maximum major principal stress in the major apices.

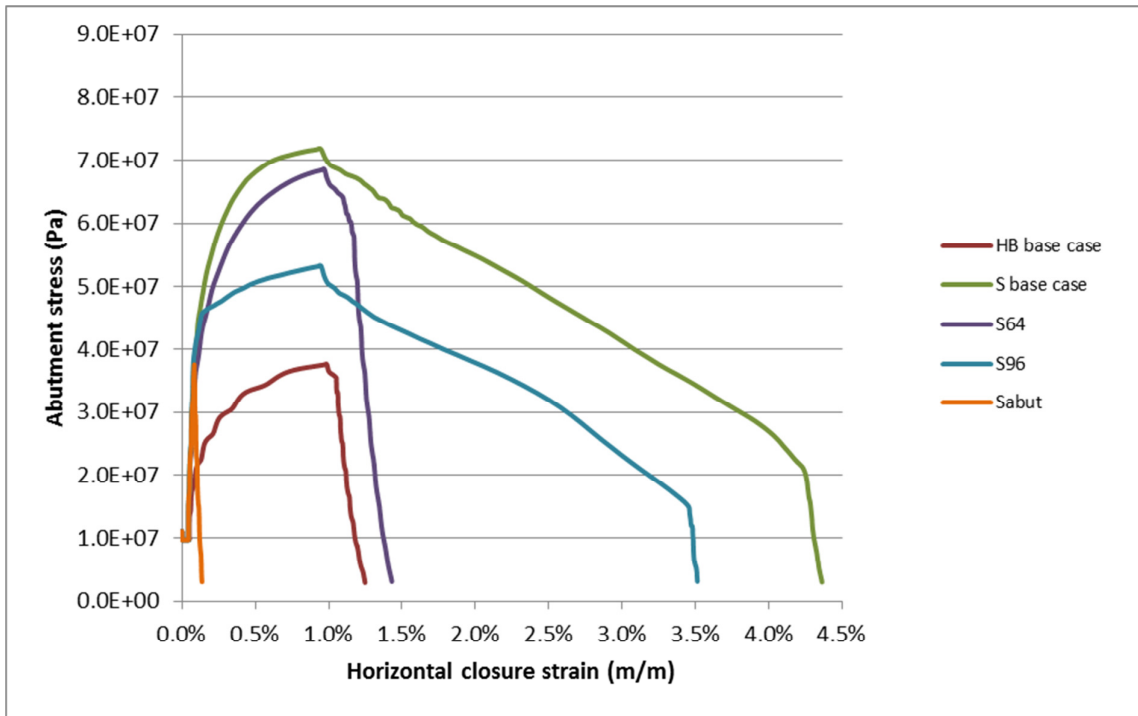**Figure 109: Abutment stress versus horizontal closure strain for each scenario.**
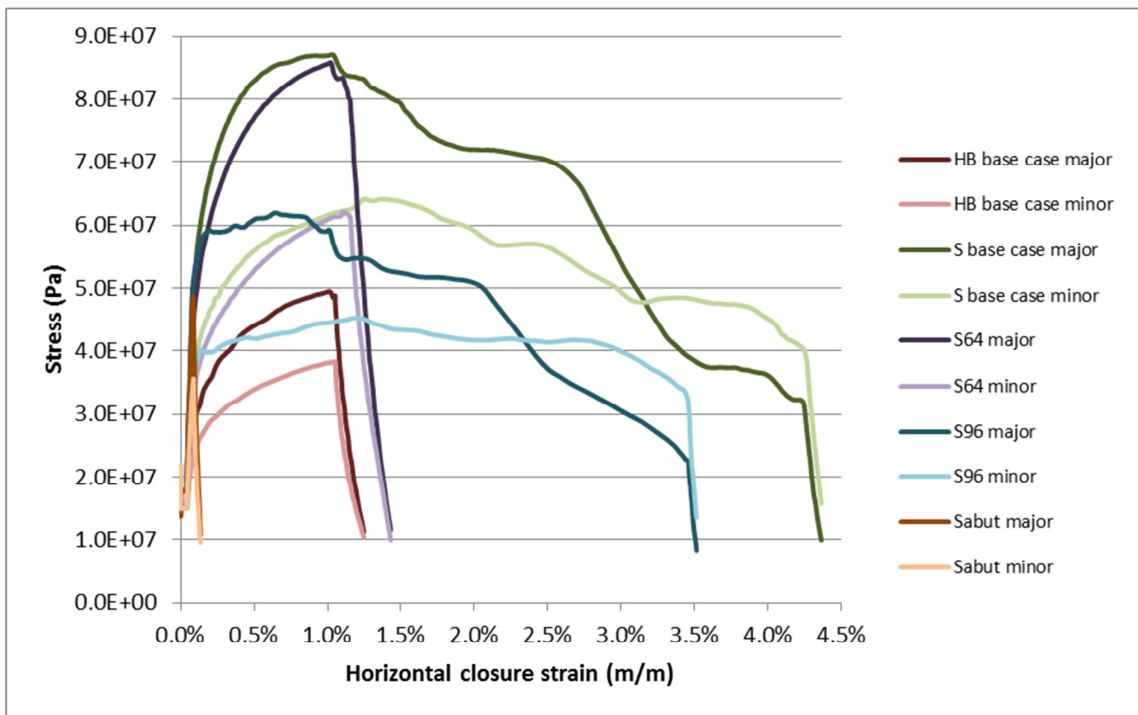

Figure 110: Vertical stress in the centre of the major and minor apex versus horizontal closure strain.
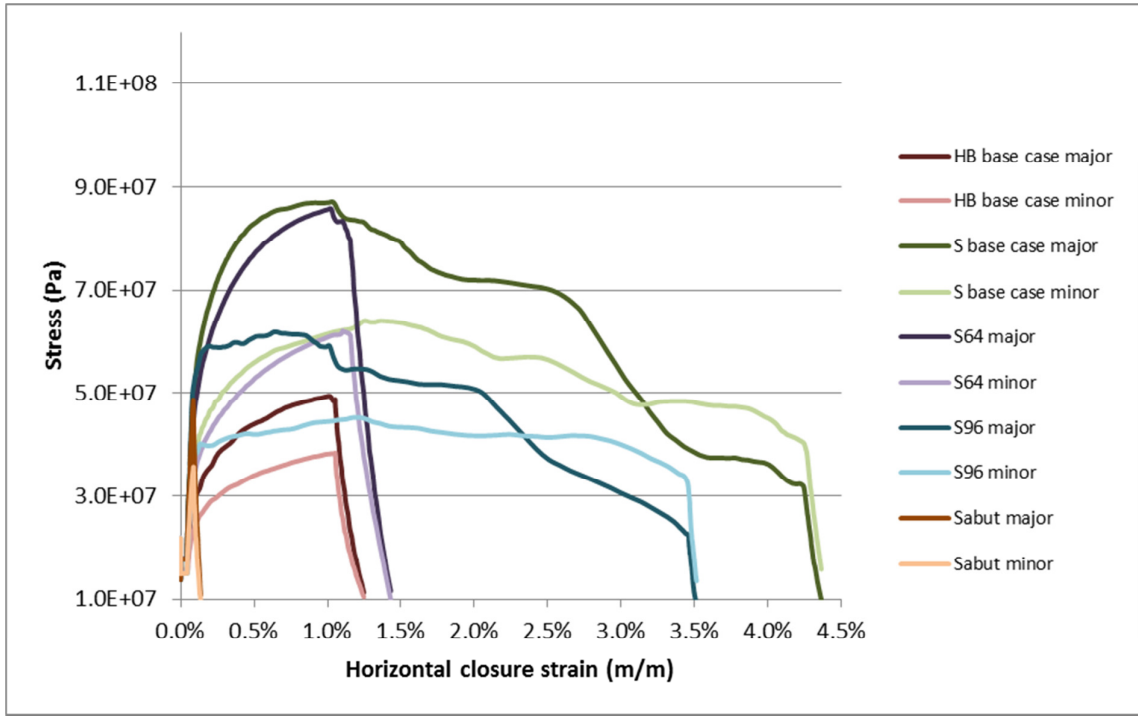
Figure 111: Vertical stress in the centre of the major and minor apex versus horizontal closure strain.
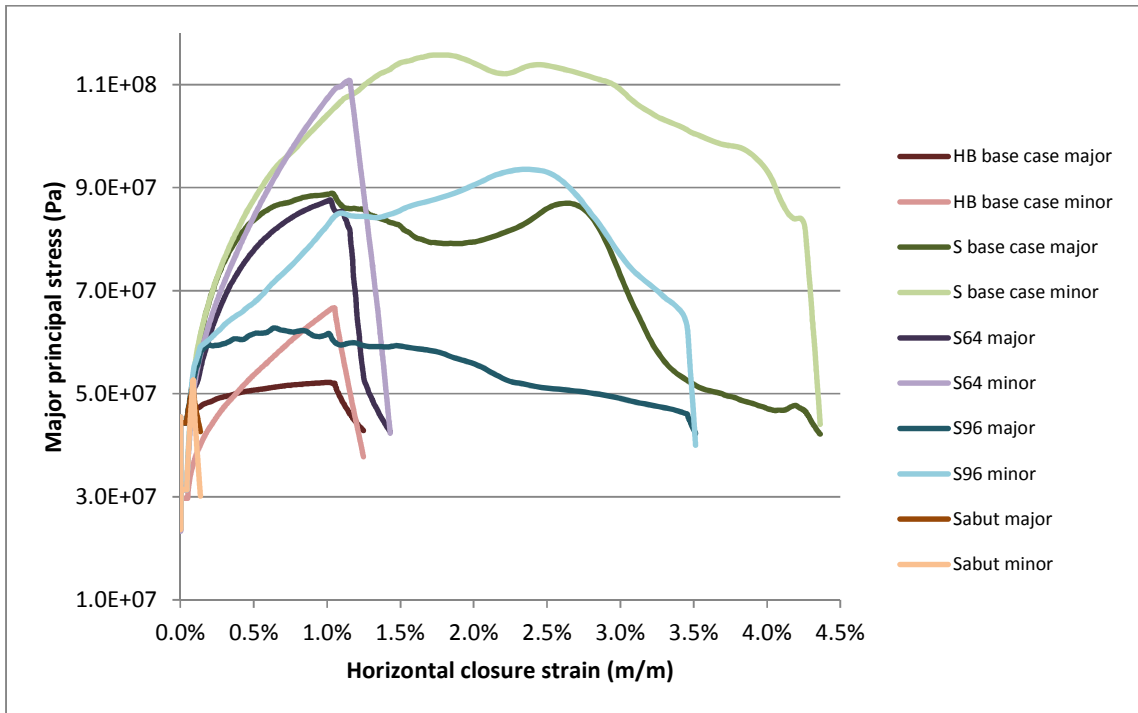

Figure 112: Major principal stress in the centre of the major and minor apex versus horizontal closure strain.

12 Conclusions

The aim of this project was to indicate differences in results derived from numerical modelling when either the S-shaped or the Hoek-Brown failure criterion was applied. The development of a user-defined *FISH*-function, that incorporates brittle spalling at low confining stresses and shear failure at relatively high confinements, has integrated brittle rock mass behaviour in a modified Hoek-Brown constitutive law. A simplified numerical model showed the functionality of the approach to implement the S-shaped failure criterion in FLAC^{3D} after which a three-dimensional, parameterized environment could be created by applying the mesh generator *KUBRIX* Geo on a Computer-Aided Design (CAD) of the extraction level. Undercut development was simulated by an adequate stress-path, characterised as a loading–unloading-loading sequence, representing the abutment stress, the stress shadow and cave load. This workflow has fulfilled two of the three objectives set at the start of the project and enables the comparison of simulated scenarios to indicate differences between the S-shaped and the Hoek-Brown failure criterion.

The remaining objective was to calibrate the numerical model in order to assess pillar stability at Northparkes Mines. The calibration of a rock mass constitutes of multiple iteration steps where initial rock properties are adjusted to match numerical modelling results and real-life measurements. The obtained rock mass parameters are only one way to represent reality. It may be that another set of parameters produces equal or better results. The horizontal closure strain threshold, used to control the transition from loading to unloading of the model, influences the simulated rock mass behaviour.

Nevertheless, a correlation between the simulated rock mass behaviour and geotechnical data has demonstrated the quality of the input parameters. The results obtained from analyses of horizontal convergence at the E48 extraction level were generally in line with a previously conducted examination of the integrity of the rock mass during undercut development. Sainsbury (2007) used a bi-linear Mohr-Coulomb failure criterion instead of a Hoek-Brown failure criterion, a slightly different set of input parameters and a different modelling approach, *i.e.* physical simulation of undercut development instead of a loading-unloading-loading sequence. The abutment stress resulting from Sainsbury's (2007) study and the HB base case scenario matched despite of these differences. This gave confidence in the selected rock mass parameters and the modelling strategy adopted in this thesis project.

Evaluation of the response of vertical MPBX stations to an advancing undercut front at Northparkes Mines block E48 lift #1, have revealed immediate dilative behaviour of the rock mass up to 6.5 m distance from the tunnel boundary, once the cave line has passed. The amount of relative displacement in the HB base case scenario matches these findings, but builds up gradually during unloading of the model and seems restricted to 5.0 m of the tunnel boundary. While the amount of relative displacement in the S base case scenario is higher than observed, the graphs explicitly show abrupt dilative behaviour. The shape of the graphs matches the measurements perfectly. Furthermore, the bigger the span of the excavation at the location of the MPBX along the centre line of the extraction drift in an off-set herringbone layout, the more dilation can be observed.

Incurred damage by the pillars is shown as plots of the Hoek-Brown s parameter, apparent cohesion, plasticity state and distribution of the major principal stress. It is obvious that pillar cores in the scenario using the S-shaped failure criterion are of superior strength. Their damage skins are similar to the HB base case scenario when stresses and cohesion are approximately twice as high after the loading stage. The bull noses area is recognised as the weakest part of the pillar which is confirmed by Lavoie and Pierce (2011b) and Peebles (2012).

The parameter M controls the degradation rate of the rock mass above the spalling limit in the S-shaped failure criterion. A limited data set was best matched by $M = 80$ (Kaiser, *et al.*, 2010; Valley, *et al.*, 2012). Enhanced pillar core stability was largely retained at a decrease of the parameter M by 20%, but abrupt dilative behaviour during unloading of the model was lost. An increase of 20% caused an unexpected, premature attainment of the horizontal closure strain limit, but retained abrupt dilative behaviour during unloading of the model. A simulation of a triaxial test in FLAC^{3D} does not show an increased amount of bulking when the S-shaped failure criterion is applied instead of the Hoek-Brown failure criterion. Along with the non-equivalent occurrence of horizontal closure strain while changing the parameter M, it can be concluded that more research is required to investigate the rock mass response to changes in parameters that define the S-shape failure criterion. Additional data of strain occurrence relative to the distance of the cave line is needed to validate results.

Since its introduction, it has taken many years to fully understand the limitations and range of application of the Hoek-Brown criterion. The S-shaped failure criterion is a state-of-the-art approach and although the basic concept is finding more support, the definition of its parameters will require more research in the coming years. Once fully developed and validated, application of the S-shaped failure criterion will have severe impact on pillar geometry, support systems and the extraction level layout and consequently will contribute to an optimisation of ore production. Altogether, this project improves the understanding of the application of the S-shaped failure criterion in continuum modelling and highlights its strengths and shortcomings.

13 Recommendations

Recommendations for future research on numerical modelling approaches for geomechanical problems at the extraction level of block caves are presented in section 13.1. Section 13.2 contains practical recommendations based on experience at Northparkes Mines to enhance the quality of data acquisition and to increase the performance of monitoring systems.

13.1 Modelling recommendations

- The difference in timing of the occurrence of horizontal closure strain during the loading-unloading cycle impedes the current use of the model. To overcome this issue, convergence measurements during undercut development have to be linked to the radial distance of the cave line towards the convergence station. These data should reveal the amount of horizontal closure strain at the moment the cave line passes a convergence station. This value should be used as stage control in a model using the loading-unloading sequence instead of the total amount of horizontal closure strain after undercut development.
- A different modelling approach that physically mimics undercut development by excavating the undercut level in increments is able to get around any issues with stage control thresholds. The downside is a lower level of detail and compromised computation times, because the complete footprint of a block cave has to be modelled in order to perform this modelling approach. It is advisable to increase mesh density in a central zone of the model to investigate the rock mass behaviour, while keeping mesh density outside this zone to a minimum.
- The loading and unloading of the model occurs at the same speed, *i.e.* the same velocity of grid points per calculation step. In reality, the change from high abutment stress to almost no vertical stress is much faster than the gradual increase in vertical stress as the cave line approaches. Future studies are needed to understand the effect of this difference on rock mass behaviour.
- The role of the shape and distribution of elements in a three-dimensional grid used in modelling of brittle rock masses is currently underexposed. Trials with hexa- and tetrahedral meshes in different compositions could reveal the mesh-dependency of the current model.
- The simulated MPBX results do not show a plateau after dilative behaviour at the last calculation steps. It would be interesting to see the rock mass behaviour during additional calculation steps without any changes to the stress field. It might even be possible to bring the model to an equilibrium state.
- A relation between the dilation angle and the confining stress and plastic shear strain, see section 6.3.2, needs to be incorporated in the S-shape constitutive law in order to simulate bulking behaviour.
- A simulation of a triaxial test of the rock mass does not show more ductile behaviour upon increasing confinement when the S-shaped failure criterion is applied. More research should indicate the reason for this behaviour and define the wanted rock mass response.
- This model does not incorporate any structural support. FLAC^{3D} is able to model structural elements of arbitrary geometries and properties. It would be interesting to see the effect of these structural elements on the rock mass behaviour. It is expected that active support has a much bigger influence on modelling results than passive support.

13.2 Operational recommendations

- It is advisable to start the monitoring of relative displacements long before commencing undercut development. This might result in detection of contractive behaviour of the rock mass prior to dilation. During undercut development, horizontal MPBX stations are expected to comply better with monitoring goals than vertical MPBX stations, because brittle failure in walls precedes de-stabilisation of the back. Preferentially, the extensometers should be installed ahead of advancing faces during development of tunnels at the extraction level to reveal initial tunnel wall displacements.

- Simultaneous installation of all eyebolts of a convergence station prior to undercut development is necessary to assess deformation of the complete tunnel profile. It is impossible to measure vertical convergence if the eyebolt in the back of the drift is missing. Improved tuning of the hand-held MPBX measurements will benefit comparative results of relative displacements across the extraction level. The time difference between the first and the last measured MPBX should be as short as possible and blasting times of drill drive rings should preferentially been taken into account.

- The installation of load and / or pressure cells will provide future studies with stress magnitudes and directions in the pillars during and after undercut development.

- Heavy machinery will less often cause downtime to parts of the monitoring system when the amount of wires is limited by implementing more wireless devices. Improved protection of extensometer stations would be beneficial as well.

- The design of a methodology to quickly spot trends of voltages that indicate malfunctioning of the extensometers or loggers would assist in the occasional interpretation of relative displacements in the rock mass.

- Results of the factual report on real-time monitoring data show that high draw rates close to MPBX stations are followed by a decline in rock mass dilation. This causality is obvious at a local scale, but further research is required to reveal correlation of convergence and draw rates at a global scale. It should be kept in mind that more factors, like cave development, are involved in this matter.

Personal communication

Atkins, R. (Rio Tinto – Geotechnical and Cave Engineering)

    a.   7 March 2013, Joint alteration of the E48 ore body [e-mail]

Bertotti, G. (Delft University of Technology)

    a.   25 March 2013, Vertical stress paradox [conversation]

Lavoie, T. (Itasca Consulting Group, Inc.)

    a.   8 March 2013, Caved rock modulus [e-mail]
    b.   10 April 2013, Implementation of *in situ* stresses in FLAC^{3D} [e-mail]

Powell, G. (Rio Tinto - Northparkes Mines)

    a.   7 February 2013, Current and previous extensometer stations [conversation]

Samosir, J. (Rio Tinto – Northparkes Mines)

    a.   4 February 2013, E48 rock mass parameters [conversation]

Sturm, P.L.M. (Rio Tinto – Mining Engineer)

    a.   19 June 2013, Initial stress equilibrium using a KUBRIX Geo grid [conversation]

Talu, S. (Rio Tinto - Geotechnical and Cave Engineering)

    a.   6 February 2013, Rock mass characterisation of E48 [conversation]

Van Hout, G. (Rio Tinto – Technology & Innovation)

    a.   5 March 2013, Interpretation of extensometer data [conversation]
    b.   23 April 2013, Preliminary simulation results [conversation]

Bibliography

Alejano, L. & Alonso, E., 2005. Considerations of the dilatancy angle in rocks and rock masses. *International Journal of Rock Mechanics & Mining Sciences,* Volume 42, pp. 481-507.

Bahrani, N., Valley, B., Kaiser, P. & Pierce, M., 2011. Evaluation of PFC2D Grain-Based Model for Simulation of Confinement-Dependent Rock Strength Degradation and Failure Processes. In: *Proc. 45th US Rock Mechanics Symposium.* San Francisco, CA, USA: American Rock Mechanics Association.

Barla, G. & Boshkov, S., 1980. Numerical modeling of block caving at the Grace Mine. In: W. Pariseau, ed. *Geomechanics applications in underground hardrock mining.* Turin, Italy: Society of Mining Engineers of the American Institute of Mining, Metallurgical and Petroleum Engineers, pp. 241-256.

Barton, N., 2002. Some new Q value correlations to assist in site characterisation and tunnel design. *International Journal of Rock Mechanics and Mining Sciences,* Volume 39, pp. 185-216.

Barton, N., 2008. Shear strength of rockfill, interfaces and rock joints, and their points of contact in rock-dump design. In: A. Fourie, ed. *Proc. Rock dumps 2008.* Perth, WA, Australia: Australian Centre for Geomechanics, pp. 3-17.

Barton, N. & Kjaernsli, B., 1981. Shear Strength of Rockfill. *Journal of the Geotechnical Engineering Division,* Volume 107, pp. 873-891.

Barton, N., Lien, R. & Lunde, J., 1974. Engineering classification of rock masses for the design of tunnel support. *Rock Mechanics,* 6(4), pp. 189-236.

Bieniawski, Z., 1976. Rock mass classification in rock engineering. In: Z. Bieniawski, ed. *Exploration for Rock Engineering.* Cape Town: Balkema, pp. 97-106.

Bieniawski, Z., 1989. *Engineering Rock Mass Classification.* New York: John Wiley and Sons.

Board, M. & Pierce, M., 2009. A review of recent experience in modelling of caving. In: G. Esterhuizen, ed. *Proceedings of the International Workshop on Numerical Modeling for Underground Mine Excavation Design.* Pittsburgh, PA, USA: Department of Health and Human Services, Centers for Disease Control and Prevention, National Institute for Occupational Safety and Health.

Brady, B. & Brown, E., 2004. *Rock Mechanics for Underground Mining.* 3rd ed. London: Chapman & Hall.

Brown, E., 2003. *Block Caving Geomechanics.* Indooroopilly, QLD, Australia: Julius Kruttschnitt Mineral Research Centre.

Brown, E., 2012. Progress and challenges in some areas of deep mining. In: *Proc. Sixth International Seminar on Deep and High Stress Mining.* Perth, WA, Australia: Australian Centre for Geomechanics.

Butcher, A., Cunningham, R., Edwards, K., Lye, A., Simmons, J., Stegman, C., Wyllie, A., 2011. *Northparkes Mines (Unpublished),* Parkes: Northparkes Mines.

Butcher, R., 1999. Design rules for avoiding draw horizon damage in deep level block caves. *The Journal of The South African Institute of Mining and Metallurgy,* pp. 151-155.

Butcher, R., 2000. Block cave undercutting - aims, strategies, methods and management. In: G. Chitombo, ed. *Proceedings MassMin 2000, Brisbane.* Melbourne: Australasian Institute of Mining and Metallurgy, pp. 405-411.

Cai, M., 2010. Practical Estimates of Tensile Strength and Hoek-Brown Strength Parameter m_i of Brittle Rocks. *Rock Mechanics and Rock Engineering,* Volume 43, pp. 167-184.

Cai, M. & Kaiser, P., 2006. Visualization of rock mass classification systems. *Geotechnical and Geological Engineering,* 24(4), pp. 1089-1102.

Cai, M., Kaiser, P.K., Tasaka, Y., Maejima, T., Morioka, H., Minami, M., 2004. Generalized crack initiation and crack damage stress thresholds. *International Journal of Rock Mechanics & Mining Sciences,* Volume 41, pp. 833-847.

Cai, M., Kaiser, P., Tasaka, Y. & Minami, M., 2007. Determination of residual strength parameters of jointed rock masses using the GSI system. *International Journal of Rock Mechanics & Mining Sciences,* Volume 44, pp. 247-265.

Carranza-Torres, C. & Fairhurst, C., 2000. Application of the convergence-confinement method of tunnel design to rock-masses that satisfy the Hoek-Brown failure criterion. *Tunneling and Underground Space Technology,* 15(2), pp. 187-213.

Carranza-Torres, C. & Labuz, J., 2006. *Class notes on Underground Excavations in Rock: The Convergence-Confinement Method (Unpublished),* Minneapolis, MN, USA: Department of Civil Engineering, University of Minnesota.

Carter, T., Diederichs, M. & Carvalho, J., 2008. Application of modified Hoek-Brown transition relationships for assessing strength and post yield behaviour at both ends of the rock competence scale. *The Journal of The Southern African Institute of Mining and Metallurgy,* Volume 108, pp. 325-338.

Chen, D., 2000. Meeting geotechnical challenges - a key to success for block caving mines. In: G. Chitombo, ed. *Proceedings MassMin 2000, Brisbane.* Melbourne: Australasian Institute of Mining and Metallurgy, pp. 429-436.

Clausen, J., 2007. *PhD Thesis: Efficient Non-Linear Finite Element Implementation of Elasto-Plasticity for Geotechnical Problems (unpublished).* Esbjerg, Denmark: Aalborg University.

Corkum, A., Lorig, L., DeGagné, D. & Jakubec, J., 2010. *Guidelines for mine tunnel support design (unpublished),* Minneapolis, MN, USA: ITASCA Consulting Group, Inc..

Coulomb, C., 1773. Application des règles de maxima et minima à quelques problèmes de statique relatifs à l'Architecture. *Memoires à l'Académie royale des Sciences par divers Savants,* Volume 7, pp. 343-382.

Crouch, S., 1970. Experimental Determination of Volumetric Strains in Failed Rocks. *International Journal of Rock Mechanics and Mining Sciences,* Volume 7, pp. 589-603.

Crowder, J. & Bawden, W., 2004. *Review of Post-Peak Parameters and Behaviour of Rock Masses: Current Trends and Research,* Toronto: Lassonde Institute, University of Toronto.

Department of Materials Science and Metallurgy, University of Cambridge, 2013. *Off-axis loading of a lamina.* [Online]
Available at: http://www.doitpoms.ac.uk/tlplib/fibre_composites/lamina_loading.php
[Accessed 21 May 2013].

deWolfe, C., 2009. *Drawpoint layouts for block caves (unpublished),* Brisbane, QLD, Australia: Rio Tinto.

deWolfe, V., 1981. Draw control in principle and practice at Henderson Mine. In: D. Stewart, ed. *Design and Operation of Caving and Sublevel Stoping Mines.* New York: Society of Mining Engineers of the American Institute of Mining, Metallurgical and Petroleum Engineers, pp. 729-735.

Diederichs, M., 1999. *PhD Thesis: Instability of Hard Rock Masses - The Role of Tensile Damage and Relaxation (unpublished).* Waterloo, ON, Canada: University of Waterloo.

Diederichs, M., Carvalho, J. & Carter, T., 2007. *A modified approach for prediction of strength and post yield behaviour for high GSI rock masses in strong, brittle ground.* Vancouver, Taylor & Francis.

Duffield, S., 2000. Design of the Second Block Cave at Northparkes E26 Mine. In: G. Chitombo, ed. *Proceedings MassMin 2000.* Brisbane: Australasian Institute of Mining and Metallurgy, pp. 335-346.

Duncan, J., Byrne, P., Wong, K. & Mabry, P., 1980. *Strength, stress-strain and bulk modulus paramters for finite element analysis of stress and movements in soil masses,* Berkeley, CA, USA: University of California.

Esterhuizen, G., 2006. An evaluation of the strength of slender pillars. *Transactions of Society for Mining, Metallurgy and Exploration,* Volume 320, pp. 69-76.

ETI Systems, 2013. *Linear Control Potentiometer - Design Guide.* [Online]
Available at: http://www.etisystems.com/lcpdesign.asp
[Accessed 20 February 2013].

Flores, G. & Karzulovic, A., 2002. *Geotechnical guidelines for a transition from open pit to underground mining. Benchmarking Report for International Caving Study II (unpublished),* Brisbane, QLD, Australia: Julius Kruttschnitt Mineral Research Centre.

Flores, G., Karzulovic, A. & Brown, E., 2004. Current practices and trends in Cave Mining. In: A. Karzulovic & M. Alfaro, eds. *Proceedings MassMin 2004.* Santiago, Chile: Mineria Chilena, pp. 83-89.

Frenzel, M., 2012. CAT Rock Flow System. In: *Proc. EXPOMIN 2012.* Santiago, Chile: Caterpillar Global Mining.

Gercek, H., 2007. Poisson's ratio values for rocks. *International Journal of Rock Mechanics & Mining Sciences,* Volume 44, pp. 1-13.

Glen, R., Walshe, J., Barron, L. & Watkins, J., 1998. Ordovician convergent margin volcanism and tectonism in the Lachlan sector of east Gondwana. *Geology,* Volume 26, pp. 751-754.

González-Nicieza, C., Álvarez-Fernández, M., Menéndez-Díaz, A. & Álvarez-Vigil, A., 2006. Comparative Analysis of Pillar Design Methods and its Application to Marble Mines. *Rock Mechanics and Rock Engineering,* 39(5), pp. 421-444.

Goodman, R. E., 1989. *Introduction to Rock Mechanics.* 2nd ed. New York: John Wiley & Sons.

Griffith, A., 1921. The phenomena of rupture and flow in solids. *Philosophical Transactions of the Royal Society of London,* Volume 221, pp. 163-198.

Grosvenor, V., 2013. *Risk assessment level 2 (unpublished),* Parkes, NSW, Australia: Northparkes Mines.

Hajiabdolmajid, V., Kaiser, P. & Martin, C., 2002. Modelling brittle failure of rock. *International Journal of Rock Mechanics and Mining Sciences,* Volume 39, pp. 731-741.

Hedley, D. & Grant, F., 1972. Stope and pillar design for the Elliot Lake uranium mines. *Bulletin of the Canadian Institute of Mining and Metallurgy,* Volume 65, pp. 37-44.

Hendrawan, D., 2011. *The geology of the upper level of E48 (E48 lift1) based on data from the relogging program in 2006 (unpublished),* Parkes, NSW, Australia: Northparkes Mines.

Hoek, E., 1994. Strength of rock and rock masses. *International Society for Rock Mechanics News Journal,* 2(2), pp. 4-16.

Hoek, E. & Brown, E., 1980. Empirical strength criterion for rock masses. *Journal of Geotechnical Engineering,* 106(GT9), pp. 1013-1035.

Hoek, E. & Brown, E., 1997. Practical estimates of rock mass strength. *International Journal of Rock Mechanics and Mining Science,* 34(8), pp. 1165-1186.

Hoek, E., Carranza-Torres, C. & Corkum, B., 2002. Hoek-Brown failure criterion - 2002 edition. In: *Proceedings of the 5th North American Rock Mechanics Symposium and the 17th Tunnelling Association of Canada conference, NARMS-TAC 2002.* Toronto: North American Rock Mechanics Society, pp. 267-273.

Hoek, E. & Diederichs, M., 2006. Empirical estimation of rock mass modulus. *International Journal of Rock Mechanics & Mining Sciences,* Volume 43, pp. 203-215.

Hoek, E. & Franklin, J., 1968. A simple triaxial cell for field and laboratory testing of rock. *Transactions of the Institution of Mining and Metallurgy,* Volume 77, pp. 22-26.

Hoek, E., Kaiser, P. & Bawden, W., 1995. *Support of underdground excavations in hard rock.* Rotterdam: Balkema.

Hudson, J. & Harrison, J., 1997. *Engineering Rock Mechanics: An Introduction to the Principles.* Oxford: Pergamon Press.

InfoMine, 2010. *Underground Mining Methods.* [Online]
Available at: http://technology.infomine.com/reviews/UgMiningMethods/
[Accessed 30 May 2013].

InfoMine, 2013. *InvestmentMine - Mining Markets & Investment.* [Online]
Available at: http://www.infomine.com/investment/metal-prices/copper/all/
[Accessed 1 March 2013].

Itasca Consulting Group, Inc., 2013. *FLAC3D Version 5.0 manual (unpublished),* Minneapolis, MN, USA: ITASCA Consulting Group, Inc..

ITM-Soil Pty Ltd., 2009. *Digital tape extensometer.* [Online]
Available at: http://www.itm-soil.com.au/content/digital-tape-extensometer-2
[Accessed 5 May 2013].

Ivars, D. M., Pierce, M., Reyes-Montes, J. & Young, R. P., 2008. *Mass Mining Technology Project; Caving Mechanics Task - Executive Summary (unpublished),* Brisbane, QLD, Australia: Sustainable Minerals Institue, University of Queensland.

Jing, L., 2003. A review of techniques, advances and outstanding issues in numerical modelling for rock mechanics and rock engineering. *International Journal of Rock Mechanics and Mining Sciences,* Issue 40, pp. 283-353.

Kaiser, P., 2010. How highly stressed brittle rock failure impacts tunnel design. In: *Proceeding of the International Society for Rock Mechanics Regional Symposium EUROROCK 2010.* Lausanne, Switzerland: Swiss Society for Soil and Rock Mechanics .

Kaiser, P.K., Diederichs, M.S., Martin, D., Sharpe, J., Steiner, W., 2000. *Underground Works in Hard Rock Tunnelling and Mining.* Melbourne, VC, Australia, Technomic Publishing Company.

Kaiser, P. & Kim, B., 2008. Rock Mechanics Challenges in Underground Construction and Mining. *Australian Centre for Geomechanics Newsletter,* 31(1-5).

Kaiser, P., Kim, B., Bewick, R. & Valley, B., 2010. Rock mass strength at depth and implications for pillar design. In: M. van Sint Jan & Y. Potvin, eds. *Proceedings of the 5th International Seminar on Deep and High Stress Mining.* Crawley, WA, Australia: Australasian Centre for Geomechanics, pp. 463-476.

Krauland, N. & Soder, P., 1987. Determining pillar strength from pillar observation. *Engineering & Mining Journal,* Volume 8, pp. 34-40.

Laubscher, D., 1994. Cave Mining - The state of the art. *Journal of The South African Institute of Mining and Metallurgy,* 94(10), pp. 279-293.

Laubscher, D., 2000. *Block Caving Manual.* Brisbane, QLD, Australia: Julius Kruttschnitt Mineral Research Centre and Itasca Consulting Group, Inc..

Laubscher, D. & Esterhuizen, 1992. A comparative evaluation of production-level layouts for block caving. In: H. Glen, ed. *Proc. MassMin 1992.* Johannesburg, South Africa: South African Institute of Mining and Metallurgy.

Laubscher, D. & Jakubec, J., 2001. The MRMR rock mass classification for jointed rock masses.. In: W. Hustrulid & R. Bullock, eds. *Underground Mining Methods: Engineering Fundamentals and International Case Histories..* Littleton, Colorado: Society for Mining, Metallurgy and Exploration, pp. 475-481.

Lavoie, T. & Pierce, M., 2011a. *Extraction-Level Stability Assessment (Unpublished),* Minneapolis, MN, USA: Itasca Consulting Group, Inc..

Lavoie, T. & Pierce, M., 2011b. *Resolution Copper Mine Extraction-Level Analysis (unpublished),* Minneapolis, MN, USA: ITASCA Consulting Group, Inc..

Leach, A., Naidoo, K. & Bartlett, P., 2000. Considerations for design of production level drawpoint layouts for a deep block cave. In: G. Chitombo, ed. *MassMin 2000, Brisbane.* Melbourne: Australasian Institute of Mining and Metallurgy, pp. 357-366.

Lorig, L., 2000. *The Role of Numerical Modelling in Assessing Caveability (unpublished),* Minneapolis, MN, USA: Itasca Consulting Group, Inc..

Lorig, L. & Pierce, M., 2000. *Methodology and Guidelines for Numerical Modelling of Undercut and Extraction-Level Behaviour in Cavind Mines (unpublished),* Minneapolis, MN, USA: Itasca Consulting Group, Inc..

Lovejoy, C., 2012. Keeping up with caving. *Mining Magazine*, June, pp. 46-67.

Lovitt, M., 2006. *E48 Drill and Blast Design (unpublished),* Brisbane, QLD, Australia: Orica Mining Services.

Lunder, P., 1994. *Hard rock pillar strength estimation: An applied empirical approach,* Vancouver BC, Canada: University of British Colombia.

Lunder, P. & Pakalnis, R., 1997. Determination of the strength of hard-rock mine pillars.. *Bulletin of the Canadian Institute of Mining and Metallurgy,* Volume 90, pp. 51-55.

Marachi, N., Chan, C. & Seed, H., 1972. Evaluation of properties of rockfill materials. *Journal of Soil Mechanics,* Volume 98, pp. 95-114.

Martin, C., 1997. The effect of cohesion loss and stress path on brittle rock strength. *Canadian Geotechnical Journal,* 34(5), pp. 698-725.

Martin, C. & Maybee, W., 2000. The strength of hard-rock pillars. *International Journal of Rock Mechanics & Mining Sciences,* Volume 37, pp. 1239-1246.

McClintock, F. & Walsh, J., 1962. Friction of Griffith cracks in rock under pressure. In: *Proceedings of the 4th United States National Congress of Applied Mechanics.* Berkeley, CA, USA: American Society of Mechanical Engineers, pp. 1015-1022.

Mine Design Technologies, 2013. *Mine Design Technologies Products.* [Online]
Available at: http://www.mdt.ca/content/
[Accessed 20 February 2013].

Mogi, K., 1966. Pressure dependence of rock strength and transition from brittle fracture to ductile flow. *Bulletin of the Earthquake Research Institute, University of Tokyo,* Volume 44, pp. 215-32.

Moss, A., 2010. *Presentation: Cave Mining Systems - An introduction (unpublished).* Vancouver, BC, Canada(BC): Rio Tinto.

Moss, A., 2011. *Global Metals & Mining Conference - An introduction to Block and Panel Caving.* [Online]
Available at: http://www.femp.org/wp-content/uploads/2011/07/CAT-workshop-Rio-Tinto-Block-Caving.pdf
[Accessed 23 May 2013].

Murrell, S., 1964. The theory of the propagation of elliptical Griffith cracks under various conditions of plane strain or plane stress. *British Journal of Applied Physics,* Volume 15, pp. 1195-1234.

Northparkes Mines, 2011. *Sustainable development report.* [Online]
Available at: http://www.northparkes.com.au
[Accessed 14 December 2012].

Onederra, I., 2005. *Extraction level design course, University of Queensland (unpublished).* Brisbane, QLD, Australia: Julius Kruttschnitt Mineral Research Centre.

Onederra, I., 2008. *Evaluation of Undercut and Drawbell Parameters of the Northparkes E48 Block Cave Development (unpublished),* Brisbane, QLD, Australia: JKTech Pty Ltd.

Ortiz, J., Serra, J. & Oteo, C., 1986. *Curso Aplicado de Cimentaciones.* 3rd ed. Madrid: Colegio Oficial de Arquitectos de Madrid.

Ortlepp, W., 1997. *Rock Fracture and Rockbursts - an Illustrative Study,* Johannesburg: South African Institute of Mining and Metallurgy.

Palma, R. & Agarwal, R., 1973. *A study of the cavability of primary ore at the El Teniente mine,* New York: Columbia University.

Pappas, D. M. & Mark, C., 1993. *Behavior of Simulated Longwall Gob Material,* Pittsburgh: United States Department of the Interior - Bureau of Mines.

Peebles, E., 2012. *E48 Re-development project: Project Execution Plan (unpublished),* Parkes, NSW, Australia: Northparkes Mines.

Pierce, M., 2006. *Application of Synthetic Rock Mass (SRM) Testing to Northparkes E48 Caving Prediction - Summary of Preliminary Study Results,* Minneapolis: Itasca Consulting Group, Inc..

Pierce, M., Cundall, P., Mas Ivars, D., Darcel, C., Young, R., Reyes-Montes, J., Pettitt, W., 2006. *Six Monthly Technical Report, Caving Mechanics (unpublished),* Minneapolis, MN, USA: Itasca Consulting Group, Inc..

Pierce, M. & Lorig, L., 1998. *FLAC3D Analysis of Cavability of the Northparkes E26 Lift 2 Orebody (unpublished),* Minneapolis, MN, USA: Itasca Consulting Group, Inc..

Pierce, M., O'Connor, C., Sainsbury, D., Lavoie, T., Garcia, X., 2011. *Predictions of Caving and Infrastructure Stability in Support of the Feasibility Study for Panel Caving at Oyu Tolgoi, Hugo North, Lift 1 [DRAFT] (unpublished),* Minneapolis, MN, USA: ITASCA Consulting Group, Inc..

Potvin, Y., Hudyma, M. & Miller, H., 1989. Rib pillar design in open stope mining. *Bulletin of the Canadian Institute of Mining and Metallurgy,* Volume 82, pp. 31-37.

Rech, W. & Lorig, L., 1992. Predictive numerical stress analysis of panel caving at the Henderson Mine. In: *Proceedings MASSMIN '92.* Johannesburg, South Africa: Southern African Institute of Mining and Metallurgy, pp. 55-62.

Richardson, M., 1981. Area of draw influence and drawpoint spacing for block caving mines. In: D. Stewart, ed. *Design and Operation of Caving and Sublevel Stoping Mines.* New York: Society of Mining Engineers, AIME, pp. 149-156.

Rojas, E., Molina, R., Bonani, A. & Constanzo, H., 2000. The pre-undercut caving method at the El Teniente Mine, Codelco - Chile. In: G. Chitombo, ed. *Proceedings MassMin 2000, Brisbane.* Melbourne: Australasian Institute of Mining and Metallurgy, pp. 261-266.

Rosling, H., 2013. *GAPMINDER - For a fact based world view.* [Online]
Available at: http://www.gapminder.org
[Accessed 1 March 2013].

Sainsbury, B., Sainsbury, D. & Pierce, M., 2011. *A historical review of the development of numerical cave propagation simulations (unpublished),* Minneapolis, MN, USA: Itasca Consulting Group, Inc..

Sainsbury, D., 2007. *Investigation of Advance- and Post-Undercut Sequences for Extraction Level Development at the E48 mine (unpublished),* Minneapolis, MN, USA: Itasca Consulting Group, Inc..

Serafim, J. & Pereira, J., 1983. Consideration of the geomechanical classification of Bieniawski. *Proceedings of the International Symposium on Engineering Geology and Underground Construction,* 1(II), pp. 33-44.

Sheorey, P., 1994. A theory for in situ stresses in isotropic and transversely isotropic rock. *International Journal of Rock Mechanics and Mining Science & Geomechanics Abstracts,* 31(1), pp. 23-34.

Sheorey, P., Das, M., Barat, D., Prasad, R., Singh, B., 1987. Coal pillar strength estimation from failed and stable cases. *International Journal of Rock Mechanics and Mining Sciences & Geomechanics Abstracts,* Issue 24, pp. 347-402.

Sheorey, P. & Singh, B., 1974. Strength of rectangular pillars in partial extraction. *International Journal of Rock Mechanics and Mining Sciences & Geomechanics Abstracts,* Issue 11, pp. 41-47.

Silveira, A., 2004. *Undercutting at E26 lift #2 Northparkes (unpublished),* Brisbane, QLD, Australia: RioTinto.

Sjöberg, J., 1992. *Failure modes and pillar behaviour in the Zinkgruvan Mine.* Santa Fe, A.A. Balkema, pp. 491-500.

Stacey, T. & Page, C., Practical handbook for underground rock mechanics. *1986.* Clausthal-Zellerfel: Trans Tech Publications, Inc..

Starfield, A. & Fairhurst, C., 1968. How high-speed computers advance the design of practical mine pillar systems. *Engineering & Mining Journal,* 5(169), pp. 78-84.

Steinberg, J., Frenzel, M. & Krings, J., 2013. *Block Cave Mine 2020 - Case study on a continuously operated Mega Mine,* Oak Creek, WI, USA: Caterpillar Global Mining.

Strata Testing Services, 2004. *Geotechnical laboratory rest report - triaxial test (unpublished),* Corrimal, New South Wales: Strata Testing Services.

Sturm, P., 2012. *MSc Thesis: Calibration of the Quartz Monzodiorite rock mass properties for the Oyu Tolgoi Cu-Au underground block cave mine (unpublished),* Delft, The Netherlands: Delft University of Technology.

Tod, J. & Lausch, P., 2003. *Interpreting and Troubleshooting SMART Instrumentation.* [Online]
Available at: http://www.mdt.ca/sites/default/files/smart_instrumentation-paper.pdf
[Accessed 6 December 2012].

Valley, B., Kim, B., Suorineni, F., Bahrani, N., Bewick, R., Kaiser, P., 2012. *Influence of confinement dependent failure processes on rock mass strength at depth.* London, Taylor & Francis Group.

van As, A., 2004. *E48 Evaluation Study (B) - Geotechnical investigations (unpublished),* Brisbane, QLD, Australia: Mine Geotechnical Services Pty. Ltd..

van As, A., 2011. *Ground control management plan (unpublished),* Brisbane, QLD, Australia: Rio Tinto.

Vermeer, P. & de Borst, R., 1984. Non-associated plasticity for soil, concrete and rock. *Heron,* 29(3), pp. 1-65.

Vink, D., 1995. *Minimising blast damage to the extraction level of Northparkes Mines E26 block cave..* Brisbane, Australasian Institute of Mining and Metallurgy, pp. 251-260.

Vlachopoulos, N. & Diederichs, M., 2009. Improved Longitudinal Displacement Profiles for Convergence Confinement Analysis of Deep Tunnels. *Rock Mechanics and Rock Engineering,* Volume 42, pp. 131-146.

Von Kimmelman, W., 1984. *The use of computer applications at BCL Limited in planning pillar extraction and the design of mining layouts.* London, British Geotechnical Society, pp. 53-63.

Wagner, H., 1980. Pillar design in coal mines. *Journal of the South African Institute of Mining and Metallurgy,* Volume 80, pp. 37-45.

Wattimena, R., 2003. *PhD Thesis: Designing undercut and production level drifts of block caving mines (unpublished),* Brisbane, QLD, Australia: Julius Kruttschnitt Mineral Research Centre, University of Queensland.

White, S., 2013. *Mines2Markets - Towards peak copper...?.* [Online]
Available at: http://m2m.riotinto.com/article/towards-peak-copper
[Accessed 1 March 2013].

Wilson, A., 1972. A hypothesis concerning pillar stability. *The Mining Engineer,* Volume 131, pp. 409-417.

Wyllie, A. R. & Webster, S. B., 2012. *Northparkes Mines - Step Change Project (unpublished),* Parkes, NSW, Australia: Northparkes Mines.

Zhao, X. & Cai, M., 2010. A mobilized dilation angle model for rocks. *International Journal of Rock Mechanics & Mining Sciences,* Volume 47, pp. 368-384.

Zuo, X., Wei, Y., Chen, J., Zeng, L., Ruan, X., 1999. 3D FEM simulation of multi-stage forging process using solid modeling of forging tools. *Journal of Materials Processing Technology,* Volume 91, pp. 191-195.